High-Temperature Ceramic Matrix Composites Prepared via Microwave Energy Enhanced Chemical Vapour Infiltration



UNIVERSITY OF BIRMINGHAM

Matthew Thomas Porter

A thesis submitted to the University of Birmingham

for the degree of DOCTOR OF PHILOSOPHY

School of Metallurgy and Materials

College of Engineering and Physical Sciences

University of Birmingham

January 2020

UNIVERSITY OF
BIRMINGHAM

University of Birmingham Research Archive

e-theses repository

This unpublished thesis/dissertation is copyright of the author and/or third parties. The intellectual property rights of the author or third parties in respect of this work are as defined by The Copyright Designs and Patents Act 1988 or as modified by any successor legislation.

Any use made of information contained in this thesis/dissertation must be in accordance with that legislation and must be properly acknowledged. Further distribution or reproduction in any format is prohibited without the permission of the copyright holder.

Abstract

SiC fibre reinforced SiC composites must be >90% dense in order to offer a superior structural material alternative to current systems used in aerospace engines. To achieve this the use of microwave energy enhanced chemical vapour infiltration (MCVI) has been investigated as a possible faster and more energy efficient manufacturing route. Key processing parameters were identified and their effects on the rate of deposition of SiC and the composite's microstructure were assessed using a suite of characterisation techniques. The rate of SiC deposition had an Arrhenius relationship with the temperature and the use of microwaves is thought to have also lowered the activation energy of the decomposition reaction. The fundamental benefit of this advanced processing method was the inverse thermal gradient produced by using microwave energy. This was studied both experimentally and via finite-difference time-domain modelling (FDTD). The latter showed a direct correlation between susceptor size and microwave absorption. A SiC slurry calendaring impregnation route was also developed to fill macro porosity in the SiC fibre preform. A number of slurries were characterised to find a suitable slurry composition that reduced the total volume of porosity in the preform to further reduce CVI processing time.

Acknowledgements

Firstly, I would like to thank my supervisor Jon Binner for your guidance, encouragement and the opportunities you provided me over the course of my PhD. Both your professional and academic advice has been invaluable from the start, and thank you for providing a laugh along the way. I will always appreciate the faith you placed in me when I first started in your group as a wide-eyed undergrad, thank you.

I would like to especially thank Andrea D'Angio for taking me on as his understudy during his PhD and showing me the ropes. His contribution to getting the equipment going, the hours of microscopy he carried out and the continued support even after leaving the project, minus a small implosion of some rather expensive glassware along the way, have all been essential to completing this project.

Lastly, I would like to extend my thanks to the broader ceramic composites group and ex-members of the group at the University of Birmingham, Ji, Virtudes, Ben, Erin, Vinu, James, Murth and Victoria to name but a few. A special thank-you goes to all the technicians as well in met & mat who have helped me out over the years. Thank you all.

To the American cohort of thank yous. I would like to thank Dr. Mike Cinibulk, Dr. Allan Katz, Lt Col David Garner and everybody at Wright-Patterson Air Force base for your guidance and support from afar. This project was jointly funded by the Air Force Office of Scientific Research (AFSOR) and the European Office of Aerospace Research and Development (EOARD) via the Materials and Manufacturing Directorate of the Air Force Research Labs (AFRL), and without their financial support, this project would not have been possible. In addition, I would like to thank Prof. Burt Tilley and Prof. Vadim Yakolev from Worcester Polytechnic institute for the opportunity to work with you both; it was a steep learning curve but provided me with a great experience despite the weather!

Now to the friends and family. Firstly, my special thanks to the chaps of 1 Newton grove who gave me the push I needed to pursue this PhD back in 2015. I would also like to thank the various residents of Kenilworth court who over the last few years who have provided me with hours of entertainment, company and excellent distractions. Next, I would like to thank my parents, sister and wider family for your continued encouragement along the way. Mum and Dad, thanks for your tireless support in anything and everything I do, you will never know just how much it means to me.

Lastly, I would like to thank Naomi. She has been my absolute rock since the beginning. Putting up with the moaning, the stress, the late night presentation rehearsals, the trips abroad and the weekends and evenings spent writing. Your ability to always put a smile back on my face has been unwavering, and for that, I am truly thankful.

"Don't forget to back it up in multiple places."

Ancient proverb, unknown origin, n.d.

Table of Contents

1. Introduction 1

2. Literature Review 7

2.1. Ceramic matrix composites 7

2.2. Fibre-reinforced ceramic matrix composites (FRCMCs) 8

2.2.1. Properties 8

2.2.2. Fracture mechanics theory and toughening mechanisms 12

2.2.3. Applications of FRCMCs 19

2.3. Silicon carbide fibre reinforced silicon carbide matrix composites (SiC_f/SiC) 20

2.3.1. Properties 20

2.3.2. Silicon carbide 21

2.3.3. Silicon carbide fibres 25

2.3.4. Applications of SiC_f/SiC 39

2.4. Fabrication of SiC_f/SiC FRCMCs 41

2.4.1. Powder processing routes 42

2.4.2. Reactive melt infiltration 43

2.4.3. Polymer infiltration and pyrolysis 47

2.4.4. Chemical vapour infiltration 49

2.4.5. Hybrid techniques 57

2.5. Chemical vapour infiltration of SiC_f/SiC composites 61

2.5.1. Reactants and SiC formation 61

2.5.2. Mechanism of deposition 64

2.5.3. CVI process variables with respect to SiC deposition 67

2.6. Microwave processing of materials 73

2.6.1. Microwave-material interaction 73

2.6.2. Volumetric heating, inverse temperature profile and thermal runaway. 79

2.6.3. High-temperature dielectric property measurement techniques 81

2.6.4. Microwave system components 86

2.6.5. Microwave heating modelling 90

2.7. Research on microwave energy chemical vapour infiltration (MCVI) 93

2.7.1. Silicon carbide and microwave heating 93

2.7.2. Concept of MCVI 95

2.7.3. Experimental results 99

3. Experimental Methodology 101

3.1. MCVI equipment 101

3.1.1. Microwave system 103

3.1.2. Temperature, pressure and gas control systems 105

3.1.3. Gas exhaust and by-product neutralisation 110

3.2. CVI of SiC_f/SiC composites 112

3.2.1. Constituent Materials 112

3.2.2. Impregnation of SiC fibre preforms 115

3.2.3. MCVI Procedure 120

3.3. Characterisation 130
3.3.1. Impregnation evaluation 130
3.3.2. Microscopy 136
3.3.3. X-ray diffraction analysis 139
3.3.4. Raman spectroscopy 141
3.3.5. Micro-computed tomography 141
3.3.6. Thermal properties 144
3.3.7. Dielectric permittivity measurements of SiC_f/SiC components 149
3.4. Simulation of microwave heating of SiC preform 150
3.4.1. Computational technique 150
3.4.2. Materials parameters 153
4. Results and Discussion 155
4.1. Microwave energy enhanced chemical vapour infiltration process 156
4.1.1. Kinetics of the MCVI process 156
4.1.2. Densification profile of SiC_f/SiC composites 169
4.1.3. Morphology, composition and crystal structure of SiC deposit 182
4.1.4. Summary 207
4.2. Inverse temperature profile development using MCVI 208
4.2.1. Thermal camera observations 208
4.2.2. Electromagnetic and thermal simulation of MCVI 211
4.2.3. Summary 233

4.3. Impregnation of SiC fibre with SiC slurry 234
4.3.1. Particle size distribution analysis 234
4.3.2. Room temperature slurry viscosity measurements.....236
4.3.3. The relative density of impregnated preforms 238
4.3.4. Dielectric properties of SiC powder.....241
4.3.5. Contact angle measurements.....245
4.3.6. Porosity network analysis of impregnated composite 248
4.3.7. Gas permeability of impregnated composites 258
4.3.8. Summary.....262
5. Conclusions and Future work..... 264
5.1. Conclusions 264
5.1.1. Microwave energy enhanced chemical vapour infiltration study 264
5.1.2. Inverse temperature profile 269
5.1.3. Fabric impregnation with SiC slurry 271
5.2. Future work.....273
6. Appendices 278
6.1. Appendix I.....278
6.2. Appendix II.....279
6.3. Appendix III 281
7. References..... 282

Table of Figures

Figure 1.1. A graph indicating the dependence of fracture toughness of ceramic materials on the increasing length/diameter ratio of potential reinforcing phases, adapted from [4], showing continuous fibre reinforced CMCs to have the most superior fracture toughness. 1
Figure 1.2. (a) The high-temperature specific strength of CMCs compared to other aerospace materials and the respective key [10] and (b) the evolution of civilian turbofan engines shape showing an increased by-pass ratio that decreases specific fuel consumption when CMC components are added [6, 11]. 3
Figure 2.1. Annotated stress-strain curve showing the fracture of a FRCMC compared to a monolithic ceramic [12]. 8
Figure 2.2. Schematic of the micro-cracking process, adapted from [44]..... 13
Figure 2.3. The transformation toughening mechanism in partially stabilised YSZ, adapted from [56]. 17
Figure 2.4. A graphical contour separating two regions of crack deflection and penetration based on toughness against the Dundur's parameter that describes the elastic mismatch between components, adapted from [20, 59]. 18
Figure 2.5. A micrograph showing the fibre pull-out mechanism in a CMC and subsequent fracture of the reinforcing fibres [62]. 19
Figure 2.6. Microstructural goals for achieving property goals of SiC_f/SiC composites. σ_{mc} = matrix crack stress, σ_u is the ultimate tensile strength and ε_u is tensile failure strain, adapted from [70]..... 20
Figure 2.7. An example of part of the SiC phase diagram [79]..... 22
Figure 2.8. (a) Zinc blend cubic structure of β-SiC and (b) the Wurtzite hexagonal structure of α-SiC. Adapted from [88]..... 25
Figure 2.9. (a) Cross sectional images showing the mesostructure of a fibre produced using the preceramic polymer technique and (b) using CVD, note the different scales [89]..... 26
Figure 2.10. Schematic representation of the cross-sections of the two commercially available CVD SiC fibres adapted from [89]. 27

Figure 2.11. Schematic cross-sectional representations of the microstructure of three generations of commercially available SiC fibres, adapted from [89, 104]. 31
Figure 2.12. Scanning electron microscope image of a single silicon carbide filament coated in a carbon interface, (b) schematic representation of a fibre tow comprised of 800 filaments [114] and (c) a photograph of a basket/matt weave SiC fabric. 34
Figure 2.13. Classification of fibre architectures [115]..... 35
Figure 2.14. Schematic illustrations showing the different orientation of lamellae in the different orientations, adapted from [116]. 36
Figure 2.15. Cross-sectional diagrams of the types of weaves, from unidirectional to 5D isotropic, adapted from [118, 119]. 38
Figure 2.16. Three load-displacement curves as a function of volume fraction (V_f), reproduced from [122]. 39
Figure 2.17. Cross-section of the next generation large three-shaft civilian turbofan engine the GE9x from General Electric [124]. 40
Figure 2.18. A SiC_f/SiC shroud component produced by Rolls Royce PLC [6]. 40
Figure 2.19. The reactive melt infiltration process adapted from [150] and SEM image from the literature showing residual silicon phase between fibres [151]. 46
Figure 2.20. (a) A liquid preceramic precursor is impregnated into the fabric; (b) curing and pyrolysis begins, resulting in shrinkage through the evolution of gaseous by-products as the polymer is converted to ceramic; (c) a porous network is formed in the preform, with micro-cracks and pores shown in the matrix phases [150]; (d) SEM micrographs of the aforementioned micro-cracks [164] and (e) bubbles created by inadequate process control [165]. 48
Figure 2.21. An illustration of the development of SiC deposit on the cross-section of the SiC fibres over time, adapted from [150]. 49
Figure 2.22. Schematic of generic CVI equipment [168]..... 50
Figure 2.23. Schematic showing the key components of the conventional process and the respective temperature profile [150]. 53
Figure 2.24. Schematic showing the key components of the thermal gradient process and the respective temperature profile [150]. 54
Figure 2.25. Schematic showing the key components of the isothermal forced flow process and the respective temperature profile [150]. 55

Figure 2.26 Schematic showing the key components of the pulsed pressure system and the respective temperature profile [150]. 56
Figure 2.27. Schematic showing the key components of the laser-assisted process and the respective temperature profile [150]. 57
Figure 2.28. Schematic representation of the combinations of matrix formation techniques after an interface material is applied and before an EBC or TPS. 58
Figure 2.29. Schematic representation of the adsorption and deposition of SiC constituents to the fibre surface, adapted from [225]. 64
Figure 2.30. Schematic showing the different steps in the iso-thermal CVI process, adapted from [9, 14]. 65
Figure 2.31. Thermodynamic yields for the solid deposition of silicon carbide and its co-deposits as a function of alpha ratio, adapted from [9]. 71
Figure 2.32. A temperature-pressure-alpha phase diagram showing the trends in the physicochemical properties of the resulting SiC deposit. 73
Figure 2.33. Series of diagrams showing the microwave-matter interactions possibilities [258]. 75
Figure 2.34. The absorption of microwaves to half-power depth (skin depth). 79
Figure 2.35. Schematic illustrations of the temperature profiles within samples heated (left to right) conventional, microwave (inverse temperature profile) and hybrid heating [256]. 80
Figure 2.36. Graph showing the principle of thermal runaway showing an instantaneous temperature increase with no change in electric field strength [266]. 81
Figure 2.37. A generic schematic of the resonant cavity set up used for measuring dielectric properties [270]. 83
Figure 2.38. A diagram of the free space method that can be used to measure dielectric properties [270]. 84
Figure 2.39. (a) A schematic adapted from [277], showing the direction of electron flow inside the anode after emissions from the cathode (red arrows) caused the intersecting magnetic field (blue arrows), (b) zoomed-in representation of a cavity, acting like a single turn inductor, showing the direction of current flow and the resultant electromagnetic wave produced extending out of the page parallel to the

magnetic field and (c) the interaction of the electron with the electric field induced by the cavity-causing the retardation of the electron. 87
Figure 2.40. Schematic diagram of a single-mode applicator [289]. 89
Figure 2.41. Diagram of a multimode cavity with mode stirrer [289]. 90
Figure 2.42. Micrographs showing the variation of deposit thickness in the CMC using MCVI; moving from the centre (far left) to 10mm from the centre (middle) and outer edge approximately 20 mm (far right) [13]. 96
Figure 2.43. Schematic comparison of ICVI vs MCVI in terms of the relative thermal gradients, gas flow and subsequent generalised pore filling with SiC. 96
Figure 3.1. (a) Labelled photos of the MCVI system and (b) a schematic representation of the system. 102
Figure 3.2. (a) Manual tuning system and (b) automatic tuners that were used to minimise the reflective power inside the MW cavity to improve the efficiency of heating. 104
Figure 3.3. From left to right: The microwave leakage detector, fibre optic arc detector behind a quartz window and the MW door safety interlock. 105
Figure 3.4. A cross-sectional view of the temperature control arrangement of two-colour pyrometers, sample and gas flows. 107
Figure 3.5. Photo of the pressure transducer that monitored the vessel pressure and the throttle valve that enacted changes to the pressure. 108
Figure 3.6. (a) Effect of pressure on the boiling point of MTS [322] and (b) a photo the MTS storage vessel connected to the evaporator that heated up the liquid to a vapour. 109
Figure 3.7. Photo of the microwave cavity with the bell jar inside and an image of the turntable and gas inlet and outlet. 110
Figure 3.8. Photo of the pumping stack with the key components labelled. 112
Figure 3.9. Preform fabrication route for a non-impregnated SiC_f/SiC composite. 114
Figure 3.10.(a) SEM micrograph of a polished cross-section of a dipped sample, and (b) the polished cross-section of a painted sample that has delaminated. 117
Figure 3.11. Schematic of the calendaring process showing the decreasing saturation of SiC fibre with SiC slurry 118

Figure 3.12. Schematic of vacuum bagging arrangement used to impregnate SiC fabric with an aqueous SiC slurry.....119
Figure 3.13. Image of the Al_2O_3 foam used and the setup of the cavity, in later experiments a quartz bridge was used to modify flow this is described in more detail in section 4.1.1.2.....121
Figure 3.14. Gas delivery system control panel, where gas flow rates, pressure and pumps could be controlled. 122
Figure 3.15. Labotron control panel for operating the microwave generator unit. ..123
Figure 3.16. Photographs showing the development of the SiO_xCl_x layer on the top of the inside surface of the top of the bell jar after 2h. 127
Figure 3.17. Adapted from [250] showing the decrease in temperature after MTS is introduced into the reaction vessel and the power increase needed to regain the lost temperature.....128
Figure 3.18. Paschen's curve in a hydrogen environment illustrating the relationship between the pressure and electrode distance on the threshold of the breakdown voltage, (b) showing the minimum spacing between electrodes as pressure changes, (c) a graph illustrating the minimum operating pressure for a given set of electrode separations, and (d) magnified images of a graph (c) showing the separation distance between fibres observed via SEM and the corresponding minimum pressure. 129
Figure 3.19. (a) schematic and (b) photograph of the permeability equipment constructed and used in its entirety and the two key components; (c) the aluminium honeycomb and the (d) epoxy washer. 136
Figure 3.20. Corresponding XRD diffractograms demonstrating the scanning orientation effect on the signal intensity. Red dashed line corresponds to the orientation. 140
Figure 3.21. Schematics showing the difference in the image stack from a micro-CT scan between a cylindrical volume and a cuboid volume. 143
Figure 3.22. Example of a single pore selected by the script and the boundary box constructed in 2D. 143

Figure 3.23.(a) LFA 427 fibre sample holder showing four key steps; (from the top left) alignment, compression, cutting and mounting in laser flash [342], (b) showing the fibre sample and the two-ringed arrangement for clamping the fibres.....147
Figure 3.24. Image of the prepared sample containing SiC fibre, which is inserted into the equipment seen in figure 3.25., indicated as 'Sample'.....149
Figure 3.25.(a) Microwave system design for measuring samples' dielectric properties as a function of temperature, adapted from [344] and (b) a photograph of the respective equipment [345]. 150
Figure 3.26. Labotron HTE M30KLB Pro; cavity, 3D view of the internal structure and components and a magnified view of the SiC_f/SiC-Al_2O_3 foam arrangement. 152
Figure 3.27. A top-down view and front-on view of the non-uniform meshes applied to the simulation. 153
Figure 4.1. SiC matrix growth rate as a function of increasing chamber pressure for samples processed at different temperatures. Gas flow rates and alpha ratio were kept constant at Q_{H2} = 300 cm^{-3} min^{-1}, Q_{MTS} = 0.2 g min^{-1} and alpha = 10 respectively. Details for samples inside the red boxes with reduced infiltration times can be seen in Figure 4.7.....157
Figure 4.2. The dielectric permittivity of the Tyranno ZMI fibre as a function of temperature, showing the fibre stops behaving as a dielectric at ~1060°C.....159
Figure 4.3. SiC matrix growth rate as a function of changing alpha ratio. All samples were processed at 925°C, 400 mbar and Q_{MTS} = 0.2 g min^{-1}. Q_{H2} was changed to alter the alpha ratio. 160
Figure 4.4. Left: Infiltration temperature over time at an alpha ratio of 10 showing a relatively constant centre and side temperature. Right: equivalent graph for alpha 70 showing significant fluctuation for both the side and centre temperatures.....162
Figure 4.5. Extrapolated plots of the densification of the SiC_f/SiC composite using natural logarithmic decay function based on the rate of mass gain seen in sample QB over the first 8 h (2+2+4 h), table 3.3. It shows a potential reduction in the time afforded by the introduction of the SiC slurry phase. 163
Figure 4.6. Natural logarithm of the SiC matrix growth rate against the reciprocal temperature for three different pressures at the same flow conditions. 165

Figure 4.7. Optical micrographs of the samples infiltrated at different temperatures and different pressures showing the densification profiles as seen by the lighter regions indicating SiC deposition. 171
Figure 4.8. The difference in fibre coating thickness between the 1st ply (top row) and the 20th ply (bottom row) in samples infiltrated at 900°C at different pressures. 172
Figure 4.9. Micrographs of the uniform deposition coating seen over the thickness and 20 mm of the sample infiltrated at 1000°C at 300 mbar. 174
Figure 4.10. Three micrographs showing the localised Si-SiC deposition on the bottom surface of the 1000°C 700 mbar sample compared to the 1st ply. 175
Figure 4.11. The top three images show the densification of the sides of the preform coated in SiC slurry. The bottom three show the transition from infiltrated powder to non-infiltrated powder, from left to right over a 250 μm distance. 176
Figure 4.12. High magnification micrographs showing the deposition of SiC onto SiC powder particles and the micro-porosity that appears to have not yet been filled by the deposit. 177
Figure 4.13. Stitched micrographs of the densification profiles of SiC_f preforms infiltrated at alpha ratios 5-70, where T = 925°C, P = 400 mbar, Q_{MTS} = 0.2 g min^{-1} were constant and the Q_{H2} was changed between samples. 179
Figure 4.14. Higher magnification micrographs of the alpha 5 sample, showing uniform densification. 179
Figure 4.15. Higher magnification micrographs of the alpha 25 sample, showing densification in the 20th ply only. 180
Figure 4.16. A series of stitched micrographs of the densification profile of a SiC_f preform. The conditions by which it was infiltrated are as follows: T = 925°C, P = 400 mbar, alpha = 10 and Q_{MTS} = 0.2 g min^{-1} Q_{H2} = 300 cm^{-3} min^{-1}. 181
Figure 4.17. Higher magnification micrographs showing the effect of the quartz bridge on another alpha 10 sample, showing densification occurring preferentially in the centre region. 182
Figure 4.18. Six micrographs showing the effect of different temperatures on the surface morphology of the SiC deposit. 183

Figure 4.19. Images of the SiC deposit at different pressures but using the same magnification showing a significantly increased surface roughness with increasing pressure. 185
Figure 4.20. SEM micrographs showing the spine-like and large pustule regions of growth seen at 1000°C and 700 mbar. 185
Figure 4.21. SE micrographs showing the variation of the SiC deposit morphology with changing alpha ratios. 186
Figure 4.22. Bar graphs showing the composition of the SiC deposit at different temperatures using EDS (left) and WDS (right). 188
Figure 4.23. Raman spectra for the semiconductor standard showing the presence of both longitudinal and transverse optical phonons. 189
Figure 4.24. Raman spectra of the SiC deposit produced at different infiltration temperatures with a constant pressure of 300 mbar. 191
Figure 4.25. Raman spectra of the SiC deposit produced at different infiltration pressures. 192
Figure 4.26. Raman spectra of the free silicon in the SiC deposit produced at high infiltration pressures. 192
Figure 4.27. Two micrographs showing the free silicon in between the SiC fibres. .193
Figure 4.28. The Si:C:O ratio in the SiC_f/SiC samples infiltrated with different alpha ratios with T = 925±15°C and P = 400±8 mbar. 194
Figure 4.29. (a) A bright-field image of a SiC_f/SiC foil taken at the centre of 900°C 300 mbar sample, (b) selected area electron diffraction pattern of the SiC matrix, (c) two overlaid and coloured dark-field images corresponding to the images in (d). ..196
Figure 4.30. (a) A bright-field image of a SiC_f/SiC foil taken at the centre of 950°C 300 mbar sample, the dashed line shows the fibre merging interface, (b) a selected area electron diffraction pattern of the SiC matrix, rotation of the pattern was applied, (c) three overlaid and coloured dark-field images corresponding to the images in (d). 197
Figure 4.31. (a) A bright-field image of a SiC_f/SiC foil taken at the centre of 1000°C 300 mbar sample, (b) a selected area diffraction pattern of the SiC matrix rotation of the pattern was applied, (c) four overlaid and coloured dark-field images corresponding to the images in (d). 198

Figure 4.32. (a) High-resolution bright field image of a supposed 'Si' inclusion seen in the 900°C 300 mbar sample, (b) corresponding Si map and (c) C map. 200
Figure 4.33. (a) A low magnification bright-field image of the 'flower' inclusion near the fibre (bottom left corner), (b) magnified image of the feature, (c) a single grain showing high contrast indicating different orientations and horizontal striations caused by stacking faults in the lattice which were confirmed in the diffraction pattern seen in (d). 200
Figure 4.34. High-resolution BF images of the microstructural features seen in 1000°C 300 mbar sample. 1. Amorphous SiO_2 banding at the fibre-matrix interface, and 2. Nano-porosity formed between converging SiC grains from neighbouring fibres. 202
Figure 4.35. Elemental maps of the amorphous oxide band, most likely SiO_2, found at the matrix-fibre interface, corresponding to 1(a) in figure 4.34. 202
Figure 4.36. Elemental maps of the amorphous oxide band found in the matrix that was produced between infiltrations, corresponding to 1(b) in figure 4.34. 203
Figure 4.37. XRD diffraction patterns for the samples infiltrated using different alpha ratios. 204
Figure 4.38. BF images showing delamination of the matrix from the fibre from alpha = 5.....205
Figure 4.39. (a) SAD pattern showing a grain α-SiC found in the alpha = 10 sample, (b) a crystalline but heavily twinned grain of SiC and (c) the transitional region between the fibre and textured region of the SiC as indicated. 206
Figure 4.40. (a) Change in the crystal size as the grain growth proceeds from the fibre in alpha = 10, (b) higher mag image of the flow-like structures produced by the sectional of crystals growing radially from a central point, as illustrated in (c). 207
Figure 4.41. Left: An annular temperature profile of 10 ply 34 mm diameter SiC preform heated using microwave energy. Right: Non-uniform heating of 34 mm diameter sample made with 30 ply showing hot edges. 209
Figure 4.42. Left: An annular temperature profile of 10 ply 55 mm diameter SiC preform heated using microwave energy. Right: Non-uniform heating of 55 mm diameter sample made with 30 ply showing hot edges. 210

Figure 4.43. The formation of inverse temperature profiles at ~700°C in a 55 mm 20 ply SiC fibre preform using microwave energy and the concordant graph showing temperature profile along the intersecting line. 211
Figure 4.44. TIC image showing the SiC preform at 1001°C after 2 minutes of heating. 211
Figure 4.45. Changing dielectric properties of the 3 types of SiC fibres, top: ε', bottom: ε''; note the unusual behaviour of the SA3 and ZMI fibres at temperatures >800°C.....214
Figure 4.46. The dielectric permittivity (primary axis) and the loss factor (secondary axis) of the Hi Nicalon S fibres after interpolation using Origin. ε' was fitted with a logistic model with R^2 = 0.99, the ε'' was fitted using a Boltzmann model with R^2 = 0.97. 215
Figure 4.47. Top: The dielectric permittivity for the Al_2O_3 foam and quartz after interpolation using Origin. ε' for the Al_2O_3 foam was fitted with a two-phase exponential decay function with R^2 = 0.96 and ε’ for the quartz was fitted using a Boltzmann model with R^2 = 0.98. Bottom: Dielectric loss factor for the Al_2O_3 foam and quartz after interpolation using Origin. ε'' for the Al_2O_3 foam with a Logistic model with an R^2 = 0.98. ε’’ for quartz was fitted using an exponential growth model with an R^2 = 0.93.....216
Figure 4.48. Measured thermal diffusivity values for the three SiC fibres. Note that the units used are SI as QWED did not require thermal diffusivity data input for the simulation. 217
Figure 4.49. Measured specific heat capacity data for the three fibres up to 900°C, in the units required for the QWED 3D simulation. 218
Figure 4.50. Thermal conductivity data for the three fibre types with increasing temperature calculated from measured values and accounting for thermal expansion. Note that the unit on the Y-axis is specific to the QWED 3D requirements and is not an SI notation. 219
Figure 4.51. Left: Specific heat capacity of the Hi NiC S SiC fibre after post-processing, which was fitted with a logistic model with R^2= 0.98. Right: the thermal conductivity of the SiC fibre after processing fitted to a logistic curve with R^2= 0.99. Note that the units are specific to the QWED 3D software.....220

Figure 4.52. Left: Specific heat capacity of the Al_2O_3 foam and quartz after post-processing. These were fitted with a Lorentz fit with R^2 = 0.99 and a logistic model with R^2= 0.99, respectively. Right: the thermal conductivity of the Al_2O_3 foam and quartz after processing, fitted to a first-order exponential decay with R^2= 0.97 and a Lorentz fit with R^2 = 0.99. The graphs are plotted on the same Y-axis scale as figure 4.50 for comparative purposes. 221
Figure 4.53. Nine graphs showing the effect of SiC fibre preform dimensions on the reflection coefficient inside the cavity and the number of induced resonances at room temperature. 222
Figure 4.54. Two graphs showing the effect of temperature on the S_{11} parameter for the 55ϕx8 mm samples. Note the extended x-axis. 225
Figure 4.55. Bar graph representing the change in the value of S_{11} parameter between RT and 1200°C, showing across all frequencies a 23% decrease in the mean value of the reflection coefficient. 226
Figure 4.56. Graph showing the ten frequencies selected and how the temperature of the SiC_f preform changed with time. 228
Figure 4.57. A graph showing the four frequencies selected as representative of the four scenarios showing how the temperature of the SiC_f preform changed with time. 229
Figure 4.58. Visualisations of the temperature profile during heating at two different frequencies, I = 2.4163 GHz and VI = 2.4901 GHz over 180 s showing how the temperature profile changes with time, temperature and frequency. 230
Figure 4.59. The particle size distribution of the three SiC powders and their respective D_{50} values are indicated by the dashed lines. 235
Figure 4.60. SEM images show agglomeration of powders on the right and ~1 μm sized powders on the right. 236
Figure 4.61. Three graphs showing the change in viscosity as a function of shear rate, with changing solids loading of the slurry and increasing particle size, from left to right UF-25, UF-05 and SuperVac. 238
Figure 4.62. The relative density of SiC_f/SiC_p preforms impregnated with different solids content slurries and different particle sizes. 239

Figure 4.63. The volume fraction as a percentage of slurry added to the SiC_f/SiC_p preforms impregnated with different solids content slurries and different particle sizes. 240
Figure 4.64. The increase in thickness as a function of the mean mass gain of the preforms when impregnated with different powders and solids content. From left to right in terms of data points (20, 22.5, 25 vol.%). 240
Figure 4.65. (a) An SEM cross-section of UF-25-25 preform, showing the fibres crossing the image horizontally and the large crack SiC powder matrix, (b) the thinner and more porous cross-section of the SV-25 preform. 241
Figure 4.66. The changing dielectric permittivity (real part) of the three powders with increasing temperature upon heating (red) and cooling (blue). 242
Figure 4.67. The changing loss component of the dielectric permittivity (imaginary part) of the three powders with increasing temperature upon heating (red) and cooling (blue). 244
Figure 4.68. A schematic representation of the sessile drop test of the SiC slurry droplet on a SiC substrate where γSL, γLG and γSG are solid-liquid, liquid-gas and solid-gas respectively. Figure adapted from [396]. 245
Figure 4.69. A photo showing the ImageJ angle-measuring tool used to measure the wetting of the droplet on the substrate. 246
Figure 4.70. Change in contact angle of SiC slurry droplet as a function of time. ...247
Figure 4.71. Difference between the least wetting and most wetting slurries respectively at T_0. 247
Figure 4.72. The total decrease in contact angle over a four-minute period of the four different slurries. 248
Figure 4.73. Series of photographs showing the change in drop shape as time increased. 248
Figure 4.74. Images from Avizo showing the identification of small closed porosity in the green SiC_f/SiC composite. 249
Figure 4.75. A bar graph showing the mean pore area inside the SiC_f/SiC. 250
Figure 4.76. Image produced by the MATLAB script highlighting the internal delamination (orange) in UF-25-25 thus skewing the error bar. 250

Figure 4.77. The mean maximum pore area measured using the MATLAB script based on micro-CT data. 251
Figure 4.78. A bar graph showing the ratio of width to height in the impregnated samples with a table below corresponding to the aspect ratio. 252
Figure 4.79. A graph showing the coefficient of variation between samples indicating the uniformity of the pore size. 254
Figure 4.80. Histograms showing the pore count distribution for one composite from each sample set as a function slice number taken from the YZ plane, with a bin size of 10 and a max range of 100 pixels. 255
Figure 4.81. Three graphs showing the initial image analysis of the impregnated samples showing the differences in pore number and area and the average error prior to the dialling in process. 256
Figure 4.82. Three graphs showing the result of the image analysis with the script variable being tuned in to align the result with that of ImageJ again showing the differences in pore number and area and the reduced average. 257
Figure 4.83. Three images detailing the differences pore detection between the ImageJ tools and the MATLAB script. 258
Figure 4.84. The effect of increasing flow rate on the pressure difference across the SiC_f/SiC_p thickness, showing the samples with higher solids content and particle size have a greater difference and vice versa. 259
Figure 4.85. Reynold's number as a function of fluid viscosity showing the quadrant the MCVI process operates in highlighted in blue. 260
Figure 4.86. The effect of slurry addition to the SiC_f preforms on the permeability, showing the slurry addition decreases the permeability by an order of magnitude for all slurry variations. 261
Figure 4.87. Radar diagrams illustrating the best performing slurry across the variety of tests was found to be UF-05-225. Note that no prioritisation was applied to the seven variables evaluated. 263
Figure 5.1. (a) Nuclear fuel cladding rods, (b) GE CMC blade from LEAP engine and (c) various components of combustor liner for simulated gas turbine engine cycle. 277

List of Tables

Table 2.1. Three different toughening mechanisms available in secondary phase reinforced ceramics, (a) crack deflection, (b) crack bowing, (c) crack bridging, (d) crack pinning and (e) particle yielding, adapted from [49-54]..... 15
Table 2.2. A table summarising the typical applications for FRCMCs in the aerospace industry [40, 63-68]. 19
Table 2.3. General properties of SiC_f/SiC composites. Note that these properties are based on a fibre volume fraction of 35-45% [10, 71]..... 21
Table 2.4. Properties of monolithic hot pressed commercial purity SiC [10]. 23
Table 2.5. Detailing the processing parameters, compositional, physical properties and respective costs [4, 63, 89, 99, 100]. 28
Table 2.6. Comparison of critical mechanical, physical and thermal properties of third generation SiC fibres [4, 63, 89, 100, 104]..... 33
Table 2.7. Schematics of the weave patterns used in four of the most common weaves, with reference to their advantages and disadvantages [117]. 37
Table 2.8. The specific precursor gases and the processing parameters needed for the deposition of a number of non-oxide ceramic materials [170]..... 52
Table 2.9. Summarising the primary advantages and disadvantages of advanced fabrication methods [63, 208, 209]. 58
Table 2.10. Showing some of the fundamental advantages and disadvantages associated with microwave processing [257]. 74
Table 2.11. High-temperature dielectric property measurements that are available and their respective attributes, adapted from [267]. 82
Table 2.12. Showing the respective dielectric properties of a number of different fibres and their constituent materials [178, 307-310]..... 95
Table 2.13. Schematics of the theoretical cross-sectional densification of ICVI vs MCVI. 97
Table 2.14. The established and potential advantages and limitations of the MCVI process; potential advantages are indicated with *. 98
Table 2.15. The historic results of MCVI when depositing SiC into a SiC fibre preform. 100

Table 3.1. Details of the physical properties of the SiC fibre used at various stages of the project [100, 324, 325]. 113
Table 3.2. Silicon carbide powders used in the preliminary trials. 114
Table 3.3. List of the SiC_f preforms infiltrated and the respective infiltration used. The dimensions of all the samples were 55x8 mm. Thick black line indicated the switch from temperature and pressure as independent variables to alpha. 125
Table 3.4. QWED input data with specific non-SI units. 153
Table 4.1. Effects of the effective diffusivity, reaction rate, Thiele modulus and effectiveness factor based on the different processing conditions from table 3.3. ..169
Table 4.2. Showing the Raman shift for the most common SiC polytypes, adapted from [372, 374]. Raman shifts in bold indicate the overlapping polytypes the commonly occur in SiC making explicit distinction difficult. 190
Table 4.3. Sample properties used in the thermal imaging evaluation of ZMI fibres 208
Table 4.4. Showing the ten frequencies selected from figure 4.54. that were used to compare four key scenarios in terms of how the respective heating rates changed with temperature. 227
Table 4.5. Nomenclature of the three powders used and the respective solids content of the slurries they were used to create. 234
Table 4.6. Details of the commercially available SiC used in the project from the manufacturer's technical datasheets. 235
Table 6.1. All the input parameters for Hi Nicalon Type S, illustrating the effect of temperature 279
Table 6.2. All the input parameters for Al_2O_3 foam, illustrating the effect of temperature 279
Table 6.3. All the input parameters for quartz, illustrating the effect of temperature 280
Table 6.4. EDS VS WDS comparison table 281

List of Symbols and Acronyms

Symbol/ Acronym	Definition	Symbol/ Acronym	Definition
⌀	Diameter / m	Micro-CT	Mirco-computed tomography
μ	Fluid viscosity / Pa S	M_{st}	Mass of standard
$\mu_{av.}$	Mean	MTS	Methyltrichlorosilane
1CP	One colour pyrometer	MW	Microwave
2CP	Two colour pyrometer	N	Integer including zero
A	Area / m^2	NITE	Nano infiltration trans-eutectic
A	Pre-exponential factor / s^{-1}	NPL	National physical laboratory
A_i	Saturation ionisation at a particular E/p	P	Pressure / KPa or mbar
alpha ratio	$\frac{n_{Carrier\ gas}}{n_{Precursor}}$	Pd	Pressure distance
A_m	Initial mass / g	PID	Proportional integral derivative
B_{ei}	Excitation and ionisation energies	PIP	Polymer infiltration and pyrolysis
B_x	Constant	PPCVI	Pulsed pressure CVI
b	Heating rate / °C min^{-1}	Q	Flow rate / cm^3 min^{-1}
B_m	Rate of infiltration / g min^{-1}	Q_0	Quality factor empty
BSE	Backscattered electron	Q_1	Quality factor with sample
C	Speed of light in free space	Q_{H2}	Flow rate of hydrogen / cm^3 min^{-1}
CCD	Charge-coupled device	Q_{MTS}	Flow rate of MTS / g min^{-1}
C_f/C	Carbon fibre Carbon matrix	r	Radius / m
C_f/SiC	Carbon fibre silicon carbide matrix	R	Ideal gas constant / J mol^{-1} K^{-1}
C_m	Final mass at T_D = 100% / g	RMI	Reactive melt infiltration
CMCs	Ceramic matrix composites	Rp	Primary range of electrons
C_{MTS}	Concertation MTS / mol m^{-3}	R_{pore}	Pore radius / m
C_{ps}	Specific heat capacity	RT	Room temperature
C_{pst}	Specific heat capacity standard	S_{11}	reflection coefficient
CTE	Coefficient of thermal expansion	S	Total effective conductivity

C_v	Coefficient of variation	SAED	Selected area electron diffraction
CVD	Chemical vapour deposition	SE	Secondary electron
CVI	Chemical vapour infiltration	SEM	Scanning electron microscopy
d	Gap distance / m	SiC_f/SiC	Silicon carbide fibre reinforced silicon carbide
D_c	Diameter of the cavity / m	t	Time / s
D	Diffusion of precursor	T	Temperature / °C
D_m	Molecular diffusion / $cm^2\ s^{-1}$	T_c	Transmission coefficient
D_k	Knudsen diffusion	T_D	Theoretical density / %
D_p	Penetration depth / m	$t_{1/2}$	Half rise time / s
D_{50}	Particle size distribution 50%	tanδ	Loss tangent
DDS	Dichloro-diethyl silane	TE	Transverse electric
D_e	Diffusion coefficient	TEM	Transmission electron microscopy
D_{eff}	Effective diffusion	TIC	Thermal imaging camera
D_{st}	Vertical displacement	TM	Transverse magnetic
E	Modulus / GPa	TPS	Thermal protection system
E_a	Activation energy / J mol^{-1}	UoB	University of Birmingham
E_{DSC}	Calorimetric sensitivity	V	Volumetric flux per area / $m^3\ s^{-1}\ m^{-2}$
E/H	Electric/magnetic field ratio	V_b	Voltage breakdown / V
EBC	Environmental barrier coating	V_f	Fibre fraction
EDS	Energy dispersive x-ray spectroscopy	V_m	Matrix fraction
E_f	Fibre modulus / GPa	VNA	Vector network analyser
E_i	Target ionisation	vol.%	Volume percentage
Ep	Electron residual energy	V_s	Sample volume
E_{po}	Incident primary range electrons	V_x	Poisson's ratio
EPD	Electrophoretic deposition	WDS	Wavelength dispersive spectroscopy
ETS	Ethyletrichlorosilane	wt.%	Weight percentage
f	Frequency / Hz	X_{on}	N^{th} root
f_0	Cavity resonant frequency of cavity / Hz	XRD	X-ray diffraction

f_1	Cavity resonant frequency with sample / Hz	Y	Mass at t_x
FCC	Face centre cubic	α_D	Dundur's
FEA	Finite element analysis	α	Thermal diffusivity / $m^2\ s^{-1}$
FEG	Field emission gun	α_{corr}	Thermal diffusivity corrected / $m^2\ s^{-1}$
FIB	Focus ion beam milling	β	CTE / $°C^{-1}$
FRCMC	Fibre-reinforced	γ	Shear rate
G_{SiC}	SiC growth rate	γ_{lg}	Liquid gas interface
HAADF	High angle annular dark field	γ_{sg}	Solid gas interface
ICVI	Isothermal CVI	γ_{sl}	Solid-liquid
IFCVI	Isothermal forced CVI	ε	Strain
IR	Infrared	ε^*	Complex permittivity
J	Imaginary number	ε'	Dielectric permittivity
J_0	Zero-order Bessel function	ε''	Loss factor
J_i	First-order Bessel function	ε'_0	Permittivity of free space
K	Permeability / m^2	ε'_{eff}	Effective relative dielectric loss
K_{1C}	Fracture toughness / MPa $m^{½}$	ε'_r	Relative dielectric permittivity
K_i	Inertial permeability / m^2	ε_u	Tensile failure strain
K_r	Reaction rate	η	Effectiveness factor
K_S	Reaction rate at the surface	θ	Angle of incidence
K_v	Viscous permeability / m^2	λ	Thermal conductivity / W mK^{-1}
L	length or Thickness of medium / m	λ_0	Free space wavelength
LCVI	Laser CVI	ρ	Density/ g cm^{-3}
LEV	Local exhaust ventilation	σ	Stress / MPa
LRP	Liquid ring pump	σ_{sd}	Standard deviation
MCVI	Microwave chemical vapour infiltration	σ_U	Ultimate tensile stress / MPa
M_f	Impregnated dry mass	σ_{mc}	Matrix cracking stress / MPa
MFCs	Mass flow controllers	τ	Shear stress / MPa
M_i	Pre-impregnation dry mass	ζ	Tortuosity

Glossary

Cavity	The metallic box that contains and reflects microwaves.
Deposition	A precursor gas reacts/decomposes yielding to a solid material on a substrate.
Fabric	Woven fibres.
Fibre	Collection of twisted together tows.
Impregnation	Process of embedding a substance inside another.
Infiltration	Deposition of material inside a porous preform using a chemical vapour to densify.
Inter-ply	Porosity between fibre sheets.
Inter-tow	Porosity between bundles of fibres.
Intra-tow	Porosity between the fibres within the tow.
Matrix	The connective medium between fibres
Ply / plies	Layers of fabric in the same plane.
Pore	Unfilled regions of ceramics
Precursor	A substance that participates in a chemical reaction to form a compound.
Preform	Two or three-dimensional fabric forms. They can be designed to have a specific shape for structural and/or functional requirements.
Slurry	Combination of ceramic powder, solvent and often a dispersant that also wet forming of green bodies.
Thresholding	Selection of a cut-off value, where every pixel with a value less than the cut off is considered a different class, while every pixel greater than that value is considered the another class
Tow	A bundle of untwisted continuous fibres

1. Introduction

Numerous structural materials used at high temperature (1260-1482°C) are more susceptible to crack propagation leading to premature failure [1]. Ceramic materials are polycrystalline materials that are composed of primarily covalent and some ionic bonding so lack slip systems that can deform the material and absorb external energy. During manufacture flaws are introduced which concentrates the applied stress and initiates crack. This cracks then can propagate in an uncontrolled manner due to the lack of energy dissipation mechanisms, see figure 1.1. This has caused the intensive development of continuous fibre reinforced ceramic matrix composites (CMCs) for high temperature structural applications. CMCs offer multiple attractive features, including improved fracture toughness, low density, high-temperature strength and modulus, excellent thermo-mechanical properties and stability in oxidative, irradiating, and corrosive environments [2, 3].

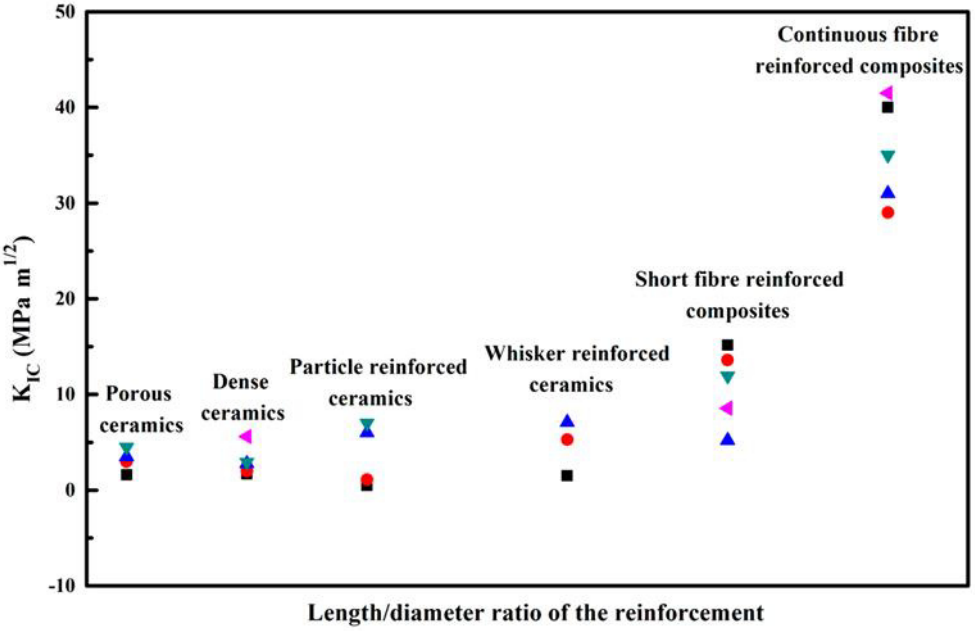


Figure 1.1. A graph indicating the dependence of fracture toughness of ceramic materials on the increasing length/diameter ratio of potential reinforcing phases, adapted from [4], showing continuous fibre reinforced CMCs to have the most superior fracture toughness.

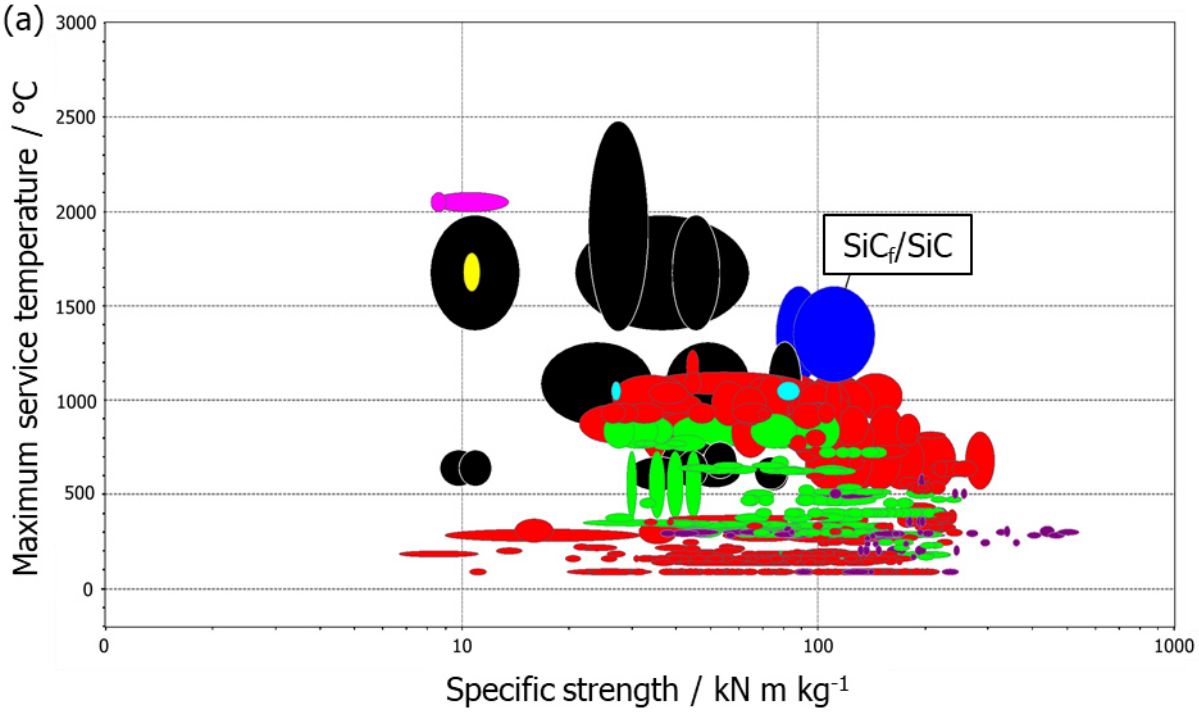
1. Introduction

Silicon carbide fibre reinforced silicon carbide matrix composites (SiC_f/SiC) have been identified as a candidate material for these applications, see figure 1.2(a). The application of SiC_f/SiC in the aerospace industry is increasing; replacing Ni-Ti super-alloy components and thus giving engines the capability to operate at higher temperatures, leading to reduced active cooling requirement and enhanced thermal efficiency [5]. Excellent high-temperature specific strength properties mean that the size and mass of the engines can be reduced, which is expected to reduce specific fuel consumption[i] by up to 25% [6] by improving the propulsive, thermal and transfer efficiencies.

The SiC fibre reinforcement provides pseudo-plastic behaviour, permitting these composites to be used as structural components at high temperature where monolithic ceramics could not. The introduction of a secondary phase allows the matrix to transfer the load to the stronger fibres when stressed. The fibres then dissipate energy through a number of mechanisms: fibre matrix debonding, crack deflection, fibre bridging and pullout [7, 8]. Consequently, when processed correctly to create a dense matrix SiC_f/SiC also has improved the resistance to crack propagation to a level similar to that of light aeronautical alloys, K_{1C} = 30-50 MPa $m^{-1/2}$ [9].

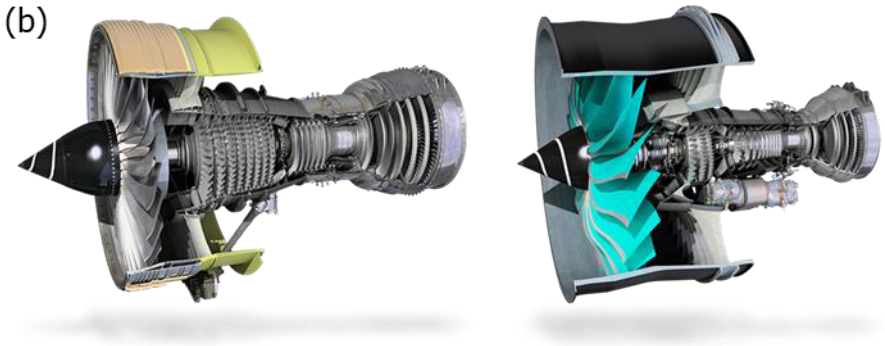
[i] Specific fuel consumption is the mass of fuel burned each hour per Newton of thrust generated.

(a)



	Material Family	Examples
	Technical ceramics	Alumina, graphite, zirconia
	Oxide composites	Alumino-silicate fibre alumina matrix
	Carbon composites	Carbon fibre carbon matrix
	Silicon carbide composite	Silicon carbide fibre silicon carbide matrix
	Metal matrix composites	Aluminium, magnesium and titanium matrix
	Ferrous metals	Alloy steels, carbon steels and stainless steels
	Non-ferrous metals	Titanium, cobalt and nickel
	Refractory metals	Molybdenum, niobium and tantalum

(b)



Trent 700 (1990) Ultra-fan (2025)

Figure 1.2. (a) The high-temperature specific strength of CMCs compared to other aerospace materials and the respective key [10] and (b) the evolution of civilian turbofan engines shape showing an increased by-pass ratio that decreases specific fuel consumption when CMC components are added [6, 11].

1. Introduction

Chemical vapour deposition (CVD) is an established method for the application of a thin coating to a substrate material; a variation can be used to infiltrate porous bodies as well. The latter is called chemical vapour infiltration (CVI) which involves the decomposition of a thermally activated gaseous mixture to deposit a solid matrix [12], in this case, SiC, which fills the porosity in a heated porous fibre preform by gradually increasing the effective diameter of the fibres. CVI is performed at relatively low temperatures to enhance infiltration, thus reducing the risk of mechanical stresses or chemical attack causing damage to the fibres. It is also possible to near or net-shape manufacture complex-shaped components, as well as control the extremely refined microstructure through control of key processing variables. Another benefit of CVI processing is that it offers a tailorable fibre matrix interface via the control of the reactive gas species enabling the deposition of interfaces with a different chemical composition. This allows control of the failure mechanism by controlling the interfacial strength. However, there are two main disadvantages, the first being that, fundamentally, CVI is very slow, taking up to 1000 hours to produce a single component to ~90% density [13]. The other is the preferential deposition of material at the surface of the sample, which causes the premature filling of surface channels. This leads to large volumes of residual porosity in the centre of the composite, which severely degrades the CMCs mechanical properties.

For both of the reasons mentioned earlier, to reduce processing times and increase product density is the subject of much industrial interest. Microwave enhanced chemical vapour infiltration has been identified as a potential method to achieve this

[14, 15]. The use of microwave energy can lead to a controllable inverse temperature gradient, which is created by the volumetric heating of the fibres coupled with surface heat losses [13]. This means that when gaseous reactants are introduced, densification initiates at the centre of the composite first and proceeds the fastest. In doing so premature pore closure at the component's surface is theoretically avoided, thus avoiding porosity formation [16].

This thesis reports the experimental and modelling efforts on the use of the microwave energy enhanced chemical vapour infiltration (MCVI) process investigating the deposition mechanism of a SiC matrix in a SiC fabric preform. The primary aims of this research were to:

- Understand the relationship between processing conditions and resultant microstructures, crystal structures and compositions.
- Produce relevant models to both verify and predict future experimental outcomes
- Develop a complimentary slurry impregnation route for further reducing processing times.

This thesis consists of five chapters. Chapter two reviews the key existing literature related to the research, ranging from CMCs constituents to manufacturing methods to the principals of microwaves. Chapter three presents the experimental works, which in turn is divided into five sections: MCVI equipment, the materials used, the production procedure, the characterisation of these materials and the modelling efforts. The results and discussion are reported in chapter four; this chapter presents and discusses the MCVI aspects of the research. The second subsection reviews the

results of the experimental and modelling efforts related to the formation of an inverse temperature profile in the SiC preform. The final section of the results details the impregnation work and the optimisation of the slurry impregnation parameters. Conclusions and future work are in chapter five.

2. Literature Review

2.1. Ceramic matrix composites

Ceramics are often defined as non-metallic inorganic solid compounds. They are shaped at low temperature and consolidated at very high temperatures. Typically ceramics generally exhibit good thermal properties, hardness, corrosion resistance, and strength under compression when compared to metals and polymers; however, they are limited mechanically as they are inherently brittle [17]. This is because they are a mixture of strong covalent and ionic bonding, which means there are limited slip systems dislocations can move along. This, in turn, means that ceramics do not undergo plastic deformation[ii] and therefore their fracture toughness, and resistance to crack propagation is low, making them susceptible to catastrophic failure. Theoretically, ceramics should exhibit excellent mechanical strength but their brittle nature means they are susceptible to the effects of Griffith's flaws, i.e. small defects act as stress concentrators. This means that in reality ceramics exhibit significantly reduced fracture stresses [18].

The brittle behaviour of monolithic ceramics that has led to the development of ceramic matrix composites. The addition of a secondary phase, which can be either particles, whiskers, platelets, laminae, continuous fibres or any combination of them. These acts to increase the fracture toughness and creep resistance of the matrix phase [19]. This gives the composite the potential to be able to operate in more

[ii] Except under rare conditions, such as grain boundary sliding in very fine-grained materials at T>0.4 of melting temperature [16].

mechanically demanding environments. Figure 2.1. illustrates the typical stress-strain behaviour of a fibre reinforced CMC versus a monolithic ceramic.

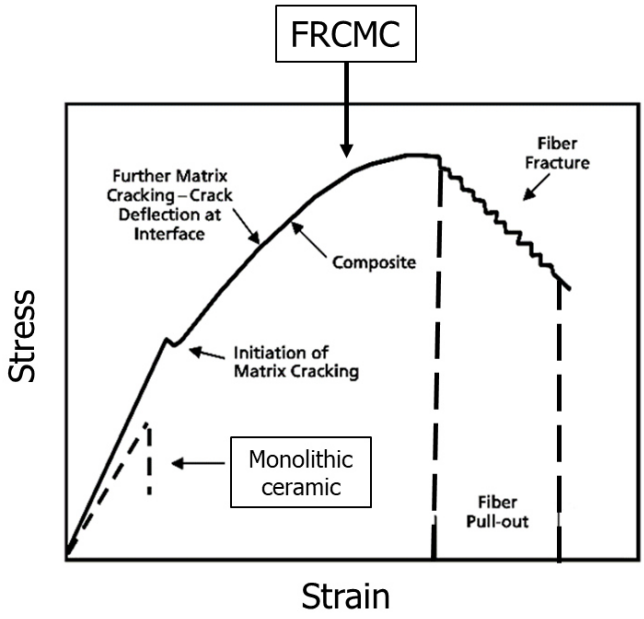


Figure 2.1. Annotated stress-strain curve showing the fracture of a FRCMC compared to a monolithic ceramic [12].

2.2. Fibre-reinforced ceramic matrix composites (FRCMCs)

2.2.1. Properties

Fibre-reinforced CMCs, often known as FRCMCs, offer greatly improved fracture toughness values that can exceed an order of magnitude higher than the equivalent pure matrix phase monolith. Critically, this means that failure is not catastrophic but gradual, thus overcoming the primary issue associated with monolithic ceramics. To achieve this, the load from the weaker matrix must be transferred to the stronger fibres, which is controlled by a number of parameters; matrix-fibre moduli mismatch, fibre volume, fibre morphology and interfacial shear strength [20, 21].

These are the principal advantages of FRCMCs:

- Increased fracture toughness.
- Extreme thermal shock resistance.

- Improved dynamic loading resistance.
- Elongation to rupture up to 1%.
- Anisotropic properties with fibre orientation.
- Reduced mass components compared to some metallic alternatives.
- Chemical inertness.

Currently, the most commercially available continuous FRCMCs are as follows; carbon fibre/carbon (C_f/C), carbon fibre/silicon carbide (C_f/SiC), silicon carbide fibre/silicon carbide and refractory oxide fibres, alumina, mullite and zirconia, with a variety of matrices. Silicon nitride and boron nitride fibres are also available but their commercialisation has been very limited to date [22, 23].

Properties of carbon fibre reinforced composites

First developed in 1958 by a subsidiary of the Dow Chemical Company, carbon fibre was first successfully utilised in polymer-based composites before transitioning into the emerging CMC market in the early 1960s. C_f/C composites were first produced for use on aerospace nose cones and other leading edges such as the space shuttles due to their superb thermo-mechanical properties [24]. More recently C_f/C has been used as brake discs in numerous applications including motorsport, high-end supercars and commercial aircraft, the most notable being Concord's braking apparatus [25]. When compared to traditional steel brakes, C_f/C composites offered a 40% mass reduction attributed to their large heat capacity (2.5 times greater than steel) and high strength at high temperatures (2 times greater than steel) [1]. C_f based composites do offer higher mechanical stiffness at 483 GPa compared to the SiC fibre at 281 GPa and are significantly cheaper £50 kg^{-1} to ~£4000 kg^{-1}. However,

poor oxidation resistance in oxygen-containing atmospheres has majorly limited their application lifespan at high temperature [1]. Despite their sublimation temperature being ~3700°C, carbon fibres experience a decrease in strength and modulus as well as mass loss above ~450°C. This is due to the increased growth rate of surface flaws caused by the fibres' active oxidation. However, if non-oxidising conditions can be maintained, carbon fibre reinforced ceramic composites can be functional beyond 2800°C. For now, that remains a problem to be solved by the scientific community and hence more recent their reassignment to less critical aerospace vehicle components [26, 27].

The exchange of the carbon matrix for a SiC ceramic matrix has helped to combat this issue due to SiC having higher oxidation resistance than carbon. It's for this reason that the C_f/SiC system has been widely explored for use in space optics, brake discs, and recently, turbine blades [28-30]. As well as improved oxidation resistance up to 600°C [26], SiC offers improved thermal conductivity compared to the carbon matrix, 105 W m^{-1} K^{-1} versus 65 W m^{-1} K^{-1}, respectively. This property of C_f/SiC has been exploited as next-generation braking discs. This is because they are more oxidation resistant, much lighter than their metal predecessors, so have a reduced angular momentum and have an increased coefficient of friction with operating temperature [31, 32]. Despite their successful utilisation, in part, due to the chemical affinity between the fibres and the SiC matrix, the addition of SiC does have its disadvantages. The mismatch in the coefficients of thermal expansion (CTE) between the two materials, 3.9x10^{-6} °C^{-1} for SiC[iii] compared to 2.0-2.9x10^{-5} °C^{-1} for

[iii] This value is polymorph specific.

pyrolytic carbon [33], cause the SiC matrix surrounding the carbon fibres to crack during preparation. The addition of SiC still does improve the oxidation resistance of the fibres [34] where it is in contact, but where it is not it exposes the carbon fibres' surfaces to air, the result is a lower than expected oxidation resistance improvement. Furthermore, this protection is lowered further still if the temperature or load is cycled as this prevents a protective silica (SiO_2) film-forming [35].

Properties of silicon carbide fibre reinforced composites

The low oxidation resistance of carbon fibres prompted the development of SiC fibres to replace C_f as the reinforcing phase. Since their development, the properties of silicon carbide fibres have improved exponentially due to the developing production methods, see section 2.3.3. The silicon carbide fibres offer better oxidation resistance and higher strength, 2.82 GPa, compared to carbon fibre's 2.39 GPa. This property means fibres have been used in both carbon and silicon carbide matrices. SiC_f/C composites do not need the interfacial layer, unlike SiC_f/SiC, which requires an interface to facilitate fibre pull-out [36].

Properties of oxide fibre reinforced composites

Oxide fibres, glass, mullite, zirconia and alumina have had limited utilisation to date but do offer a number of enhanced properties compared to the aforementioned carbon-based fibres. Primary qualities of these fibres are their inherent oxidation resistance and low thermal conductivity, which make them serious candidate materials for insulating application such as heatshields for reusable spacecraft [37]. They are also lower cost compared to SiC_f as the production process and raw

material is less complicated and cheaper, respectively [38]. The fibres typically have a higher density, lower modulus and lower strength than non-oxide fibres [39, 40]. Currently, it is the fibres mechanical properties that are limiting load-bearing applications becoming more prevalent, should the processing route improve these the fibres will see a more widespread utilisation [41].

The fabrication of dense CMC structures are based on the same principle, the densification of a porous, fibrous body, varying from 10-80% of theoretical density (TD), known as 'preforms'. Fibre architectures are typically constructed by weaving. These can be 2D, a simple fabric mat or unidirectional fibre or 2.5D where the same mats are linked by the needle punching using another continuous fibre or complex 3D weaves that can be tailored to offer anisotropic properties, see section 2.3.3.3. for more details.

2.2.2. Fracture mechanics theory and toughening mechanisms

The primary role of the reinforcing phase is to reduce the energy that is supplied to the crack tip; this reduces, diverts or stops a cracks' propagation through the brittle ceramic matrix phase, which, in turn, increases the material's fracture toughness. There are a number of energy dissipating mechanisms available in CMCs, which are outlined below. Continuous fibre reinforcement is the most common form of toughening mechanism and it is this type of reinforcement that will later be focused on [42].

2.2.2.1. *Micro-cracking*

This is where smaller cracks propagate ahead of the main crack front when the material is in a stress state, figure 2.2. The micro-cracks dissipate energy, reducing the potential for the primary crack to grow to a critical length, thus increasing the material's toughness [43]. Note, however, that this mechanism will result in an overall lower strength.

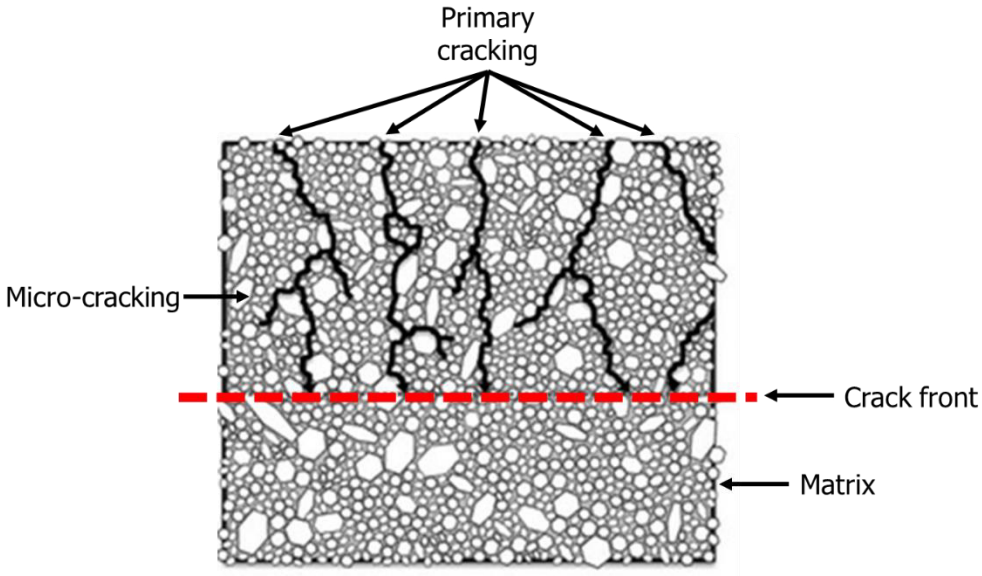


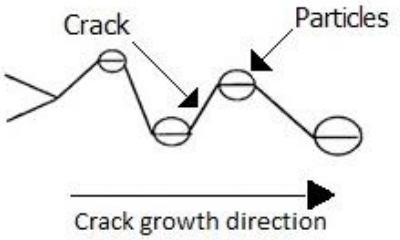
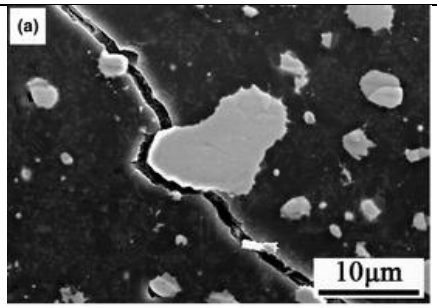
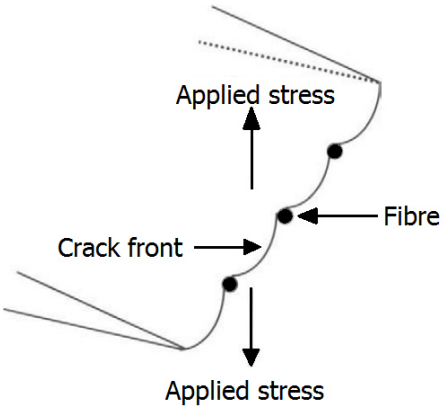
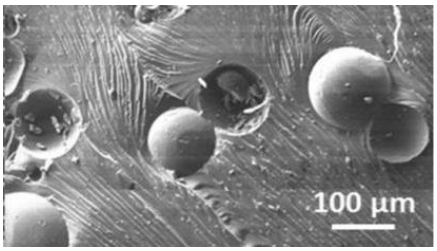
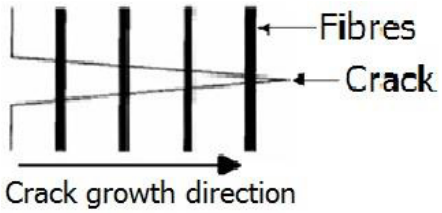
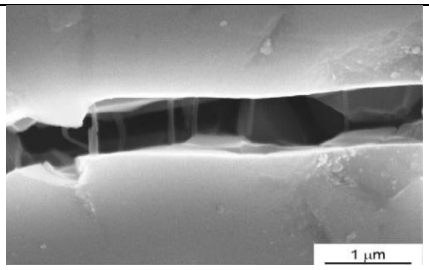
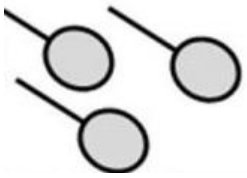
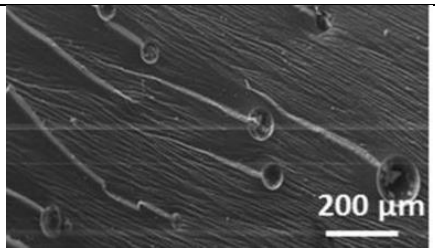
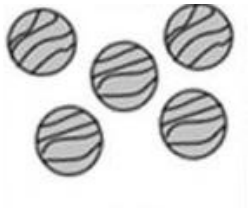
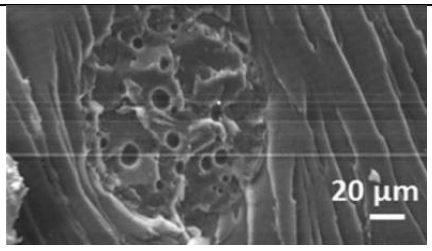
Figure 2.2. Schematic of the micro-cracking process, adapted from [44].

2.2.2.2. *Particle, whisker or discontinuous short fibre toughening*

This is the addition of a reinforcing phase to the matrix and produces a number of sub-mechanisms. These include crack deflection, crack bowing and crack bridging, all of which increase toughness. Crack deflection occurs when a crack propagates into a higher strength reinforcing phase, which forces the crack tip to change direction and proceed in a more tortuous manner thus losing energy, table 2.1.(a) [45]. Crack bowing occurs when a crack front intersects multiple obstacles. The discrepancy in strength between the matrix materials and toughening phase cause the crack to bend as its entirety cannot propagate at the same velocity, resulting in a secondary

crack front forming again dissipating energy, table 2.1.(b) [46]. Crack bridging occurs behind the crack tip and is a result of the matrix failure where only ligaments remain across the crack width. This creates compressive stress on the crack resisting it from opening further, table 2.1.(c) [47]. In all cases, the energy release rate is decreased, and hence, the critical stress intensity factor is increased slowing propagation [46, 48].

Table 2.1. Three different toughening mechanisms available in secondary phase reinforced ceramics, (a) crack deflection, (b) crack bowing, (c) crack bridging, (d) crack pinning and (e) particle yielding, adapted from [49-54].

	Method	Schematic	Micrograph
(a)	Crack deflection		
(b)	Crack bowing		
(c)	Crack bridging		
(d)	Crack pinning		
(e)	Particle yielding		

2.2.2.3. *Transformation toughening*

This is a subdivision of particle toughening where the inherent material property of a compound is used to resist crack growth. One example of this is yttria-stabilised zirconia (YSZ); zirconia exhibits three different crystallographic forms, monoclinic at room temperature, tetragonal (~1200°C) and cubic (~2400°C) structures at higher temperatures. This tetragonal phase is metastable at room temperature when doped with Y_2O_3 when cooled. Full stabilisation requires 8 mol.% of Y_2O_3 and partial stabilisation which requires the addition of 4 mol.%. This stabilisation is achieved by the substitution of Zr^{4+} ions for Y^{3+} ions, which have a larger ionic radius that prevents the lattice from contracting when cooled. If the quantity of metastable tetragonal zirconia is sufficiently high, i.e. >90%, it is able to provide a toughening mechanism. This means, when stressed due to the presence of a crack, the tetragonal phase transforms back to the more stable monoclinic structure, see figure 2.3. This dissipates the cracks energy and induces a volumetric expansion of 4-5% of the crystal structure due to the monoclinic phase having a larger unit cell than tetragonal. This volume change inside the composite creates a compressive back stress on the crack, causing it to be retarded or close altogether [55].

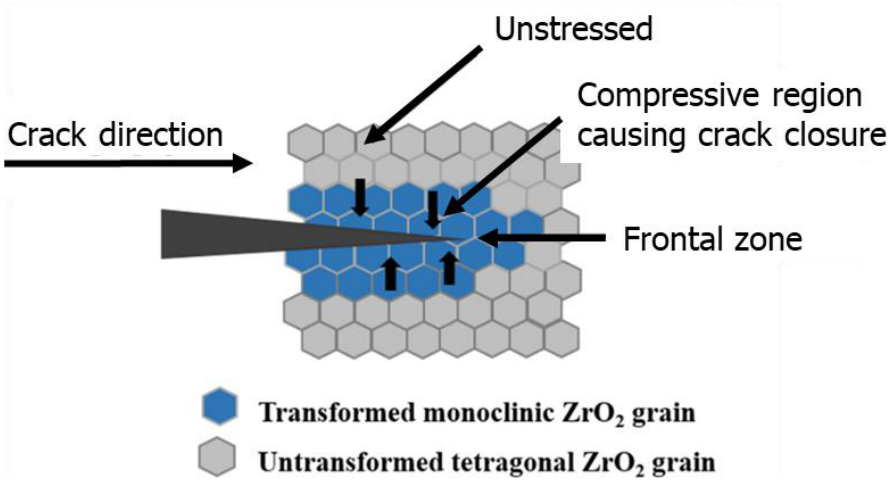


Figure 2.3. The transformation toughening mechanism in partially stabilised YSZ, adapted from [56].

2.2.2.4. *Continuous fibre reinforcement*

The fibres are the primary energy-absorbing component of the composite, which produce a number of secondary fracture mechanisms, all of which provide routes for dissipating a crack's energy. The primary mechanism is fibre pullout. This, together with crack bridging, is the toughening mechanism that is most relevant to the research conducted during this project (though there can also be elements of crack deflection and crack bowing). Fibre pullout enhances the toughness of the matrix phases via the frictional resistance to crack opening as the fibres are pulled out of their sockets in the matrix, figure 2.5. To achieve this necessitates having an appropriate interface between the fibre and matrix. To achieve crack deflection, the interface toughness must be at least one-quarter of the fibre or matrix toughness and the Dundur's parameter[iv] greater than zero to achieve crack deflection, figure 2.4. [57, 58]. A positive value for the Dundur's parameter (α_D) means that the fibre is stiffer than the matrix and is governed by the following equations;

[iv] Dundur's parameter is the elastic mismatch between the fibre and matrix

Equation 2-1 $$\alpha_D = \frac{\bar{E}_f - \bar{E}_m}{E_f + E_m}$$

Equation 2-2 $$\bar{E}_x = E_x\,(1 - {v_x}^2)$$

Where E is the modulus, subscript f is fibre and m is matrix and v_x is Poisson's ratio [20].

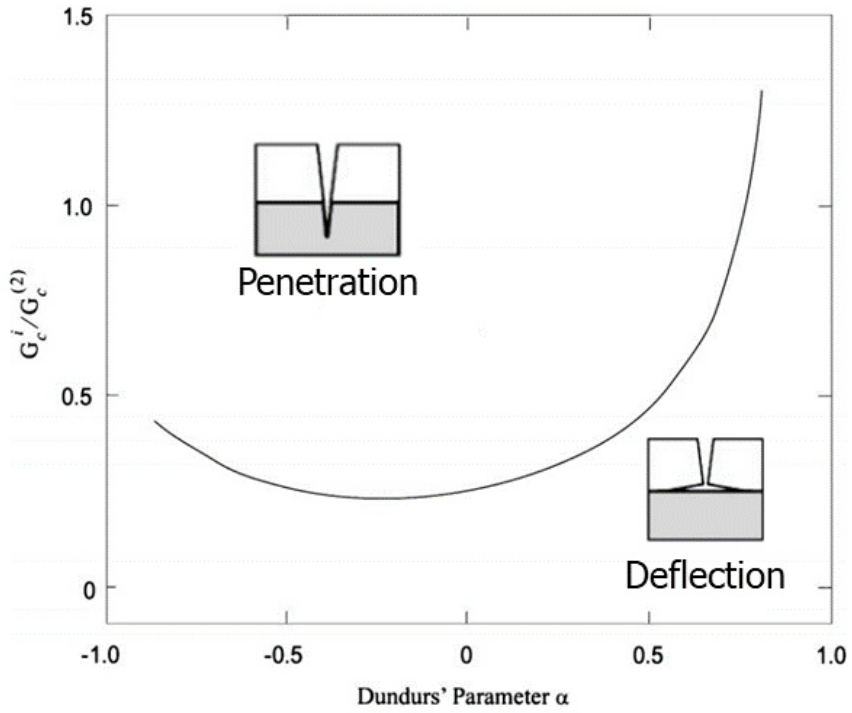


Figure 2.4. A graphical contour separating two regions of crack deflection and penetration based on toughness against the Dundur's parameter that describes the elastic mismatch between components, adapted from [20, 59].

For SiC_f/SiC, an intermediate strength interfacial bond is required, either between the matrix-interface or the interface-fibre to facilitate fibre pullout [60, 61] where interfaces are typically <0.5 μm thick. Compressive pre-stressing of the matrix can also enhance toughening; placing the fibres in tension prior to incorporation in the matrix will place the latter in a compressive state, making it harder for cracks to initiate but this can be very difficult to achieve in practice [19].

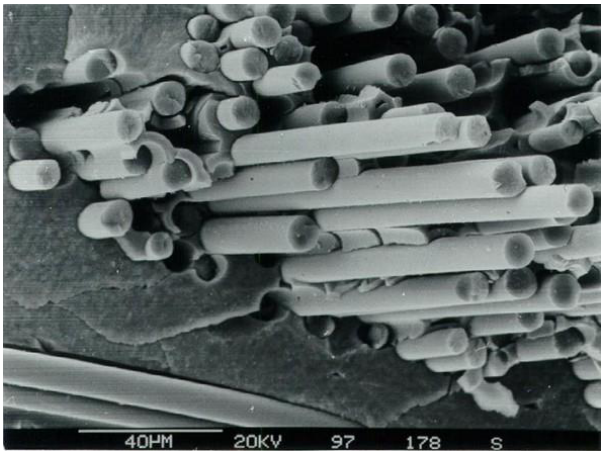


Figure 2.5. A micrograph showing the fibre pull-out mechanism in a CMC and subsequent fracture of the reinforcing fibres [62].

2.2.3. Applications of FRCMCs

Table 2.2. A table summarising the typical applications for FRCMCs in the aerospace industry [40, 63-68].

Fibre type	Fibre Reinforcement	Matrix	Typical application(s)
Organic	C	C	Braking systems in aerospace and re-entry nozzles
		SiC	
Non-oxide	SiC	C	Combustion section of a subsonic jet turbine engine
		SiC	
	Si_3N_4	SiO_2	
Oxide	Al_2O_3	Al_2O_3	Exhaust nozzles in subsonic jet turbine engines
		Aluminosilicate	
	Mullite	Mullite	
	Yttrium aluminium garnet (YAG)	Al_2O_3	
	Aluminosilicate	Al_2O_3	

2.3. Silicon carbide fibre reinforced silicon carbide matrix composites (SiC_f/SiC)

2.3.1. Properties

The main properties that make SiC_f/SiC attractive to industry are listed below, and numerical values for the statements can be seen in table 2.3. [69]:

- Low density relative to in-service Ni-Ti superalloys.
- Good chemical resistance.
- Excellent thermo-mechanical properties up to 1300°C.
- Good thermal shock resistance.
- Relatively high toughness compared to monoliths.
- Good oxidation resistance (compared to carbon fibre-based SiC composites).
- High neutron irradiation tolerance.
- Good wear resistance.

To achieve these properties the material must have a specific microstructure and processing to achieve this as seen below:

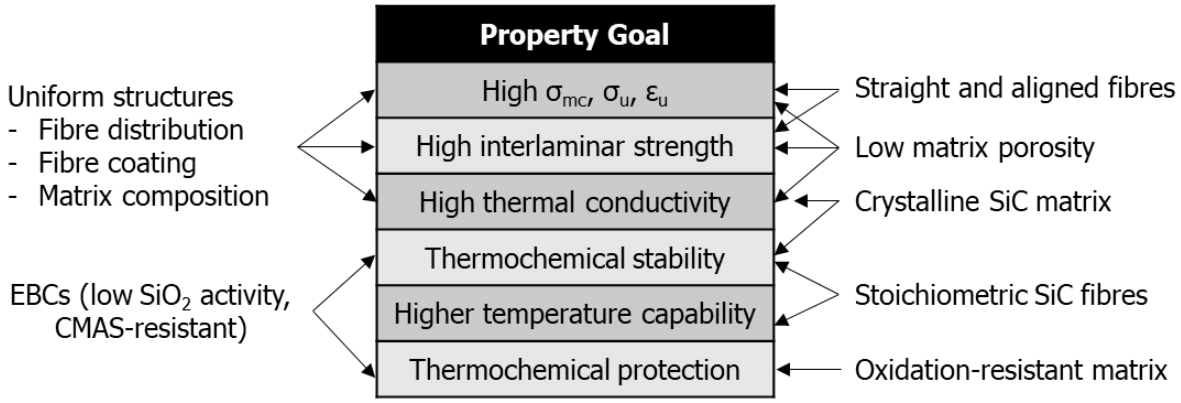


Figure 2.6. Microstructural goals for achieving property goals of SiC_f/SiC composites. σ_{mc} = matrix crack stress, σ_u is the ultimate tensile strength and ε_u is tensile failure strain, adapted from [70].

Table 2.3. General properties of SiC_f/SiC composites. Note that these properties are based on a fibre volume fraction of 35-45% [10, 71].

Property	Value	Unit
Price	2180-3860	GBP kg^{-1}
Density	2300-2900	$kg\ m^{-3}$
Young's modulus	129-270	GPa
Yield strength	225-363	MPa
Tensile strength	220-363	MPa
Elongation at fracture	8-28	%
Compressive strength	577	MPa
Flexural strength	292-472	MPa
Shear strength	0.03-0.06	GPa
Poisson's ratio	0.12-0.26	-
Hardness – Vickers	1900-3500	Hv
Fracture toughness	26-30	$MPa\ m^{-0.5}$
Maximum service temperature in air	1100-1673	°C
Thermal conductivity	7-20	$W\ m^{-1}\ K^{-1}$
Coefficient of thermal expansion	4-4.6	10^{-6} °C
Embodied energy, primary production	2410-2670	$MJ\ kg^{-1}$
Open porosity	3-15	vol.%

2.3.2. Silicon carbide

Silicon carbide is of considerable interest to industry because of its inherent oxidation, corrosion and creep resistance at elevated temperatures. As well as this, it has very high hardness, high neutron tolerance and the combination of high thermal conductivity and low thermal expansion, as well as high-temperature strength, making it highly resistant to thermal shock [72, 73].

Commercial grade SiC is produced by the carbothermal reduction of silicon dioxide and petroleum coke at 2540°C ± 40 in a graphite electric arc furnace called the Acheson process [74, 75]. The process has not changed significantly since it was first developed in the late 1800s when a mixture of clay and carbon was heated to >1600°C in a furnace. The resulting product is either a fine powder or a reaction bonded mass that subsequently requires milling to produce a powder form [76]. Further processing using an acid treatment over a period of days can remove any remaining metallic impurities [77]. The properties of monolithic SiC can be found in table 2.4. SiC can also form at temperatures below the melting point of silicon at 0.75 at.% of carbon; SiC also has a peritectic point at 2540°C at 27 at.% carbon [78]. The phase diagram is quite complex as two polymorphs exist at room temperatures; hence why the below diagram ranges from 1000°C to 3000°C, figure 2.7.

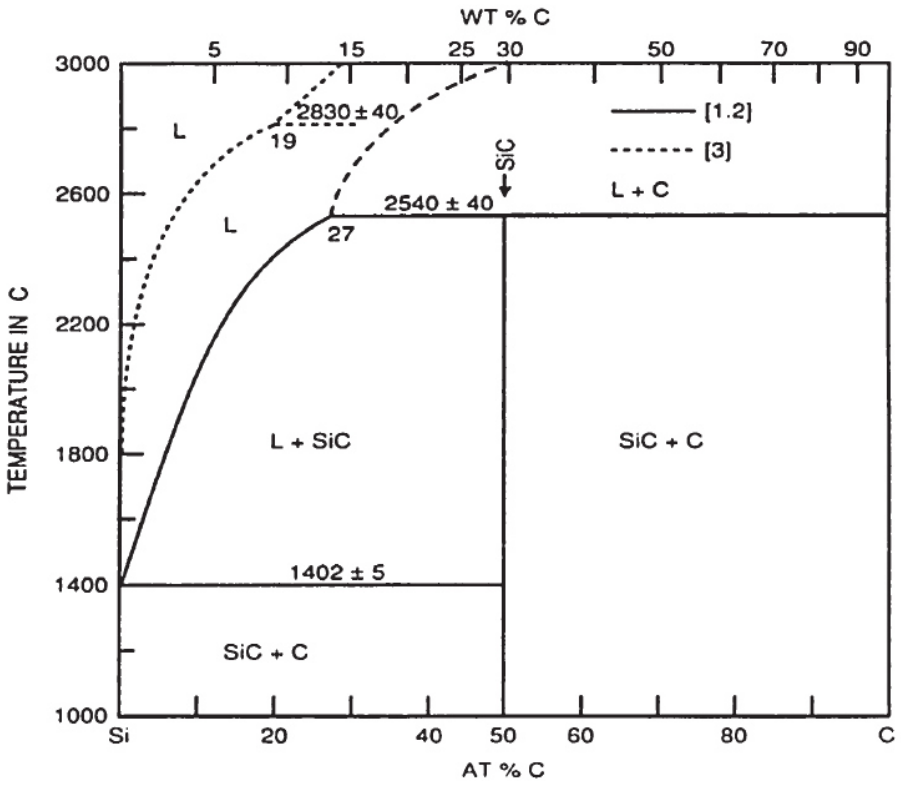


Figure 2.7. An example of part of the SiC phase diagram [79].

Silicon carbide is inert up to 800°C, beyond this point it forms a protective solid silicon dioxide coating up to ~1400°C in air. The protective SiO_2 coating slows the diffusion of oxygen to the SiC surface and therefore decreases the oxidation rate. The passivation layer is, however, susceptible to contamination, which can lower the viscosity of the film and promote oxygen diffusion. The SiC will remain stable with no loss of strength up to 1600°C because of strong covalent bonding in the crystal lattice [80]. Above 1600°C, the oxidation changes from passive to active as the SiO_2 starts to interact with the SiC surface producing gaseous products ($SiO_{(g)}$) that disrupt the passive film, further, encouraging oxygen diffusion. SiC will not melt under normal atmospheric conditions but will sublimate at temperatures exceeding 2730°C [81].

Table 2.4. Properties of monolithic hot pressed commercial purity SiC [10].

Structure and properties	**Value**	**Unit**
Price	10.2-14.6	GBP kg^{-1}
Density	3.21	g cm^{-3}
Young's modulus	437-459	GPa
Yield strength	130-340	MPa
Tensile strength	130-340	MPa
Elongation at fracture	0.03-0.08	%
Compressive strength	1300-3400	MPa
Flexural strength	550-608	MPa
Poisson's ratio	0.16-0.18	-
Hardness – Vickers	2570-2840	Hv
Fracture toughness	3-3.7	MPa $m^{0.5}$
Maximum service temperature in air	1910-2000	°C
Thermal conductivity	3.43-3.57	W m^{-1} K^{-1}
Embodied energy, primary production	2410-2670	MJ kg^{-1}

Table 2.4 continued		
Melting temperature	Sublimate at 2726	°C
Thermal conductivity	75-81	W m^{-1} K^{-1}
Coefficient of thermal expansion	3.43-3.57	10^{-6} °C
Lattice	Hexagonal (α polytype) Zinc blend (β polytype)	
Lattice constant	0.308; 1.51 (α polytype) 0.436 (β polytype)	nm
Electron mobility	900	cm^2 V^{-1} s^{-1}
Bandgap	3.05 (α polytype) 2.36 (β polytype)	

SiC is composed of primarily of strong covalent bonding and around 8-12% contribution of ionic bonding in its crystal lattice due to the small electronegativity discrepancy [82] and exists as two polymorphs, alpha and beta. All structures of SiC can be represented by a tetrahedral unit cell that comprises of one silicon atom bonded to four carbon atoms and vice versa, as shown in figure 2.8. α-SiC has a hexagonal/rhombohedral crystal structure, often called wurtzite and β-SiC has the cubic structure of the zinc blende and is the thermodynamically stable phase up to 1700°C. Between 1700-2000°C a phase transformation occurs turning the (3C) β-phase into (6H) α-SiC, which is subsequently more stable, though both are stable at ambient temperature [77]. There are over 200 different polytypes of SiC [83] that differ in the stacking sequence of the bi-atomic layers 180° about the z-axis, which has a significant effect on the material's electrical properties [84, 85]. The most prevalent of these polytypes in the bulk materials are α-6H and β-3C [86], but it also commonly occurs as 2H, 2R, 4H, 8H, 10H and 15R. With reference to the nomenclature of the polytypes, the number denotes the sequence and the letter the structure; 6H would be composed of 0°, 0°, 0° tetrahedral followed by 180°, 180°,

180°, with this pattern continuing toward the higher-order polytypes. The rationale behind this large quantity of polytypism is the 'endless permutations of stacking sequences' as stated by Jeeps [87], which is what makes processing in terms of nucleation and crystallisation of SiC notoriously difficult.

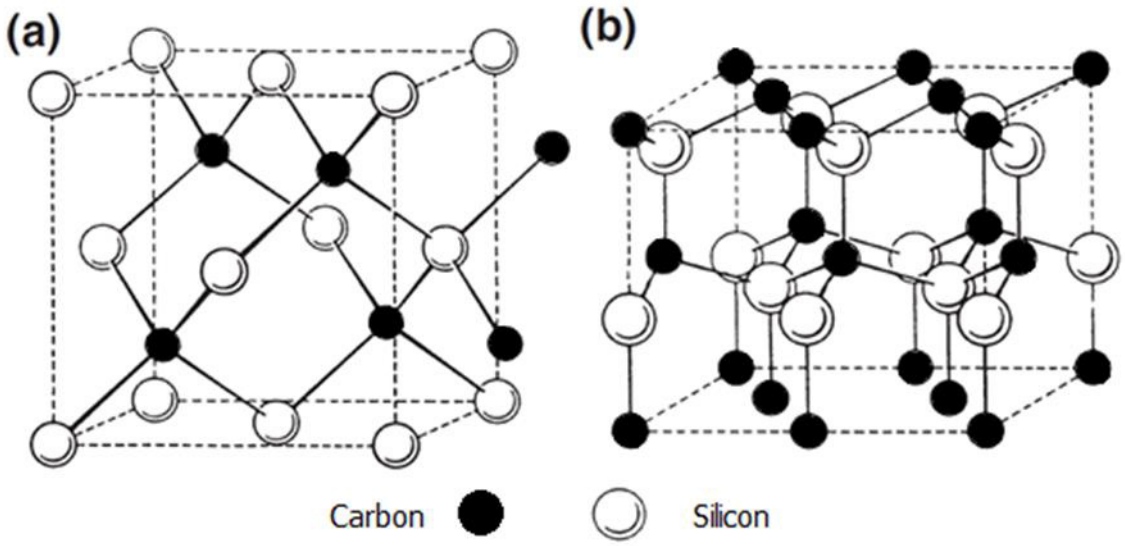


Figure 2.8. (a) Zinc blend cubic structure of β-SiC and (b) the Wurtzite hexagonal structure of α-SiC. Adapted from [88].

2.3.3. Silicon carbide fibres

Work began in the 1970s looking at the development of a fibre that offered better oxidation resistance than carbon fibre which was found to be SiC fibres [26]. There are currently two established commercial methods of production; chemical vapour deposition and polymer-derived ceramic fibres [89], often called preceramic polymer fibres, figure 2.9. A number of emerging techniques are also covered in this review.

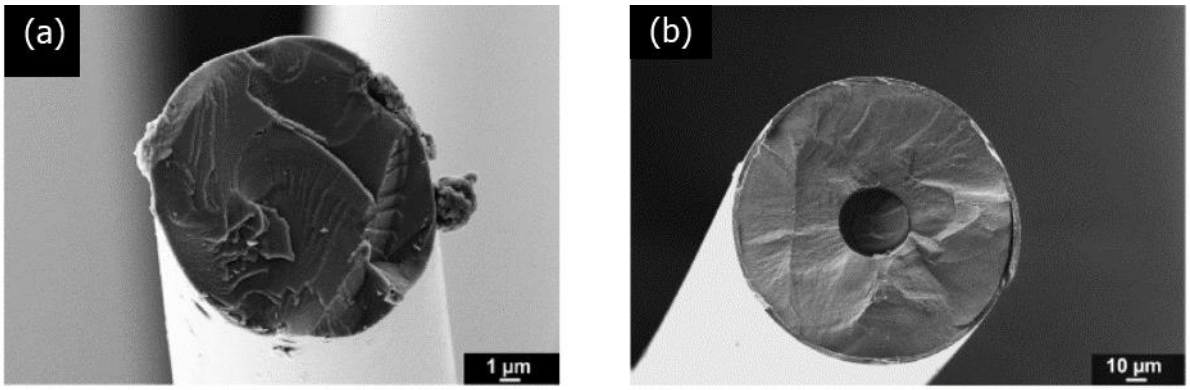


Figure 2.9. (a) Cross sectional images showing the mesostructure of a fibre produced using the preceramic polymer technique and (b) using CVD, note the different scales [89].

2.3.3.1. *Chemical vapour deposition*

In this process, a monofilament, often carbon, is used as a substrate onto which SiC is deposited using CVD, see figure 2.10. Filaments are passed through a furnace in a reductive atmosphere first before the precursor gases are introduced. The latter includes methyltrichlorosilane (MTS), which decomposes to deposit solid SiC onto the carbon fibre [38]. The main disadvantage with this route is that the final SiC fibre diameter is typically >100 µm so they have a high stiffness relative to the preceramic fibres and subsequently cannot be woven into a fabric. There are two industrial producers of CVD-SiC fibres, SCS-6 and Tisics Sigma, and although they are not used in ceramic composites due to their large diameters, they are used in titanium and aluminium metal matrix composites as unidirectional reinforcement providing enhanced creep resistance and strength [90].

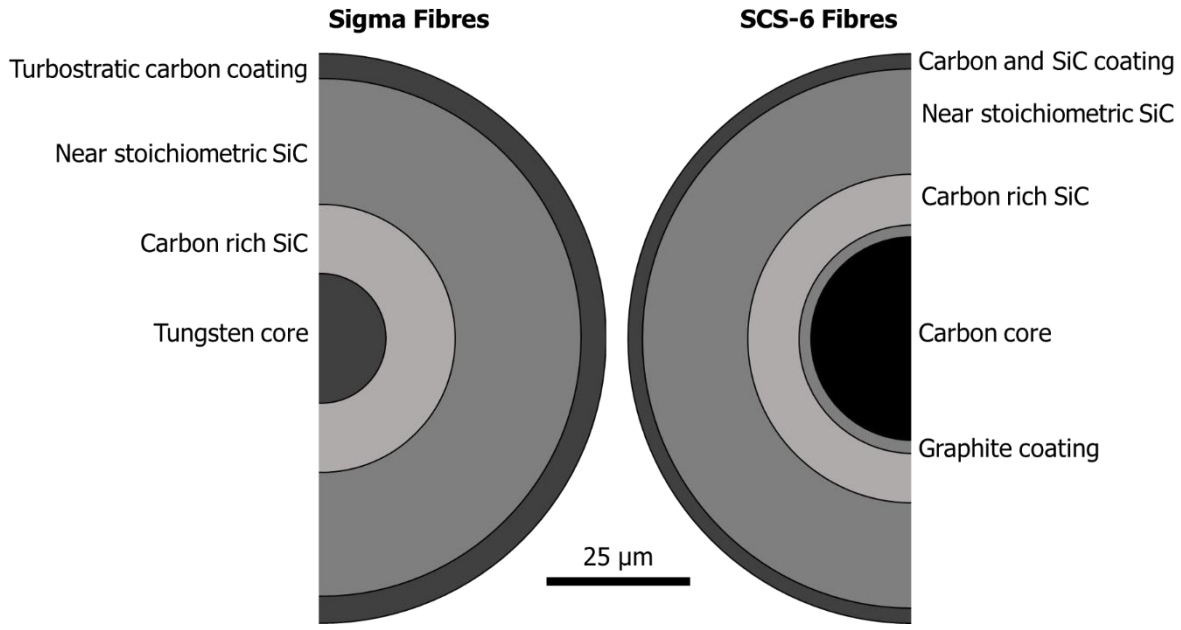


Figure 2.10. Schematic representation of the cross-sections of the two commercially available CVD SiC fibres adapted from [89].

2.3.3.2. *Preceramic polymer*

The process initially involves the creation of high molecular weight poly(organo)silanes that have an intermediate viscoelasticity and are thermally stable [91]. The polymer blend is then spun into filament using the melt spinning process at approximately 300°C [92] to create very fine fibres with diameters as fine as 6 µm [91]. The polymer fibres are then converted to ceramic in a two-step process. The first step is to cure the fibres, this can be done thermally, chemically, by electron beam radiation or via infrared laser [93-97]. The green fibre is then pyrolysed at between 1200-1800°C to convert the preceramic polymer into SiC [98]. The processing conditions of this step directly affect the microstructure and properties of the fibres so conditions are strictly controlled; this is summarised in table 2.5.

Table 2.5. Detailing the processing parameters, compositional, physical properties and respective costs [4, 63, 89, 99, 100].

Gen.	Trade name	Precursor material	Curing method	Processing temperature/°C	C/Si ratio	Density / g cm^{-3}	Fibre dimeter / µm	Fibres per tow	Approx. Fibre Cost per kg/ GDP (2013)
First	Nicalon 200N	Polycarbosilane	Thermal (air)	1200	1.31	2.55	14	500	2250
	Tyranno Lox-M	Polytitanocarbosilane	Thermal (air)	1200	1.37	2.48	11	800	1200
	Tyranno S	Polytitanocarbosillane	Thermal (air)	1200	1.37	2.35	11 or 8.50	800 or 1600	1000
Second	Hi-Nicalon	Polycarbosilane	Electron beam	1300	1.35	2.74	14	500	6750
	Tyranno ZMI	Polyzirconoc- arbosilane	Thermal (air)	1300	1.44	2.48	11	800	1700
Third	Hi Nicalon S	Polycarbosilane	Electron beam	>1500	1.05	3.10	12	500	9700
	Tyranno SA	Polyalumincarbosilane	Thermal (vacuum)	>1700	1.08	3.10	10 or 7.50	800 or 1600	6700
	Sylramic	Polytitanocarbosilane	Thermal (vacuum)	>1700	1.00	3.20	10	800	15800
Fourth	Free form fibres	CVD of SiC	Laser beam	Precursor dependant	-	2.85	25	-	N/a
	Cef-NITE	Polyalumincarbosilane	Oxygen	~1600	1.06	N/a	7	800 or 1600	N/a

(Gen. = Generation)

To date, there have been three generations of commercially available SiC fibres produced by a very small number of companies that use this method [89].

Fibre manufacturers:

- Nicalon fibres – NGS Advanced Fibres Co. Ltd. (General Electric, Nippon Carbon and Safran).
- Tyranno – UBE Industries, Japan.
- Sylramic – COI Ceramic and Dow Corning/NASA, USA.

First-generation SiC fibres

The first-generation had a fine microstructure but were impaired, both thermally and mechanically as they are thermally cured in air. This created an amorphous silicon oxycarbide glassy matrix with oxygen rich regions that are up to 20 wt.% in some areas [101]. This meant that when the material was above 1200°C, the glassy phase would decompose, causing a catastrophic decrease in strength. Alongside this, the fibre has a low modulus and thermal conductivity due to the intergranular glassy phase and small SiC crystallites [100, 102, 103], see figure 2.11. These flaws prompted the development of a second-generation fibre.

Second-generation SiC fibres

The second generation utilised ultra-violet light or an electron beam to cure the polymer precursor, thus lowering the oxygen content to less than 10 wt.% [100, 103, 104]. These fibres were also processed at higher temperatures and are often described as semi-crystalline fibres. The higher temperature form larger SiC grains,

see figure 2.11., in the microstructure, which reduced the creep rate [104] and meant the maximum operating temperature of these fibres also increased [89].

Third-generation SiC fibres

The more recent third-generation fibres have been produced with a near stoichiometric and a fully crystalline microstructure, see figure 2.11. [89]. This is attributed to processing temperatures in excess of 1700°C; consequently, this lowers the creep rate as larger grains reduce grain boundary sliding, particularly in stage II creep [89, 105]. These fibres were the first to utilise sintering aids, aluminium and boron, to increase their density [104]. A more detailed property comparison can be found in table 2.6.

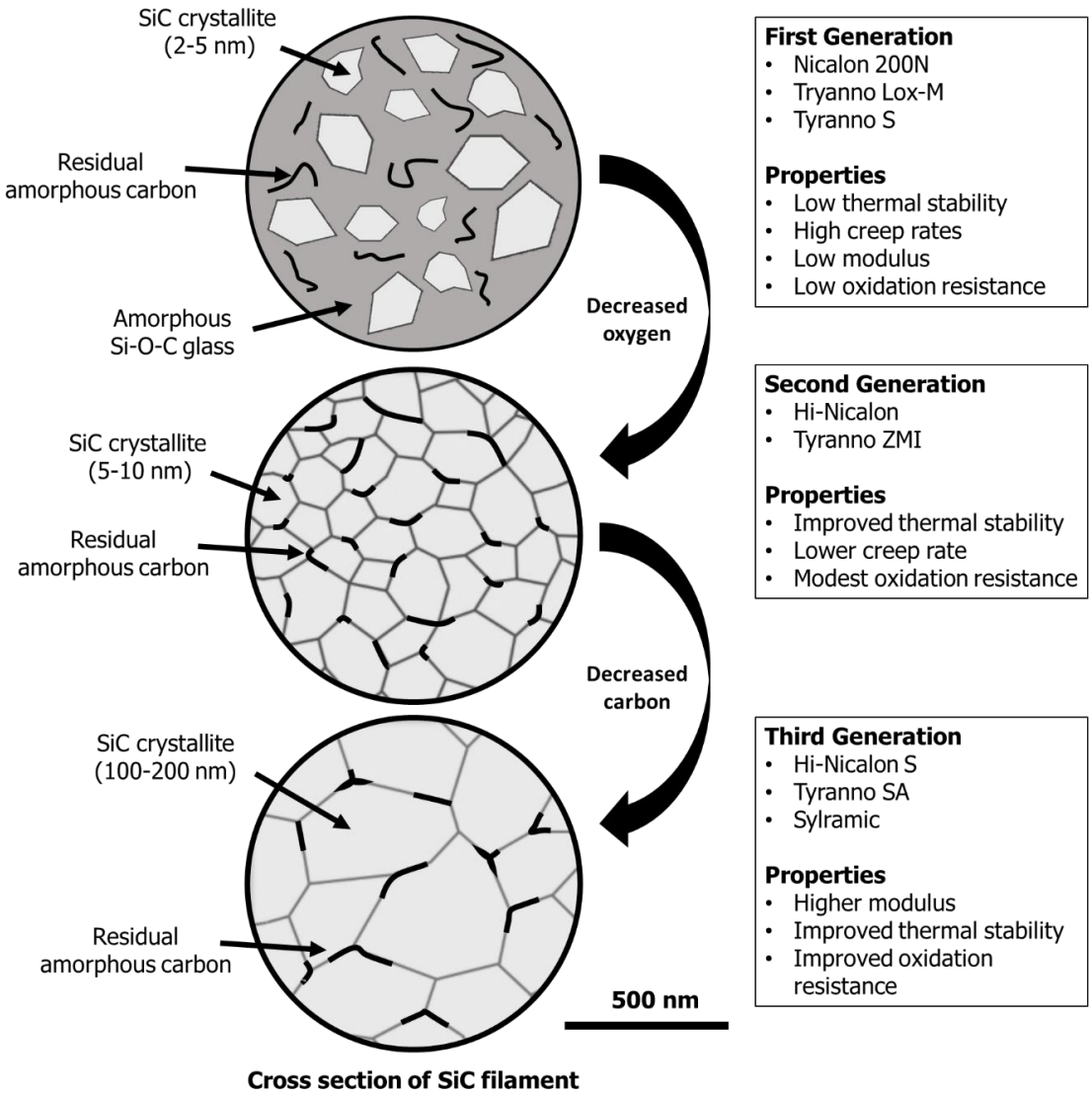


Figure 2.11. Schematic cross-sectional representations of the microstructure of three generations of commercially available SiC fibres, adapted from [89, 104].

Fourth-generation fibres

There are still significant issues with the commercially available fibres today. With the primary concerns being variable composition, creep resistance, grain size and residual phases. There are a number of new developing fibre manufacturing techniques that may resolve the aforementioned issues; however, they are still very much in their infancy, and scale-up feasibility is yet to be realised. One of these methods is the Cef-NITE process [106, 107]. Nano-infiltration and transient eutectic-phase (NITE) [3] is a liquid phase sintering process that can be used to produce both

SiC fibres and a SiC matrix [108, 109]. The fibre process is based on the Tyranno SA method with the difference being how the thermal treatment of the fibre is carried out. In the CEF-NITE process, the fibres pass through a horizontal furnace rather than a vertical set up with a complex temperature distribution [99]. It is claimed that this method yields a larger grain size and improved grain size uniformity compared to third-generation fibres and near stoichiometric composition with low quantities of residual amorphous phases [110]. However, the fibres surface roughness increases which will affect interfacial properties affecting the pullout mechanism.

Another developing an additive manufacturing technique called laser-driven CVD from Free Form Fibres (Saratoga Springs, New York) used a laser to deposit solid material from a gas phase to form free-standing fibres [97]. This involves the use of a gas chamber with fibre ends that acts like seeds mounted at the top of the chamber. The laser beam then breaks down the gas at the gas-fibre tip interface as the fibre is heated by the laser. The CVD process occurs when the temperature is sufficiently high causing the growth of the SiC down the length of the fibre at rates of 0.1 mm s^{-1}, at which point the fibre is extracted from the cavity in a continuous process [97]. This method has been demonstrated successfully pulling 90 filaments at a time. The fibres have a reduced grain size and near stoichiometric composition. Another benefit of the additive manufacturing technique [111] is the ability to introduce coatings and variable compositions by merely controlling the precursor gases in the chamber [112]. Having said that, there are a few drawbacks to this technique; one is the fibre diameter is ~25 μm [63], and excess silicon is often found on the periphery of the fibre, a common consequence of the CVD process [113].

Trade name	Density / g cm^{-3}	Fibre diameter / µm	Fibres per tow	Grain size / nm	Tensile strength / GPa	Modulus / GPa	Creep resistance* / °C	Strength retention temperature / °C	Thermal conductivity / W $m K^{-1}$	Thermal expansion / $10^{-6} K^{-1}$
Hi Nicalon S	3.10	12	500	100	2.3-2.6	380-420	1400	1600	18-24.1	5.1
Tyranno SA	3.10	10 or 7.50	800 or 1600	200	2.4-2.8	375-380	1400	1700	65	4.5
Sylramic	3.20	10	800	100	3.0-3.2	310–400	1300	1700	46	N/a

* = Creep resistance for 1 h at a bend-stress-relaxation ratio of 0.8.

Table 2.6. Comparison of critical mechanical, physical and thermal properties of third generation SiC fibres [4, 63, 89, 100, 104].

2.3.3.3. *Fibre preform properties and architectures*

A continuous fibre preform can be classified into three subsects in terms of scale. The smallest being a fibre filament that is approximately ~10 μm in diameter and forms a larger structure called a tow, which is typically comprised of 800 filaments as seen in figure 2.12. These tows are then used to form a preform in which the matrix is then added to make up a CMC. The design of the preform can be tailored to provide specific properties such as ease of manufacture, thermal properties or mechanical properties.

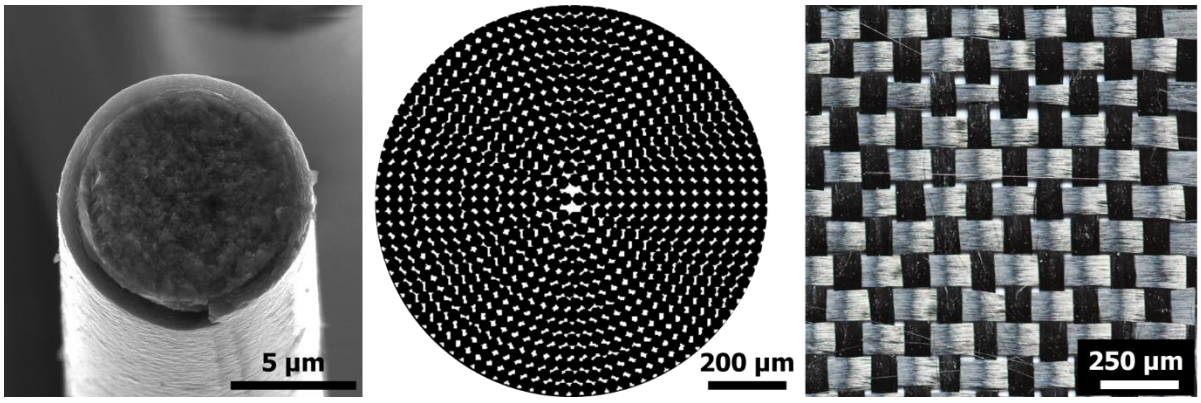


Figure 2.12. Scanning electron microscope image of a single silicon carbide filament coated in a carbon interface, (b) schematic representation of a fibre tow comprised of 800 filaments [114] and (c) a photograph of a basket/matt weave SiC fabric.

This forming is carried out via a number of techniques such as weaving, knitting, braiding, etc. that all originated in the textiles industry. This is very important as to how the preforms are constructed controls the morphology of the porosity network. This determines the tortuosity, and consequently, the permeability of the preform to matrix-forming materials be that solids, liquids or gases. Fibre preforms are classified into four categories, typically by their orientation in space; discrete (chopped), continuous (unidirectional), planar interlaced (two-dimensional) and fully integrated

(three-dimensional), see figure 2.13. [115]. The critical criteria for selecting a fibre architecture for structural ceramic composites are:

- The capability for in-plane multiaxial reinforcement.
- Through-thickness reinforcement between ply.
- The capability to be formed and/or net-shaped for manufacturing.

Depending on the processing of the fibres and the ultimate end-use requirements, some or all of these features may be required.

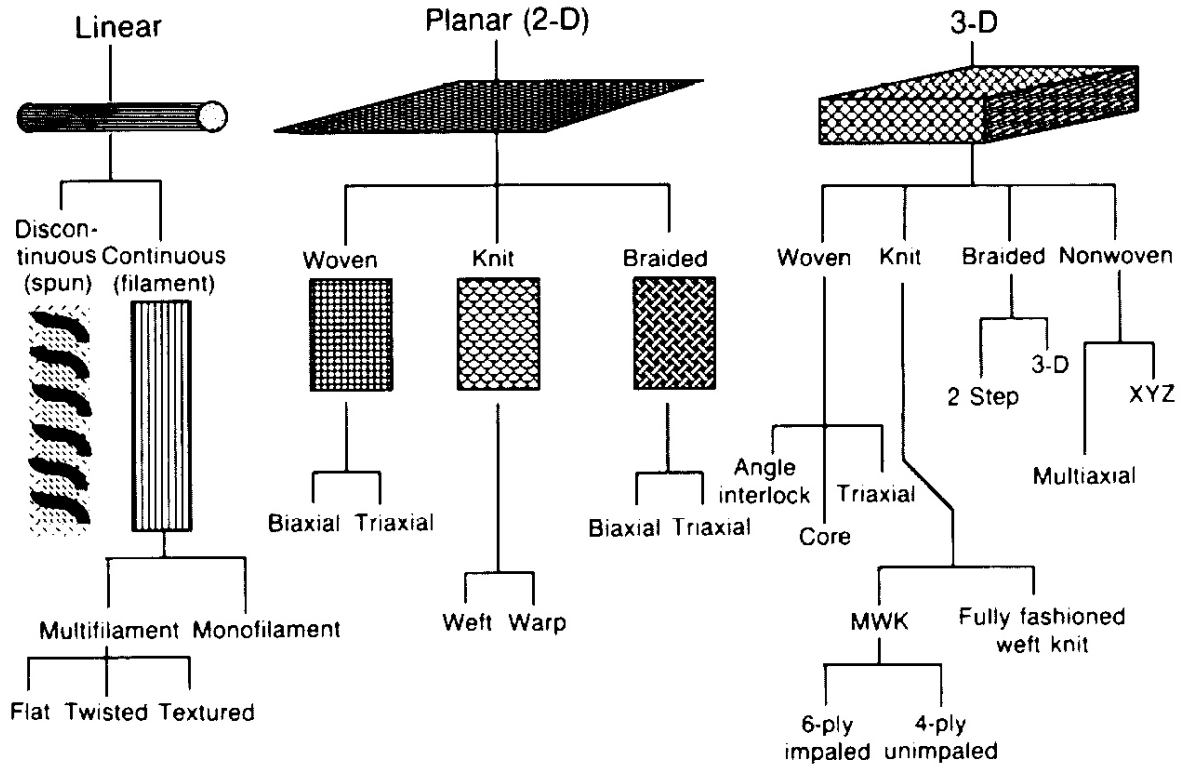


Figure 2.13. Classification of fibre architectures [115].

2D preforms typically refer to fibres that have been interlocked in some fashion and without layup have bi-directional strength. These fibres are then typically stacked in a (0°, 90°, 0°, 90°) or (0°, +45°, 90°, 0°, -45°, 90°) arrangement thus giving bi-directional strength and quasi-isotropic properties, see figure 2.14. Weaving interlaces the fibre tows (0°, 90°); in knitting, fibres are pulled by loops of fibre over other loops (0°, 90°); and in braiding is the twisting of fibres together. Below are

four schematic weave patterns commonly used when weaving SiC preceramic fibres and table 2.7. outlines their benefits and drawbacks. Neither knitting nor braiding has yet been widely utilised commercially for making preforms with ceramic fibre.

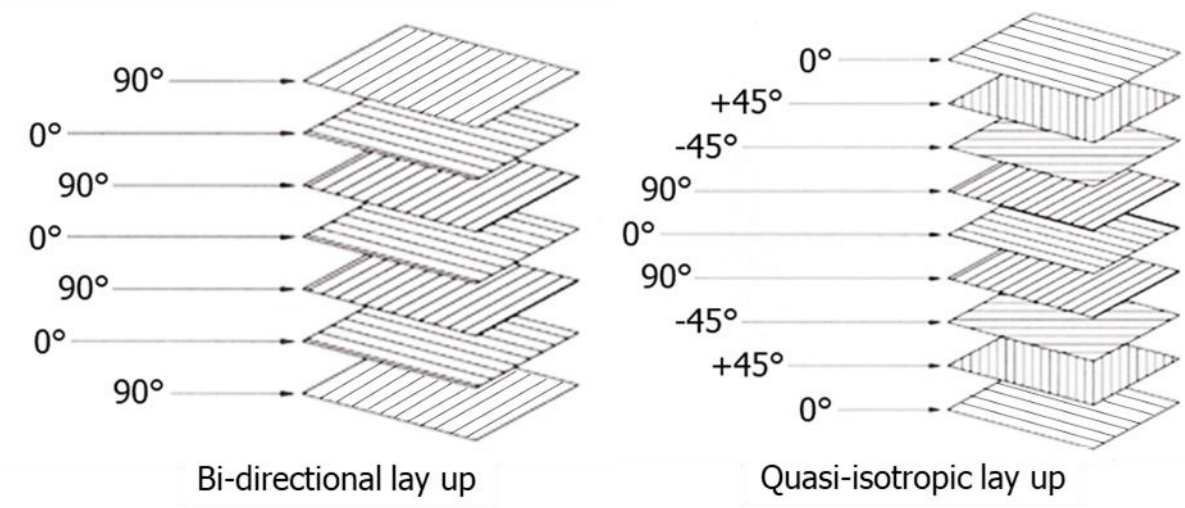
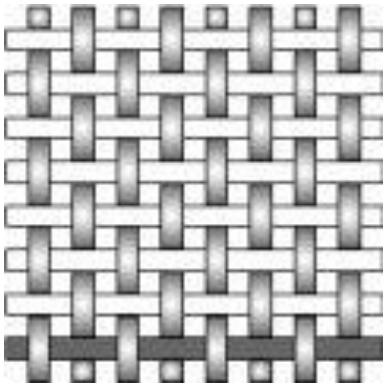
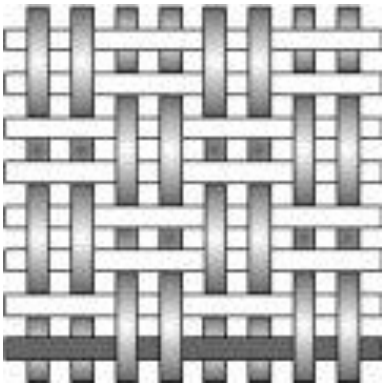
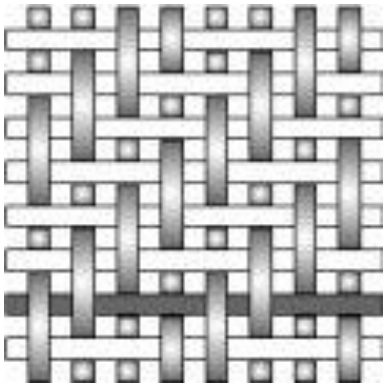
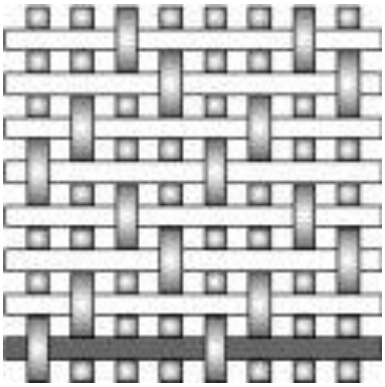


Figure 2.14. Schematic illustrations showing the different orientation of lamellae in the different orientations, adapted from [116].

Table 2.7. Schematics of the weave patterns used in four of the most common weaves, with reference to their advantages and disadvantages [117].

Plain weave	**Matt or Basket weave**
 Advantages • Symmetry • Balance • Stability Disadvantages • Drape • Smoothness • Crimp	 Advantages • Balance • Symmetry • Drape Disadvantages • Smoothness • Crimp • Low density
Satin weave	**Twill weave**
 Advantages • High density • Smoothness • Low crimp Disadvantages • Stability • Symmetry • Balance	 Advantages • High density • Balance • Drape Disadvantages • Smoothness • Stability • Symmetry

Though shaping is flexible in 2D preform design, it is limited mechanically because there are no connective fibres in the Z-axis, so composites are prone to delamination as the strength in the Z-axis is almost entirely governed by the matrix/interface bonding. To overcome this 2.5D, 3D, 4D and 5D reinforced structures have been developed both computationally and using robotic manufacturing methods to give the composite materials in-plane support, figure 2.15.

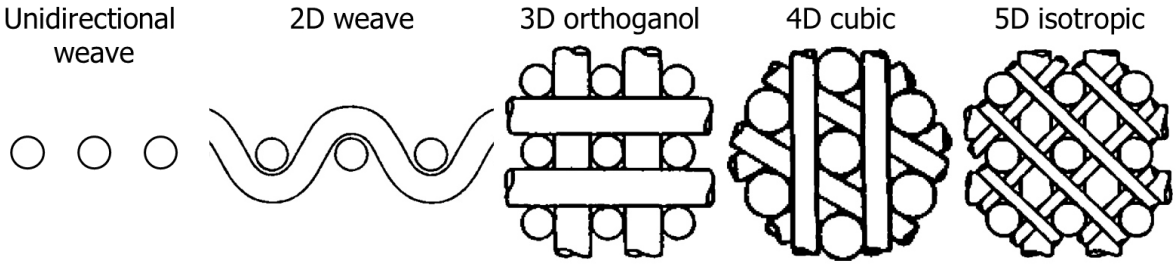


Figure 2.15. Cross-sectional diagrams of the types of weaves, from unidirectional to 5D isotropic, adapted from [118, 119].

Fibre volume fraction also has a significant role in determining the mechanical performance of the composite. The fraction is commonly described as a percentage and has a very wide range but typical values fall between 10-30 vol.%, though this is material, processing and application-specific. It has been shown that high volume fractions of fibre can often lead to a reduction in the maximum principal stress the composite can withstand [120]. Volume fraction also has a significant role in the fracture mechanics, as it, along with the interface, governs the fibre-matrix load transfer. If the volume fraction is too high, tensile stresses are more significant at the fibre matrix interface of the component causing failure, whilst if then too low the tensile stresses are focused at the component surface [121]. Lee et al. [120] observed this transition through the finite element analysis (FEA), which found the maximum stress experienced switched from the surface to the interface above 20 vol.%. This is also shown by Xu et al. [122] in showing the experimental load-

displacement curves for three SiC_f/Si_3N_4 composites with different fibre fractions, see figure 2.16.; this nicely illustrates the observations made by Lee et al. using FEA [120].

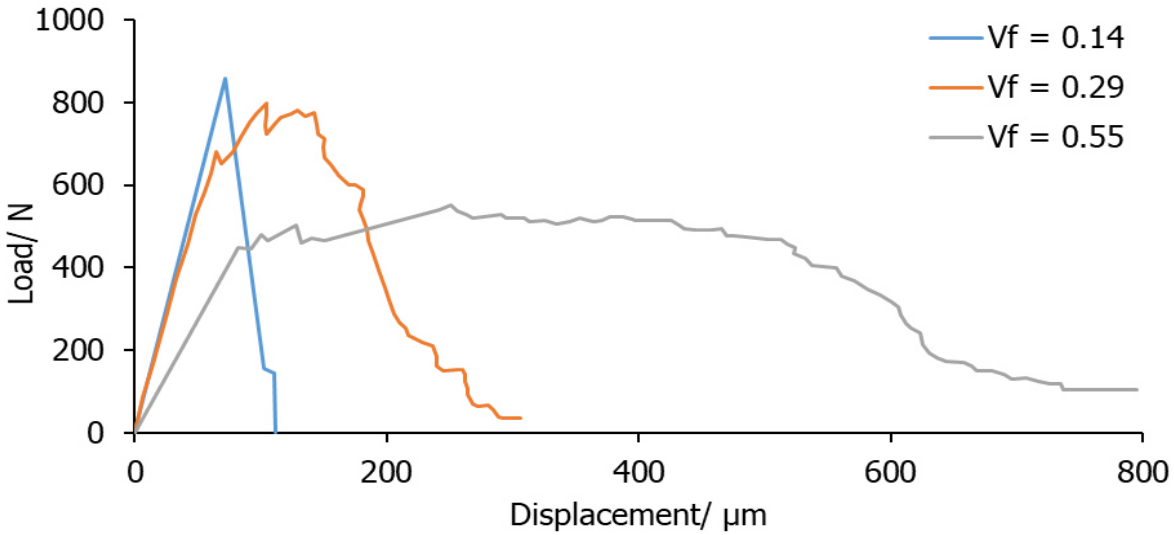


Figure 2.16. Three load-displacement curves as a function of volume fraction (V_f), reproduced from [122].

2.3.4. Applications of SiC_f/SiC

SiC_f/SiC composites are desirable materials for a number of applications that operate in demanding conditions that require a components minimum life span to be several tens of thousands of hours [123]:

Aerospace industry (figure 2.17.)

- Aerofoil blades and vanes
- Nozzle flaps
- Shrouds and blade tracks of the seal segments (figure 2.18.)
- Combustor liners
- Aircraft brakes

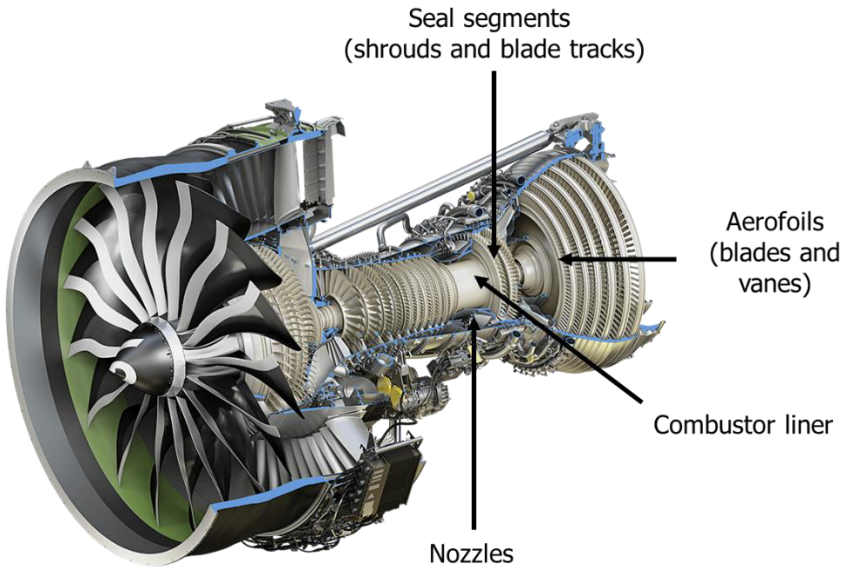


Figure 2.17. Cross-section of the next generation large three-shaft civilian turbofan engine the GE9x from General Electric [124].

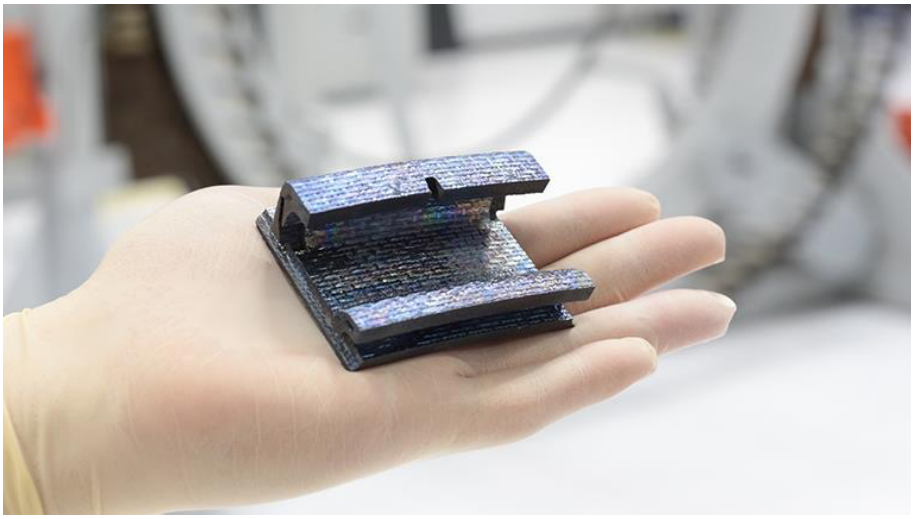


Figure 2.18. A SiC_f/SiC shroud component produced by Rolls Royce PLC [6].

Other applications include:

The energy industry

- Land-based gas turbines.
- Components in nuclear fusion reactors.
- Nuclear fuel cladding tubes and channel boxes.
- In-core components of 5^{th} gen. reactors.
- Heat exchangers.

The automotive industry

- Brake discs in high-end sports cars.

2.4. Fabrication of SiC_f/SiC FRCMCs

There are three steps in the typical production of an FRCMC:

1. Preform production – The weaving, laying up and/or shaping of, in this case, the SiC fabric to form a 2D, 2.5D or 3D fibrous structure.
2. Matrix formation – The porosity inside the fibre preform is filled with a ceramic matrix. Note that as discussed earlier in section 2.2., interfacial layers are usually added to weaken the interfacial bond between matrix and fibre.
3. Matrix consolidation – This typically involves high temperatures and modified pressures to densify the matrix once it has been added. This might be pyrolysis or sintering or hot isostatic pressing, for example.
4. Finishing – The addition of any coating that might be required for the application, e.g. an environmental barrier coating (EBC) or thermal protection system (TPS).

The majority of the variations in the production of these composites, therefore, occurs at the second matrix formation stage. There are numerous techniques that can be used, however, each has its advantages and disadvantages [19]. There are a number matrix formation/consolidation techniques that are readily available, three of which are considered advanced manufacturing methods that are currently of great interest to industry and hence subject to intensive research, viz:

Conventional methods

- Powder processing.

Advanced methods

- Reactive melt infiltration.
- Polymer impregnation and pyrolysis.
- Chemical vapour infiltration.
- Hybrid techniques and developing techniques.

Conventional processing routes will be briefly reviewed, whereas advanced techniques discussed more thoroughly.

2.4.1. Powder processing routes

Typically used for the traditional processing of monolithic ceramics, powder-based infiltration routes are often utilised to form a ceramic matrix in a fibrous preform. The slurry is commonly prepared using powder, binder, a dispersant and a suitable solvent and then combined with the reinforcement. For more complex fibre architectures a vacuum is often used to assist slurry infiltration [125]. The composite is then dried before the consolidation occurs.

Powder routes are generally used for, though not limited to, smaller-scale reinforcements such particulates and chopped fibres [40, 126]. Homogenous distribution of the reinforcements through the matrix can prove challenging, particularly if the properties of the slurry, such a pH, dispersion, rheological properties, zeta potential and wettability are not carefully controlled [127]. Issues also arise when it comes to processing continuous fibres due to the matrix formation and consolidation step of CMC production, which often leads to fibre damage when the harder powder is forced inside fabric tows [128].

2.4.2. Reactive melt infiltration

Often referred to as liquid silicon infiltration this is the technique was pioneered by General Electric (GE) [129] for the mass production of SiC_f/SiC CMCs in their CFM LEAP engine range, which was launched in 2016 [130, 131]. SiC_f/SiC composites produced via reactive melt infiltration (RMI) route are the first CMCs to be used in the civil aviation industry. They have also been used in GE's adaptive cycle engine in military aircraft, setting new records for the hottest operating temperatures ever recorded in aviation. Their use in the hottest sections of the turbo fan and turbo jet engines means that higher temperature are achieved without additional cooling system and at one third the mass of an engine using superalloy components. This enhances engine performance, durability and fuel economy of the engine by up to 25% [132].

The process involves the preparation of a SiC fibre preform structure into which a porous carbon matrix is introduced. This is not an iterative process; hence, there the ceramic yield must be high with the correct spatial and molar balance of pre-matrix material. To achieve this, carbon deposited via CVI or slurry route must be added beforehand [133] as shown in figure 2.19. Liquid silicon is subsequently introduced at >1400°C and using an atmosphere of <100 kPa; the latter helps prevent the entrapment of residual air in the composite and reduces the oxidation of the carbon that occurs at this temperature. The molten silicon travels along the channels in the porous carbon matrix, reacting with it to form a dense silicon carbide matrix [31, 134].

The reactive metal infiltration process has several advantages [5]:

- A near fully dense ceramic matrix is produced.
- Processing time is much shorter relative to other advanced CMC fabrication techniques and is therefore relatively inexpensive in comparison.
- Oxidation resistant coatings are often not required due to the closed porosity at the surface.
- The ceramic matrix formed is reaction bonded.

This process has four major disadvantages. For fibre composites, the high temperatures used in reactive metal infiltration exposes the SiC fibres to incredibly aggressive molten silicon, often above 1400°C [135]. The reaction between the constituents is exothermic, which further increase the temperature locally, causing more fibre damage [135]. Silicon in this form is very reactive, and if infiltration processing conditions are not tightly controlled significant degradation of the silicon carbide fibre preform [133, 136-138] will occur [5]. Often an interface material is needed to protect the fibres, this can be a CVI deposited coating or slurry matrix but sometimes this is not sufficient to shield the fibres entirely [136, 139] and such methods have met with limited success to date.

Although the quantity of silicon required can be precisely calculated, due to the inability to obtain complete mixing not all of it will react with the carbon leaving residual pure silicon and carbon phases as well as intermediates and non-stoichiometric phases [134, 140, 141]. Composites produced via this method have approximately 5-10 vol.% residual silicon phases [135], as shown in figure 2.19.,

which have low oxidation resistance and a significantly lower melting point than the SiC matrix present. Subsequently, this residual silicon lowers the operating temperature of the composite to around 1400°C. Despite this, the operational temperature is still >100°C hotter than the highest in service operating superalloy today [142]. The metallic silicon phase also effects mechanical properties leading to an enhanced creep rate, increased crack propagation and resulting in further attack when operating at high temperature [143, 144]. These issues are further exacerbated by the mismatch in the coefficient of thermal expansion between the phases, which also introduce residual stresses into the material [145]. The final issue is due to the molten silicon reacting with carbon to form the SiC in situ. The rate of reaction is limited by four primary factors: available surface area per unit volume, the molar volume of the SiC produced during the reaction, the thickness of the reaction barrier and the rate the fibre preforms become saturated [146]. One of the fundamental characteristics of the RMI process is the wettability of the silicon melt on the substrate [147, 148], fortunately for molten silicon on a silicon carbide substrate this is nearly 0°, i.e. wetting occurs readily [149].

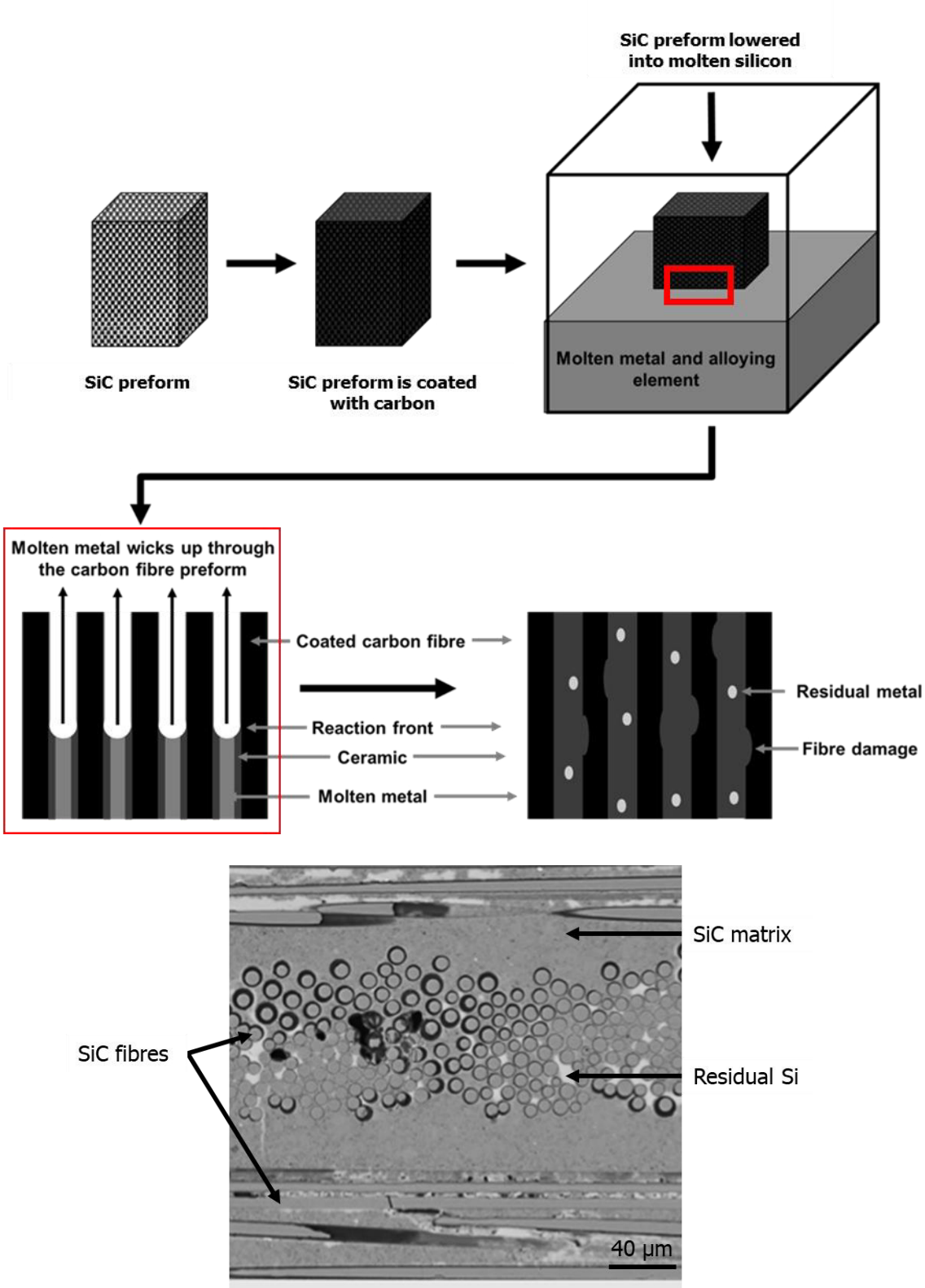


Figure 2.19. The reactive melt infiltration process adapted from [150] and SEM image from the literature showing residual silicon phase between fibres [151].

2.4.3. Polymer infiltration and pyrolysis

The polymer infiltration and pyrolysis (PIP) process draws its origins from the wet lay-up process used to make polymer matrix composites. In this case, the SiC fibre is coated in a liquid precursor polymer that is then pyrolysed at temperatures up to 850-900°C [152]. Thereafter, atomic rearrangement occurs to form amorphous SiC before the onset of crystallisation beyond 1200°C [153-155]. This pyrolysis produces the solid corresponding ceramic material specific to the precursor used, see figure 2.20. In the case of SiC_f/SiC composites polycarbosilanes, a preceramic polymer, are typically used [156]. This method of production provides reasonable control of matrix composition, is relatively easy to execute and can produce near net shape products.

The preceramic polymer is firstly infiltrated into the fibre's preform before being cured to introduce crosslinking between the hydrocarbon chains. This happens via both hydrosilation and dehydro-coupling before the transition to pyrolysation at approximately 400°C, though this is dependent on precursor [152]. At approximately 900°C mass losses can be seen beyond this amorphous SiC forms as a result of the higher temperatures, which produces more crystalline material [157].

However, there are a number of drawbacks, primarily due to the evolution of gaseous species during the pyrolysis step, which produces an undesirable microstructure. The evaporation of constituents of the precursor means there is also a volume shrinkage and approximately 20% mass loss, which leads to a pre-cracked matrix, porosity and residual stress [158]. This makes the process iterative, and multiple impregnations of the fibre are needed (up to 12) to achieve near full density

as ceramic yield per cycle is typically lower than 30% [159]. Another drawback of the pyrolysis step is that high temperatures up to 1800°C can often damage the fibres [160-162]. This can have the knock-on effect of changing the interfacial properties and reducing the toughening effect of the secondary phase. Therefore to optimise this process, a high ceramic yield is the most critical factor in terms of both creating a dense composite and reducing the number of energy-intensive pyrolysis treatments required [150]. This can be achieved to a point through the use of high molecular weight polymers over a narrow molecular weight distribution which prevents smaller more volatile oligomer evolution during heat treatment, thus improving yield [163].

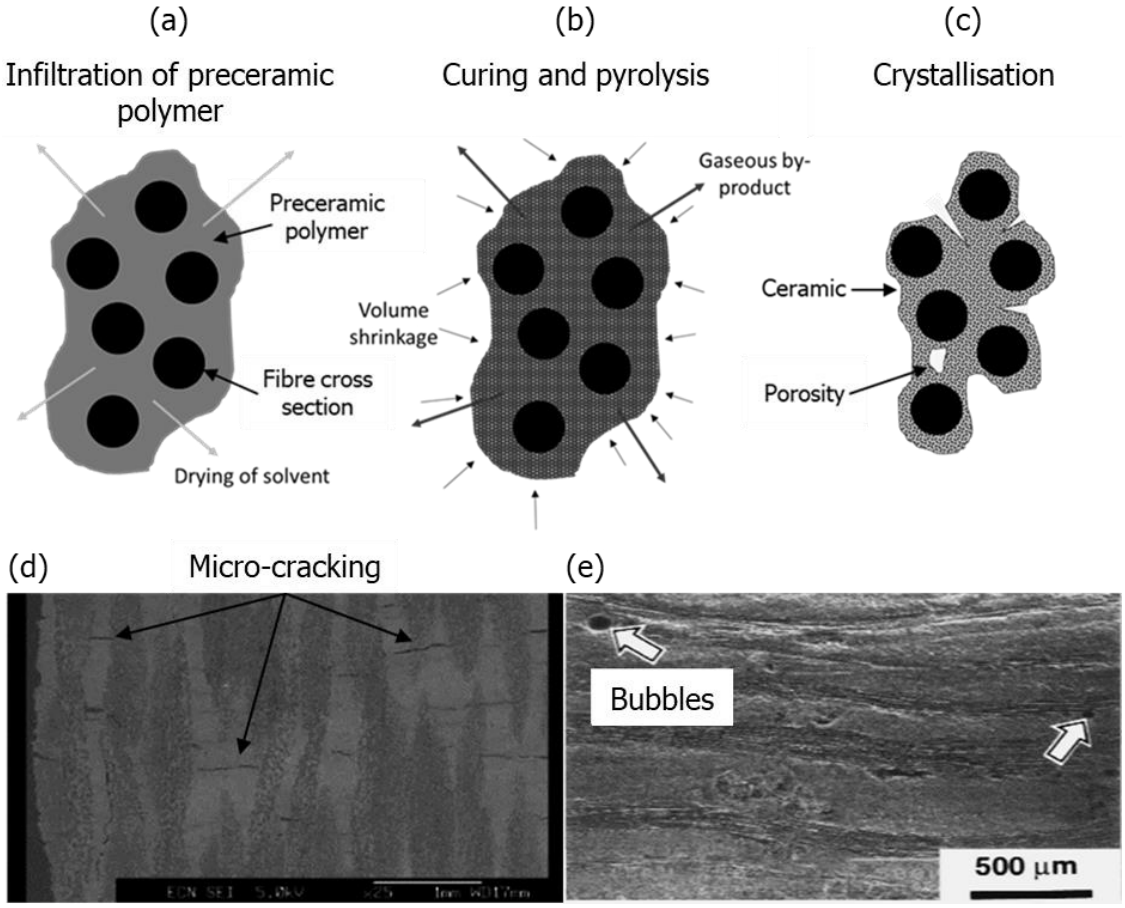


Figure 2.20. (a) A liquid preceramic precursor is impregnated into the fabric; (b) curing and pyrolysis begins, resulting in shrinkage through the evolution of gaseous by-products as the polymer is converted to ceramic; (c) a porous network is formed in the preform, with micro-cracks and pores shown in the matrix phases [150]; (d) SEM micrographs of the aforementioned micro-cracks [164] and (e) bubbles created by inadequate process control [165].

2.4.4. Chemical vapour infiltration

The CVI process was initially developed in the 1960s and evolved from CVD. The only difference is that it is used for depositing a matrix inside a porous body rather than depositing a coating on the body's surface. Now a well-established process, it uses gaseous precursors to deposit solid matrices. These build up gradually closing porosity to form a dense CMC, see figure 2.21.

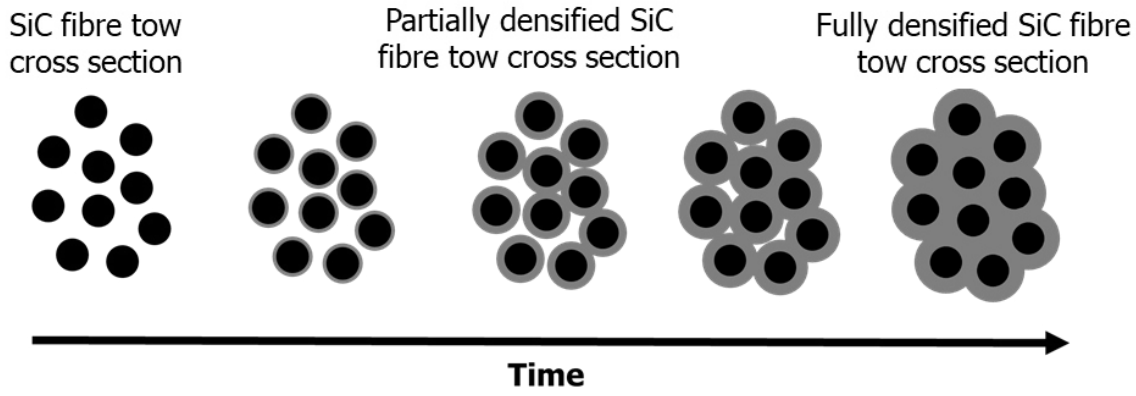


Figure 2.21. An illustration of the development of SiC deposit on the cross-section of the SiC fibres over time, adapted from [150].

Methyltrichlorosilane is typically used between 800-1400°C to deposit solid SiC [12]. The process is performed at low pressures between 10-200 mbar in an attempt to ensure penetration of the gas throughout the composite's porosity network. The MTS is carried by $H_{2(g)}$ into the reaction chamber which serves as a catalyst for the decomposition of MTS [166, 167]. Figure 2.22. shows a conventional processing set up. There are a number of advantages of CVI, primarily the low temperatures relative to other advanced techniques so fibre degradation is lessened, there is no shrinkage of the matrix and net shape manufacture can be achieved. Nevertheless, processing is very slow, as a distribution of isothermal temperature must be maintained over the preform to prevent premature pore closure at the surface of the

composites. Even then the process has to be paused periodically for machining to reopen the surface porosity that closed prematurely. This is to prevent residual porosity forming within the final composite [156].

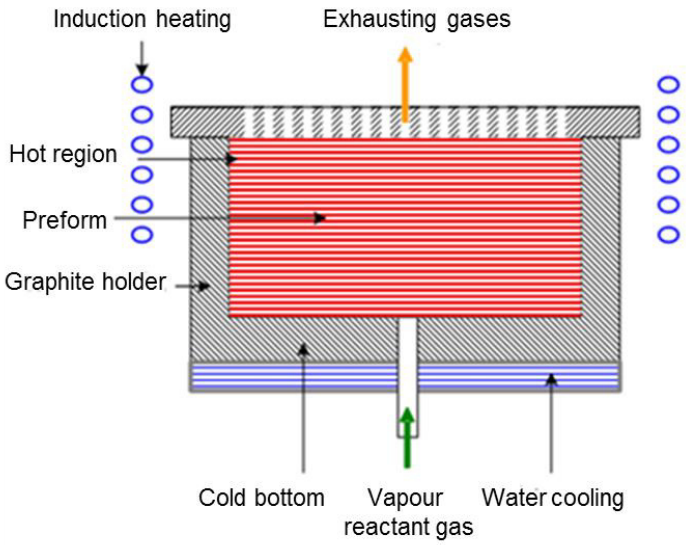


Figure 2.22. Schematic of generic CVI equipment [168].

These decomposition reactions are usually accompanied by the production of HF and HCl that are removed from the chamber along with any unreacted precursor gases. CVI is very flexible in comparison to the other advanced processing methods, since a wide variety of ceramic compositions can be deposited, see table 2.8. The resultant deposit is dense, has a fine grained microstructure (from a few to hundreds of nanometres) and theoretically is free of impurities if processing parameters have been controlled correctly [169, 170]. CVI is most appropriate for the deposition of borides and carbides ceramics, which otherwise require processing at much higher temperatures using powder sintering techniques. Multiple materials systems can also be infiltrated into the preform by alternating the gaseous precursors introduced into the reaction chamber [171-175]. This means mesostructures can be tailored and tuned by the process parameters including chamber pressure, temperature, and the

feed rate of the precursor. The CVI process is complex because it requires a comprehensive understanding of the deposition reaction chemistry and associated kinetics, the temperature distribution seen in the preform, the effects of processing pressure, sample geometry and the porosity network [9, 176]. The final microstructure is dependent on all these variables and thus so are the thermo-mechanical properties. Subsequently, a range of CVI processes have been developed which are categorised by i) temperature, ii) pressure and iii) heating method [177, 178]. One example is the infiltration can be carried out in both cold-wall and hot-wall reactors, at pressures as low as 1 mbar or at a positive pressure, with or without carrier gases, and at temperatures ranging from 200-1600°C. In addition, there are a number of enhanced CVI methods that utilise various energy sources. These include lasers, plasmas, combustion reactions and hot filaments to lower deposition temperatures and increase densification rates.

The main advantages of CVI are [14, 168, 179-181]:

- The deposited material is typically very pure.
- A relatively low-temperature process meaning fibre degradation does not occur.
- It is an adaptable process. Numerous binary systems can be deposited, see table 2.8. Multi-coatings and functionally graded materials can also be achieved without interrupting the process.
- The microstructure of the coating can be customised to have specific properties by altering temperature, pressure and precursor gas feed rate.
- It is highly repeatable.

The limitations of CVI are [182-184]:

- Currently, processing times of industrial-scale CVI are very long, taking in the region of 2-3 months. This is because isothermal heating rates must be used to prevent a thermal gradient forming which results in surface porosity prematurely closing, which causes the process to be paused for surface machining.
- Large overall energy input is required due to the lengthy process times.
- Highly corrosive by-products require enhanced safety precautions, the equipment is expensive and subsequently, maintenance costs are high which further increases the cost of the process.
- It is very difficult to obtain near fully dense composites that are more than 2 mm thick; theoretical densities of <90% of are therefore considered as acceptable.

Table 2.8. The specific precursor gases and the processing parameters needed for the deposition of a number of non-oxide ceramic materials [170].

Matrix deposited	**Reactant gases**	**Temperature / °C**
C	CH_4-H_2	900-1200
HfC	$HfCl_4$-(CH_4 or C_3H_6-H_2-Ar)	900-1600
ZrC	$ZrCl_4$-(CH_4 or C_3H_6-H_2-Ar)	900-1600
TaC	$TaCl_5$-(CH_4 or C_3H_6-H_2-Ar)	900-1500
SiC	CH_3SiCl_3-H_2	900-1400
Si_3N_4	SiCl-NH_3-H_2	1000-1400
TiB_2	$TiCl_4$- BCl_3-H_2 $TiCl_4$- B_2H_6-H_2	800-1200 600-1100
ZrB_2	$ZrCl_4$-BCl_3 -H_2-Ar $ZrCl_4$- B_2H_6-H_2	900-1200 600-1100
HfB_2	$HfCl_4$-BCl_3 -H_2-Ar $ZrCl_4$- B_2H_6-H_2 $Hf(BH_4)_4$	900-1200 600-1100 ≤300°C

2.4.4.1. *Chemical vapour infiltration variants*

2.4.4.1.1. Isothermal/Isobaric CVI

Isothermal CVI (ICVI), figure 2.23., is the most frequently used variant used in industry but although the benefits are plentiful, ICVI suffers from a critical drawback. The deposition of the ceramic material occurs preferentially close to the outer surface where the reactant concentration and temperature are highest [170]. As a result, 'crusting' occurs due to the increased deposition rates, which fills the porosity at the surface of the body trapping porosity inside. This means the CVI process has to be paused, the samples removed from the furnace and the preform's surface machined to reopen this closed porosity.

To reduce premature closure, the options are to: i) decrease the processing temperature, which decreases the SiC deposition rate at the pore entrance by promoting diffusion of reactants down the pore channels, or ii) work at a low pressure again improving diffusion into the centre of the composite. Nevertheless, the production time can be upward of 1000 h due to the crusting, and the parts are expensive [178, 185, 186].

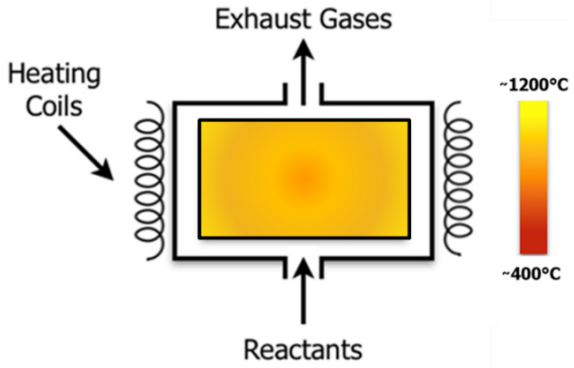


Figure 2.23. Schematic showing the key components of the conventional process and the respective temperature profile [150].

2.4.4.1.2. Isobaric thermal gradient CVI

A thermal gradient is applied to the preform, as shown in figure 2.24., and this can be radiantly or inductively [178, 187]. In the hottest region, this temperature gradient causes the deposition to be quickest. The densification then continues from the hotter area to the composite's colder side. The hot zone is thought to expand because of the increased thermal conductivity of the product due to the increased density and the closure of porosity creating increased concentrations of reactants in the surrounding open porosity.

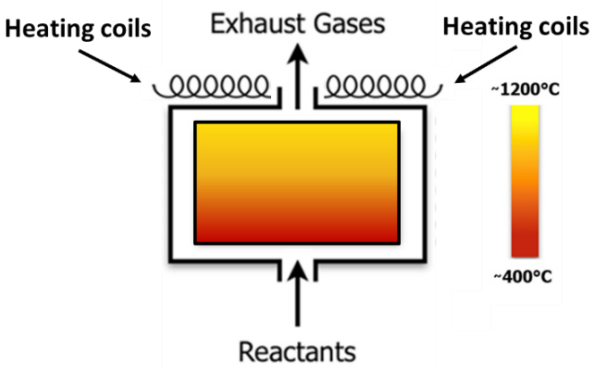


Figure 2.24. Schematic showing the key components of the thermal gradient process and the respective temperature profile [150].

2.4.4.1.3. Isothermal forced flow CVI

In isothermal forced flow (IFCVI) [188-190], the temperature is kept constant but a pressure gradient is exerted over the preform driving the reactants through the pores. Typically, the sample is sealed around its edges so the free path for the gas is through the composite. By controlling the transport of reactants through the preform, the depletion of the precursor's gases is decreased and therefore favourable conditions for increased deposition rates can be used. This method must be careful to control variations in pressure across the sample as different regions can densify quicker resulting in negative effects on the matrix infiltration homogeneity [191].

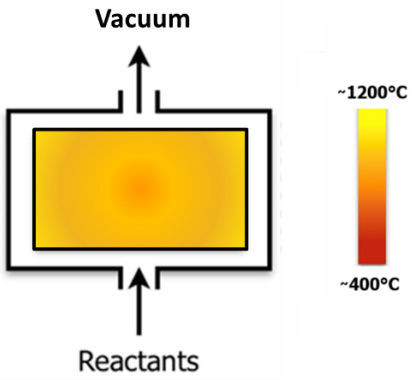


Figure 2.25. Schematic showing the key components of the isothermal forced flow process and the respective temperature profile [150].

2.4.4.1.4. Thermal gradient forced flow CVI

The most explored variant of CVI is thermal-gradient forced-flow CVI (TFCVI) [192-199], which combines the benefits of thermal gradient and pressure gradient CVI. When the pressure gradient is too large, the cycle is concluded: this means that the flow passages are closed and the porosity is mostly filled. The result is a homogeneous matrix with a density of >90% [192] and a deposition rate of up to 1 mm h^{-1} in a relatively short processing time of 10-40 h [200]. However, the controls on gas flow and temperature are extremely complex , particularly when processing multiple and/or complex components and the thermal conductivity of the fibres is high [178]. One version of this technique that has been researched for over 40 years is MCVI; this will be reviewed in more details in section 2.7. as it is the major theme of this research.

2.4.4.1.5. Pulsed pressure CVI

In pulsed pressure CVI (PPCVI) the gas flow is pulsed within the chamber, see figure 2.25. A pump evacuates the chamber and then adds the reactants; this process is repeated several times producing a 'breathing' effect. The effect is the cyclical flow of reactants into and out of the preform [178, 201, 202]. This ensures a fresh supply of

precursor gas is fed into the fibrous composite in the chamber and removes any by-products of the reactions that become trapped in the pores. Furthermore, if the preform is periodically fed with different compositions of reactants multi-layered ceramic systems can be prepared in-situ [203]. Another variation is to combine PPCVI, figure 2.26., with thermal-gradient CVI to create pulsed, thermal gradient CVI, (PPTGCVI). This has been shown to be able to generate an inverse density gradient therefore overcoming the aforementioned crust [196]. Despite this though theoretically attractive, the extreme cost of the equipment reduces its appeal drastically.

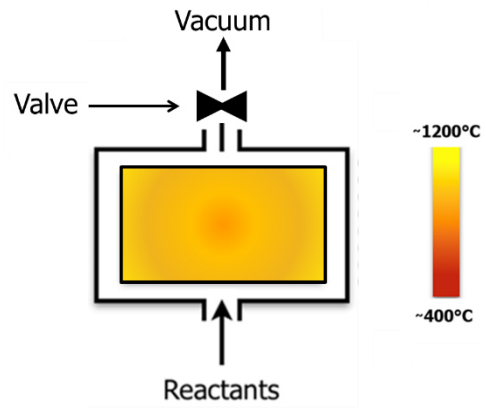


Figure 2.26 Schematic showing the key components of the pulsed pressure system and the respective temperature profile [150].

2.4.4.1.6. Developing CVI technique

Laser chemical vapour deposition (LCVI) uses a focused laser beam to locally heat an infra-red-absorbing preform to provide the required thermal energy to activate the thermal decomposition of the reactants [204, 205]. Both mono-chromaticity of the laser and its directionality can be utilised to enhance the deposition process. Dimensional control is afforded by the use of a laser and allows accurate deposition on very small substrates if required. The chromaticity determines the materials' interaction with the laser, whether it absorbs or is transparent to the laser. These

factors combine to allow very specific modulation of input energies permitting lower temperatures of deposition [206]. A typical thermal gradient profile for laser CVI is shown in figure 2.27.

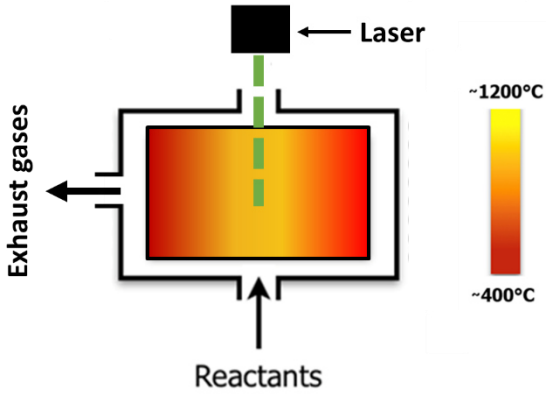


Figure 2.27. Schematic showing the key components of the laser-assisted process and the respective temperature profile [150].

2.4.5. Hybrid techniques

There are multiple combinations of techniques that can be used to densify CMCs, these are collectively referred to as hybrid techniques, see figure 2.28. Within the combinations, there is also an ordering variable as well, i.e. CVI before PIP or PIP before CVI etc. This is because it has not been conclusively established in the literature what best practice is when it comes to the order of filling intra-tow, inter-tow or inter-ply porosity with the ceramic matrix. For the purpose of this review, only advanced methods with the addition of slurry impregnation will be evaluated. The concept behind using hybrid techniques is the same as why composite materials were developed, the idea being that the advantages could be maintained and disadvantages compensated by using the benefits of another technique [207], see table 2.9.

Table 2.9. Summarising the primary advantages and disadvantages of advanced fabrication methods [63, 208, 209].

	RMI	**PIP**	**CVI**
Fabrication time	✓	-	X
Shaping	-	✓	✓
Cost	✓	-	X
Technical maturity	✓	-	-
Filling large porosity	✓	X	X
Filling small porosity	X	-	✓
Microstructure quality	X	-	✓
Fibre degradation	X	X	✓
Operating temperature	X	✓	✓
Residual stress	X	✓	-
Creep resistance	X	X	✓
Thermal conductivity	✓	-	✓

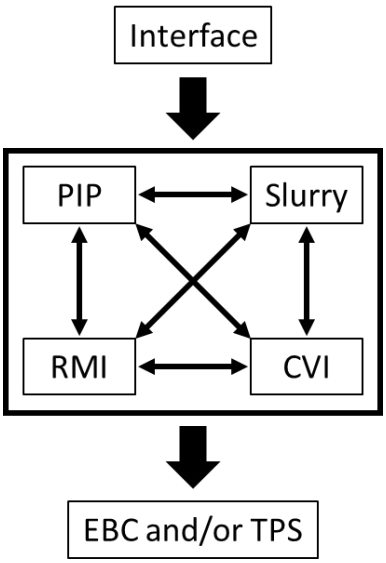


Figure 2.28. Schematic representation of the combinations of matrix formation techniques after an interface material is applied and before an EBC or TPS.

From the literature, it appears the most explored technique combination is CVI and PIP. Ortana et al. [210] used first CVI to deposit a pyro-C interface of approximately 0.1 μm and then a SiC matrix. The amount of time the CVI SiC matrix was applied for was varied from 20-60 h. This resulted in a decrease in residual porosity from approximately 68% to 59.8% for 20 h and 54.7% for 60 h respectively. These

specimens were then impregnated with preceramic polymer and pyrolysed. It was found that samples that had had a longer CVI time could not be densified to the same degree using PIP as samples that had been infiltrated for a shorter period. Samples infiltrated for only 20 h were densified to have 28% residual porosity whereas 60 h CVI samples only reached 39.3% residual porosity. Ortana goes on to explain this is because of the volume of closed porosity created during the longer CVI times. In similar work by Nannetti et al. [211], SiC_f/SiC composites were prepared again with a 0.1 μm C interface and then all subjected to 30 h of SiC CVI and then seven iterations of the PIP process. The greatest reduction of porosity seen was to 13.3% in a 3D Hi Nicalon S preform. This was hypothesised to be because of the reduced fibre fraction in the Z-direction compared to the other samples, which increased the permeability of the composite to the liquid polymer. Work by Park et al., also explored this route but the CVI process was carried out at a higher temperature for shorter times than the previous two reports. However, they also found similar results in that samples that gained less mass from the CVI stage showed an increased degree of densification during the PIP stage and ultimately a higher final density [212].

The next most prevalent technique combination is CVI with RMI. This approach has widely been used by NASA to produce composites that have low residual porosity with good mechanical properties, the first property is afforded by RMI and the second by CVI [63, 213]. As illustrated in figure 2.28. the processes can often be combined with a slurry infiltration step as well [214]. This is the case in the NASA production route and the one used by Li et al. [215]. Both use a slurry infiltration

step prior to the RMI stage to both protect the fibres and create a porous body with high capillarity that aids the wicking of the molten silicon into the composite. In both cases the fibre preforms are infiltrated using CVI until 30-40% porosity is left before the slurry and then RMI routes are used, ultimately resulting in a composite with ~15% porosity left. Xu et al. also used the same method but without the slurry infiltration stage [149]. Though it is not stated, the volume of porosity can be estimated to be approximately 20% as the density of the samples was 2.1 g cm^{-3}.

The theme of using slurry is continued in PIP related research as well. Ivekovic et al. [216] prepared SiC_f/SiC composites using electrophoretic deposition (EPD) to introduce a submicron SiC powder to the fibre ply. Following this, the samples were vacuum infiltrated with a warmed SMP-10 preceramic polymer that had a viscosity of 0.025 Pa s before being pyrolysed at 1600°C in a vacuum. The resulting composite after six PIP cycles was 86.5% of TD, which is typically achieved using 10+ cycles of just PIP indicating a reduction in processing time. Zhu et al. [217], also looked at this method of densification but were less successful in closing porosity. This is possibly because they used a vacuum infiltration route to introduce the powder rather than EPD or because the pyrolysis temperatures used were noticeably lower. The authors also do not state how many cycles of PIP were used, it is suspected <5 as the residual porosity after pyrolysis was still >20%.

The least explored combination of techniques appears to be RMI and PIP. This is potentially because neither is particularly good at filling small porosity particularly which is pivotal to the mechanical performance of these composites, thus rendering it a dubious route to investigate.

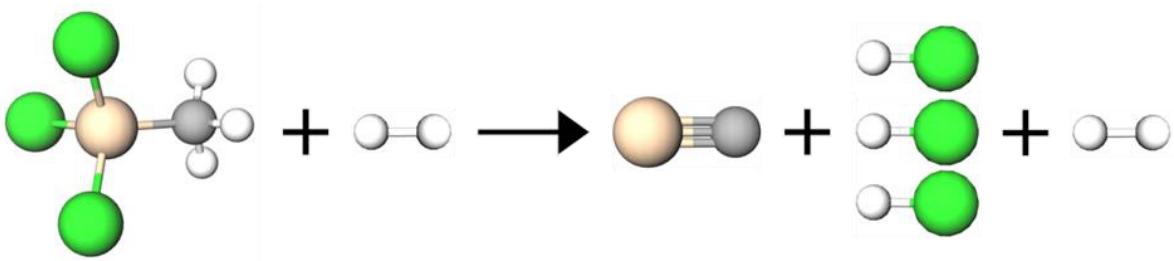
2.5. Chemical vapour infiltration of SiC_f/SiC composites

2.5.1. Reactants and SiC formation

There are a number of precursors that can be used to synthesise SiC in the CVI process. These are outlined by Vignoles [184], the precursor most commonly used in the literature is MTS, though ethyltricholosilane (ETS) and dimethyldichlorosilane (DDS) can also be used. It was previously thought that MTS was a superior precursor material due to its equal Si:C ratio as is intended in the deposit, more recent literature has shown that this is not the case [184]. As the decomposition of MTS happens, first into constituent elements, a series of heterogeneous reactions of Si and C-containing intermediates then occur at the deposition site of the cubic β-SiC [14]. This deposition occurs in the presence of a carrier gas, typically hydrogen or argon. Hydrogen is preferred as it is hypothesised that its presence can reduce the Si-Cl bond during the intermediate phase of the process and increase the SiC formation rate by lowering the activation energy (E_a) [218, 219]. The overall reaction is shown below, but the theoretical route of decomposition is significantly more complex. It involves a possible 114-stage reaction mechanism [220, 221] and is affected by the processing variables that will be discussed in more depth in the next section.

Methyltrichlorosilane + Hydrogen → Silicon carbide + Hydrogen chloride + Hydrogen

$$CH_3SiCl_{3(l)} + (n)\ H_{2(g)} \rightarrow SiC_{(s)} + 3HCl_{(g)} + (n)\ H_{2(g)}$$



Due to the complex interplay between processing conditions and the reaction mechanism, the formation of secondary phases, such as carbon or silicon, are very common and reduces the yield of SiC [14]. Codepostion of secondary phases has been linked to carrier gas composition with argon producing C-codeposition and hydrogen producing Si-codepositon. Several routes have been proposed in the literature to describe the decomposition of MTS, using thermodynamic and kinetic modelling, ab initio calculation, mass spectrometry and experimentation but findings often vary due to the different conditions used. In the literature, there is a general consensus that the Si-C bond in the MTS molecule has the lowest dissociation enthalpy and therefore will initiate the decomposition reaction into radicals of $SiCl_3$ and CH_3 [14, 183, 222]. The literature suggests that these Si-containing and C-containing radical species then proceed along different and separate pathways and do not recombine until they are adsorbed to the substrate site, whereupon there is an ejection of HCl. The aforementioned radicals are subject to change and, consequently, so is the route of decomposition when the temperature is higher. Roman [223] carried out an extensive literature survey in 1994 on this mechanism and proposed a simplified and most probable mechanistic route. The route posed by Roman is in good agreement with a number of more recent publications [224-226] detailing the most probable intermediate steps with respect to depositing stoichiometric SiC and was based on bond dissociation enthalpies, which is shown below. A few additional reactions have been included below, full reaction series can be found at [220, 221]:

Initation of reaction/ decomposition of MTS (* denotes a free radical)

$$CH_3SiCl_3 + H_2 \rightarrow *SiCl_3 + *CH_3 + H_2$$

$$*SiCl_3 + H_2 \rightarrow HSiCl_3 + *H$$

$$*SiCl_3 + *H \rightarrow SiCl_2 + HCl$$

$$*CH_3 + H_2 \rightarrow CH_4 + *H$$

$$*CH_3 + *CH_3 \rightarrow C_2H_4 + H_2$$

$$*CH_3 + *H \rightarrow CH_4$$

Reactions at the substrate surface/ chain propagation/ adsorption ((•) denoted free bonding site on the substrate surface)

$$SiCl_2 + (\bullet) \rightarrow SiCl_2(\bullet)$$

$$H_2 + (\bullet) \rightarrow 2H(\bullet)$$

$$HCl + 2(\bullet) \rightarrow H(\bullet) + Cl(\bullet)$$

$$*CH_3 + (\bullet) \rightarrow CH_3(\bullet)$$

Reaction termination/ surface reaction/ desorption

$$SiCl_2(\bullet) + (\bullet) \rightarrow Si* + 2Cl(\bullet) + (\bullet)$$

$$CH_3(\bullet) + 3(\bullet) \rightarrow C* + 3H(\bullet) + (\bullet)$$

$$CH3* + 3H* \rightarrow C* + 3H_2$$

$$SiCl_3* + 4H* \rightarrow 3C* + 4H_2$$

$$SiCl_3* + 3H* \rightarrow Si*$$

$$H(\bullet) + Cl(\bullet) \rightarrow HCl$$

$$2H(\bullet) \rightarrow H_2 + 2(\bullet)$$

$$Si* + C* \rightarrow SiC$$

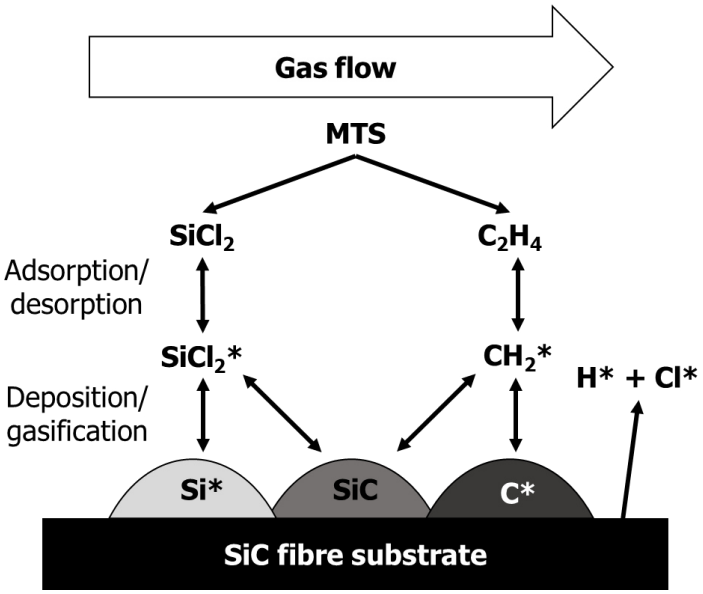


Figure 2.29. Schematic representation of the adsorption and deposition of SiC constituents to the fibre surface, adapted from [225].

It must be noted that MTS has to be stored and handled carefully because it reacts violently with water to produce heat and toxic HCl fumes of that are very hazardous to users' health and detrimental to metallic equipment [227].

2.5.2. Mechanism of deposition

As mentioned, understanding and controlling the reaction chemistry and kinetics of the CVI process is far from trivial. The complex heterogeneous reactions that are taking place inside the fibre preform to deposit the ceramic material are governed by five mechanisms, first described by Naslain [176]:

1. Diffusion of gaseous reactants through the hydrodynamic boundary layer on the fibre preform's surface.

2. Diffusion of the gaseous reactants along the pore channel until reactants are adsorbed on the channel's inner surface, i.e. a SiC fibre.

3. A series of reactions take place yielding a solid ceramic deposit and an adsorbed gaseous by-product.

4. Desorption of gaseous by-products, which then travel along the pore channel toward the pore entrance.

5. Diffusions of the by-products through the boundary layer on the pore surface.

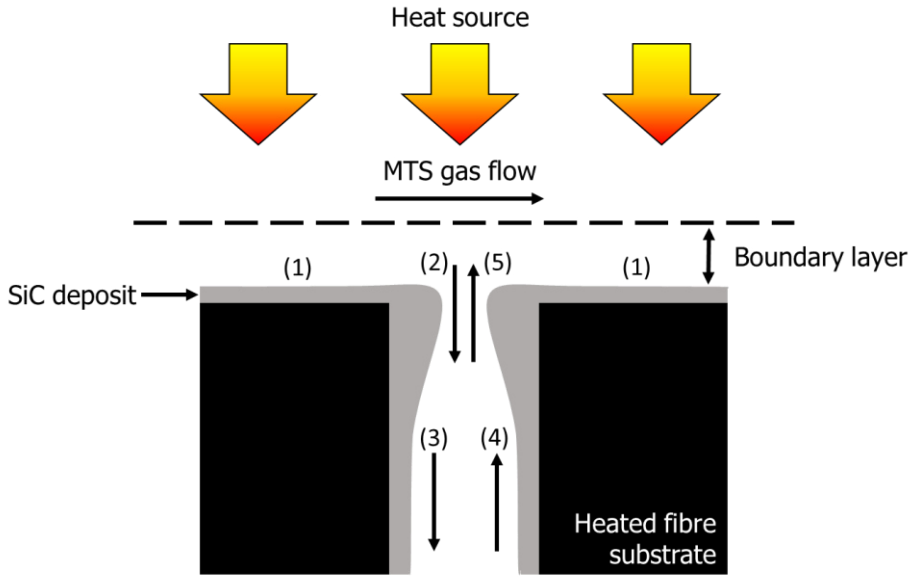


Figure 2.30. Schematic showing the different steps in the iso-thermal CVI process, adapted from [9, 14].

The filling of porosity involves two competing mechanisms; the mass transport and subsequent diffusion of species into pore channels and, secondly, the surface or kinetic limited reaction at the preform surface and pore entrance. The slower of the two determines the rate of deposition. Temperature, pressure and gas flow rate determine which of these two mechanisms is controlling the deposition. The diffusion of the reactants is also affected by the pore size, for larger pores, Fickian diffusion[v] is the governing mechanism but for smaller pores, Knudsen diffusion[vi] must also be accounted for [228]. When surface reactions are slower, the deposition of the

[v] Molecule-molecule collisions dominate due to large pore channel.
[vi] Molecule-channel wall collisions are most frequent due to small diameter pore channel.

ceramic occurs in the pore channels at a faster rate; however, when mass transport is the rate-limiting step, this results in the premature closure of these channels. This is why isothermal heating profiles and low pressures are specifically used in order to promote the mass transport of precursors into and along the pore channels, thus keeping the surface reaction the limiting step [228]. These competing mechanisms, mass transport and surface kinetics, are described and can be assessed by a dimensionless parameter called the Thiele or the second Damkohler number[vii] (Φ) [9, 229]. This number is applicable when describing the heterogeneous reaction resulting in deposit forming on or in the fibre preform at the entrance of a cylindrical pore at a uniform temperature:

Equation 2-3 $$\phi = \sqrt{\frac{2\kappa_s L^2}{D R}}$$

Where: κ_s = First order reaction rate of the surface reaction

D = Diffusivity of the precursor gases / $m^2 s^{-1}$

R = Radius of pore channel / m

L = Length of pore channel / m

An effectiveness factor (η) that describes the ratio of pore channel deposition against pore surface deposition can be coupled with the Thiele modulus to become an accurate descriptor of the relationship between mass transport and surface kinetics [14].

[vii] Relates the reaction rate timescale to the transport phenomena rate timescale

Equation 2-4 $$\eta = \frac{\tanh \emptyset}{\emptyset}$$

Therefore, keeping the effectiveness factor as close to one as possible promotes in-pore deposition, again ensuring the surface reaction is rate-limiting. Fitzer [218] verified this relationship experimentally, showing that the maximum length of the cylindrical pore channel (L_{max}) was equal or less than the parameter shown below:

Equation 2-5 $$L_{max} \leq 0.4 \sqrt{\left[\frac{R\, D_e}{2\kappa_s}\right]}$$

Where: D_e = Diffusion coefficient

R = Pore radius / mm

In further work by Rossignol et al. [228], they modelled the closure of porosity using experimentally derived kinetics data and concluded a number of important statements. The model showed that when the temperature (800°C) and pressure (20-200 mbar) were sufficiently low, the thickness of the deposit was homogenous in large porosity ($\emptyset$ = 100 µm), which is typical of a low Damkohler number. They also found raising the temperature and pressure favoured deposition at the pore entrance, an effect that was exaggerated for smaller porosity (1 µm). In an attempt to improve this, Rossignol lowered the temperature, which had minimal effect before lowering the pressure, which had no effect. This is thought to be because the mass transfer is already limited by Knudsen diffusion below 200 mbar.

2.5.3. CVI process variables with respect to SiC deposition

Silicon carbide composition, morphology, crystal structure and deposition rate are governed by a number of critical processing parameters that determine decomposition route of precursor materials. The literature shows there is substantial

interplay between each of the processing parameters; temperature, pressure, gas-phase composition and flow rate have been identified as the most critical of these parameters. Each variable has a specific effect on SiC formation when it is changed and in turn, alters the effect other parameters have.

Temperature is the most influential parameter on the properties of the SiC deposit. The consensus of the vast majority by the literature is that lower temperatures <1000°C, favour the co-deposition of silicon with silicon carbide [225, 230-238] and higher temperatures, >1200°C, favour carbon co-deposition [230, 231, 239]. A number of authors have proposed that silicon co-deposition at low temperatures is a consequence of the low reactivity of the primary carbon-bearing species in this temperature range, methane, and the highly reactive chlorosilanes, $SiCl_2$ [226, 231, 237, 240]. Conversely at higher temperatures >1200°C, CH_4 is substituted for the more reactive C_2H_4 and the $SiCl_2$ for more stable $SiCl_4$ [241, 242]. Subsequently, this favours carbon co-deposition and thus indicates there is an optimum temperature between 1000-1200°C to produce stoichiometric SiC. However, this is also heavily dependent on other processing conditions. As to be expected, the rate of deposition of SiC obeys an Arrhenius relationship but this can also change depending on the precursors used. The temperature also affects the location of the deposition, as high temperatures favour a surface reaction as opposed to diffusion that is favoured at lower temperatures, see figure 2.30. Precursors with a lower activation energy, such as MTS, due to their higher electronegativity at the C-Si bond will deposit material at a faster rate than more stable precursors like dichloromethylsilane and dimethyldichlorosilane. Increasing temperature also has an effect on the morphology

and crystal structure of the deposit, with the SiC grains become more elongated and faceted and the surface topography rougher [232, 234, 237, 243, 244].

Deposition pressure has a less significant impact on the infiltration process though it does still effect SiC composition and physical appearance. It was first reported by Langlais in 1989 [236] who observed that Si codeposition was favoured at pressures closer to atmospheric. This is considered very high relative to conventional CVI processing, which is usually carried out at the lowest possible pressure. This was also reported later on in a number of other publications in agreement with Langlais' findings [235, 238, 239, 245, 246]. There is, though, conflicting reports on the effect pressure has on deposition rate, with some literature citing it has no effect, especially at higher temperatures [247, 248]. Whilst others state that as pressure increases growth rate of the deposit increases due to increased residence times [233, 234, 239]. In terms of the effect of pressure on morphology and crystal structure, Cheng et al. [249] and Jacobson [250] found that at high pressure the SiC that was deposited had a more angular appearance. Similar results were found by Sibieude and Benezech [251], who went on to show, using X-ray diffraction (XRD), that smaller crystallite SiC was deposited at lower pressures. This was further clarified by Chin et al. [252] and Lespiaux et al. [232], who explained that the surface topography was related to the supersaturation of the gas at the gas-solid interface. As the pressure increased, this supersaturation decreased, resulting in a more angular, larger and more facetted morphology, whereas the opposite was seen at lower pressure due to high supersaturation.

Second only to temperature, the gas composition has the most significant impact on the composition and growth rate of the silicon carbide deposit. The gas composition is described as the alpha ratio, which is a molar ratio of the carrier to precursor, as seen below.

Equation 2-6 $$alpha\ ratio = \frac{n_{Carrier\ gas}}{n_{Precursor}} = \frac{n_{H_2}}{n_{MTS}}$$

The literature comprehensively reports that a high α ratio results in silicon co-deposition as this favours chlorosilane production [9, 231, 237, 239]. Naslain in the 1980s [9] produced a phase diagram that shows how an increasing ratio affects thermodynamic yields and the composition of the SiC. It showed high dilutions favoured silicon production, an effect that is exacerbated at low temperatures. Conversely lower-alpha ratios and high-temperature favour carbon deposition. Naislain's paper reports again an optimal alpha ratio range between alpha 100-10000 at a pressure of 100 mbar and at a temperature range of 1000-1400 K, figure 2.31. Typically, this would be considered a very dilute ratio, which is consistent with other literature in terms of the trend, i.e. increased dilution leads to co-deposition of silicon. However, the dilution is multiple orders of magnitude too high and in disagreement with all other literature on the topic. It is currently thought by the present author that the log scale is incorrectly plotted, figure 2.31.

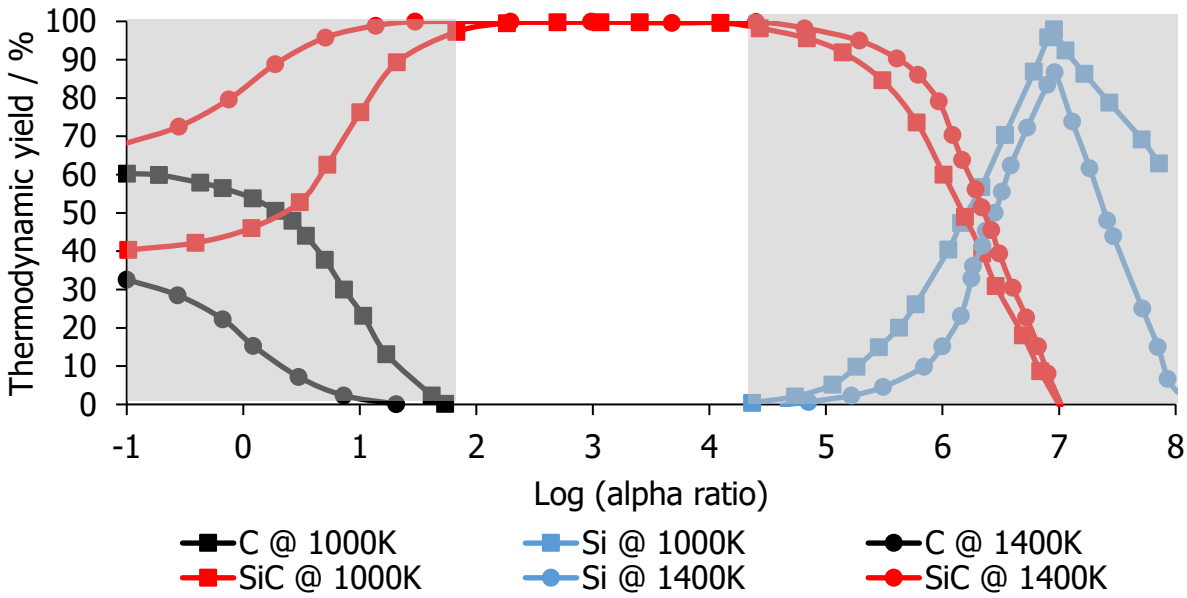


Figure 2.31. Thermodynamic yields for the solid deposition of silicon carbide and its co-deposits as a function of alpha ratio, adapted from [9].

Van der Putte goes further to explain that lower alpha ratios have decreased silicon content because of the etching effect of the more concentrated hydrogen chloride by-product [253]. This effect is useful to understand how the reaction can be used to control the composition, but a number of authors have also found the concentration of HCl in the system has an inverse relationship with deposition rate [222, 231, 233, 235, 246, 247, 254]. Chiu et al. [241], looked at the effect the molar ratio of reactants had on morphology and showed that decreasing the alpha ratio increased the surface roughness. This is the same as effectively decreasing the degree of supersaturation, as explained previously by Lespiaux et al. [232] and Chin et al. [252]. It has also been observed that higher dilutions decrease the deposition rate, which is to be expected [231, 237, 248].

The literature also reports that higher flow rates increase the rate of deposition by providing a faster supply of precursors to the substrate deposition sites; however, this does have an inflection point where the delivery will exceed the rate of reaction

and available site of deposition. This has been demonstrated by Zhang [238, 240] who shows the ratio of substrate surface area to volume ratio affected the rate of deposition. They also found that silicon co-deposition was favoured by a low ratio, but they did not postulate a theory for this. Another key observation that has been reported is the effect of the carrier gas used on the SiC composition; Caligstro, Kim and Yu [230, 244, 255] all found that use of hydrogen favoured Si-SiC and use of argon C-SiC. Kim also saw a change in the rate of deposition with both gases. At lower temperatures, the rate of deposition was higher with hydrogen up to 1150°C, but beyond this, the rate of deposition using argon was higher.

The most comprehensive paper detailing the effect of processing conditions on the CVI process was produced by Loumagne in the earlier 1990s [235]. They produced the figure 2.32., shown below, a phase diagram summarising the effect of three of the four previously mentioned parameters. Most significantly, they suggested that stoichiometric SiC is possible at lower temperatures if the alpha ratio and pressure are suitably low enough.

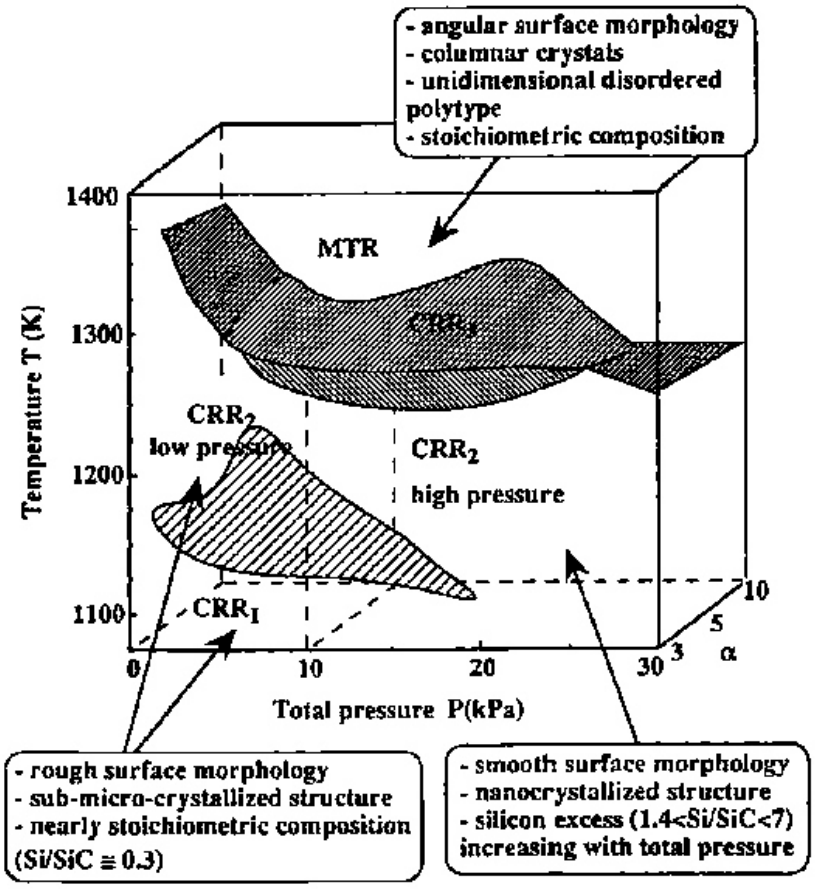


Figure 2.32. A temperature-pressure-alpha phase diagram showing the trends in the physicochemical properties of the resulting SiC deposit.

2.6. Microwave processing of materials

2.6.1. Microwave-material interaction

Microwaves are a type of electromagnetic radiation with wavelengths and frequencies ranging from 0.001 m to 1 m and 0.3 GHz to 300 GHz, respectively. In contrast with visible waves, apart from lasers, microwaves are both coherent and polarized [256]. This makes them suitable for a number of applications which have varying frequencies; communications, navigation, radar, astronomy, spectroscopy and heating. These frequencies are divided into a number of bands that span the whole range, with microwave ovens being categorised as S-band with a frequency

range of 2-4 GHz. Table 2.10. lists a number of advantages and disadvantages of using microwave energy as a means of heating materials.

Table 2.10. Showing some of the fundamental advantages and disadvantages associated with microwave processing [257].

Advantages	**Disadvantages**
Direct coupling creating volumetric heating, potentially lowering temperatures	Heating can be complicated
Dielectric losses accelerate heating	High input of engineering experience for successful application
Selective heating capabilities	Thermal runaway
Reversed thermal gradients	Non-uniform heating
Internal stress reduction	Temperature measurement can be difficult
Rapid processing	Dielectric properties can change with temperature unpredictably
Reduced processing costs	
New material synthesis	

The way microwaves interact with materials is highly variable, especially with changing temperature and frequency. When the microwaves are incident on a material they can be reflected, absorbed (lost) or transmitted or any combinations of the three, see figure 2.33 [258]. An electromagnetic wave has two components, an electric and magnetic field, both of which strongly influence how a material will interact with a microwave. These interaction mechanisms can be generalised as dielectric losses, conductive losses and magnetic losses though there are many more [259]. The primary effect of these microwave interaction with materials is heating such as joule, magnetic, dielectric and ohmic, all of which are again materials specific [260].

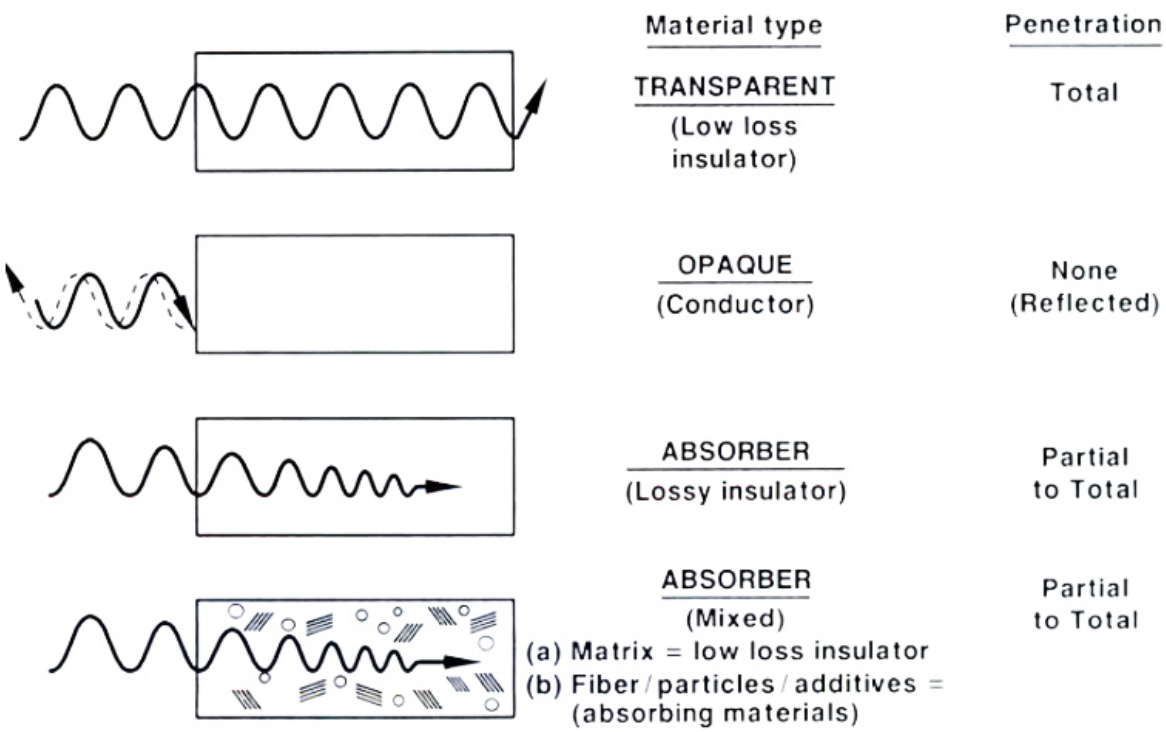


Figure 2.33. Series of diagrams showing the microwave-matter interactions possibilities [258].

For brevity, this review will only discuss microwave interaction with an alternating electric field component that creates dielectric and ohmic heating, more information on microwave interaction with other material types and magnetic field heating can be found in [259]. SiC will also heat via a direct current and is most commonly used in furnace heating elements. The electric field component of the microwave is responsible for dielectric loss heating and ohmic heating.

In the dielectric loss mechanism, dipoles in the material orientate themselves to align to the electric component of the microwave field to minimise the system's total energy. Microwaves can do this via a number of different routes [243];

- Dipole polarisation – permanent dipoles are orientated by an external applied electric field.

- Electronic polarisation – impermanent distortion of the electronic arrangement around the nucleus of an atom in a unit cell.
- Ionic polarisation – unbalanced charged distribution caused by a larger scale redistribution of the charge due to ion and cation movement because of the applied electric field.
- Maxwell-Wagner-Sillars polarisation – is charge build-up that occurs in dielectric materials that are layered or heterogeneous.

As the microwave field oscillates at a high frequency, the dipoles in the material are unable to remain synchronised causing a phase lag resulting in dielectric loss [261]. This phase lag is particularly high around the polarisation mechanisms resonance frequencies. As the polarisation lags behind the field reversal it causes an interaction between the field and the dielectric's poles that results in heating [258]. To ensure more even heating the frequency used should be slightly different from the frequency at which maximum dielectric loss occurs to prevent all of the microwaves being absorbed by the first surface of the material.

In the ohmic mechanism, any free charged species such as electrons and ions will move with the oscillating electrical field inducing a current. As the flowing electrons move through the atomic structure, they encounter resistance to flow through collision with atoms and causing vibration resulting in heat. The degree of interaction experienced by a material in a microwave field is governed by the materials complex permittivity. Complex permittivity is composed of a real and imaginary part called the dielectric permittivity and the loss factor, respectively, see equation 2-7. It is effectively a measure of a material's ability to polarise in an electric field. The

dielectric permittivity can be defined as the ratio of the relative permittivity of a material to the permittivity of free space, equation 2-8. It, therefore, indicates a material's ability to store absorbed electrical energy when in an electric field [262]. Loss factor is the ability to dissipate this energy through the movement of charged species in an alternating electromagnetic field as the polarisation of the material switches direction.

Equation 2-7 $$\varepsilon^* = \varepsilon' - j\varepsilon'' = \varepsilon_0 (\varepsilon'_r - j\varepsilon''_{eff})$$

Equation 2-8 $$\varepsilon' = \frac{\varepsilon'_r}{\varepsilon'_0}$$

Where: ε* = Complex permittivity

ε' = Dielectric permittivity

ε'' = Loss factor

J = √-1 or i

ε'_0 = Permittivity of free space (8.86×10^{-12} m^{-3} kg^{-1} s^4 A^2)

ε'_r = Relative dielectric permittivity

ε''_{eff} = Effective relative dielectric loss

There are a number of loss mechanisms that govern how energy is dissipated as the charged species are moved, these are [263]:

- Short-range hoping of charged species between available sites, resulting in reorientation and is the primary loss mechanism in a dielectric material.
- Charge carrier tunnelling through energy barriers resulting in relaxation.

- Ohmic electronic or ionic conduction from the thermal excitation of charged species in the conduction band.
- Lattice-incident photon coupling causing resonance in the crystal.
- Localised space charge build-up.

The sum total of these losses results in volumetric heating, which means the entire dielectric material experiences the same energy input throughout its entire volume. These losses are commonly grouped under the term "loss tangent", which is indicative of a material's ability to convert absorbed electromagnetic energy into thermal energy; this is dependent on the frequency, loss factor, dielectric permittivity and electric field intensity, see equation 2-9. The phase angle in the tanδ relates to the time lag associated with the time taken to polarise a material's dipoles.

Equation 2-9 $$\tan\delta = \frac{\varepsilon''_{\mathrm{eff}}}{\varepsilon'_{\mathrm{r}}} = \frac{\mathrm{S}}{2\pi \mathrm{f} \varepsilon\prime_0 \varepsilon'_{\mathrm{r}}}$$

Where: tanδ = Dielectric loss tangent

S = Total effective conductivity / S m^{-1}

f = Frequency / GHz

The dielectric loss of a material is not the only determining factor in terms of the effectiveness of microwave heating. The penetration depth of the incident wave into the material can be used to quantify the heating uniformity and efficiency. Often referred to as skin depth, it is a measure of the distance from the surface of the material to the point when the magnitude of the field strength decreases by e^{-1} (=0.368) of its original value at its surface, figure 2.34 [260]. These depths can have a vast range, for example, 38 μm and 187 m for graphite and high purity alumina, respectively [256, 258]. A larger skin depth than the sample dimension means that

the total interaction of the microwave is achieved. The opposite is true for a sample larger than the skin depth making uniform heating impossible [258]. The penetration depth also varies with frequency and effective dielectric and magnetic loss factors. If a material has a high loss factor, the penetration depth is often low; the opposite is true for a material like quartz, which, with an almost zero loss factor, can be considered effectively transparent to microwaves.

Equation 2-10 $$D_P = \frac{3\lambda_0}{(8.686\pi)(\tan\delta)\sqrt{\frac{\varepsilon'_r}{\varepsilon'_0}}}$$

Where: D_p = Penetration depth at half power / m

λ_0 = Free space wavelength / m

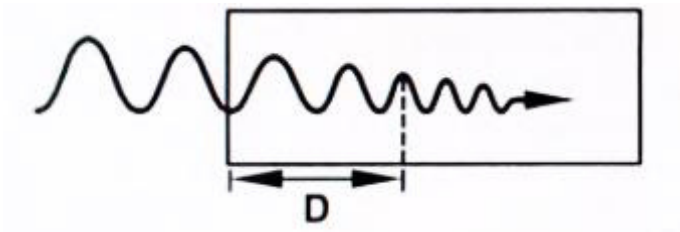


Figure 2.34. The absorption of microwaves to half-power depth (skin depth).

2.6.2. Volumetric heating, inverse temperature profile and thermal runaway

As mentioned in section 2.6.1. materials that absorb microwaves can be heated volumetrically. This means that the atmosphere surrounding the material being heated in the microwave field is cooler than the dielectric material being heated, as it does not interact with the field. This, in turn, means that a thermal gradient will develop spanning the dielectric-atmosphere interface so that the surface of the dielectric loses thermal energy to the surroundings. It is therefore implied that due to the volumetric heating, the centre of the sample, the region furthest from the

surroundings, is the best insulated and hottest. This produces an inverse temperature profile the fundamental benefit of the MCVI process, see section 2.7. The severity of this gradient can be influenced by slowing the rate of surface heat loss by using an insulating material in contact with the surface. Conversely, for conventional heating, the heat transfer mechanism is only by conduction and radiation. This means the temperature of the sample's surface temperature is higher than the centre unless the time of heating is suitably long so that the gradient is neutralised.

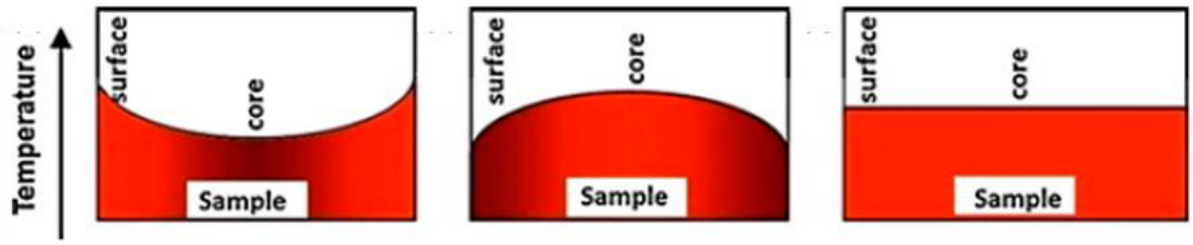


Figure 2.35. Schematic illustrations of the temperature profiles within samples heated (left to right) conventional, microwave (inverse temperature profile) and hybrid heating [256].

There are also a number of thermal phenomena associated with the use of microwave energy. The primary, and most problematic, is called thermal runaway. This applies only when the temperature dependence of the power absorption is less than the temperature of the loss factor. This is most common in materials that possess low thermal conductivity and dielectric loss factor that increases dramatically as the temperature increases creating an uncontrolled "hot spot". When a hot spot forms due to a non-uniform heating profile the dielectric loss factor increases locally, exacerbating the effect and resulting in an uncontrolled temperature increase. This effect has been modelled in a number of ceramic materials in the form of an S-shaped power-temperature curve that shows there is critical power threshold below which the material will heat in a stable manner [264, 265]. If power exceeds this

value, the temperature will jump to the upper branch in an uncontrolled fashion, see figure 2.36.

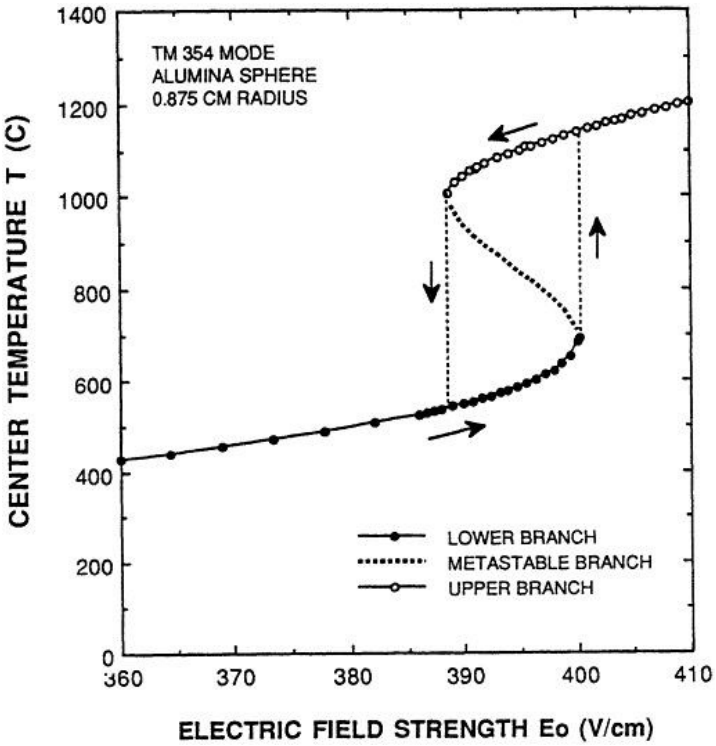


Figure 2.36. Graph showing the principle of thermal runaway showing an instantaneous temperature increase with no change in electric field strength [266].

2.6.3. High-temperature dielectric property measurement techniques

There are many methods of dielectric property measurement from direct current methods to 1000 GHz at ambient temperatures. The need to measure dielectric properties at temperatures >300°C, however, has become more prevalent with the expanding use of microwave processing technology in industry, whilst numerous methods are available, only a small number are suitable to do this, these are:

- Resonant cavity
- Free space
- Waveguides and coaxial lines

Table 2.11. shows a number of possible methods for measuring high-temperature dielectric properties. For the purpose of this review, only the resonant frequency and

free space methods will be discussed in more detail as these are the techniques used later on to collect data of the SiC_f.

Table 2.11. High-temperature dielectric property measurements that are available and their respective attributes, adapted from [267].

	Technique	**Advantages**	**Disadvantages**
Resonant methods	Resonant cavity	Accurate for low loss material	Frequency limitations Cooling of the sample
	Dual and single frequency dielectrometer	Rapid measurements	Frequency limitations Complex set up
Non-resonant methods	Free space	Suitable for sheet-like materials	Requires a large sample

2.6.3.1. *Resonant cavity method*

In principle, the method of measurement associated with the resonant cavity system is based on perturbation theory with a sample heated via either conventional means or a microwave source to a specific temperature [267]. Depending on cavity shape, a microwave field is applied and the resonant frequencies of this applied field are measured [268]. The material in question is then inserted into the field, see figure 2.37., thus perturbing the cavity's resonant frequencies and quality factor. The latter relates the thermal energy stored in the material to the dissipated energy [269].

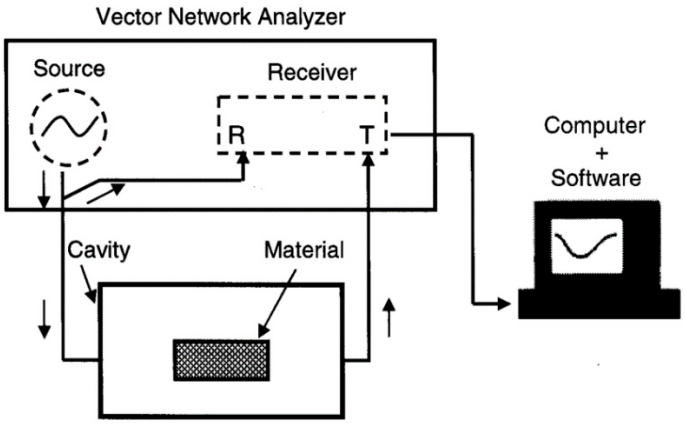


Figure 2.37. A generic schematic of the resonant cavity set up used for measuring dielectric properties [270].

The change in resonant frequency can be used to calculate the dielectric permittivity of the material, equation 2-11, whilst the change the quality factor is used to calculate the loss factor of the material [271], equation 2-12:

Equation 2-11 $$\varepsilon' = 1 + 2{J_1}^2(x_{0n})\left(\frac{D_c}{d}\right)^2 \frac{f_0 - f_1}{f_0}$$

Equation 2-12 $$\varepsilon'' = {J_1}^2(x_{0n})\left(\frac{D_c}{d}\right)^2 \left(\frac{1}{Q_1} - \frac{1}{Q_0}\right)$$

Where; J_1 – First order Bessel function

x_{0N} – N^{th} root of $J_0(x) = 0$

J_0 – Zero-order Bessel function

D_c – Diameter of cavity / m

d – Diameter of specimens / m

f_0 – Resonant frequency of empty cavity / Hz

f_1 – Resonant frequency of sample-loaded cavity / Hz

Q_0 – Quality factor of an empty cavity

Q_1 – Quality factor of sample loaded in the cavity

The major issues associated with this technique are resonant frequency shift; changes in Q-factor when the sample is in the cavity and particularly due to cooling during the measurement, therefore its measurement, and correction is needed to account for this [263]. This is often based on empirical data, which allows for the prediction of temperature when the measurement of dielectric properties is made; this can introduce error if the prediction of temperature is incorrect making the ability to measure in situ essential [272].

2.6.3.2. *Free space method*

In the free space measurement, the material in question is heated to the desired temperature at which point a near-plane-wave beam is projected at the sample [273]. This wave beam is then partly transmitted through the sample and partly reflected, these signal magnitudes are measured by detectors [274], see figure 2.38.

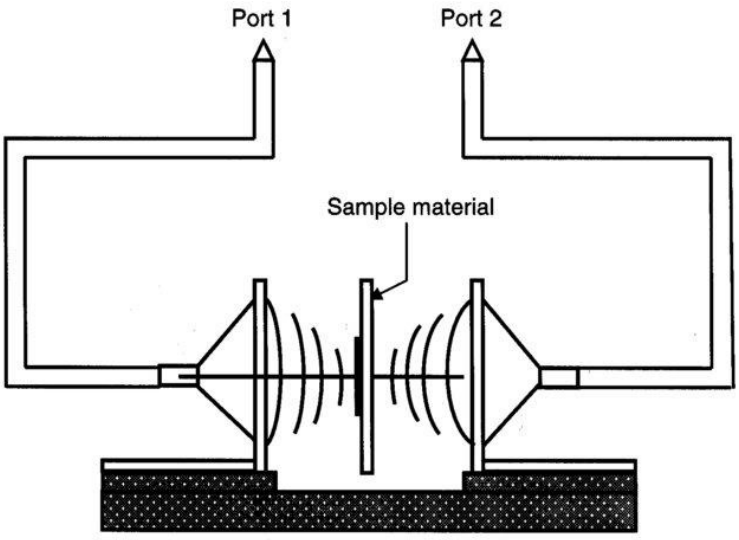


Figure 2.38. A diagram of the free space method that can be used to measure dielectric properties [270].

From these transmission and reflection coefficients, the dielectric properties can be calculated based on the sample's dimensions [275] using equation 2-13 to 16.

Equation 2-13 $$\varepsilon' = \left(\frac{Nc}{2Lf_N}\right)^2 + \sin^2\theta$$

Equation 2-14 $$tan\delta = -\ln(A_N)\frac{2(\varepsilon' - \sin^2\theta)}{N\pi\epsilon'}$$

Equation 2-15 $$A_N = \frac{1}{2}\left[\left(\frac{(1-a^2)^2}{a^4T^2} + \frac{4}{a^2}\right)^{\frac{1}{2}} - \frac{1-a^2}{a^2T}\right]$$

Equation 2-16 $$a = \frac{\left(\frac{\varepsilon' - \sin^2\theta}{\cos^2\theta}\right)^{\frac{1}{2}} - 1}{\left(\frac{\varepsilon' - \sin^2\theta}{\cos^2\theta}\right)^{\frac{1}{2}} + 1}$$

Where: N – Integer including zero

f_N – Observed frequencies / Hz

T – Transmission coefficient

c – Speed of light in free space / ms^{-1}

L – Thickness of sheet sample / m

θ – Angle of incidence / °

To optimise the accuracy of this technique, the frequency that provides the highest value of transmission and lowest reflection should be used [267]. Another drawback as stated in table 2.11. is that if the material's microwave absorption increases as the temperature increases, the noise of the signal increases. This limits the temperature range and the detectors need for shielding to prevent damage when exposed to the high-temperature samples, which can add further complications [274].

2.6.4. Microwave system components

A microwave system consists of three main components:

1. Source – magnetrons, solids state, travelling wave tubes, klystrons and gyrotrons.
2. Transmission line – antennas and waveguides
3. Applicators – single-mode, dual-mode and multimode.

2.6.4.1. *Microwave source*

In terms of sources, the magnetron is by far the most frequently used due to its low cost resulting in successful implementation into microwave ovens in both industry and domestic applications from the 1970s [276]. A magnetron is composed of a solid metallic rod (cathode) that conducts an electric current through a larger diameter metallic ring (anode) that contains small cut outs called cavities [277]. There are also two large magnets either side of this ring, which applies a magnetic field in parallel to the cathode. When current is flowing in the cathode, electrons are emitted via thermionic emission and are carried to the anode across the gap between the rod and the ring. These electrons also experience the force of the magnetic field causing them to circulate in a curved motion because of Lorentz force [277]. These electrons spiral outwards towards the cathode and when they reach the anode they induce a potential difference across the entrances of the cavities [277]. This effectively forms a capacitor with a single turn inductor; see figure 2.39(b).

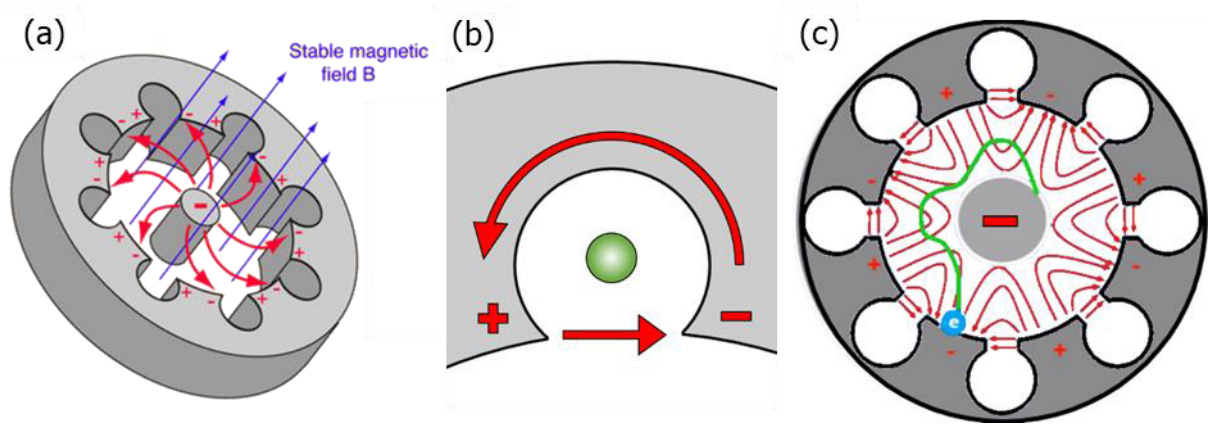


Figure 2.39. (a) A schematic adapted from [277], showing the direction of electron flow inside the anode after emissions from the cathode (red arrows) caused the intersecting magnetic field (blue arrows), (b) zoomed-in representation of a cavity, acting like a single turn inductor, showing the direction of current flow and the resultant electromagnetic wave produced extending out of the page parallel to the magnetic field and (c) the interaction of the electron with the electric field induced by the cavity-causing the retardation of the electron.

The capacitor creates an electric field due to the potential difference, which in turn causes the cavity to create a perpendicular oscillating magnetic field as the current travels around the cavity circle creating the electromagnetic radiation, which is extracted via an output antenna. The electric field created by the potential difference across the cavity entrances also extends inwards towards the central cathode. This means that emitted electrons are also retarded by the field as they travel in the opposite direction to the electric field toward the anode figure 2.39(c). This retardation causes the electrons to transfer energy to the radio frequency produced by the resonating cavities, which gives the magnetron the ability to amplify a lower power electromagnetic wave [278].

Magnetron generators are reliable and simple in terms of operation and has a very high power output and efficiency. However, they have a variable frequency output, a limited lifespan and require warming up [279]. This variable frequency is

unpredictable even with automatic tuning features, which can lead to high reflection inside microwave chamber. One example is microwave kitchen ovens, which are stated to operate at 2.45 GHz, but this quoted value is an average. In reality, a magnetron has an output frequency range of 2.4-2.5 GHz due to the associated frequency drift. This has prompted the ongoing development of solid-state generators, which do not suffer from this variable frequency and can actually be set to a specific frequency. Furthermore, solid-state generators have nearly an order of magnitude better operating lifetime and do not require a warm-up period before functioning [280]. The current drawback preventing widespread utilisation of this technology is the low power output of the current technology [281].

2.6.4.2. *Waveguides*

Once the field has been extracted from the microwave via an antenna the wave propagates along a waveguide, a hollow rectangular metallic tube. The waves travel as linear combinations of transverse electric (TE) and transverse magnetic (TM) modes to the microwave applicator [282]. The electric field in TE mode is equal to zero in the direction of propagation and the same is true for the magnetic field for the TM modes. Hybrid transverse electromagnetic modes are also possible [283]. These modes are electromagnetic field patterns that are created by the boundary conditions imposed on the wave modes by the waveguide [282].

2.6.4.3. *Applicators*

In general, microwave applicators are closed metal chambers where the electromagnetic waves are constrained and reflected numerous times before

reaching steady-state. There are a number of varieties of applicators, but for the purpose of this review only single and multi-mode version will be described.

Single-mode applicators

Single-mode applicators by definition only operate at a single resonance that is determined by the dimensions of the waveguide. For this reason, regions of high and low field strength are found in the cavity and consequently the heating of the susceptor is not homogenous. This does mean, however, that predictable field patterns and tailorable heating profiles can be devised [284]. This property of high field strength has been exploited in specific applications such as silent drilling of rock [285], joining of ceramics and composites [286, 287] and polymer processing [288].

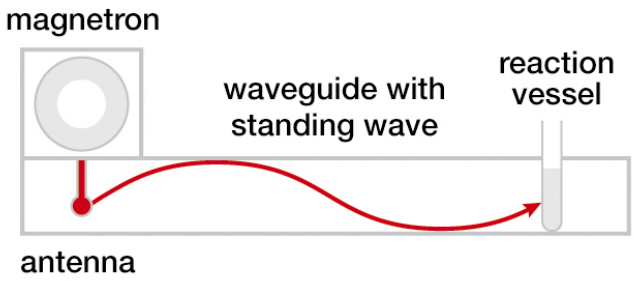


Figure 2.40. Schematic diagram of a single-mode applicator [289].

Multimode applicators

Multimode applicators are typically larger cavities, much larger than the wavelength, making them more suitable for bulk processing [259]. They are less sensitive to geometry as multiple hot spots are created by a large number of different spatial electromagnetic standing waves that exist near the operating frequency in the microwave [284]. The overall field can be seen as a superimposition of different electromagnetic waves in different directions due to multiple reflections. Good

uniformity can be achieved using mode stirrers and/or turntables, which help to create a time-averaged uniformity of the electromagnetic field [282].

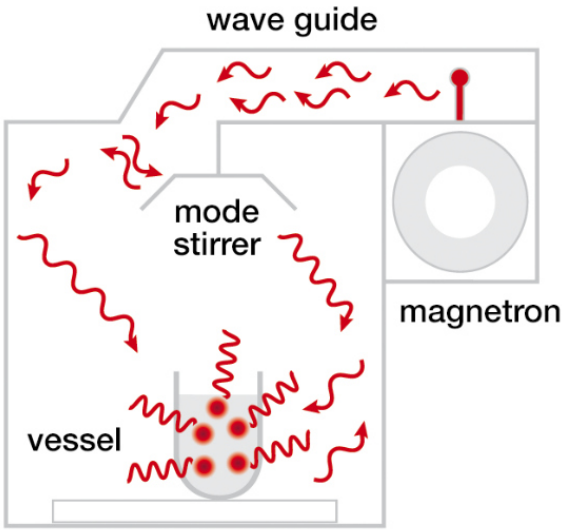


Figure 2.41. Diagram of a multimode cavity with mode stirrer [289].

2.6.5. Microwave heating modelling

There has recently been significant increase in the need for modelling of microwave applications and processes, though microwave modelling has been around since the 1980s. This has not been due to the lack of microwave specific technical data, rather it has been facilitated by the increased capability of a number of commercial software packages such as COMSOL™, ANSYS™ and QWED™ [290, 291]. The primary motivations for performing microwave modelling are [292]:

- To provide insight into the non-uniform heating associated with microwave energy.
- Assess the multiple factors that affect microwave power absorption such as such as material geometries, reflection coefficients (S_{11}), electric field distributions, dissipated power and corresponding temperature patterns evolved [293].

However, in order to do this there are two major challenges associated with simulating heating using microwave energy [294]:

- The dielectric and thermal properties of the materials change with temperature and frequency.
- Reconstruction of accurate CAD models, which can account for actual microwave chamber reflection and refractions.

The most two commonly used techniques to do this are Finite-Difference Time-Domain (FDTD) and FEA. FDTD algorithms are generally used to solve the electromagnetic problem as they require only a short time and relatively small computation resource, conversely the FEA approach is widely used for resolving the thermal problem due to reduced computation time required [295]. The primary difference when using these two methods for solving the coupled problem is the location of the field solutions. FDTD solvers utilise a rectangular mesh structure, which can have conformal boundary conditions applied [294]. The field value corresponding to this cell are calculated at the centre of the cell, whereas FEA solves the equations at nodes where elements meet. It is generally accepted that FEA has been adapted to electromagnetics whereas FDTD has been introduced specifically for solving EM problems [296].

As 3D electromagnetic fields vary both spatially and temporally, numerical techniques must be used to solve Maxwell's equation based on properties assigned to that cell/node and adjacent cells/nodes to determine the power dissipation. When solving for field distributions the metallic walls of the microwave cavity provide a physical and numerical boundary for the solution [294]. The interactions of the microwave at

the conducting walls are accounted for by boundary conditions where electric field is equal to zero as it is reflective and subsequently no temperature rise is seen. A heat transfer model can then be applied to convert this dissipated power into the source term in the heat equation to determine the temperature profile. The heat equation requires the initial temperature of the material, the material's properties and the boundary conditions specific to that cell in order to be computed. There are multiple boundary conditions available. The Dirichlet condition requires the explicit mention of the temperature at the boundary. The Neumann boundary condition assumes that the heat flow is through a boundary while the Robin condition, which is commonly referred to as the convective boundary condition, is an amalgamation of these two.

In order to find a numerical solution, the successful coupling of the two problems timescales is required which is difficult as the EM problem time scale is in nanoseconds and the thermal problem in seconds [296]. This can be achieved by the appropriate selection of a heating time step, which significantly influences the convergence of the model, computation time and accuracy of the temperature prediction [297]. The selection of the time step should not be too small or too big. In the case of too small, the convergence of the temperature distributions will be achieved but the simulation longer the necessary. If too big then there will be immediate divergence of the temperature distribution that will not be resolved. Hence when deciding selection, a relatively small time step should be favoured. The longer simulation time can be offset with mesh size optimisation. Optimising the mesh using conformal meshing technology can result in better simulations by forcing smaller mesh sizes in critical regions and larger cells in non-critical regions.

The physical scenarios simulated often have rapid changes in material properties with increasing temperature making the problem non-linear. This non-linearity drives the solution of the coupled problem in a cyclic manner. At each time step, the model updates the information of electric field distribution in every cell, which is then used to calculate temperature change in that cell according to the heat transfer equations and materials properties [294]. This results in a temperature change, most likely a rise, which in turn then alters the electromagnetic properties so the Maxwell equations must be solved again and the cycle starts over. This has been successfully demonstrated in a number of applications in the ceramics field such as microwave sintering, microwave heat exchangers, drying and binder removal [298-300].

2.7. Research on microwave energy chemical vapour infiltration (MCVI)

2.7.1. Silicon carbide and microwave heating

Silicon carbide has an intermediate loss factor value relative to other ceramics, therefore will readily absorb and heat up in a microwave field. This happens because SiC atoms will polarise in an electric field due to the higher electronegativity of carbon, subsequently electrons in the bond shift toward the carbon atom, creating two poles. The dipole then follows the reversals of the applied electric field. However, there is a characteristic lag time between the polarization and the reversal of the electric field, known as the relaxation time [301]. As previously mentioned time is due to the dissipation of energy as heat due to the phase lag between the dipole rotation and the field [19, 302].

At higher temperatures, losses from dielectric heating can be neglected, as ohmic heating becomes the dominant mechanism in the microwave heating of SiC, as it is a semiconductor. The ability to carry current is dependent on temperature because the lattice's atomic vibration increases with temperature, thus further impeding electron movement. This increases the resistance and translates to an increase in the dissipation in thermal energy; as ε" becomes large so too does the loss tangent [303]. This transition to ohmic heating is also explained by the fact SiC is also a semiconductor; a small but non-zero bandgap exists between the valence band of electrons and the conduction band in silicon carbide's electronic structure. This means that SiC will behave as an insulator at absolute zero but thermal excitation of electrons is possible into the conduction band from the valence band as temperatures increases. This behaviour is exacerbated by larger atomic vibrations that result in larger interatomic spacing, which, in turn, decrease the potential experienced by the orbital electrons.

In terms of SiC_f/SiC composites, both the fibres and matrix properties have to be considered. A key variable that applies to both the matrix and fibres is the Si:C ratio as the amount of carbon will determine the dominant heating mechanism [304]. It is a balance, however; a Si:C ratio <1 means more dominant ohmic losses, which may help heat the material to high temperatures [305, 306]. However if the carbon level is too high the impedance matching properties and oxidation properties will deteriorate [261]. On the contrary, if the ratio is >1 the material may not heat in a microwave field and reflect microwaves. Details of the dielectric properties of the matrix and various fibres are shown in table 2.12.

Table 2.12. Showing the respective dielectric properties of a number of different fibres and their constituent materials [178, 307-310].

Material	Resistivity/ Ω cm	Skin depth/ cm	Comment
Nicalon fibre (Low resistivity)	0.5–5	0.07-0.23	Heated to > 1000°C
Nicalon fibre (High resistivity)	$>10^6$	>100	Heated to > 1000°C
Nicalon fibre (Ceramic grade)	1000	3.2	Heated to > 1000°C
Bulk β-SiC	0.01-100	0.01-1	Reflects microwave at 1000°C
Silicon	10^5	32	Increase matrix resistivity
Carbon (graphitic)	0.0003-0.006	~0.004	N/a
Silicon oxy-carbide	0.14-0.00045	-	N/a

2.7.2. Concept of MCVI

The CVI process was described in section 2.5. The reason behind the development of the microwave energy enhanced CVI process is to eradicate the premature pore closure that can occur in the isothermal conventional CVI method. Table 2.13. shows the conceptual cross-sections of the pore closure in the SiC_f/SiC composite vs the conventional method. This is achieved by the creation of an inverse temperature profile due to the volumetric heating microwave energy causes and the surfaces losses of the component [311, 312]. This means that the deposition preferentially initiates at the centre of the preform, where it is hottest, figure 2.42. From there, the deposition reaction front proceeds outwards reducing and potentially preventing, the entrapment of pores [5].

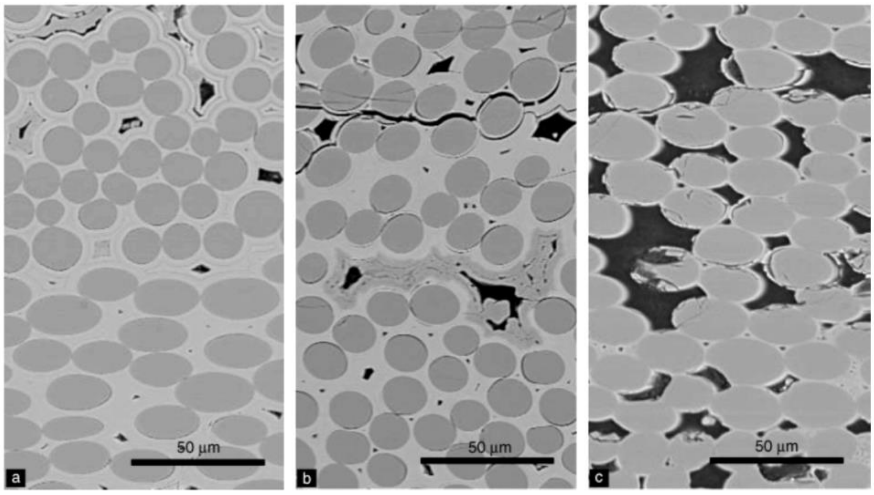


Figure 2.42. Micrographs showing the variation of deposit thickness in the CMC using MCVI; moving from the centre (far left) to 10mm from the centre (middle) and outer edge approximately 20 mm (far right) [13].

This is also demonstrated using the Thiele modulus as previously mentioned in section 2.5.2; as pore radius and gas diffusivity value is larger, the Thiele modulus decreases favouring diffusion into the pore channel as shown in figure 2.43. When combined, these factors combined are expected to lead to a reduction in processing time from 2-3 months [313] to potentially <100 hours.

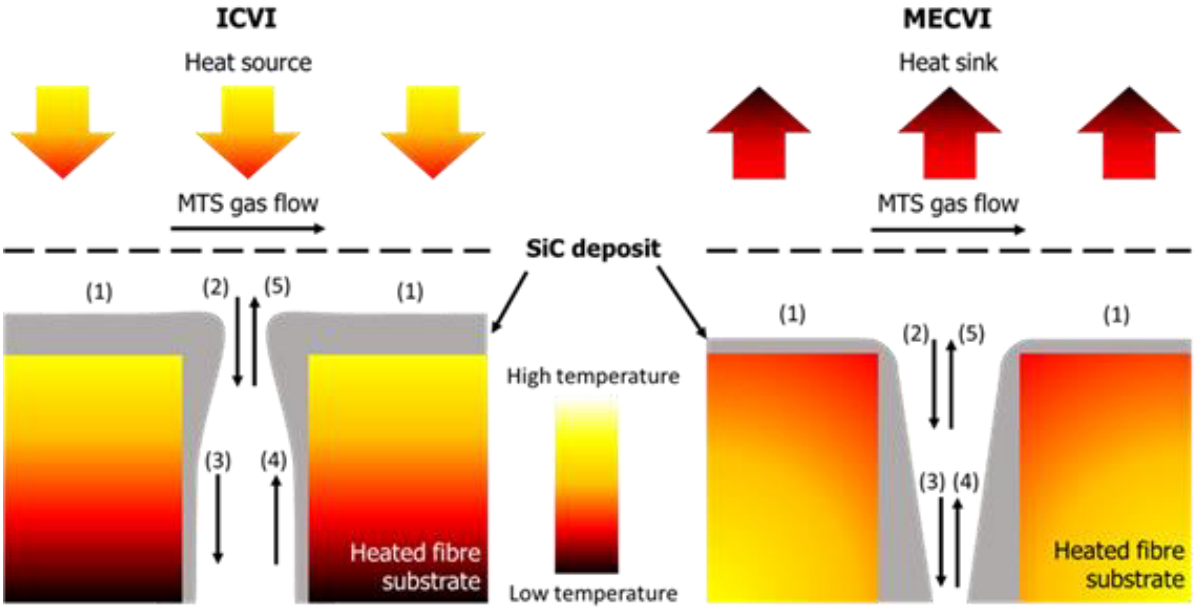
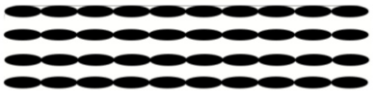
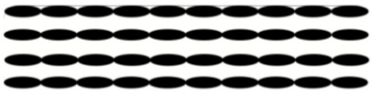
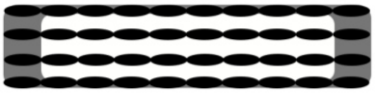
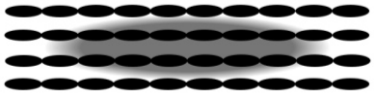
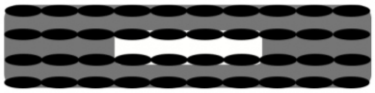
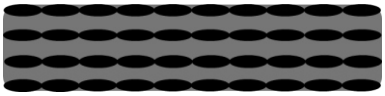


Figure 2.43. Schematic comparison of ICVI vs MCVI in terms of the relative thermal gradients, gas flow and subsequent generalised pore filling with SiC.

Table 2.13. Schematics of the theoretical cross-sectional densification of ICVI vs MCVI.

Stage	ICVI	MCVI
Start		
Intermediate		
Final		

The use of microwaves, however, brings about its own complexities, its advantages and disadvantages are shown in table 2.10. On top of the variables used in the CVI route, i.e. pressure, temperature, gas ratio and flow rate, microwave specific parameters also need to be factored in. The dielectric properties of the SiC_f change with increasing temperature making the process potentially harder to control [314] and incremental power increases are typically required during heating [13]. Since the fundamental deposition process in MCVI is not changed, merely the physical location of the deposition, filling large pores is still very time-consuming and increases the risk of the deposition front creating residual porosity, potentially resulting in a lower density final product.

Table 2.14. The established and potential advantages and limitations of the MCVI process; potential advantages are indicated with *.

Advantages	Disadvantages
Potentially shorter processing times to producing CMCs with relative densities >90%*, by an order of magnitude*	Plasma formation at low temperatures
Inverse densification profile has been demonstrated on a number of occasions	The macroscopic surface finish of fibre preform must be as smooth as possible i.e. no stray fibres, to prevent arcing
Lower processing temperature due to volumetric heating vs conventional means*	The penetration depth of 2.45 GHz microwave limits sample size
Enhanced rates of SiC deposition because of the effect of microwave radiation*	Microwave heating can be difficult to control
Reduced machining because of the inverse densification*	Single preform production per run
More energy efficient and material-efficient as only the sample is heated	Spatial non-uniformity of the electric field

One solution is to ensure that there are no large pores (>500 μm) that CVI has to fill. A number of techniques have been investigated to fill the largest pores prior to the CVI stage. Jaglin [70] found that using vacuum bagging and/or electrophoretic impregnation to impregnate the fibre preforms prior to CVI with SiC powder had a significant effect on filling the inter-ply porosity, which helped to reduce the overall processing time. He found that this complementary process was able to produce infiltrated samples as dense as 75% after 17 h of infiltration via MCVI, see table 2.15. for details.

2.7.3. Experimental results

A relatively small number of studies have been carried out in relation to the MCVI process since its inception in the early 1990s; table 2.15 provides experimental details and major results of the key experimental studies into this topic to date.

This review has looked at the reinforcement mechanisms used to improve the strength of ceramic materials to prevent brittle failure. It has shown that FRCMCs have the potential to exhibit the properties desired by the aerospace industry and discussed the various established and developing methods to manufacture them to achieve this. It has reviewed the literature, theory and empirical data on the materials that were used in this project and commented on the findings of specific publications related to the chemical vapour infiltration technique. This thesis reports the experimental and modelling efforts of the MCVI process investigating the deposition mechanism of a SiC matrix in a SiC fabric preform. The primary aims of this research were to:

- Investigate whether creating near fully dense SiC_f/SiC CMCs in a reduced time with superior microstructure was possible using MCVI.
- Develop an understanding of the relationship between various processing conditions and resulting microstructures, crystal structures and compositions of the deposited SiC.
- Produce relevant models to verify the creation of an inverse temperature profile using SiC fibre preforms.
- Develop a complimentary SiC slurry impregnation route for further reducing processing times in the MCVI without detrimentally affecting densification.

P	Preform characteristics	Processing conditions	Microwave conditions	Key results	Deposition rate	Comments	Refs.
Iso	SiC Nicalon cloth, Ø = 70 mm	P = 400-800 mbar, Q_{H2} = 500-4000 cm^3 min^{-1}, P_{MTS} = 1-25 mbar	2.45 GHz, 0.7 kW	11.5 wt.% gain in 3 h	0.03-0.42 g h^{-1}	Si-SiC deposit	[315]
Iso	SiC Nicalon fibres, L = 0.5-1.0 mm	P = 730 mbar	2.45 GHz, 0.7 kW Single-mode cavity	N/a		Non-Arrhenius kinetics	[316]
Iso	30 ply of Nicalon cloth, Ø = 48 mm, T = 10mm	T= 800-1050°C, P =700 mbar, QH_2 = 300 cm^3 min^{-1} MTS fraction at inlet (vol.%)= 1.3	2.45 GHz, 0.5-5 kW Multi-mode cavity	ρr=55% Centre density= 73%, t=24h (10 h if pre-infiltrated with SiC slurry)	2.3-22.1 mg min^{-1}		[5, 13]
Iso	15 layers Nicalon NL 202, 20x40x80 mm	T= 1000-1100°C, P = 1 bar, QH_2 = 180 mol hr^{-1},H_2/MTS = 500-1000, MTS fraction = 0.15-0.30	2.45 GHz, 6 kW Multi-mode cavity	Weight gain = 70% t =18 hr	N/a		[317]
Iso	30 ply Nicalon NL 202, Ø = 48 mm, L = 10 mm	T= 1000°C, P = 700 mbar, QH_2 = 300 cm^3 min^{-1}, H_2/MTS~10-30	2.45 GHz, 3kW Multi-mode cavity	Centre density= 75% t = 24 h	N/a		[318]
Iso/ FF	20 ply ZMI, Ø = 55 mm, L = 8 mm	T= 900°C, P = 200 mbar, QH_2 = 300 cm^3 min^{-1}, H_2/MTS~10	2.45 GHz, ~ 1.2 kW	~68% dense after 20 h	N/a	Non-Arrhenius kinetics	[243]
FF	SiC/Nicalon Vf = 42-46 vol.%	T = 975°C P < 100 kPa Qt = 140 cm^3 min^{-1} (50 cm^3 min^{-1} of N2) mg = 10	2.45 GHz	t = 35 h ρr = 57.8%	Matrix growth rate: 11.4 µg cm^{-2} h^{-1}		[319]
FF	Nicalon cloth Φ = 50mm, L = 7-10 mm	T = 1000°C P = 95-97 kPa QH2 = 250 cm^3 min^{-1} QMTS = 0.575 g min^{-1}	2.45 GHz, 5 kW Multi-mode cavity	ρr = 75% Centre density= 100% t = 17 h	Centre reaching near full density		[320]
P = Pressure conditions: iso = Iso baric, FF = forced flow. Ø = diameter, T = thickness							

Table 2.15. The historic results of MCVI when depositing SiC into a SiC fibre preform.

3. Experimental Methodology

This chapter describes the experimental work carried out during the research project. It is divided into four sections: section 3.1. outlines the MCVI equipment; raw materials, sample preparation, physical characterisation and experimental protocol are reported in section 3.2.; section 3.3. summarises the material characterisation and analytical techniques employed and finally section 3.4. covers the modelling aspect of the research.

3.1. MCVI equipment

Figure 3.1. shows a photograph and schematic of the forced flow microwave energy enhanced chemical vapour infiltration unit used in in the project. The unit is comprised of four subsystems:

- The microwave unit
- The gas delivery system
- The waste gas removal system
- Local exhaust ventilation safety system

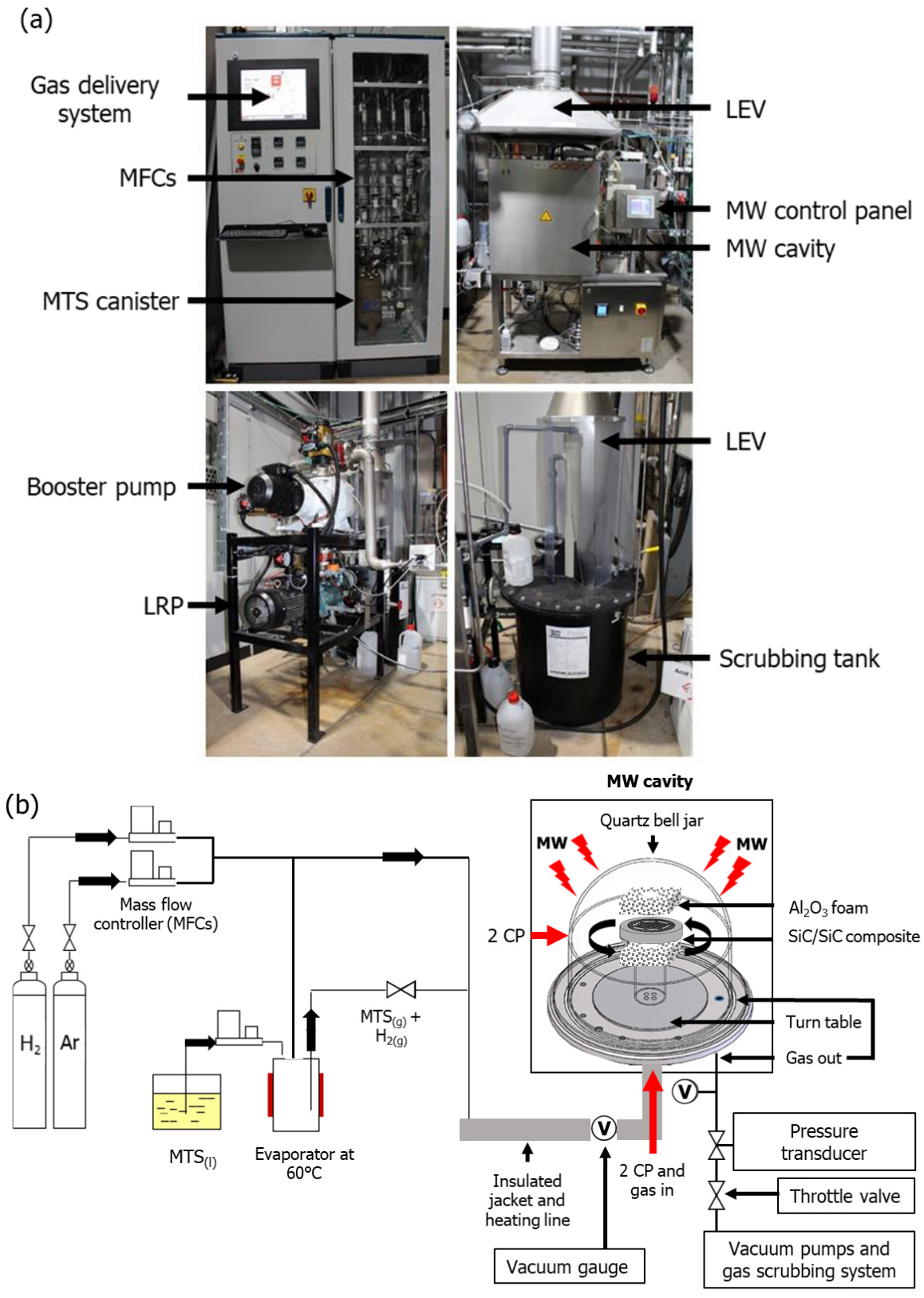


Figure 3.1. (a) Labelled photos of the MCVI system and (b) a schematic representation of the system.

All the units except the LEV system were electronically interconnected. Pressure and gas flow were controlled by the gas delivery system based upon feedback from the pressure transducer and throttle valve. The microwave circuit had a safety interlock on the gas delivery system to prevent the accidental powering on of the microwaves with the door open. The microwave power was controlled by a feedback loop between the two-colour pyrometers and a set point control on the microwave system. A multi-level alarm system was developed by the manufacturers of the gas system and microwave, to address the health and safety issues associated with the use of electromagnetic radiation, explosive gases and hazardous chemicals that were contained in the quartz bell jar that was the reaction vessel for the MCVI process.

3.1.1. Microwave system

The customised microwave energy system (Labotron HTE M30KB CL PRO, Sairem, Lyon, France) included a microwave generator, a control unit and 55 x 55 x 61 cm 316l polished stainless steel cavity. The generator from Muegge Electronics GmbH (Magnetron 2M265-M12WJ, Germany) operated at a frequency of 2.45 ± 0.05 GHz and had a maximum power output of 3.00 kW that could be adjusted in 0.01 kW increments. The generator could also be operated in both a controlled pulse and continuous ramp modes and was water-cooled with a minimum water flow of 4000 cm min^{-1}, to prevent it from burning out. The cavity, waveguide and turntable were also water-cooled below 50°C; this improved the efficiency of microwave generation and prevented the thermal expansion of the components, which could have affected the microwave frequency and propagation. A turntable with an adjustable rotation speed continuously perturbed the electromagnetic field with the aim of producing

homogenous heating. The metallic rectangular wave-guide was located at the top of the cavity in the back right-hand corner. The microwaves produced by the magnetron were attenuated by a manual E/H tuner (Sairem, Lyon France) and a four-stub auto tuner (Sairem, Lyon France), see figure 3.2. Their combined use aimed to minimise the reflected power within the cavity and optimise the impedance matching, coupling and subsequent heating of the SiC samples. A secondary role was to protect the magnetron from extremes of reflective power that might result in overheating and shutdown.

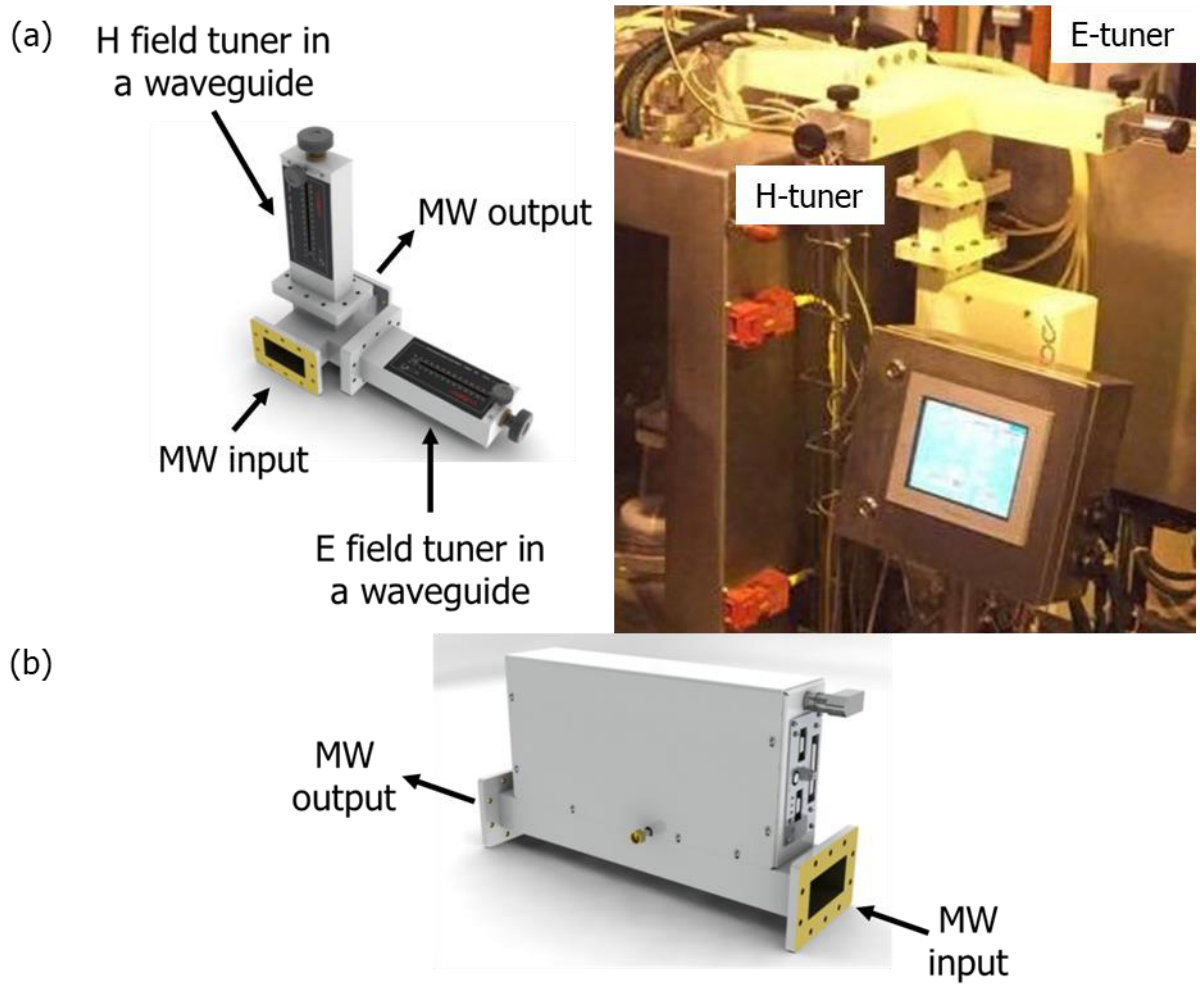


Figure 3.2. (a) Manual tuning system and (b) automatic tuners that were used to minimise the reflective power inside the MW cavity to improve the efficiency of heating.

The microwave system was also equipped with a microwave survey metre (DFM M24DC, Sairem, Lyon, France) that would detect any microwave leaks for safety purposes, see figure 3.3.; with a safety threshold set at $5x10^{-3}$ Wcm^{-2}. The cavity door also had two safety-interlock switches (Trojan Guardmaster, Allen-Bradley, Rockwell Automation Inc., WI, USA) that again prevented accidental switch on, see figure 3.3. A fibre optic arcing detector was installed and interlocked with the MW generator to protect the microwave and users, figure 3.3.



Figure 3.3. From left to right: The microwave leakage detector, fibre optic arc detector behind a quartz window and the MW door safety interlock.

3.1.2. Temperature, pressure and gas control systems

Temperature control

Measuring and controlling the temperature accurately was a critical element of the MCVI process and was carried out using three contactless pyrometers that were integrated into the Labotron system. A 1-colour pyrometer (1CP) (thermoMETER CTM3, Micro-epsilon, NC, USA) was positioned in the top face of the cavity and monitored the top surface temperature up to 750°C[viii]; 0.9 was used as the emissivity

[viii] The top pyrometer was never used to control temperature because it was not accurate due to the fogging effect, see section 3.2.3.6.

value of SiC [321]. 2x two-colour pyrometers (2CP) (thermoMETER CT ratio M1, Micro-epsilon, NC, USA) were also used to measure the side temperature and bottom surface temperature, see figure 3.4. The pyrometers used had a response time of 5 ms and an accuracy of ± 0.5% of the measured temperature; their working range was 700-1800°C. The bottom pyrometer controlled the set point temperature via a feedback loop; modulating the power supplied to the cavity with the help of a proportional, integral and derivative (PID) system keeping the sample as close to the set point temperature as possible which was normally within ± 15°C. It was assumed that the temperature observed on the lower surface was always lower than the actual temperature in the centre due to the thermal gradient in the vertical direction caused by the volumetric heating and surface losses. An upper-temperature limit of 1400°C was set for safety purposes to prevent any thermal runaway. The pyrometer was also never in direct contact with the gas stream and was heated to prevent MTS condensing on the quartz lens.

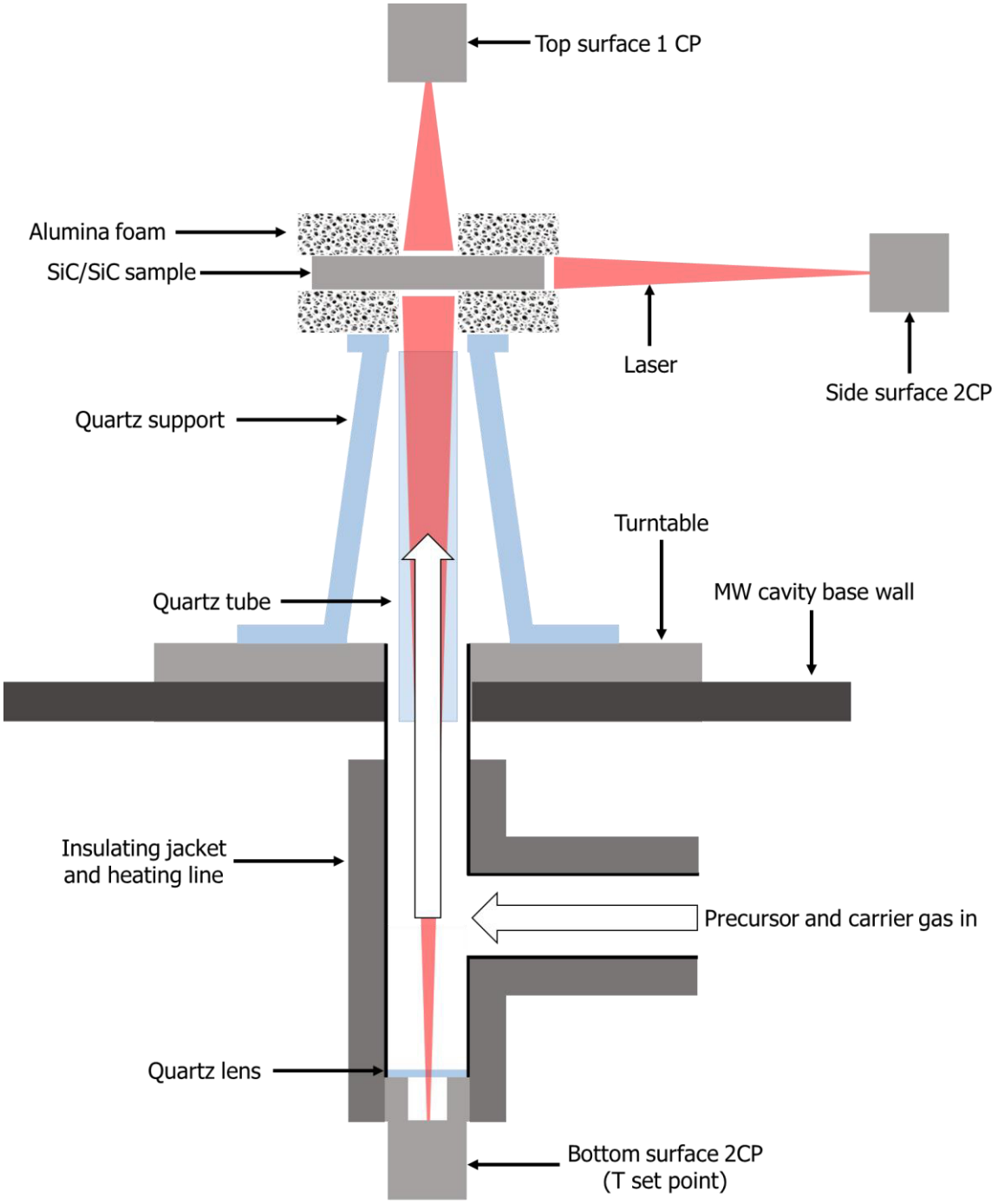


Figure 3.4. A cross-sectional view of the temperature control arrangement of two-colour pyrometers, sample and gas flows.

Pressure control

The pressure of the reaction vessel was monitored by a pressure transducer (Baratron 747B, MKS Instruments Ltd, Crewe, UK) and controlled by a throttle valve (T3Bi High-Speed Exhaust Throttle Valve, MKS Instruments Ltd, Crewe, UK), see

figure 3.5. The pressure transducer used an Inconel all-welded sensor, which provided the maximum possible resistance to the corrosive gases. In addition to this, the transducer was heated to 45°C, again to prevent the MTS condensing. The vessel pressure was set on the control system, and then the transducer relayed the current pressure to the throttle valve, which, using a self-tuning algorithm, opened and closed a rotating valve to lower and raise the pressure inside the bell jar respectively, as a vacuum was being pulled and gases were flowing.

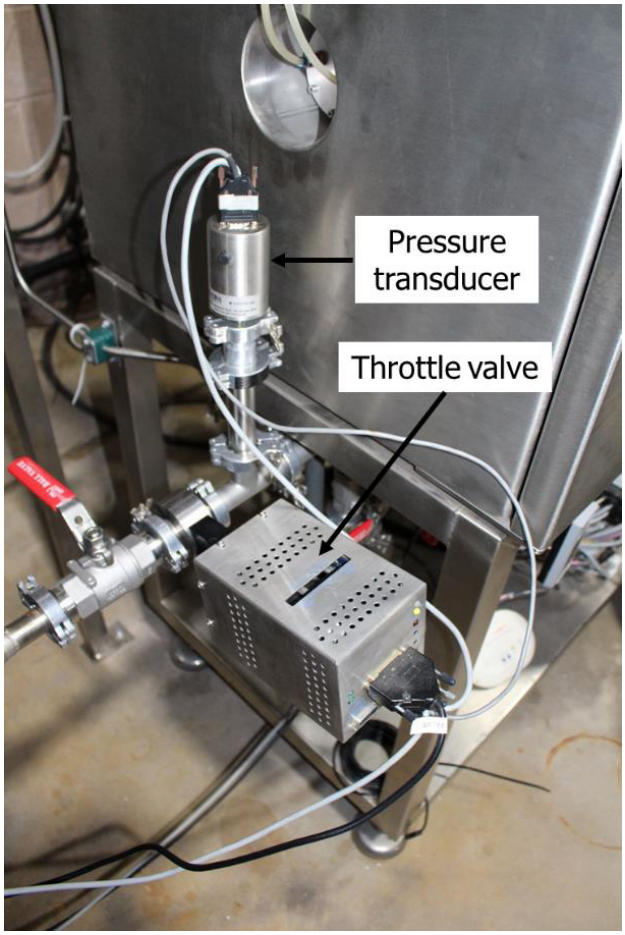


Figure 3.5. Photo of the pressure transducer that monitored the vessel pressure and the throttle valve that enacted changes to the pressure.

Gas flow control

The flow of gases into the reaction vessel was metered digitally using calibrated mass flow controller (MFC) (Coriflow, Bronkhorst Ltd, UK). High purity H_2 and Ar

(The BOC group plc, UK) could be passed into the system at a maximum flow rate of 2000 cm^3 min^{-1} with an accuracy of 0.05% of the full scale. MTS was stored as a liquid in a 6000 cm^3 stainless steel vessel, which was kept at a pressure of 1.3 bar to highlight any leaks in the vessel that could be potentially dangerous and to help with the flow of the vapour. The vessel was fitted with a pressure relief valve set at 6 bar that would open and release MTS directly into the scrubbing tank should the pressure ever get dangerously high. Like the carrier gases, MTS flow was controlled by an MFC with a precision of 0.017 g min^{-1} (Coriflow, Bronkhorst Ltd, Newmarket, UK). The MFC could be operated at a minimum flow of 0.17 g min^{-1} to a maximum of 3.3 g min^{-1}. The MTS flow rate was controlled after the liquid had been vaporised at 65°C, which was 1.4℃ cooler than the boiling point, as seen in figure 3.6.

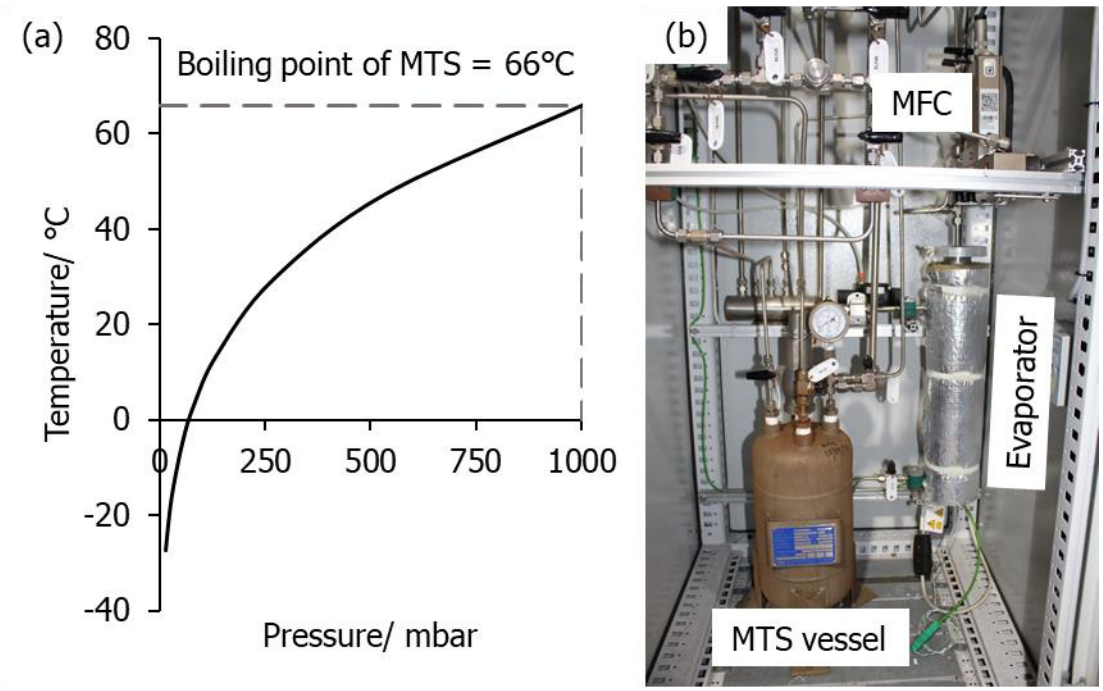


Figure 3.6. (a) Effect of pressure on the boiling point of MTS [322] and (b) a photo the MTS storage vessel connected to the evaporator that heated up the liquid to a vapour.

3.1.3. Gas exhaust and by-product neutralisation

To carry out the CVI process a controlled atmosphere needed to be created inside the microwave cavity. The bell jar was made of 8 mm thick quartz (Quartz scientific, High Wycombe, UK) with an internal diameter and height measuring 300 mm. The bell jar's flange sat on a Kalrez™ O-ring that was greased with Krytox™ (Dupont, USA). Both the Kalrez and Krytox products can be used continuously up to 360°C and have excellent chemical inertness. The incoming gases were mixed in the pipeline and transported in through the bottom of the microwave cavity via a heated pipeline to the sample before being removed via the vacuum port, see figure 3.1. The sample was placed on a quartz tube on a turntable rotating at 9 RPM to prevent hot spot formation. The installation and synchronisation of the gas flow and pressure controls were provided by Archer Technicoat Limited. (High Wycombe, UK).

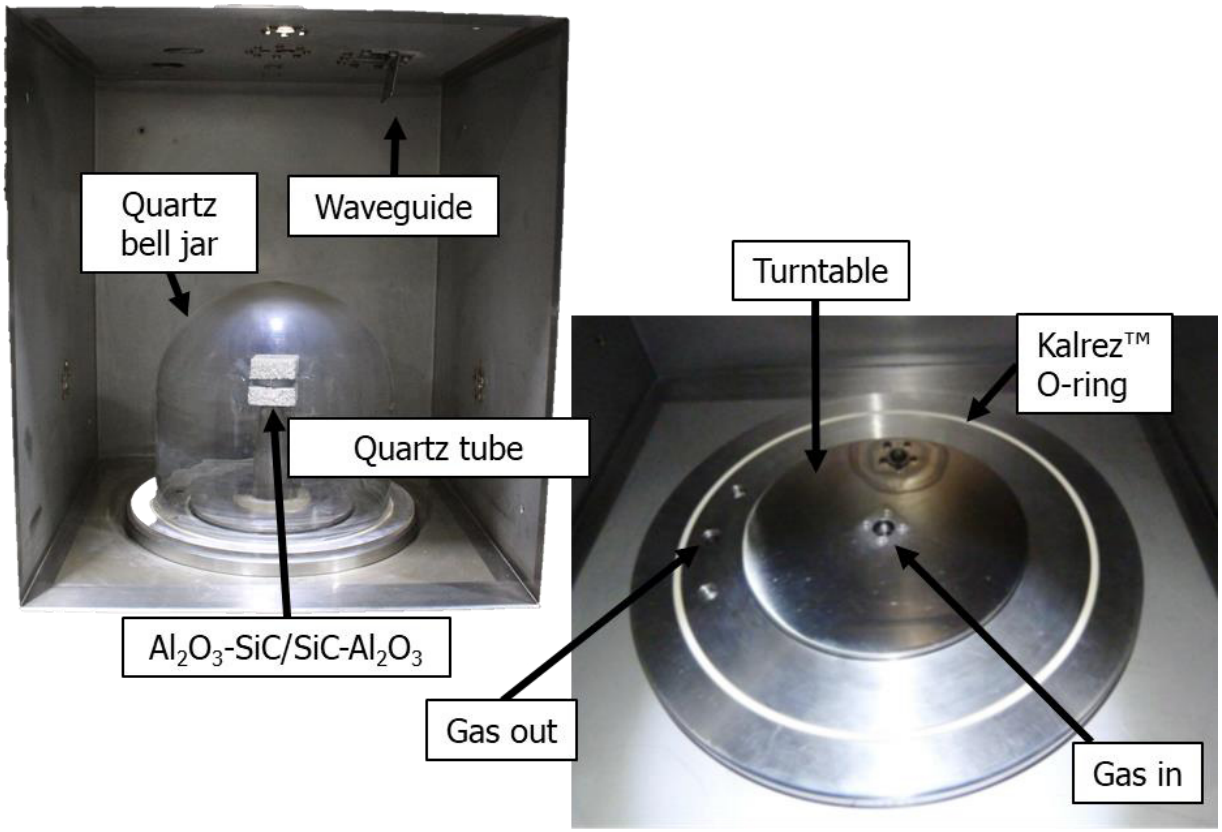


Figure 3.7. Photo of the microwave cavity with the bell jar inside and an image of the turntable and gas inlet and outlet.

The deposition of SiC from MTS, as described in section 2.5.1., is a thermally activated process. As a result, the exhaust gases produced by the reaction are a volatile mixture of unreacted MTS, H_2, HCl and all of the associated by-products and intermediates. These gases passed through the vacuum pump stack, before being bubbled into and neutralised in a scrubbing tank. The pump stack, as seen in figure 3.8., was comprised of a liquid ring pump (LRP) (TRHE 32-60/C-M/A3, Pompe Travaini srl, Italy) and a booster pump (RUVAC WAU 251 FP, Leybold Vacuum, Germany) that pulled the vacuum and removed the by-products in the bell jar, see figure 3.1. The booster pump was only used for the initial vacuuming of the chamber and not during MCVI processing for product removal as it only operated at pressures below 50 mbar. This was because of the increased change of arcing below 200 mbar and low pressure plasma forming below 50 mbar [323]. The liquid ring pump's efficiency was dependent on the water temperature of the chiller system, which was typically kept at around 10°C. The 250 l scrubbing tank was made out of polyvinyl chloride and contained approximately of alkaline NaOH solution; the pH was controlled by an automatic pumping system that kept pH between 8-10 by adding the 0.5 mol solution from another vessel whilst being continually flushed with cold water. The concentration of this solution was dependant on the flow rate of precursor gases since that altered the concentration of acidic substances that were being evacuated into the tank.

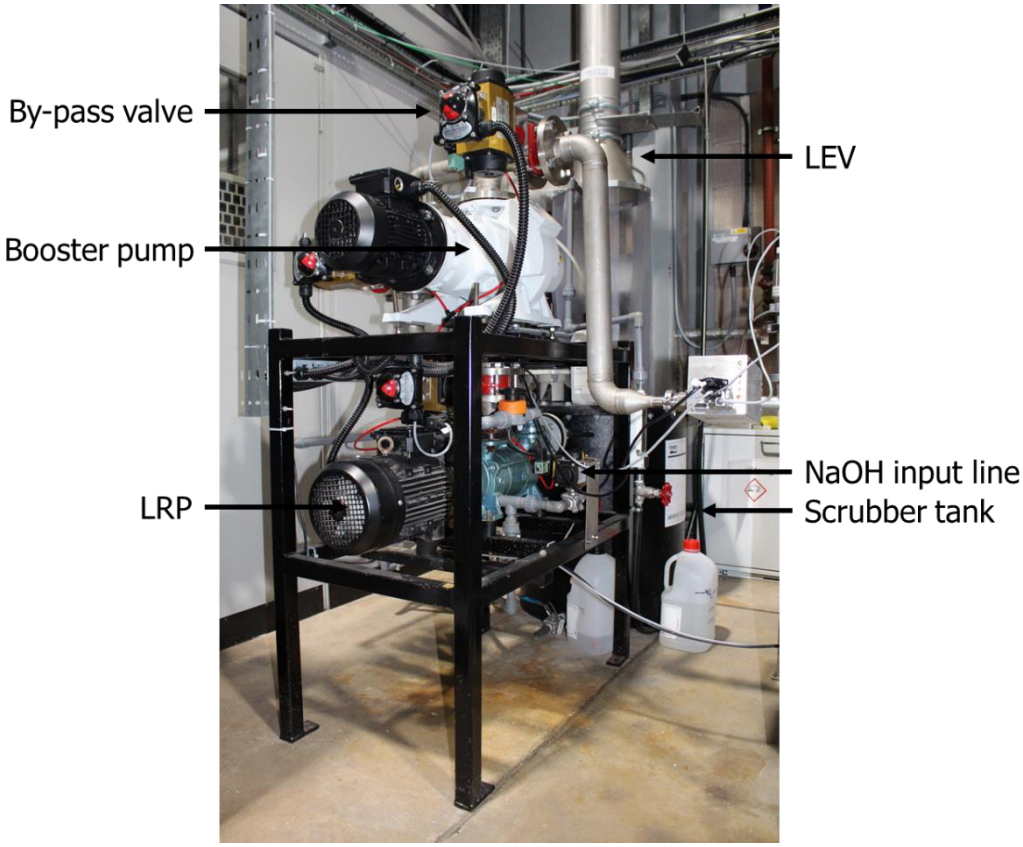


Figure 3.8. Photo of the pumping stack with the key components labelled.

3.2. CVI of SiC_f/SiC composites

3.2.1. Constituent Materials

3.2.1.1. *SiC fabric*

The fibres available for the project were Tyranno ZMI & SA3 fibres and Hi Nicalon Type-S fibres that were manufactured by UBE Industries (Japan) and Nippon carbon (Japan), respectively. Both the UBE fabrics were woven into a two-dimensional cloth with a matt weave whilst the Type-S was woven into an 8-harness satin weave. The physical properties of the fabrics can be found in table 3.1.

Table 3.1. Details of the physical properties of the SiC fibre used at various stages of the project [100, 324, 325].

	Tyranno™ ZMI	Tyranno™ SA3	Hi Nicalon Type-S
Density / kg m^{-3}	2.48	3.1	3.1
Aerial weight / kg m^{-2}	0.25 ± 0.02	0.25 ± 0.03	0.348 ± 0.02
Thickness / μm	0.27	0.21	0.23
Weave	Plane	Plane	8H-Satin
Specific surface area / m^2 kg^{-1}	124*	147*	141*
Fibre diameter / μm	11	10	10
Fibres per tow	800	800-1200	500
* = calculated value [326]			

All the fabrics were first boiled in deionised water for 10 minutes to the remove PVA sizing that covers the tows to minimise fraying. After this, the fabrics were washed with ethanol and dried under an infrared lamp and the mass recorded. As expected, the fabrics lost ~1 wt.% due to the removal of sizing, which is consistent with the technical data from the suppliers. Preforms for the MCVI process were prepared by layering up fabric sheets, one on top of another. Typically, 20 disc-shaped plies were used to create one sample. These discs were produced using a 55 mm diameter wad punch, which was used to cut discs from the cloth. For non-impregnated samples, see section 3.2.2. for details of the impregnation process, the 20x stamped out plies were aligned and stitched together by hand in the Z-direction using a fine cotton thread to hold the plies together, see figure 3.9. The average thickness for a 20-layer preform was 7.2 ± 0.5 mm and was measured with a digital calliper before MCVI. A 25 vol.% SiC slurry was painted around the circumference for all assembled preforms

(impregnated and non-impregnated) to shield any sharp points (e.g. sticking out fibres) from the electric field.

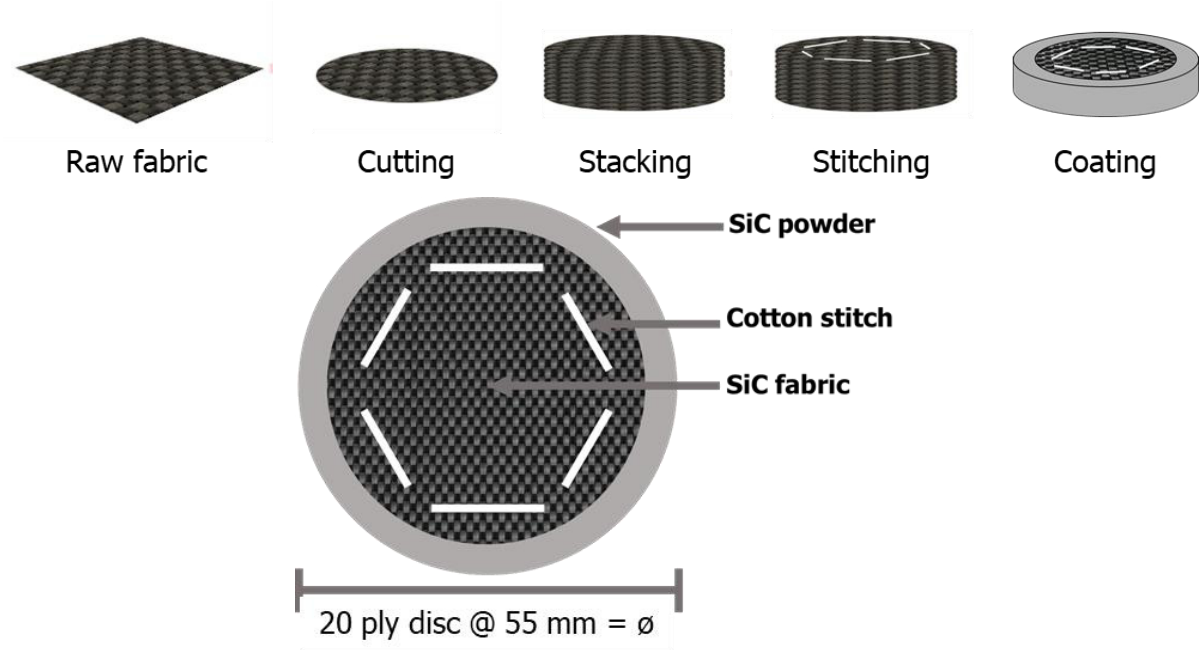


Figure 3.9. Preform fabrication route for a non-impregnated SiC_f/SiC composite.

3.2.1.2. *SiC powder*

A large variety of SiC powders from different suppliers and particle sizes (0.3-10 μm) were, see figure 3.2, evaluated during preliminary testing. The powders that were selected for further trials are shown in table 3.2 as indicated by the asterix;

Table 3.2. Silicon carbide powders used in the preliminary trials.

Manufacturer	**Powder particle size/ μm (as stated by the manufacturer)**	**Manufacturer nomenclature**
H.C. Starck, Germany*	0.3-0.4	UF-25
H.C. Starck, Germany*	1.0-2.0	UF-05
Testbourne, UK	3.0-4.0	SuperVac
Testbourne, UK*	6.0	SuperVac
Testbourne, UK	7.0-8.0	SuperVac
Electron Microscopy Sciences, US	10.0	Silicon carbide powder

* = Selected for further testing

3.2.1.3. *SiC matrix via CVI*

Methyltrichlorosilane (75-79-6, Sigma Aldrich Corporation, St. Louis, MO, USA) was used as the precursor gas for the deposition of SiC using the MCVI process. MTS is a colourless liquid with a pungent, acrid odour. The molecular weight of MTS is 149.48 g mol^{-1} and has a density of 1.273 kg m^{-3}. As outlined in section 3.1.3, the MTS boiled at 66°C at atmospheric pressure, upon which it was diluted with H_2 gas, which acted as both a carrier and catalyst for the reaction. MTS had to be handled very carefully; it is both flammable and an irritant and reacts violently with water or steam to produce heat and HCl fumes, which are very dangerous for users and corrosive for the equipment.

3.2.2. Impregnation of SiC fibre preforms

SiC preforms were impregnated with various aqueous SiC slurries to fill the larger porosity in the structure to both reduce the mean pore size and the total volume that needed to be filled during the MCVI process. Preliminary trials were carried out to narrow down the range of solids content of the slurries to be used in future tests. Initial trials ranged from 10-35 vol.% and were assessed for the stability and drying rate when applied to the SiC fibre. Following this the 22.5 vol.% and 25 vol.% solids content slurry was selected as they showed good stability and didn't dry too quickly; all the powders used are shown in table 3.2.

The slurry was prepared using 80.250 g of SiC powder (for a 25 vol.% slurry) which was measured out in a plastic weighing boat on a high precision balance that measured to three decimal places with a maximum capacity of 250 g (Sartorius

Analytical balance, Germany). The powder was then added to a 150 ml HDPE roller bottle and placed back on the scale and the scale was then tared. The typical volume of slurry produced per preform impregnation was 100 ml, therefore 73.796 g of deionised water was then added to the bottle. This amount accounted for the water content is the dispersant, which was 60%. 1% by volume of dispersant (Dispex® AA4040, BASF SE, Germany) was then added to the mixture using a disposable pipette adding. Once the slurry composition was made up, it was shaken by hand to mix the components together and then 100g of 5 mm spherical alumina milling media was added to the same bottle. The slurry was then milled for 2 h on a Capco roller mill (Capco Test Equipment, UK) at ~120 rpm to break up any soft agglomerates.

Three methods were trialled to assess the overall effectiveness of the method of slurry application to the SiC woven fabrics. The techniques used were dipping, painting and rolling. The dipping process firstly cut the SiC fibre into 20x discs using a 55 mm wad punch (Priory, UK). The individual discs were then submerged in a SiC slurry bath thus impregnating them with the slurry. They were they removed and stacked on top of one another inside a vacuum bag to be dried and pressed, see figure 3.12. The preform once dried were very thick with a dense powder layer between the SiC plies meaning that were not permeable to gas so were discounted from any further trials at this stage, see figure 3.10.(a). The painting method used a 2.5 cm width, fine bristled brush to apply the SiC slurry to the SiC fabric by hand as uniformly as possible. Whilst still wet the 55 mm discs were punched out of the fabric. At the slurry application stage, this technique appears to work based on a

visual inspection, albeit with minor fabric weave disruption, but the preforms after vacuum bagging readily delaminated. This was found to be because only very small amounts of the slurry were added to each ply, as shown in figure 3.10(b).

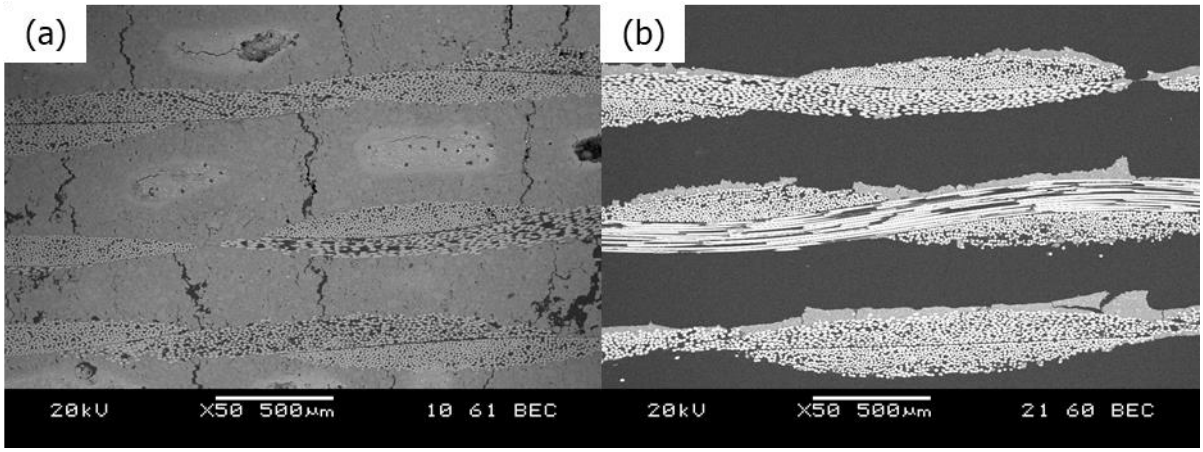


Figure 3.10.(a) SEM micrograph of a polished cross-section of a dipped sample, and (b) the polished cross-section of a painted sample that has delaminated.

Preliminary work quickly identified that rolling, and later calendaring, was the most effective, in terms of creating, preforms with high enough relative density to make them robust with a uniform slurry distribution. The calendaring method that was used firstly cut the SiC fabric into 120x120 mm square sheets and then submerged in a SiC slurry bath of the desired composition. The wet fabric was then rolled twice through a modified pasta sheet maker (Lakeland, UK), which applied a uniform pressure in either side of the fabric removing the excess slurry and uniformly distributed the slurry across the squares. The rolled squares were then transferred to a cutting mat upon and four circular discs were cut from each of the squares. The cut out discs were then stacked in a random orientation to form a cylindrical shape. This process was repeated five times to produce 20 plies thick, 55 mm diameter samples.

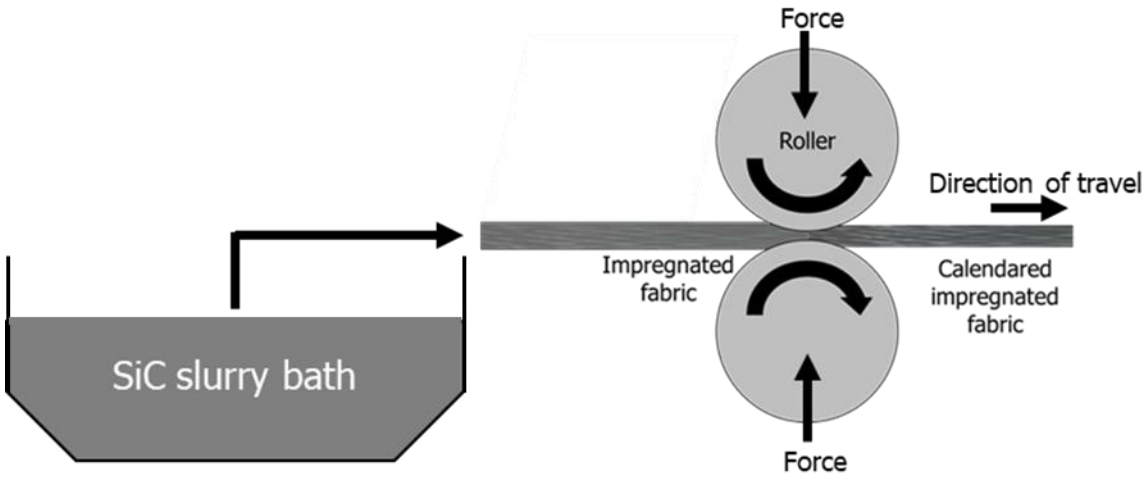


Figure 3.11. Schematic of the calendaring process showing the decreasing saturation of SiC fibre with SiC slurry.

Vacuum bagging (VB) was then used to consolidate and dry the SiC slurry in the 2D SiC fabric plies to fill any macro porosity that remained in the preform when laid up. This technique was found to be the most effective route for CMC preform production due to its ease of use, speed and effectiveness in creating dense preforms as per [16]. The alternative route to this was electrophoretic infiltration, which can provide uniform powder distribution in the inter-tow porosity. However, it is also reported in the literature that preforms produced were "particularly weak and delaminate easily during handling" a property that is highly undesirable to industry so was therefore excluded from preliminary trials.

To create the vacuum bag, a folded over polypropylene sheet, three times the width and length of the sample, was prepared and sealed along the edge length with manufacturing grade vacuum gum approximately 25 mm in from the edge of the bag. The different accessories were then arranged inside, see figure 3.12.; from the bottom upwards toward the valve they included: a breather cloth, perforated

polyester release film, impregnated SiC fibre sample, another perforated release film, another breather cloth, perforated aluminium plate and then another bleeder cloth. The number of layers of bleeder cloth required was dependent on the slurry's viscosity; the lower the viscosity the more slurry was likely to flow out the composite when the vacuum was applied so bleeder fabric was needed to prevent slurry getting into the vacuum pump.

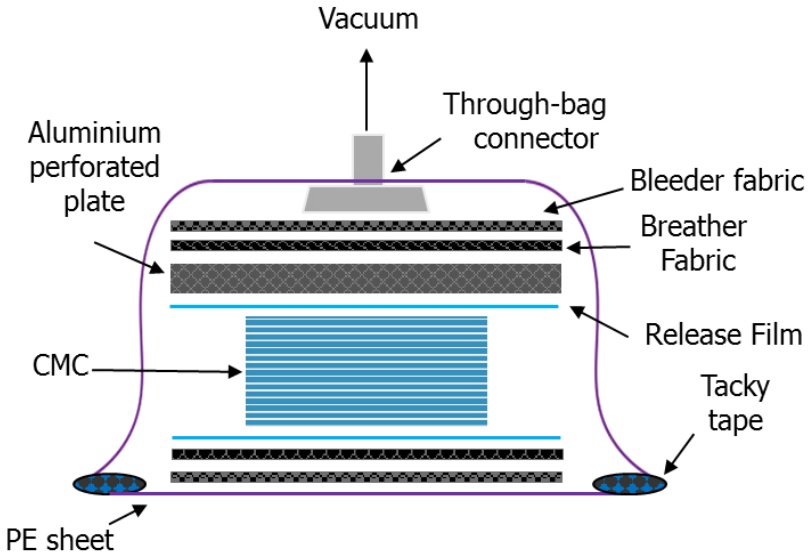


Figure 3.12. Schematic of vacuum bagging arrangement used to impregnate SiC fabric with an aqueous SiC slurry.

Once the fabric was impregnated and the discs cut out they were stacked on top of one another then the impregnated SiC preform was placed in the vacuum bag and sealed in by pressing the bag into the gum. The bag was carefully placed into an oven at 50°C to help the drying process and a rough vacuum, ~100 mbar, applied for 4 h. The vacuum removed the air within the preform and bubbles in the slurry and applied an isostatic pressure spreading the slurry uniformly between the SiC fabric ply, see figure 3.12. This created a silicon carbide fibre, silicon carbide powder preform, SiC_f/SiC_p, with the silicon carbide CVI matrix composite to be added at the next stage.

3.2.3. MCVI Procedure

3.2.3.1. *Loading the sample into the cavity*

SiC fibre preforms were loaded into the MW cavity in-between two 25 mm thick Al_2O_3 foams (>99% pure, Selee Corp., USA) with a TD of 18% and cut into 70x70 mm squares with a ~14 mm hole drilled into the middle. The holes in the foams were aligned with the lasers of the pyrometers so the samples' surface temperatures could be measured, figure 3.4. The foams were highly porous, approximately 12 pores per cm, and were used to increase susceptor size and prevent excessive heat loss. The foams with the sample in-between were placed on top of a vertical quartz tube (Quartz Scientific, UK). A quartz bell jar (Quartz Scientific, England) was then positioned over the sample sitting on a large O-ring creating a controllable atmosphere. Quartz had to be used as it is effectively transparent to microwaves and has a negligible loss factor.

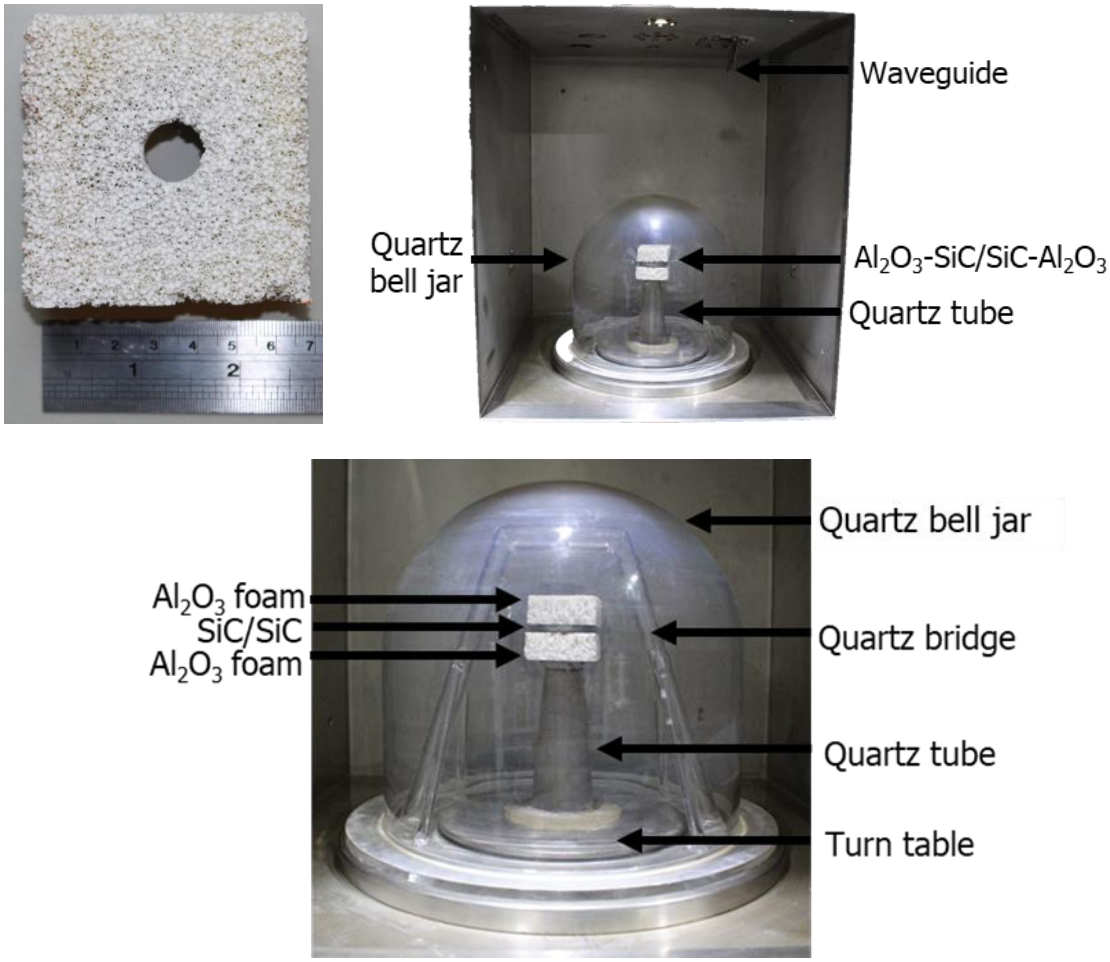


Figure 3.13. Image of the Al_2O_3 foam used and the setup of the cavity, in later experiments a quartz bridge was used to modify flow this is described in more detail in section 4.1.1.2.

3.2.3.2. *Purging the microwave chamber*

As detailed in section 3.1.2, the vacuum was first generated using the LRP and then amplified to the final vacuum using the booster pump. Initially, the chamber pressure was set to 0 mbar on the controller and the system left to equilibrate at the minimum stable value achievable, typically <5 mbar. The insulated heating line to the microwave was switched on and set to 300°C. A leak test was then performed to observe the vacuum integrity if the leak rate was less than 0.2 mbar min^{-1} the experiment could proceed. Ar was then introduced to the bell jar at a rate of 2000 cm^3 min^{-1} and backfilled to 500 mbar before being evacuated again. This process was repeated three times. Once completed, the same procedure was carried out

using H_2, totalling six purges. Finally, the chamber pressure was set to the desired value and flushed with hydrogen for a further five minutes. All these actions were controlled by the gas delivery system seen in figure 3.14.

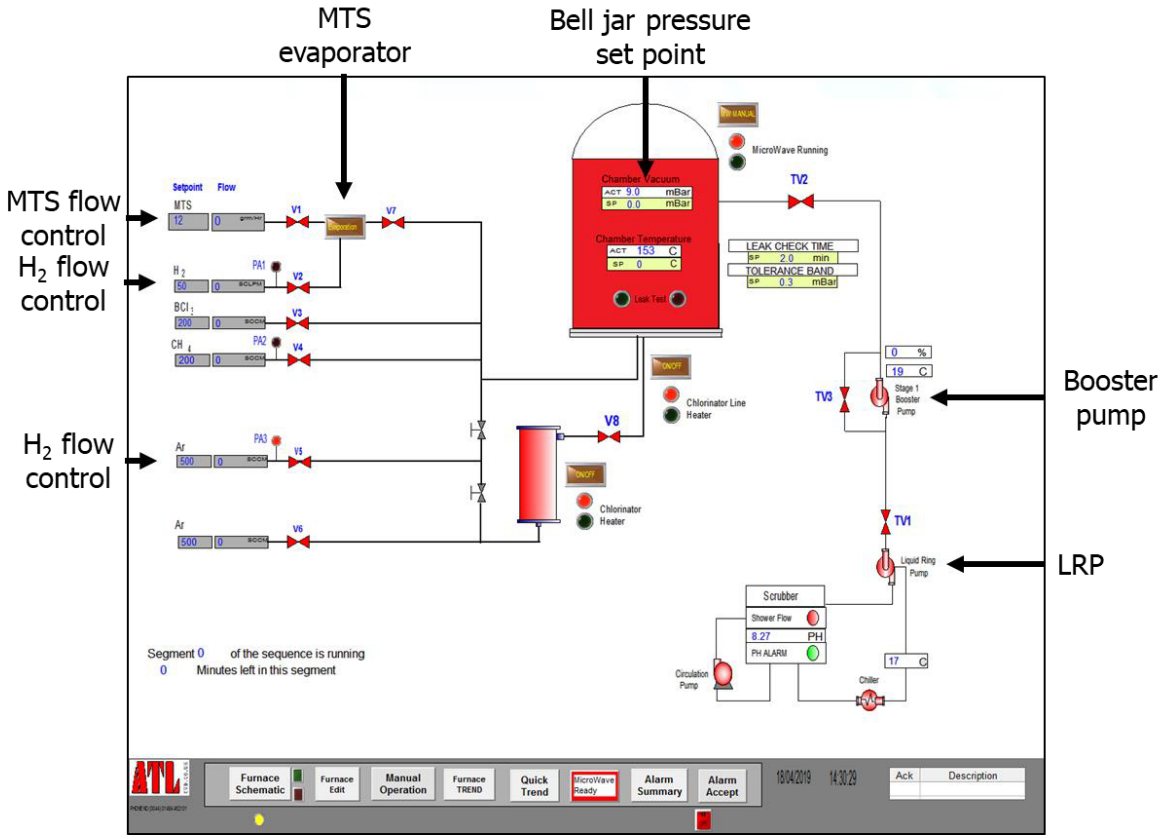


Figure 3.14. Gas delivery system control panel, where gas flow rates, pressure and pumps could be controlled.

The turntable in the microwave chamber was switched on and the E and H field manual tuning wands positioned to zero. The microwave power interlock then activated and the power on the MW control panel was set to an initial value of 0.5 kW and switched on.

3.2.3.3. *Microwave heating*

Both manual and automatic tuning were used to reduce the reflective power and maximise the forward power that was supplied to the sample, whilst keeping the density of the field as low as possible, <20%, see figure 3.15. Power supplied was

increased incrementally in steps of 0.05 kW when the temperature was perceived to have stopped increasing. Each of the samples took between 10-20 min to reach the target temperature; this was highly dependent on the sample construction and the power supplied. The process required constant monitoring to retune the microwave applicator to minimise reflections and hence keep the sample at the desired temperature, typically between 900-950°C. This was made more difficult due to SiC's dielectric properties changing with temperature. Once the target temperature was achieved, it was left to stabilise at the set point temperature for 5 minutes before the MTS vapour was introduced. The gas flow was also reduced from 2000 cm^3 min^{-1} to the typically 300 cm^3 min^{-1}.

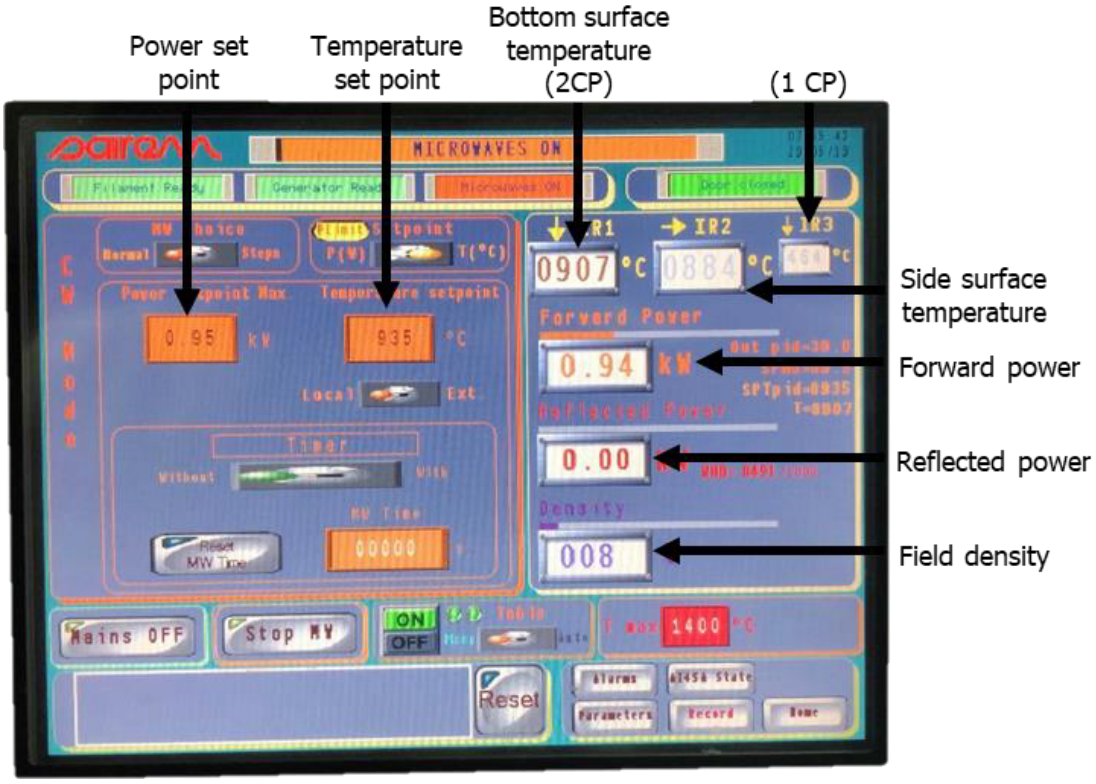


Figure 3.15. Labotron control panel for operating the microwave generator unit.

3.2.3.4. *Infiltration of the SiC preform*

Once the temperature was stable, the MTS was introduced at a specified flow rate and ratio. It was quickly established that the introduction of reactants caused a drop in temperature after five minutes so the power usually had to be increased by ~0.1 kW or the E/H wands repositioned to continue the heating. Samples were typically infiltrated for different periods of 2, 4, 8 h; experiments could be carried out for a maximum of 8 h due to health and safety regulations at the University preventing overnight work. The infiltration time did vary for some samples depending on the parameters being used that made some infiltrations not possible, which will be discussed in section 4.1.1.1. Table 3.3. Reports the range of preforms infiltrated by MECVI in this experimental work with the conditions of the infiltration.

Table 3.3. List of the SiC_f preforms infiltrated and the respective infiltration used. The dimensions of all the samples were 55x8 mm. Thick black line indicated the switch from temperature and pressure as independent variables to alpha.

Sample	T / °C	P / mbar	Q / g min^{-1} and cm^3 min^{-1}	Alpha	t / h	no. of ply
1	900	300	MTS = 0.2 H_2 = 300	10	8 h (**2**+**2**+**4**)	20
2	900	500	MTS = 0.2 H_2 = 300	10	8 h (**2**+**2**+**4**)	20
3	900	700	MTS = 0.2 H_2 = 300	10	8 h (**2**+**2**+**4**)	20
4	950	300	MTS = 0.2 H_2 = 300	10	8 h (**2**+**2**+**4**)	20
5	950	500	MTS = 0.2 H_2 = 300	10	8 h (**2**+**2**+4)	20
6	950	700	MTS = 0.2 H_2 = 300	10	8 h (**2**+**2**+4)	20
7	1000	300	MTS = 0.2 H_2 = 300	10	8 h (**2**+**2**+**4**)	20
8	1000	500	MTS = 12 H_2 = 300	10	8 h (**2**+**2**+4)	20
9	1000	700	MTS = 0.2 H_2 = 300	10	8 h (**2**+2+4)	20
10	925	400	MTS = 0.2 H_2 = 150	5	8 h (**2**+**2**+**4**)	20
11	925	400	MTS = 0.2 H_2 = 300	10	8 h (**2**+**2**+**4**)	20
12	925	400	MTS = 0.2 H_2 = 750	25	8 h (**2**+**2**+**4**)	20
13	925	400	MTS = 12 H_2 = 2000	70	8 h (**2**+**2**+**4**)	20
QB	925	400	MTS = 0.2 H_2 = 2000	70	8 h (**2**+**2**+**4**)	20
n.d. The time values that have been bolded represent the actual infiltrations time that was used, details for this can be found in section 4.3.1.						

3.2.3.5. *Cooling and terminating an infiltration*

Once an infiltration was completed, the MTS precursor gas flow was stopped but the microwave left on, so the sample was heated at the same temperature for a further 15 min to remove and react any residual MTS in the cavity. The microwave was then switched off and a cold purge was carried out in flowing argon for a further 15 min at 2000 cm^3 min^{-1} whilst the pressure of the vessel was incrementally decreased to a 10 mbar. Once completed, the sample was cooled down to room temperature and

the cavity was brought to atmospheric pressure before the bell jar was removed and the sample was taken out. Between each infiltration run, the sample's mass was recorded and change in porosity calculated. After each infiltration, the system was purged with argon and bell jar cleaned with deionised water before the next run could be undertaken. The consequences of this approach will be discussed in section 4.1.3.3.1.

3.2.3.6. *Issues encountered during MCVI experiments*

The highly corrosive precursors and by-products of the CVI process caused a number of breakdowns of essential pieces of equipment. Components that were most susceptible were the two pumps, which despite regular cleaning suffered three breakdowns due to corrosion. This was improved by the addition of NaOH cleaning lines, which prevented the build-up of corrosive pyrophoric powders, and limiting, as much as possible, oxygen exposure. The corrosion of metallic components was not limited to the pumps, the turntable and pipework sustained prolonged attack as well. Other factors that prompted redesign was the deposition of a fine white film on the dome surface of the bell jar, see figure 3.16. It was found this film was not transparent in the infrared range and subsequently effected the measurement of the two colour pyrometer, which was originally mounted alongside the 1CP, an effect also seen in a European project [327]. This effect was only observed after approximately 2 h as the film reached a critical thickness. This effect was verified by moving the side pyrometer beneath the sample, which recorded a >300°C difference which increased as the forward power was increased. Energy-dispersive X-ray spectroscopy of this compound found it was likely to be Si_xOCl_x [328, 329] from the

reaction of residual oxygen and Si_xCl_x species and which condensed on the cooler top surface of the bell jar.

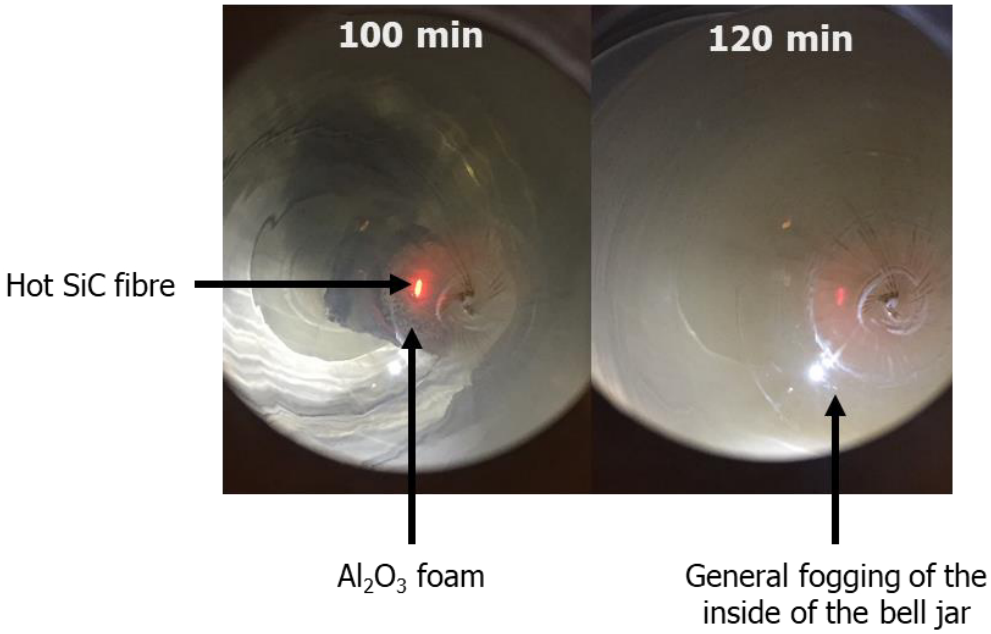


Figure 3.16. Photographs showing the development of the SiO_xCl_x layer on the top of the inside surface of the top of the bell jar after 2h.

Oxygen contamination was a persistent issue. Its presence interfered with the chemistry of the deposition process by forming silica, thus lowering the yield and affecting the microstructure of the deposit. D'Angio [243] also reported that since the SiO_2 formation from MTS is an endothermic process, the effect, which was observed in the first five minutes of infiltration and led to a decrease in temperature as the residual oxygen in the bell jar was consumed by the MTS, figure 3.17.

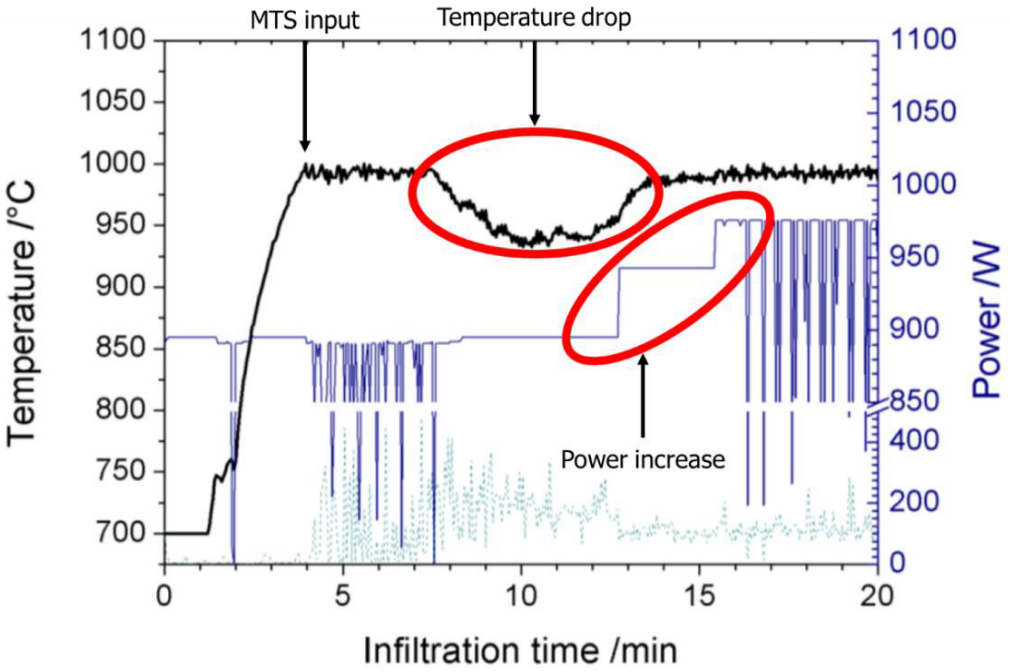


Figure 3.17. Adapted from [250] showing the decrease in temperature after MTS is introduced into the reaction vessel and the power increase needed to regain the lost temperature.

Another issue related to heating of the SiC fibres in a microwave field was arcing, which made heating very difficult at times. The formation of the discharge is described by Paschen's law, which determines the voltage necessary to initiate an electric arc between two electrodes in a gas as a function of pressure and gap length [29], equation 3-1.

Equation 3-1 $$V_B = \frac{A_i P\, d}{\ln(Pd + B_{ei})}$$

Where: V_B = Voltage breakdown / V

P = Pressure / Pa

d = Gap distance / m

A_i = Constant: Saturation ionisation at a particular E/p (electric field/pressure)

B_{ei} = Constant: Excitation and ionisation energies

Differentiating with respect to V_B and making the derivative equal to zero, a minimum voltage can be calculated for a specified distance, given by equation 3-2;

Equation 3-2 $$\mathrm{Pd} = e^{1-B}$$

It can be demonstrated using the above equation that when the pressure-distance (Pd) ratio decreased, so did the minimum voltage that was required to create an arc, figure 3.18. Measurements of the distance between individual fibres in a tow were made using a scanning electron microscope and were found to be typically between 200-250 µm. Factoring this into Paschen's equation showed that these gap distances were small enough that at pressures between 0-150 mbar, the minimum threshold voltages were achieved. This meant that a higher pressure, >300 mbar, was needed to be used since creating larger distances between fibres was not possible.

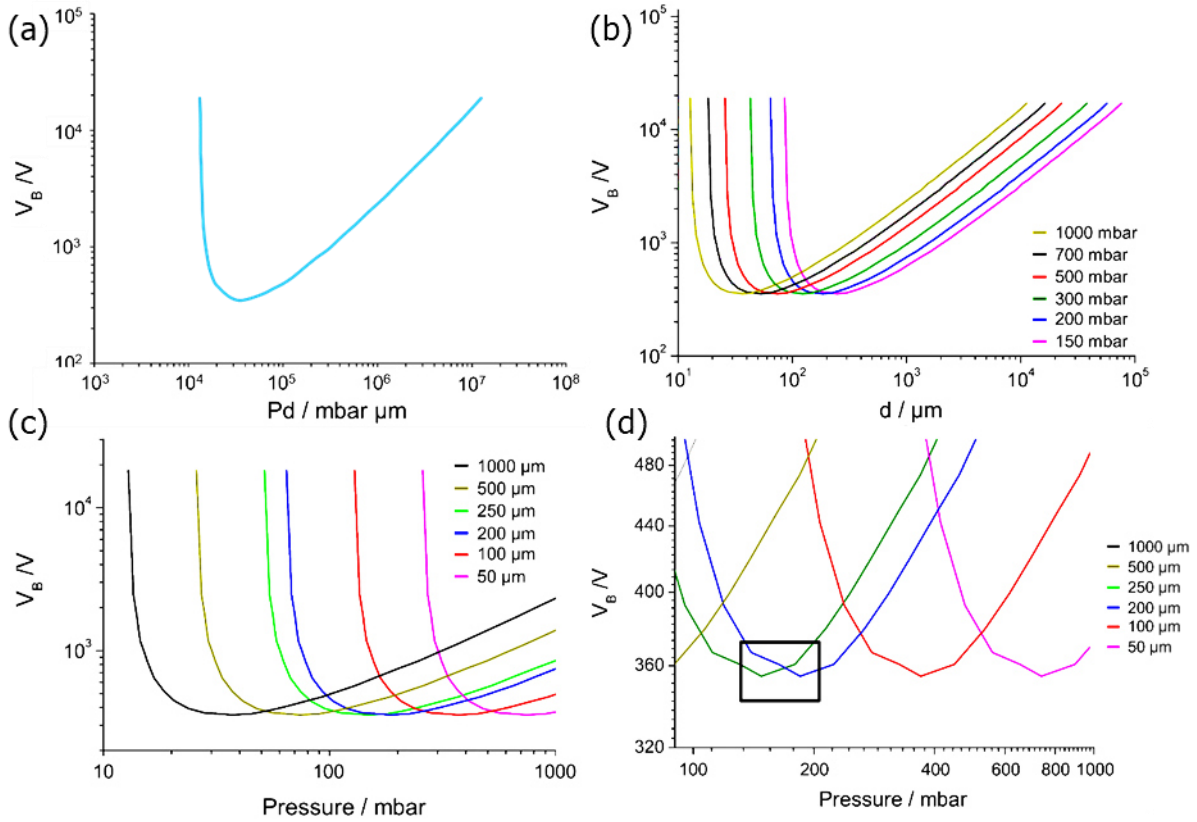


Figure 3.18. Paschen's curve in a hydrogen environment illustrating the relationship between the pressure and electrode distance on the threshold of the breakdown voltage, (b) showing the minimum spacing between electrodes as pressure changes, (c) a graph illustrating the minimum operating pressure for a given set of electrode separations, and (d) magnified

images of a graph (c) showing the separation distance between fibres observed via SEM and the corresponding minimum pressure.

3.3. Characterisation

3.3.1. Impregnation evaluation

After preliminary trials, a number of physical requirements for an impregnated SiC_f/SiC preform were established. Section 3.3.1 details how these objectives were characterised; the requirements were as follows:

1. Physically robust and does not delaminate when handled.

2. Has a maximum pore size of no more than ~400 μm.

3. Allows a uniform slurry distribution to form between the plies.

4. Achieves a final green density of >30%, but retains a high permeability.

5. Avoids intra-tow infiltration, since the presence of SiC particles within the tows damages the fibres.

3.3.1.1. *Particle size analysis*

All commercial SiC powder size distributions were analysed to ensure the powders were not agglomerated, of the correct distribution and not contaminated before making the slurry. After dry ball milling for a minimum 4 h with alumina milling media, the different SiC powder's particle size was measured using the laser diffraction method (H0972 HELOS, Sympatec, Germany). Software on the equipment produced a cumulative size distribution, density distribution and calculated the specific area and volume. Each powder was tested three times with thorough rinsing of the sample vessel carried out between each test with deionised water to prevent sample-to-sample contamination.

3.3.1.2. *Room temperature slurry viscosity measurements*

SiC slurries were prepared using the method outlined in section 3.2.2. 30 ml samples were prepared with an initial range of solids content between 10-35 vol.%, which was initially tested. This was then down selected from processing observations to a range between 20-25 vol.% in increments of 2.5%. Samples were tested using a rheometer (Micromeritics AR500, TA Instruments, US) with a plate geometry and solvent trap to prevent the slurry drying too much during the tests, particularly at higher solids content. Approximately 6.2 ml samples were placed onto the test fixture using a 10 ml syringe. Samples were tested up to a shear rate of 500 s^{-1} and then back to 0 s^{-1} with the shear stress being measured and the viscosity then calculated as according to equation 3-3, where μ is viscosity / Pa s, τ = shear stress / Pa and γ is shear rate / s^{-1}.

Equation 3-3 $$\mu = \frac{\tau}{\Upsilon}$$

3.3.1.3. *Contact angle measurements*

A sessile drop test was used to measure contact angle at a solid/liquid interface between a SiC substrate and the SiC slurry. 0.6 ml of SiC slurry was dropped onto a polished SiC substrate using a 1 ml syringe, a backlit photo was then taken of the drop using a camera with a macro lens. SiC slurries, were used in the sessile drop test to compare their wetting characteristics over a four-minute period. Images were captured at t=0 , t = 2 and t = 4 min, to see the effect of time on the spreading and contact angle. This process was repeated three times for each slurry and a mean

contact angle was then calculated at each time using the angle measurement function on ImageJ [330].

3.3.1.4. *Relative density calculation of impregnated preform*

The samples' thickness and diameter were measured using Vernier callipers with three measurements made for each dimension before calculating the mean value. The volume fraction of powder matrix (V_m) and fibre fraction (V_f) of each preform was calculated from the samples' dry fibre mass (M_i), see equation 3-4 and equation 3-5, impregnated dried mass (M_f) and the volume of the sample (V_s). The density of the Tyranno ZMI fibres used was 2.48 g cm^{-3}, with a powder density of 3.21 g cm^{-3};

Equation 3-4 Volume fraction of fibres:

$$V_f = \frac{M_i}{V_s \ \rho_f}$$

Equation 3-5 Volume fraction of powder matrix:

$$V_m = \frac{M_i - M_f}{V_s \ \rho_m} = \frac{\Delta M}{V_s \ \rho_m}$$

Equation 3-6 Theoretical density of composite:

$$\rho_C = V_f \rho_f + (1 - V_f)\rho_{SiC}$$

Equation 3-7 Relative density:

$$\rho_r = V_f + V_m$$

Equation 3-8 Porosity:

$$\Phi_v = 100 - (V_f + V_m)$$

3.3.1.5. *Porosity measurements of slurry impregnated composite*

Reducing the size of the pores is the fundamental aim of the CVI process, therefore quantifying the filling of said pores is essential. Large pores are very frequent in non-impregnated SiC_f/SiC samples, however, they were partially filled by the addition of a SiC slurry which aimed to reduce the time required to completely fill the porosity using CVI. Porosity measurements on the SiC_f/SiC_p samples were carried out using a

MATLAB [331] script and verified using ImageJ. The script detected the contrast difference between fabric tows and pores in images produced via micro-computed tomography (micro-CT). The script then calculated the area of these pores in pixels, the total number of pores and a number of other parameters; more detail is provided in section 3.3.5.2.

3.3.1.1. *Gas permeability of composites*

One of the primary parameters of the preforms produced that needed measuring was their permeability to gas. They needed to be permeable to allow the precursor gases to penetrate them, make contact with the maximum surface area and provide them with the opportunity to decompose and deposit SiC. Whilst beneficial overall, adding the slurry to the composite reduced the volume of pathways the precursors could traverse. Furthermore, preforms with a low permeability after the powder had been added would potentially contain some closed porosity, which could not be accessed by the reactant gases and so would reduce densification. To be able to quantify the permeability of the preform, simultaneous measurements of the backpressure generated and the flow rate of the gas through the material were needed. This is the principal of Darcy's Law, which describes the relationship between backpressure and flow rate through an incompressible porous medium and is given by equation 3-9;

Equation 3-9
$$\frac{\Delta P}{L} = \frac{P_i - P_o}{L} = \frac{\mu V}{k}$$

Where k = Darcian permeability constant / m^2

P_i and P_o = Pressure at the inlet and out let, respectively / Pa

ΔP = Pressure difference across medium / Pa

μ = Fluid viscosity / Pa S

L = Thickness of medium / m

This can be simplified to equation 3-10:

Equation 3-10 $$k = \frac{Q\mu L}{A(\Delta P)}$$

Where Q = Flow rate / $cm^3\ min^{-1}$

A = Area of the medium / m^2

At the time of writing, there is no standardised direct method for measuring the permeability of fibre reinforced CMCs. After an extensive multidisciplinary literature review, a test rig was built based on designs from [332, 333]. This enabled permeability measurements to be made to quantify the effect of impregnation on the preform's permeability [334]. Validation of the rigs capability was carried out using 64 g m^{-2} paper and results were compared to results reported in [191].

A SiC preform was placed between two custom epoxy washers with an O-ring (45 mm ID x 5 mm thick CS Nitrile 70 ShA, Polymax, UK) glued to the top of the bottom washer, see figure 3.19. These were used to prevent damage to the sample occurring during positioning and removal. The edges of the washer were coated with vacuum grease to prevent radial airflow out of the preform's edges inside the transparent PVC pipe that was 55 mm in diameter. An aluminium honeycomb with a 6.4 mm cell size (Easy Composites, UK) was positioned directly above the inlet and its edges sealed with silicone paste to promote laminar gas flow inside the tube. Two conical frustum shaped rubber bungs (RB053, Hilltop, UK) with two holes machined

into the top, one central and the other offset by 1 cm from the centre, were positioned at the top and the bottom of the PVC pipe, respectively. The central holes were the gas inlet and outlet, one was connected to an argon supply (The BOC Group Plc, Manchester, UK) via a gas flow metre (1000-10000 cm^3 min^{-1} airflow metre, Cole-Parmer, UK) and the other vented the system to an LEV. The two offset holes were connected to a differential pressure meter (Kane 3500-1, Kane, UK), which measured the pressure difference between the inlet and outlet.

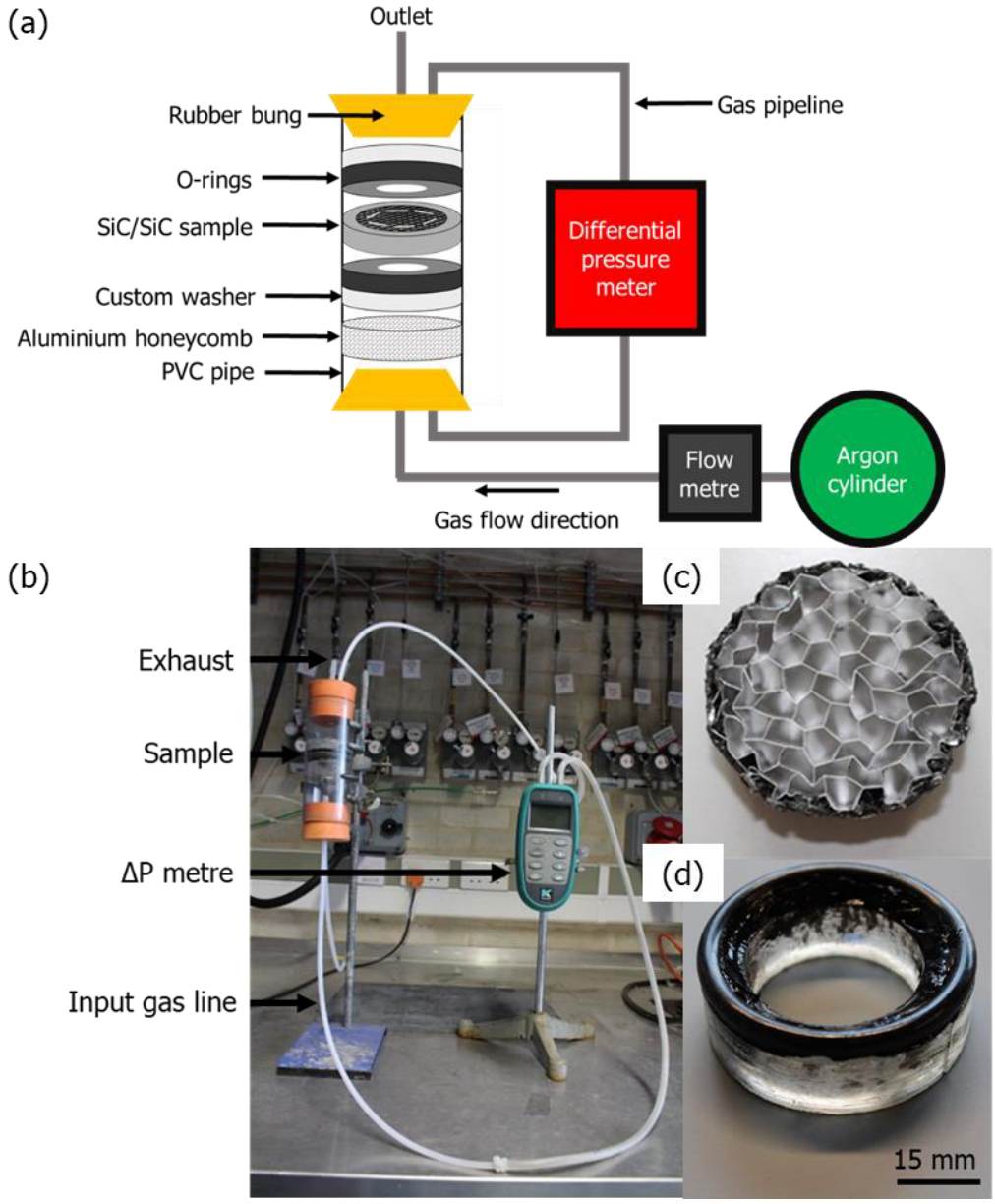


Figure 3.19. (a) schematic and (b) photograph of the permeability equipment constructed and used in its entirety and the two key components; (c) the aluminium honeycomb and the (d) epoxy washer.

3.3.2. Microscopy

3.3.2.1. *Sample preparation*

Impregnated and infiltrated SiC fibre preforms were embedded in epoxy resin (Epofix Resin, Struers Ltd., UK). The samples were then sectioned using a 0.6 mm diamond-tipped cutting wheel (Metprep Ltd., UK) and then ground and polished to a mirror finish using 1 µm diamond suspension (DiaDuo-2, Struers, UK). Samples were initially mounted in a 60 mm container, then cut in half and sectioned into approximately 20 mm-sized sections to be remounted in smaller 30 mm containers, which had to be used for the auto-polishing system. A typical polishing routine to prepare the samples started with an 80-grit grinding disc for 2 min, progressing to a 220-grit for 4 min then 500-grit for 6 min and completing the grind with 8 min at 1200-grit with the same magnitude of pressure applied for the whole process. This was then followed by the polishing stage starting with a 9 µm diamond suspension through to 1 µm with time, again, increasing linearly as the suspension particle size decreased in increments of 3 µm. Between each polishing stage samples were degreased and washed with deionised water in an ultrasonic bath. After the final step, the samples were cleaned with ethanol in an ultrasonic bath for 10 min to remove any surface contaminants that might remain.

3.3.2.2. *Optical microscopy*

An optical microscope (AxioScope A1, Carl Zeiss Microscopy GmbH, Germany) fitted with a 14 M pixel camera, capable of automatically scanning the entire cross-

sectional surface of a preform's (55 mm) diameter was then used to analyse the densification profile. The microscope and its software took approximately 500 images at a magnification of 5x and then stitched the images together using its mosaic function based on a 10% overlap of each photo to create a macroscopic image.

3.3.2.3. *Scanning electron microscopy*

Specimens were coated with an approximately 20 nm layer conductive layer of either gold, chromium or carbon depending on the observations that were being carried out, using a rotary-pumped plasma sputter coater (Q150R ES, Quorum Technologies Ltd., UK). Various SEMs were used to carry out the analysis of the cross-sections of the samples. For lower magnification images, a JEOL 6060 was used; for imaging greater than >2000x it was the XL30 ESEM-FEG (Philips, Netherlands) and for higher magnification images, >15000x, a JSM-7000F (JEOL USA Inc., Massachusetts, USA) was used. Secondary (SE) and back-scattered electron (BSE) imaging were used to observe the deposited silicon carbide. Scanning conditions were typically in the range of 15-20 kV with a working distance of 10 mm. For higher magnification imaging, the acceleration voltage and working distance was decreased and both were equipped with chemical analysis capabilities as well.

3.3.2.4. *Energy-dispersive X-ray spectroscopy (EDS)*

EDS was used to evaluate the stoichiometry of the SiC formed and the quantities of other elements present in the deposit. Due to the small quantities of the SiC deposit around the fibres in some regions, especially within the fibre bundle, a lower accelerating voltage was used in cases where the deposit was sufficiently thin to

reduce the interaction volume and reduce measurement error from fibres interaction. At an acceleration, voltage of 10 kV the interaction volume for SiC corresponded to a penetration depth of ~0.5 μm and a hemisphere of ~1 μm in diameter. These values were calculated from the Thomson-Whiddington law for calculating the average energy of penetrating electrons into a medium [335]:

Equation 3-11 $$\mathrm{E_p^2} = \mathrm{Ep_0^2} - b_x \rho \mathrm{x} = b_\rho \, (R_p - x)$$

Equation 3-12 $$x = R_p - \left(\frac{E_p^2}{b\rho}\right)$$

Where: E_p = Electron residual energy

E_i = Target ionisation energy / eV

b_x = Constant – 6.2×10^{11} / eV g^{-1} m^2

x = Penetration depth / m

E_{p0} = Incident primary energy / eV

R_p = Primary range of electrons/ eV

ρ = Density / g m^{-3}

3.3.2.5. *Wavelength-dispersive X-ray spectroscopy*

Wavelength-dispersive X-ray spectroscopy (WDS) was used to quantify the composition of the SiC deposit. WDS has a higher spectral resolution than EDS as it counts X-rays from a single source at a time, rather than collecting a broad spectrum of wavelengths. Moreover, its ability to quantify lighter elements such as carbon with a greater degree of accuracy was considered particularly important. A semiconductor grade transparent polished SiC sample was used as the reference standard. Standardisation was carried out every time the microprobe was used. However, the

processing time per measurement using the WDS was approximately an order of magnitude great than EDS, as it required greater computational resources, which meant it was used primarily for validation of EDS results. Another drawback of the WDS process was the larger interaction volume, relative to EDS, which was typically 3 µm in diameter so the risk of fibre interaction with the measurement was much greater.

3.3.2.6. *Transmission electron microscopy*

Crystallographic analysis of the SiC deposit was performed to observe features of the grain growth process, orientation and texture. Three TEMs were used to carry out this analysis: JEOL JEM 2000FX (JEOL Ltd., Japan), FEI Phillips TECHNAI F20 (ThermoFisher Scientific, US) and Talos F200X (ThermoFisher Scientific, US). Observations of the grain morphology and crystal subsets characteristics were made using both the bright field and dark field imaging modes, respectively. Corresponding diffraction patterns of the Bragg-reflecting orientations were taken using the selected area diffraction modes (SAED) to observe the crystal structures. High-angle annular dark-field (HAADF) analysis was also used to observe the compositions of the deposit. TEM samples were prepared and analysed at the Air Force Research Laboratory (AFRL), Wright-Patterson Air Force Base, OH, USA, courtesy of Dr. Pavel Mogilevsky.

3.3.3. X-ray diffraction analysis

X-ray diffraction (XRD) was carried out on a D8 Advance (Bruker, Germany) with a monochromator with the help of Dr Ji Zou. Cu Kα radiation with a wavelength of 0.154 nm was used in a Bruker diffractometer, and no filter was used. Generator

settings were 40 kV and 40 mA and data was collected between 20° and 80° with a step size of 0.02° and a 1 s dwell. Scans were carried out on samples that had been polished as if for microscopy analysis, but not etched. XRD data was then evaluated using the Match software [336]. Spectra produced were smoothed, had the background signal and the contribution of $K\alpha^2$ removed and peaks selected using the automatic peak fitting function built into the software. Scans were taken first of the resin material, then the fibre material and then the MCVI SiC composite. The first two spectra were subtracted from the latter to allow for specific observations of the deposited SiC crystal structure. It was found that scanning the composites perpendicular to the ply direction yielded a greater intensity signal than is the parallel direction, see figure 3.20.

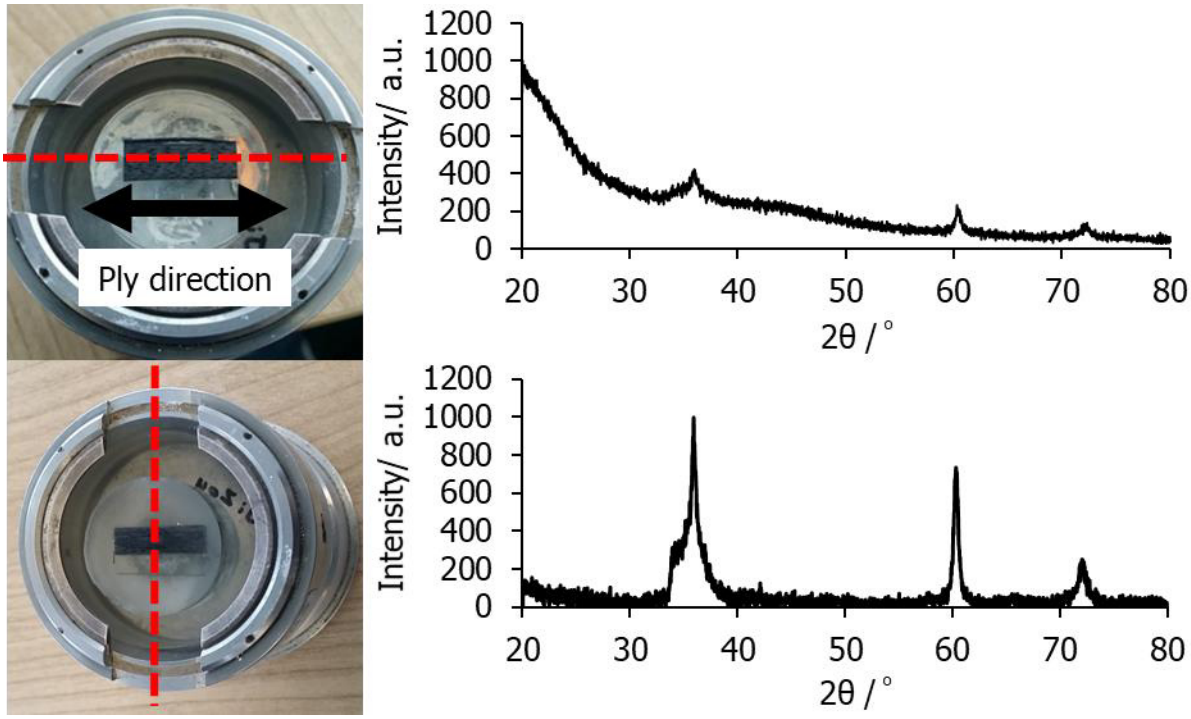


Figure 3.20. Corresponding XRD diffractograms demonstrating the scanning orientation effect on the signal intensity. Red dashed line corresponds to the orientation.

3.3.4. Raman spectroscopy

The Raman spectrometer assessment of the fibres and deposit was carried out using an InVia™ Qontor confocal Raman microscope (Renishaw, UK). Using the red 532 nm laser with an 1800 l/mm diffraction grating, a calibration was carried out on a silica substrate to ensure the laser was correctly aligned using Wire™ 5.1 software [337]. Calibration of the laser alignment onto the charge-coupled device (CCD) detector and slits were then performed. Initial measurements were made to establish the optimum laser power, exposure time and objective lens to minimise the noise in the measurement. Using the video facility-specific regions of deposit could be selected and evaluated over a range of 100 cm^{-1} to 3200 cm^{-1}.

3.3.5. Micro-computed tomography

3.3.5.1. *Scanning of SiC_f/SiC samples*

X-ray micro-computed tomography (micro-CT) is a 3D imaging technique that uses X-rays to capture a stack of 2D planar images. These slices can be processed to reconstruct 3D models to provide information of internal features and volumetric information about the microstructure, non-destructively. Impregnated and non-impregnated preforms were scanned using an XT H 225 (Nikon Metrology, UK) to evaluate the porosity distribution inside the preforms. The system was fitted with an X-ray source that had a maximum current and voltage of 1 A and 225 kV; typically 0.05 A and 180 kV were used. The CCD resolution was 2300x3200 pixels, leading to a minimum resolvable resolution of 4-6 µm. The scanning process used 1800 projections through 360° and took four frames per projection, from which it calculated an average. Shading correction was also carried out. Once the scan was

complete, reconstruction was achieved using CT pro 3D, where parameters such as the centre of rotation, beam hardening and noise reduction could be altered. This data was then extracted to VG studios where post-processing was undertaken.

3.3.5.2. *Image analysis*

From the reconstruction, an image stack was created of the through-thickness of the scanned sample. This produced a stack of images, typically 1200, that were spaced 20 µm apart. This value of slice separation was selected based on deposition rates in the literature that showed 20 µm pores are filled by CVI relatively easily [338, 339]; therefore, resolution of the stack, in terms of slice separation, was sufficient to capture all large pores that CVI might not fill. These images were then cropped in ImageJ to reduce the total file size and processing time. Calculations were then to crop the image stack so the largest cuboid that could possibly fit inside the sample's volume was selected. This was very important in terms of understanding the pore size distribution, which would provide an invalid result if the MATLAB script were to measure a cylindrical volume. This is because $slice_X$ and $slice_Z$ in figure 3.21. are much smaller volumes and therefore have fewer pores than $slice_Y$, resulting in a perceived higher density in the distribution plot.

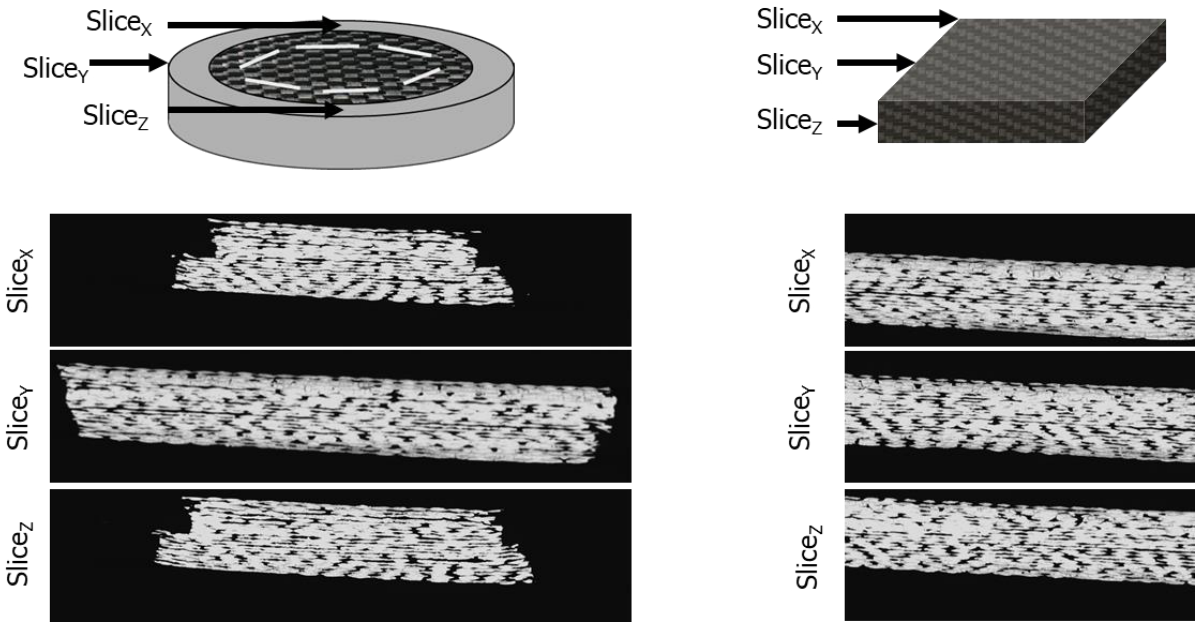


Figure 3.21. Schematics showing the difference in the image stack from a micro-CT scan between a cylindrical volume and a cuboid volume.

Measurements were then made using the thresholding and particle size distribution tools in ImageJ on three randomly selected slices from the image stack. The data from these images were used to calibrate the MATLAB script. Images were then evaluated by the MATLAB script, which used the difference in contrasts to select individual pores before drawing a bounding box around each one using the extrema of the pores to construct the box. The script then calculated the total area of the box in pixels and then subtracted the area of the selected contrast from the total box area to provide the area see in figure 3.22.



Figure 3.22. Example of a single pore selected by the script and the boundary box constructed in 2D.

The script was then developed further to post-process the images to calculate metrics such as average areas, bounding box aspect ratio, standard deviation and number of pores. Use of a threshold value of pore size in the script removed single

pixel-sized pores that were artefacts of the scanning procedure. The threshold that was applied removed any pore that was 64 pixels or smaller, which equates to a 20 μm diameter equiaxed pore. The script also produced a histogram that showed a pore size distribution as a function of the through-thickness of the sample to provide insight into the uniformity of slurry distribution from the vacuum bagging procedure.

3.3.6. Thermal properties

3.3.6.1. *Specific heat capacity measurement using differential scanning calorimetry (DSC)*

The procedure used for the specific heat measurement was derived from ASTM E1269 ratio method [340]. Two identical (Ø=6.8 mm, 85 μl) Pt/Rh crucibles (NETZSCH Gerätebau GmbH, Germany) were cleaned and weighed before the measurement. A baseline empty crucible and a synthetic sapphire reference sample were placed into the differential scanning calorimeter (DSC 404 C, NETZSCH Gerätebau GmbH, Germany). The chambers were then heated to 900°C at 10°C min^{-1} and held for four minutes to establish an equilibrium in a flowing Ar atmosphere (100 cm^3 min^{-1}). This was the maximum temperature used to protect the sensor from platinum-platinum diffusion between pan and sensor that occurs around 1000°C. The baseline and sapphire were then cooled, the powdered fibre sample (± 0.1% the mass of the sapphire standard) placed into the empty baseline crucible after being weighed and the heating procedure repeated. The sensitivity of the measurement was produced by the software in real-time according to equation 3-13.

Equation 3-13 $$E_{DSC} = \left[\frac{b}{60\ D_{st}}\right][M_{st}\ Cp_{st} + \Delta MCp_c]$$

Where E_{DSC} = Calorimetric sensitivity of the DSC apparatus/ μV mW^{-1}

b = Heating rate / °C min^{-1}

D_{st} = Vertical displacement between the sample thermal curve and sapphire thermal curve at a specific temperature / mW

M_{st} = Mass of sapphire standard / mg

ΔM = Mass difference between baseline holder and specimen holder / mg

Post-processing of the data was carried out using Proteus thermal analysis (NETZSCH Gerätebau GmbH, Germany) using the sensitivity calculation produced by the software the specific heat capacity of the sample was calculated according to the following ratio method;

Equation 3-14 $$Cp_s = Cp_{st}\frac{D_s W_{st}}{D_{st} W_s}$$

Where: Cp_s = Specific heat capacity of the sample / J $g^{-1}k^{-1}$

Cp_{st} = Specific heat capacity of the sapphire / J $g^{-1}k^{-1}$

D_s = Vertical displacement between the sample crucible curve and sample thermal curve at a specific temperature / mW

D_{st} = Vertical displacement between the sample crucible curve and sapphire thermal curve at a specific temperature / mW

W_s = Mass of sample / mg

W_{st} = Mass of sapphire / mg

3.3.6.2. *Thermal diffusivity measurement of SiC fibre*

The laser flash apparatus (LFA) was used to measure the through-thickness diffusivity of SiC fibres. A heavily adapted method of ASTM E1641 was used [341]; because of its fibrous morphology, the test specimen required a very specific preparation method, figure 3.23. Short (10-12 mm) lengths of SiC fibre were stacked

and aligned inside a ceramic split ring jig with an internal diameter of 12.5 mm so the fibres protruded 3 mm over the ring. A flat spatula was used to align tows. When enough fibre had been added, the stack of fibres was compressed with the upper anvil. When the fibres stack was nearly fully compressed, the second half of the split ring was placed above the fibre mass and the stack fully compressed. The outer ceramic ring was then placed over the two half rings before the pressure was eliminated carefully by removing the upper anvil. The outer ring and split rings were removed from the jig and the outer ring slid over the two inner rings to make the end surfaces of the rings coplanar by eye. Cyanoacrylate adhesive was then dripped over the fibre mass and rings on both faces to rigidize the entire mass. This required about 0.8 ml of adhesive, which was then left to harden. The excess fibre of both sides of the clamping rings was removed using a diamond saw to prevent damage occurring to the rings. A flat diamond lap was then used to grind both faces of the fibres down to the exact ring thickness. The adhesive was then removed by firing the sample in air at 600 °C for 1 h, no graphite coating was necessary.

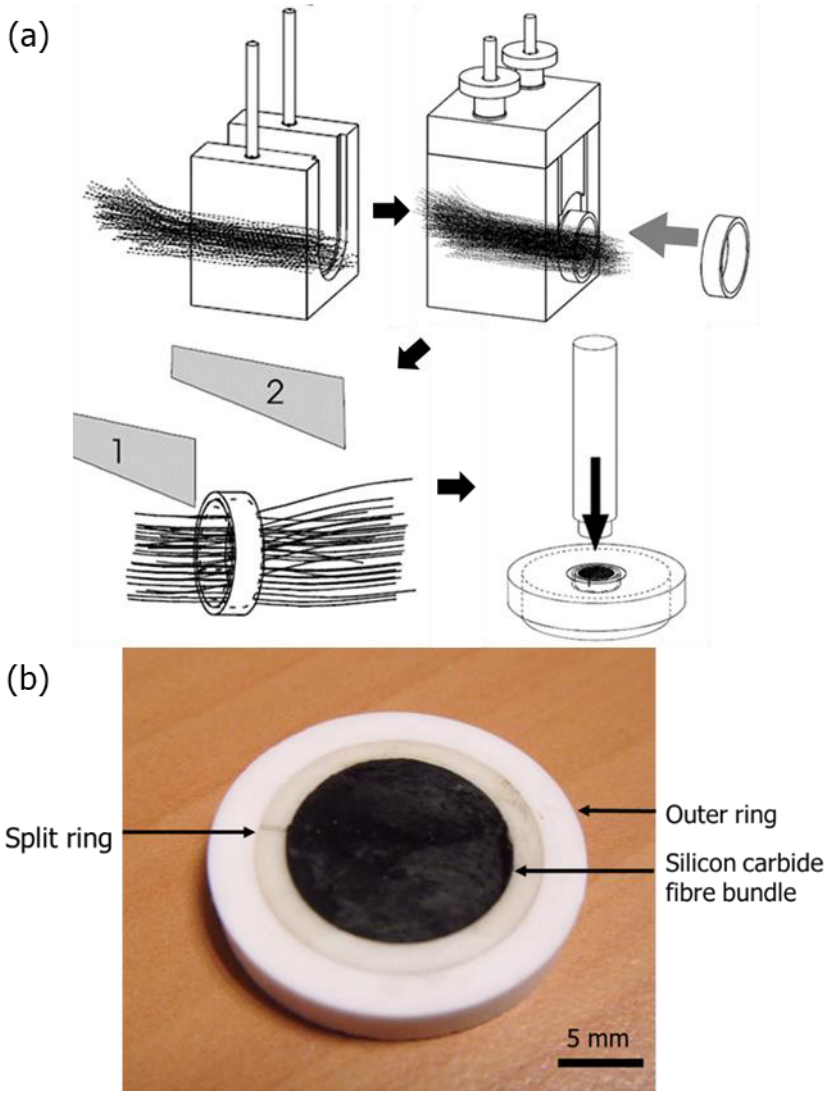


Figure 3.23.(a) LFA 427 fibre sample holder showing four key steps; (from the top left) alignment, compression, cutting and mounting in laser flash [342], (b) showing the fibre sample and the two-ringed arrangement for clamping the fibres.

Thermal diffusivity measurements were carried out at the National physical laboratory (UK) by Dr. Roger Morell. The sample's thickness was measured as 4.5 ± 0.02 mm and from this the packing density calculated as ~50%. The sample was then placed into the column of the LFA (LFA 427, NETZSCH Gerätebau GmbH, Germany) and a vacuum applied before flowing argon was introduced. The laser voltage ranged from 350-450 V and the pulse width of the laser was 0.8 ms. Samples were then heated in increments of 100°C up to 700°C, and at each increment, three

measurements were taken and an average value calculated. Diffusivity was then calculated using the Netzsch LFA measurement and analysis software (V 4.8.1) with the following equation:

Equation 3-15 $$\alpha = 0.13879 \times \frac{L^2}{t_{\frac{1}{2}}}$$

Where: a = Thermal diffusivity / $mm^2\ s^{-1}$

L = Sample thickness / mm

$t_{1/2}$ = Half rise time to reach maximum temperature increase during the laser pulse

Thermal diffusivity was then corrected for CTE using the equation below:

Equation 3-16 $$\alpha_{corrected} = \alpha(1 + \beta \Delta T^2)$$

Where: $a_{corrected}$ = Thermal diffusivity / $mm^2\ s^{-1}$

a = Thermal diffusivity / $mm^2\ s^{-1}$

β = Coefficient of thermal expansion / $°C^{-1}$

ΔT = Change in temperature / °C

From the measurements made in 3.3.6. thermal conductivity was then calculated using literature data on the fibres' density while accounting for the coefficient of thermal expansion.

Equation 3-17 $$\lambda = \alpha\ C_p\ \rho$$

Where: λ= Thermal conductivity / $W\ m^{-1}\ K^{-1}$

α = Thermal diffusivity / $m^2\ s^{-1}$

C_p = Specific heat capacity / kg K

ρ = Density / $kg\ m^{-3}$

3.3.7. Dielectric permittivity measurements of SiC_f/SiC components

3.3.7.1. *High–temperature-dielectric measurements*

Dielectric property measurements were carried out on the SiC powder and SiC fabrics by the Microwave Division at the research institute (ITACA) of the Universitat Politecnica de Valencia (Spain). The equipment, illustrated in figure 3.25., measured both the dielectric permittivity and loss tangent at room and elevated temperatures in a flowing argon environment to prevent oxidation [343]. Samples of SiC fibre were prepared by first removing the sizing and then a combination of cutting, milling and grinding to turn the fabric into a powder. The sample had to fill a 9x15 mm volume (powder) and had to be as densely packed as possible to reduce the impact of porosity on the measurement.

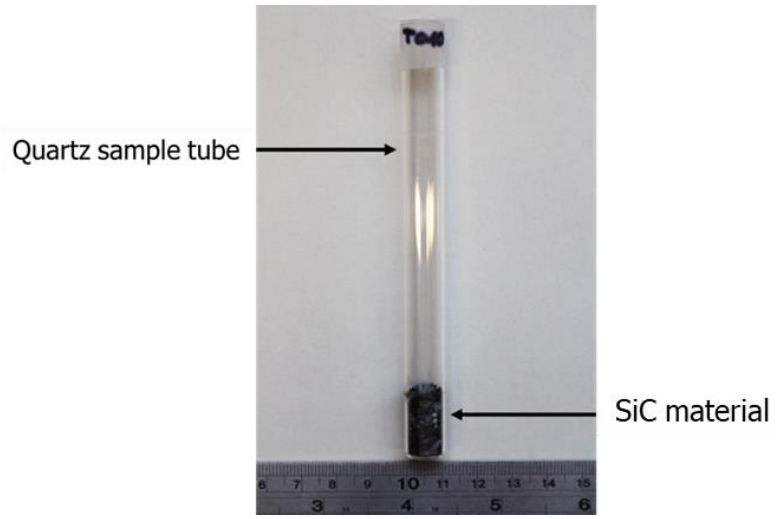


Figure 3.24. Image of the prepared sample containing SiC fibre, which is inserted into the equipment seen in figure 3.25., indicated as 'Sample'.

The system used operated simultaneously in two modes, one for heating samples, and the other for measuring. The heating probe, which operated at 2.45 GHz in TE_{111} mode, was inserted into the cavity's sidewall, whilst the measuring probe was inserted in through the bottom of the cavity, operating at TM_{010} mode. A vector network analyser (VNA) connected to an amplifier created the incident signal for the

heating mode of 150 W. A second VNA was fitted with a cross-coupling filter to avoid creating signal interference between the two sources. The sample in the quartz vial was then lowered into the cavity, which also had a video camera and infrared (IR) pyrometer fitted into the sidewall. Once the sample was in position, the software in Labview mode controlled the heating rate, temperature measurement, video recording and cavity response in both heating and cooling modes. A PID algorithm adjusted the microwave source bandwidth to adapt to changes in the material's properties and cavity responses. This maintained the specified heating rate [344] by adjusting the forward power to the cavity. The temperature was controlled with an IR thermometer and the cavity was water-cooled to minimise thermal expansion. The procedure described above was carried out on all samples tested.

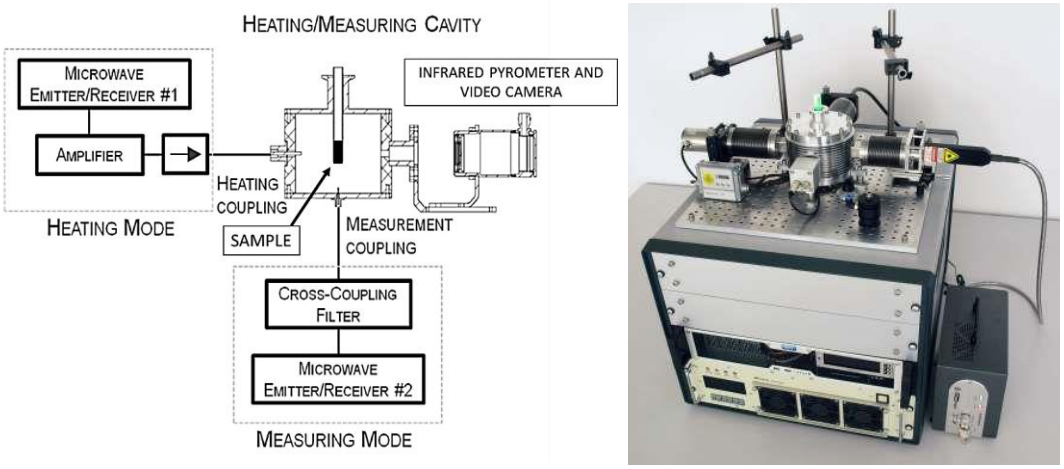


Figure 3.25.(a) Microwave system design for measuring samples' dielectric properties as a function of temperature, adapted from [344] and (b) a photograph of the respective equipment [345].

3.4. Simulation of microwave heating of SiC preform

3.4.1. Computational technique

Computational simulation of the electromagnetic and thermal heating of the SiC_f sample in the MCVI cavity of the Labotron HTE M30KB CL Pro was undertaken. The

methods used were established by Celuch (2009) and Koypt (2007) [346, 347] for solving an electromagnetic-thermal two-way coupling problem via an iterative solution. The solution provided a highly representative insight into the heating of the SiC fibre preform using microwaves by accounting for the temperature-dependant dielectric and thermal properties of the materials. The simulation updated all the respective properties of the materials in the cavity after each time step.

The internal structure of the cavity was reproduced and parameterised into a 3D model to be used by the software QWED 3D, a finite-difference time-domain simulator. The internal layout of the cavity and the material components, such as the bell jar, alumina foams, quartz tube and sample, are shown in figure 3.26. The QWED algorithms were applied using the electromagnetic solver, which fed the results into QW's basic heating module, which in turn relayed the resulting temperature changes back to the EM solver for each cell at each time step. The EM boundary conditions applied to the cavity assumed that the 316L stainless steel walls were perfectly reflective to microwaves. Neumann (thermal insulation) boundary conditions [348] were applied to all the surfaces of the SiC preform and Robin conditions [349] (convective) applied where the SiC fibre was in contact with the alumina foam.

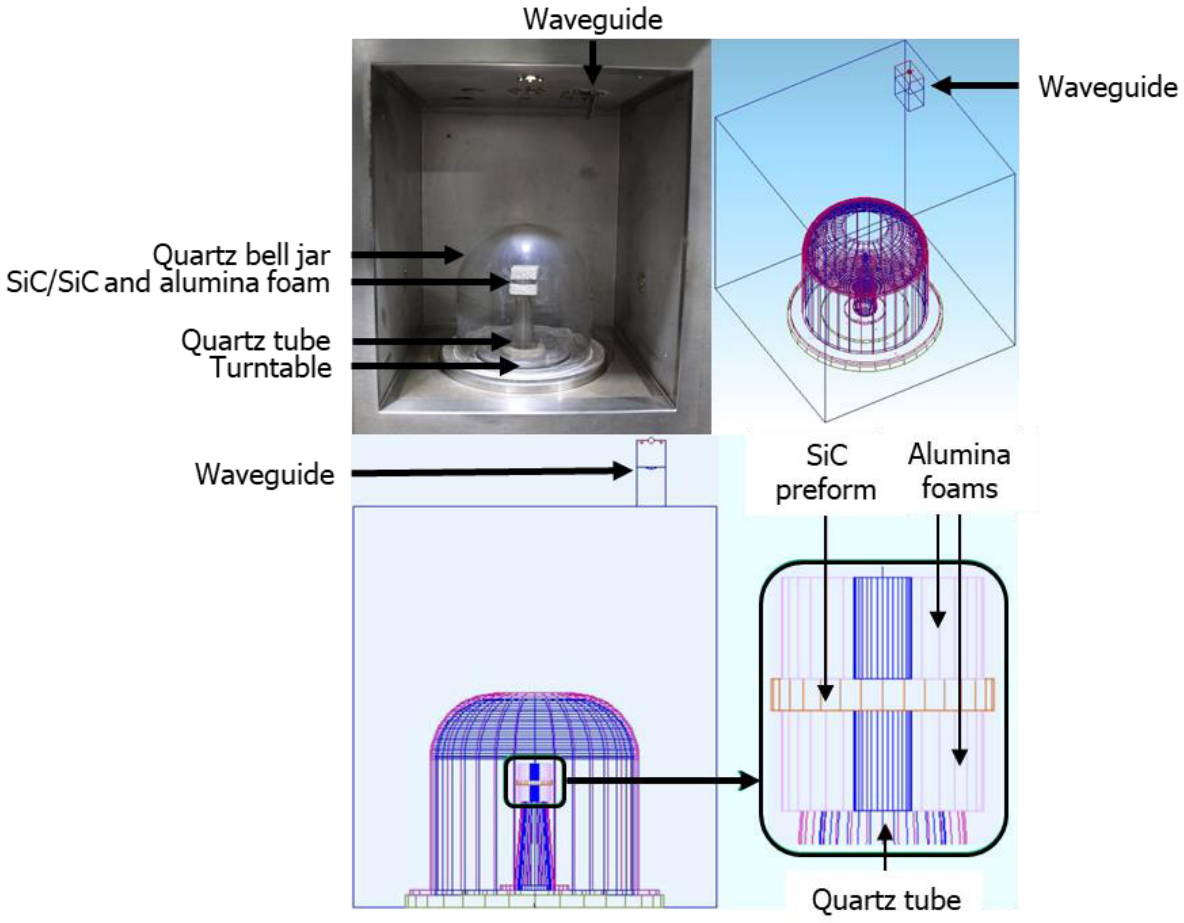


Figure 3.26. Labotron HTE M30KLB Pro; cavity, 3D view of the internal structure and components and a magnified view of the $SiC_f/SiC\text{-}Al_2O_3$ foam arrangement.

Simulations were conducted on a Dell workstation (64-bit Windows 10) with two Intel Xeon gold 5120 processors with a peak frequency of 3.2 GHz. All simulations were carried out at Worcester Polytechnic University by Prof Vadim Yakovlev. The simulation ran on 14 cores via 28 threads on an NVIDIA Quadro P500 with a total of 1TB RAM. To reduce computational resources and therefore the time of simulations, non-uniform meshes with adjusted cell sizes, depending on the wavelength of the media, were applied to discretise the sample and foams to ensure a high degree of accuracy of the simulation. The SiC composite ranged from 2.2-3.6 million cells for the smallest and largest samples, respectively. When solving the coupled problem, the EM and thermal time step were set depending on the heating rate of the sample;

it was typically one second, meaning the entire process took 2 h of CPU time for the shortest scenario and 14.5 h for the longest.

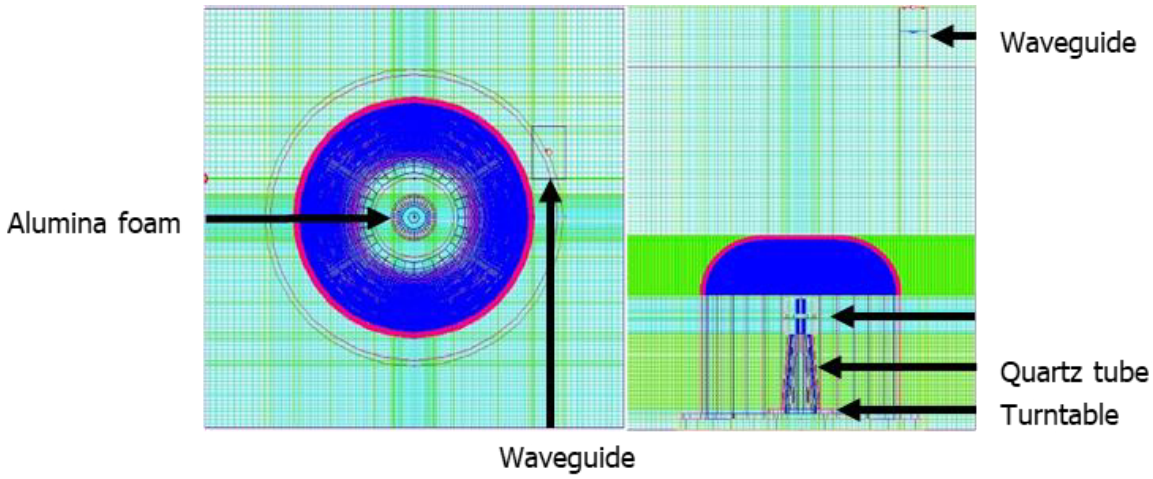


Figure 3.27. A top-down view and front-on view of the non-uniform meshes applied to the simulation.

3.4.2. Materials parameters

The simulation also required the input of specific material parameters as a function of temperature up to 1200°C to reproduce the MCVI process. To do this a number of parameters needed to be known, see table 3.4.

Table 3.4. QWED input data with specific non-SI units.

Parameter	Symbol	SI unit	Unit required for QWED 3D
Temperature	T	K	°C
Dielectric permittivity	ε′	-	-
Loss factor	ε″	-	-
Siemens	S	Ω^{-1}	Ω^{-1}
Enthalpy	ΔH	J kg^{-1}	J g^{-1}
Specific heat capacity	C_p	J kg K^{-1}	J g°C^{-1}
Density	ρ	Kg m^{-3}	g cm^{-3}
Thermal conductivity	λ	W m K^{-1}	W cm°C^{-1}

See sections 3.3.6 and 3.3.7 for measurement details. The EM problem was solved using the dielectric permittivity, loss factor and density but to solve the coupled problem all parameters were required. The three material components were the SiC

fibres, the alumina foams and quartz glass. The SiC powder was not included in this simulation as the objective was to reproduce the experimental set up that was used to investigate the processing parameters. All data used for the SiC fibres were collected experimentally, whereas all the data for the Al_2O_3 foams and quartz was obtained from the literature and modified accordingly to the material's morphology; this will be presented in section 4.2.2.

4. Results and Discussion

This chapter is divided into three sections. The first section focuses on the physicochemical properties of the SiC deposit by infiltrating a SiC_f preform[ix] to establish the processing-microstructure relationship using various microscopy techniques to evaluate the morphology, composition and crystal structure. The second section is dedicated to the modelling of the electromagnetic-thermal interaction between the SiC_f preforms and the microwave field. This provided insight that experimental work could not. It enabled assessment of the effects of dimensions and temperature on the reflection coefficient and the corresponding temperature profiles developed at various frequencies providing explanation for a number of observations in section 4.1. The third and final section presents the results of the optimisation of a slurry impregnation route used to increase the green density of the SiC_f preforms. This work encompassed a range of multidisciplinary techniques to select a slurry that provided a composite that met established hypothetical criteria for the MCVI process. The results of all three chapters should be combined for the next stage of this work that investigate infiltrating an impregnated preform as outlined in more details in chapter 5.2.

[ix] Note this was just a SiC fibre preform with no infiltration of SiC slurry between the ply, but with slurry coated on the edges, see section 3.2.1.1. and 3.2.3.6 for more details.

4.1. Microwave energy enhanced chemical vapour infiltration process

4.1.1. Kinetics of the MCVI process

The objective of this part of the work was to establish the processing parameter relationships that govern the kinetics laws that affect the thermally activated deposition of SiC from MTS. The overarching aim of this work was to establish the processing conditions that were most likely to achieve >90% density in the SiC_f/SiC composites in the shortest time possible whilst depositing pure stoichiometric SiC.

4.1.1.1. *Effect of temperature and pressure*

Figure 4.1. shows the growth rate (G_{sic}) of the SiC matrix material on the ZMI SiC_f. The deposition rate of the SiC matrix increased with increasing temperatures between 900-1000°C. This was consistent with the literature that all reported an Arrhenius relationship with temperature [233, 236, 239, 243, 350, 351]. The two shaded regions marked 'plasma formation' and 'untenable arcing' were non-operable regions of infiltration conditions. Low pressures in a microwave environment cause gases in the cavity to ionise, resulting in uncontrolled plasma formation that can be hazardous to users and damage equipment. The untenable arcing region is described by Paschen's law, as seen in section 3.2.3.6. Table 3.3 lists the infiltration conditions for all of the samples that are discussed below.

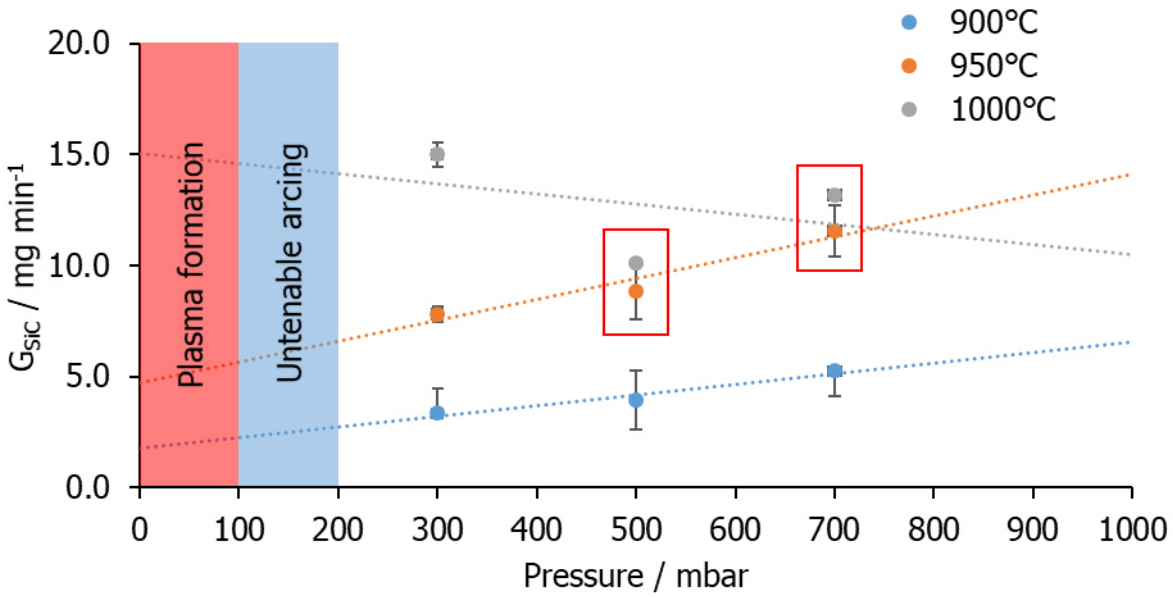


Figure 4.1. SiC matrix growth rate as a function of increasing chamber pressure for samples processed at different temperatures. Gas flow rates and alpha ratio were kept constant at Q_{H2} = 300 cm^{-3} min^{-1}, Q_{MTS} = 0.2 g min^{-1} and alpha = 10 respectively. Details for samples inside the red boxes with reduced infiltration times can be seen in Figure 4.7.

The 900 and 950°C samples showed an increasing linear relationship between pressure and deposition rate, figure 4.1. This is because of the increased residence time of the precursor gases inside the preform at higher pressures. The increased residence time, as according to collision theory, increases the likelihood of a successful reaction occurring because the atoms have more time to gain sufficient kinetic energy and an increased chance of colliding combining to overcome the activation energy barrier, as shown by [233, 243]. It is expected that this trend would be seen at higher temperatures as well if the ZMI fibres could have been infiltrated at 1000°C for 8 h at higher pressures than 300 mbar. D'Angio [243] reported that flowing the carrier gas at a rate of 300 cm^3 min^{-1} increased the residence time from 0.1 s at 200 mbar to 0.45 at 900 mbar, which is consistent with the characteristics of a kinetics-limited process. D'Angio also went on to describe that at higher temperatures the deposition rate of the SiC matrix became independent of

the process pressure, which is in good agreement with other literature [234, 239, 248].

All samples were intended to be processed for a total of 8 h (2+2+4 h). This was not possible for the four samples highlighted in the red boxes, which after a 2 h initial infiltration were unable to be heated up again to the desired deposition temperatures despite a number of attempts. Longer infiltrations were successfully attempted at 900°C and 300 mbar for 20 h but not trialled at higher temperatures and pressures. This inability to heat preforms was only seen when temperature and pressure were both ≥ 950°C and ≥500 mbar. This is thought to be in part because of the change in the dielectric properties of the ZMI fibres at elevated temperatures, see figure 4.2. This is because above 1000°C the ε' decreases rapidly from 23 at 1000°C to 0 at 1064°C, an indicator that the fibre is now not absorbing microwaves. It is expected that preforms would be hotter in the samples' centre since that was being measured by the 2CP. Mo et al. [301] reported microstructural changes in the ZMI fibre after annealing for 2 h at >1000°C. They go on to state that at these temperatures there was a "thermal decomposition of SiO_yC_x" phase in the fibres, which had a low electrical conductivity, and growth of "highly conductive free carbon nano-domains" that at high temperature will become resistive [352]. Further to this, they explain this causes an increase in the ε', which contradicts the results shown in figure 4.2. This is

potentially an artefact of the measurement frequency, which was between 8.5 – 12.5 GHz, whilst the frequency used in figure 4.2 was 2.45 GHz.

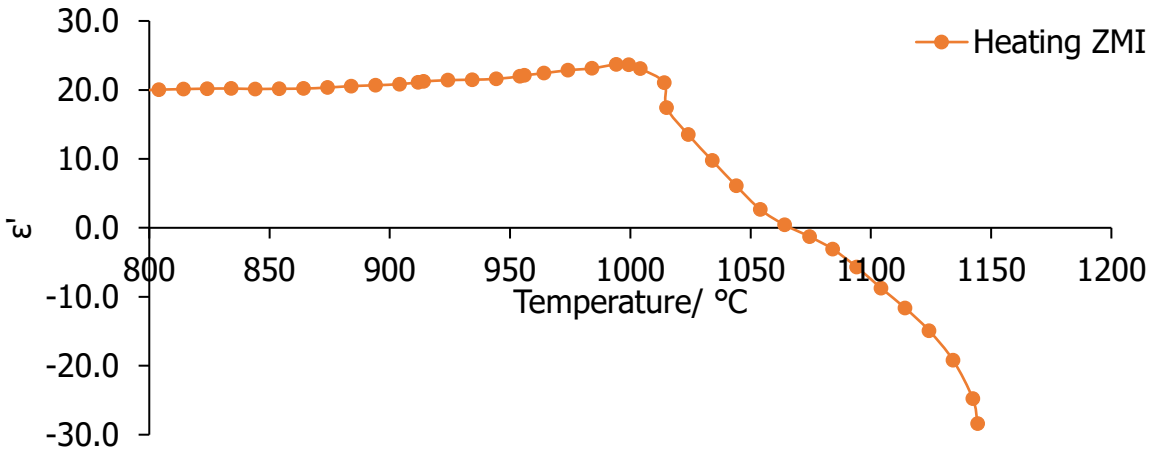


Figure 4.2. The dielectric permittivity of the Tyranno ZMI fibre as a function of temperature, showing the fibre stops behaving as a dielectric at ~1060°C.

A potential explanation for this in terms of the elevated pressure preventing reheating is the SiC deposited was Si codeposition at high pressures. The literature reports higher pressures produced Si-rich SiC [235, 236, 246], which was later confirmed to be the case in this work, see figure 4.25. and figure 4.27. This makes the deposit reflect microwaves [178], which may have prevented it being reheated, assuming the 10 µm layer that was deposited was sufficient to have had this effect. For this reason and because intra tow infiltration is not favoured at high pressure a longer infiltration run at high temperature and pressure was not attempted.

4.1.1.2. *Effect of alpha ratio*

Figure 4.3 shows the effect of changing the alpha ratio on the SiC deposition rate. These tests were carried out using a chamber pressure of 400 mbar at a constant temperature of 925 ± 15°C as these conditions were found to yield favourable kinetics, densification profile and microstructures. The different ratios were achieved

by fixing the MTS flow rate at 0.2 g min^{-1} and altering the H_2 flow rate. These values were selected based on the temperature-pressure kinetic results (section 4.1.1.1.), the densification profiles (section 4.1.2.1.) and the Si:C ratio of the samples (section 4.1.3.2.1.). The results show that an alpha ratio of 10 had the fastest deposition rate of 9.6 mg min^{-1}, whilst alpha = 5 yielded a slightly lower deposition rate of 8.6 mg min^{-1} and the results from the alpha ratios of 25 and 70 were both significantly lower. Due to time constraints and equipment breakdown the production of multiple samples was not possible. It is expected that there is not significant difference between alpha = 5 and 10.

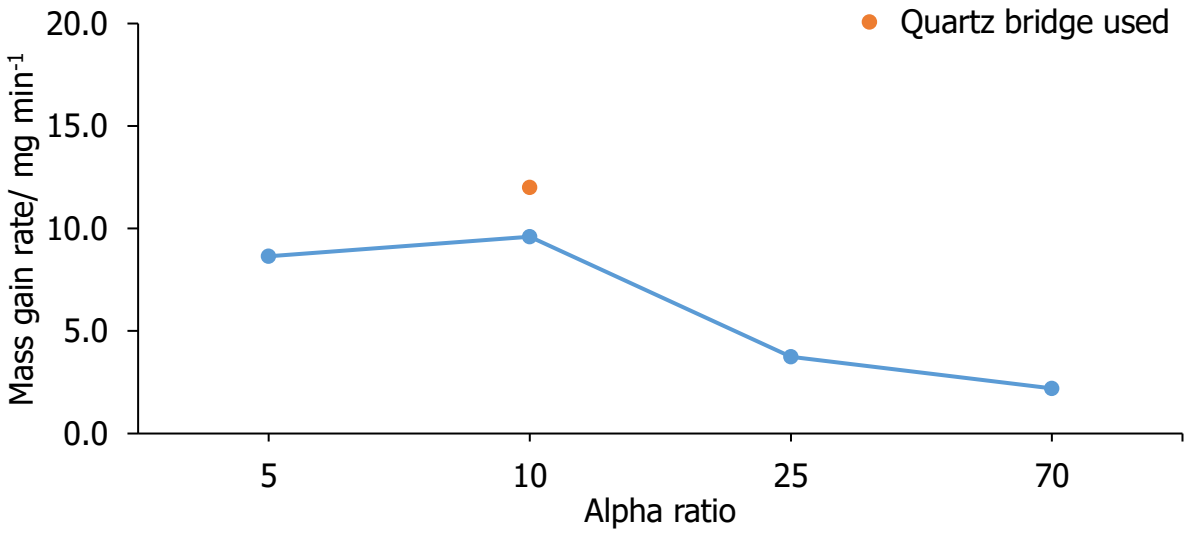


Figure 4.3. SiC matrix growth rate as a function of changing alpha ratio. All samples were processed at 925°C, 400 mbar and Q_{MTS} = 0.2 g min^{-1}. Q_{H2} was changed to alter the alpha ratio.

The values selected for these four tests were based on figure 2.31 from [9], with a secondary aim of understanding the Si:C ratio dependence on the alpha ratio. The results shown in figure 4.3 are in agreement with a number of reports in the literature, [236, 237, 248], that also found lower alpha ratios yielded higher deposition rates. All authors state that this is because of the higher concentration of MTS. Langais et al. [248] goes on to explain that the kinetics of the deposition

process are quasi-independent when T>950°C, but are thermally activated at lower temperatures. Due to the lack of repeats that were possible due to time constraints' a value of 10 was selected for further testing as it had shown the absolute highest deposition rate and was widely reported in the literature. It is expected, however, that alpha = 5 would likely produce a deposition rate that is within the range bars of the alpha = 10 sample.

Figure 4.3 also shows the effect of the addition of the quartz 'bridge' that is pictured in figure 3.13. The bridge was used to reposition the vacuum port above the sample since the original location of the vacuum port resulted in some of the carrier/precursor mixtures not passing through the preform. The addition of the bridge showed a 25% increase in the deposition rate under otherwise identical conditions suggesting that it is reasonable to infer that the quartz bridge increased the concentration of the precursor flowing through the sample.

Another observation made during these tests was the influence of the gas flow rate on temperature stability. Higher gas flow rates (>2000 cm^3 min^{-1}) caused a greater fluctuation in the centre and side temperatures than the lower flow rates used with the low alpha ratios. Figure 4.4 shows the centre and side temperatures for the alpha ratios of 10 and 70. Alpha = 10 had a standard deviation for the centre and side temperature of ±5°C and ±20°C, respectively, whereas the alpha = 70 values were ±12°C and ±35°C, respectively. This is because the higher flow rate meant a lower heat transfer from the heated pipeline, which increased the effect of transpiration cooling when the gas met the sample in the cavity.

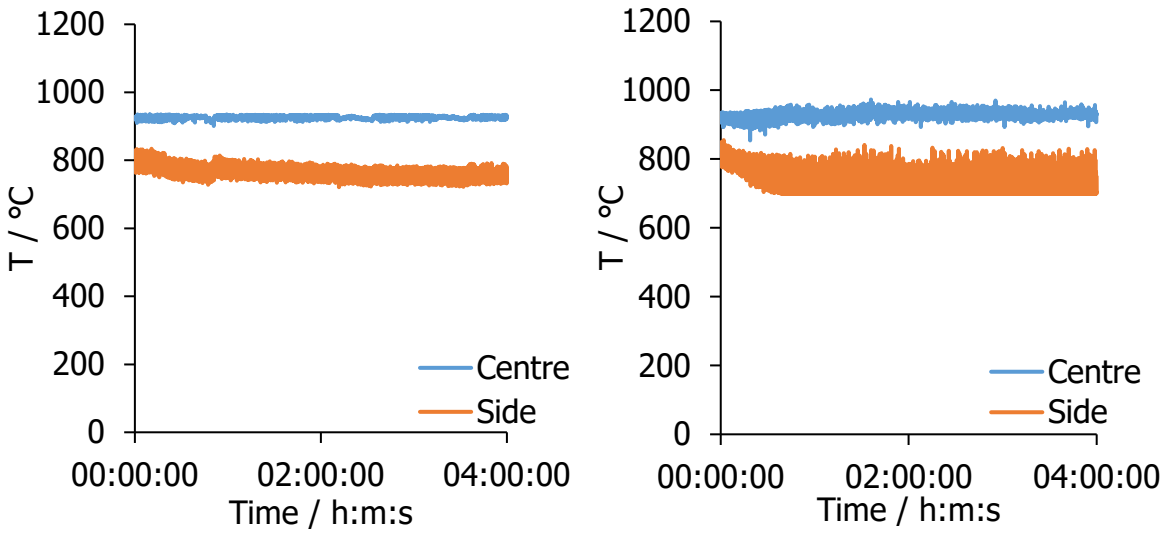


Figure 4.4. Left: Infiltration temperature over time at an alpha ratio of 10 showing a relatively constant centre and side temperature. Right: equivalent graph for alpha 70 showing significant fluctuation for both the side and centre temperatures.

The kinetic data from the quartz bridge tests (figure 3.13), were subsequently used to predict the time to 90% of TD, the value that is typically achieved in ICVI [35, 353]. No experiments could be attempted in this project due to multiple equipment breakdowns and the projects time constraints. The sample that achieved the highest relative density was the 1000°C infiltrated at 300 mbar reaching 44% in only 8 h an increase of 25 % density. The infiltration was stopped because this section of work was optimising the processing parameters not trying to achieve full density at this stage. The rate of densification will experience natural logarithmic decay because as the volume of porosity left to fill decreases with time the mass gain will decrease as well. Using equation 4-1 and the initial mass gain rate from first 8 h from sample QB, which showed the fastest mass gain rate of all samples, an estimated total time to reach TD=90% was able to be predicted.

Equation 4-1 $$y = -Ae^{-Bt} + C$$

Where y = Mass at t_x

A = Initial mass / g

B = Rate / g min^{-1}

t = time / min

C = Final mass at 100% of TD / g

Figure 4.5 shows the extrapolated data for both non-impregnated and impregnated samples to 90% of TD, as indicated by the horizontal dashed line. The non-impregnated sample is expected to take 124 h to densify and the impregnated 96 h, a saving of 28 h because of the addition of powder. Comparing this to iso-thermal CVI, which takes ~1000 h to produce a sample with ~10% porosity, this indicated there might be a significant reduction in time [13].

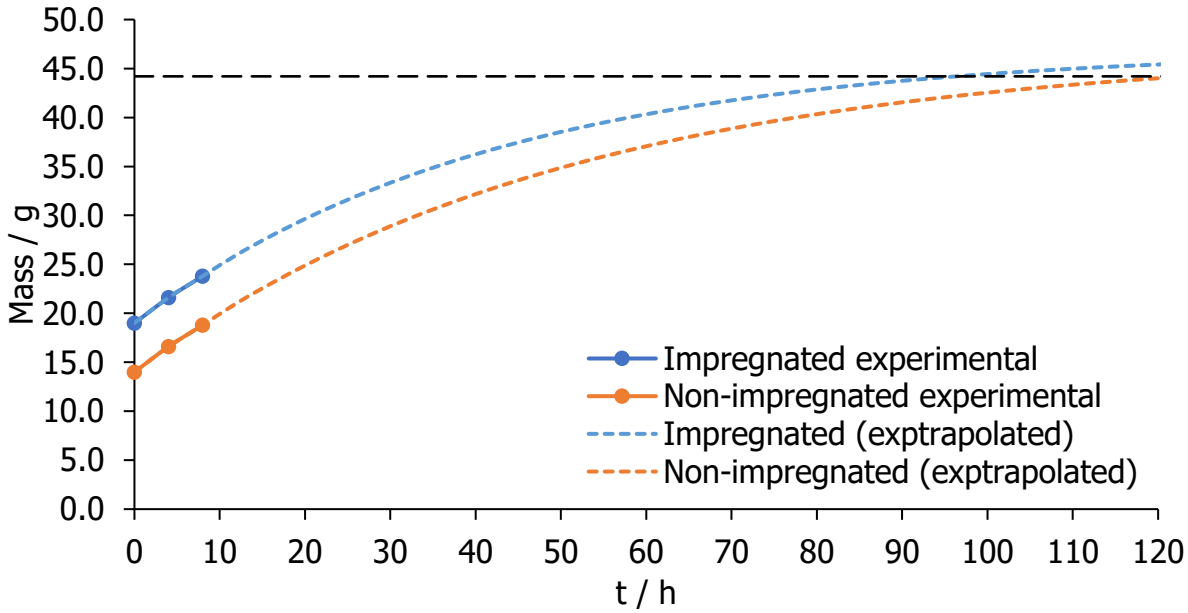


Figure 4.5. Extrapolated plots of the densification of the SiC_f/SiC composite using natural logarithmic decay function based on the rate of mass gain seen in sample QB over the first 8 h (2+2+4 h), table 3.3. It shows a potential reduction in the time afforded by the introduction of the SiC slurry phase.

4.1.1.3. *Activation energy*

Figure 4.6. shows the natural logarithm of the SiC matrix growth rate against the reciprocal of temperature for the three different pressures used. The SiC matrix deposition shows an Arrhenius behaviour consistent with the literature as all three data sets show an increasing growth rate as a function of increasing temperature [13, 236, 239, 243, 350, 351]. This indicates that the growth mechanism is limited by a chemical reaction due to its linear dependence, which is preferable for CVI. Using the intercepts for the three different pressures and rearranging the rate constant equation to solve for activation energy, the mean E_a across all temperatures and pressures was calculated to be 125 ± 4 kJ mol^{-1} using equation 4-2.

Equation 4-2 $$k = Ae^{\frac{-E_a}{RT}}$$

Where K = rate constant

A = Pre-exponential factor / s^{-1}

E_a = Activation energy / J mol^{-1}

R = Universal gas constant / J mol^{-1} K^{-1}

T = Absolute temperature / K

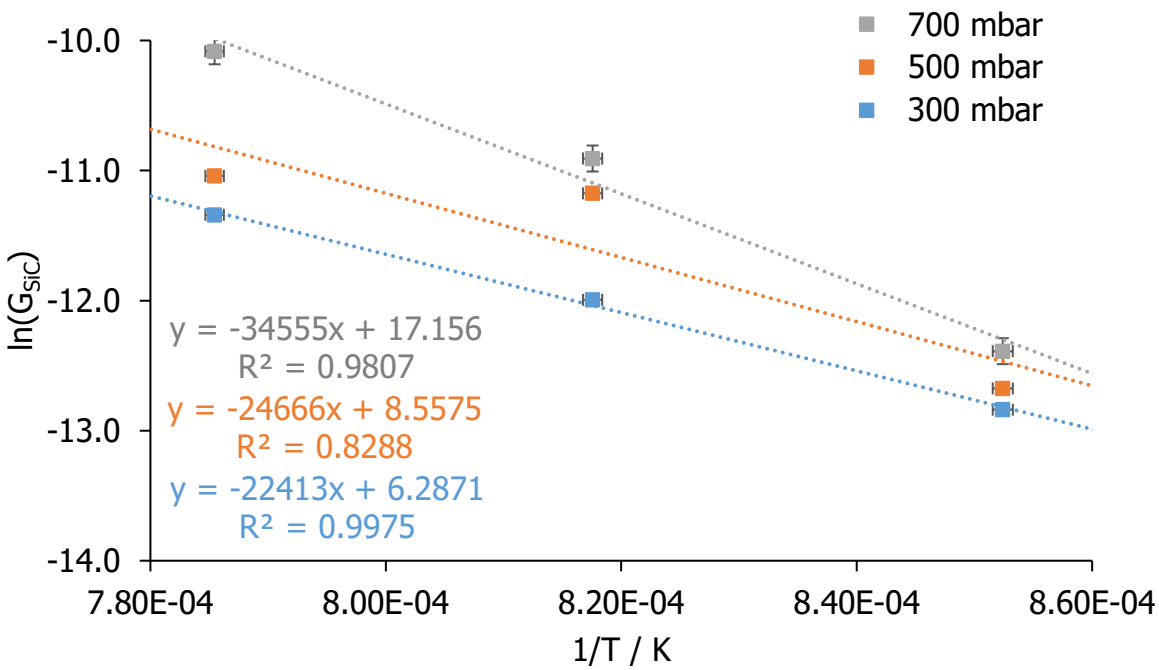


Figure 4.6. Natural logarithm of the SiC matrix growth rate against the reciprocal temperature for three different pressures at the same flow conditions.

The activation energy required to initiate the reduction of the MTS precursor ranges from 120 – 500 kJ mol^{-1} [218, 222, 233, 236, 239, 241, 244, 246, 248, 354] depending on processing set up and parameters used, this is in good agreement with the findings presented in this work. However, it should be noted that the results were obtained under conditions where a deliberately inhomogeneous temperature distribution across the sample (a hotter centre) was being used.

125 kJ mol^{-1} is at the low end of the range of reported values in the literature, which is thought to be a direct result of the use of microwaves. It has been consistently reported in the literature that the use of microwave indirectly lowers the activation energies and increases sintering rates of various ceramic materials, but the exact reason for this is still a topic of discussion [258]. The debate is centred on whether the observed effects can be explained by thermal microwave effects such as inverted

temperature gradients, overheating, hot spots and inhomogeneities or if these enhancements can be explained by non-thermal microwave effects [355]. The former is much better understood, but proving the cause of this effect by separating them from the non-thermal effects experimentally is difficult [356]. Booske et al. 1992 [357] and 1998 [358] showed non-thermal effects are due to the Ponderomotive force, which due to non-thermal phonon distribution enhances ion mobility enhancing mass transport and diffusion rate, which indirectly lowers activation energy. This has been demonstrated experimentally by Freeman et al. 1995 [359] and Wang et al. 2005 [360], looking at vacancy transport processes in NaCl and sintering rates of various ceramic using a hybrid (microwave and radiative) heating process, respectively. A number of publications have also recently proposed that this force effects the orientation of electronic structures of gaseous intermediates [361-363]. As a result, the pre-exponential factor and/or the activation energy terms are altered in the Arrhenius equation [364]. In the case of MCVI, it could be that the MTS is interacting directly with the microwave field resulting in the lowering of the activation energy.

4.1.1.4. *Thiele modulus estimations*

As mentioned earlier, porosity closure involves two competing mechanisms; mass transport and the surface deposition reaction. For CVI, it is preferable to have the surface reaction be the rate-limiting step as this encourages diffusion into pore channels via the mass transport mechanism. To evaluate this relationship a dimensionless parameter called the Thiele modulus or the second Damkohler number can be used according to equation 2-3. A low Thiele modulus indicates the surface

reaction is the rate-limiting step whilst the inverse is true for mass transport if the number is large.

A number of terms of the equation had to be solved in order to estimate the Thiele modulus. According to equation 4-3, the reaction rate term in the Thiele modulus calculation can be deduced from the G_{sic} value when a first-order reaction is considered with respect to the MTS concentration:

Equation 4-3 $$G_{SiC} = \mathrm{K}_r \times C_{MTS}$$

Where K_r = reaction rate

C_{MTS} = MTS concentration in mol m^{-3}

The effective diffusivity ($cm^2\ s^{-1}$) of the preform also had to be calculated as per equation 4-4:

Equation 4-4 $$D_{eff} = \frac{\rho_r}{\xi}\left(\frac{1}{D_m} + \frac{1}{D_k}\right)^{-1}$$

Where D_m = molecular diffusivity / $cm^2\ s^{-1}$

D_k = Knudsen diffusivity / $cm^2\ s^{-1}$

P_r = relative density of the preform = 0.22

ζ = Tortuosity.

In order to solve equation 4-4, both D_m and D_k needed to be found. D_m was dependant on pressure and temperature according to equation 4-5 [365].

Equation 4-5 $$D_m = K_m \frac{T^{0.5}}{P}$$

Where K_m can be found using the Chapman-Enskog relationship for MTS [197]. Lastly, D_k is calculated according to equation 4-6, which is independent of pressure but proportional to $T^{0.5}$ and its contribution can only be considered in small cylindrical pores, such as those found during intra-tow infiltration.

Equation 4-6 $$D_k = \frac{r_{pore}}{3}\sqrt{\frac{2RT}{\pi M_{MTS}}}$$

Where r_{pore} = pore radius / m

M_{MTS} = Molecular mass of MTS / g mol^{-1}.

In order to estimate the Thiele modulus, a number of assumptions must also be made:

- The average intra-tow and inter-tow pore radii were taken from the MATLAB script, which were 5.5 μm and 215 μm respectively.
- The tortuosity was calculated to be 0.31 by assuming the arc-chord length ratio was one-quarter of the circumference of a fibre.
- The pore channel length (L) was again calculated from the MATLAB script to be 47.5 mm due to the open porosity network at t = 0.

Table 4.1 shows that the SiC deposition in the inter-tow spacing was limited by the surface reaction due to the small Thiele number; this is confirmed by the deposition on the fibres not showing a variable thickness along their lengths. It should be noted that in both the samples, higher pressures and temperature resulted in higher values of Φ, indicating a faster surface reaction, which is consistent with the deposition patterns observed in the intra-tow regions and in the literature [228]. However, this is not seen in the much larger inter-ply regions, which is to be expected. It must be stated that these calculations do not account for any slurry addition to the preform and are only valid when t = 0 because as soon as deposition begins the available surface area decreases, which impacts the molecular diffusivity, density and tortuosity. The effectiveness factor has also been calculated that describes the ratio

for pore channel deposition to surface reaction; this reiterates the previous finding as values closer to one indicate favourable in-pore deposition.

Table 4.1. Effects of the effective diffusivity, reaction rate, Thiele modulus and effectiveness factor based on the different processing conditions from table 3.3.

Sample no.	D_{eff}	K_r	Φ (intra)	Φ (inter)	η (intra)	η (inter)
1	1.98	1.19E-05	0.070	0.011	0.9984	1.0000
2	1.63	1.40E-05	0.084	0.013	0.9977	0.9999
3	1.38	1.86E-05	0.105	0.017	0.9963	0.9999
4	2.04	2.76E-05	0.106	0.017	0.9963	0.9999
5	1.69	6.26E-05	0.175	0.028	0.9900	0.9997
6	1.44	8.18E-05	0.216	0.035	0.9847	0.9996
7	2.11	5.31E-05	0.144	0.023	0.9932	0.9998
8	1.76	7.15E-05	0.183	0.029	0.9890	0.9997
9	1.50	1.87E-04	0.320	0.051	0.9672	0.9991
10	1.84	6.12E-05	0.166	0.026	0.9910	0.9998
11	1.84	3.30E-05	0.122	0.019	0.9951	0.9999
12	1.84	5.30E-06	0.049	0.008	0.9992	1.0000
13	1.84	1.11E-06	0.022	0.004	0.9998	1.0000
QB	1.84	4.25E-05	0.138	0.022	0.9937	0.9998

4.1.2. Densification profile of SiC_f/SiC composites

4.1.2.1. *Effect of temperature and pressure*

The densification profile is the best representation of the theory underpinning MCVI as it shows where the SiC has been deposited in the preform and a time-weighted average of the temperature profile. Figure 4.7. shows the cross-sectional densification profiles of the disc-shaped preforms where temperature and pressure have been altered. The brighter regions are areas of higher density, where SiC has been deposited inside the porous body. The darker regions are areas of non-

infiltrated fibre or areas of lower density. Approximately 500 images were taken using an automatic program built into the optical microscope (Carl Zeiss Axioscop 2 MAT mot, USA) and then stitched together in post-processing. From the images, it is clear that both temperature and pressure affected the densification profiles. The samples infiltrated at 900°C at 300 and 500 mbar show localised SiC deposition in the centre of the sample, albeit 10 mm off the central axis for the 300 mbar sample. A closer inspection of the bright region of these two samples using BSE showed that the inter-ply and inter-tow porosity had not been filled, but a significant portion of the intra-tow porosity had. However, in both instances, there was a distinct lack of deposit on the lower surface. The top surface of this sample had a coating thickness of 12 μm but the bottom surface only <2 μm. This is thought to be because the gas flow cools the bottom of the heated preform reducing deposition until the gas has been sufficiently heated by its passing into the preform.

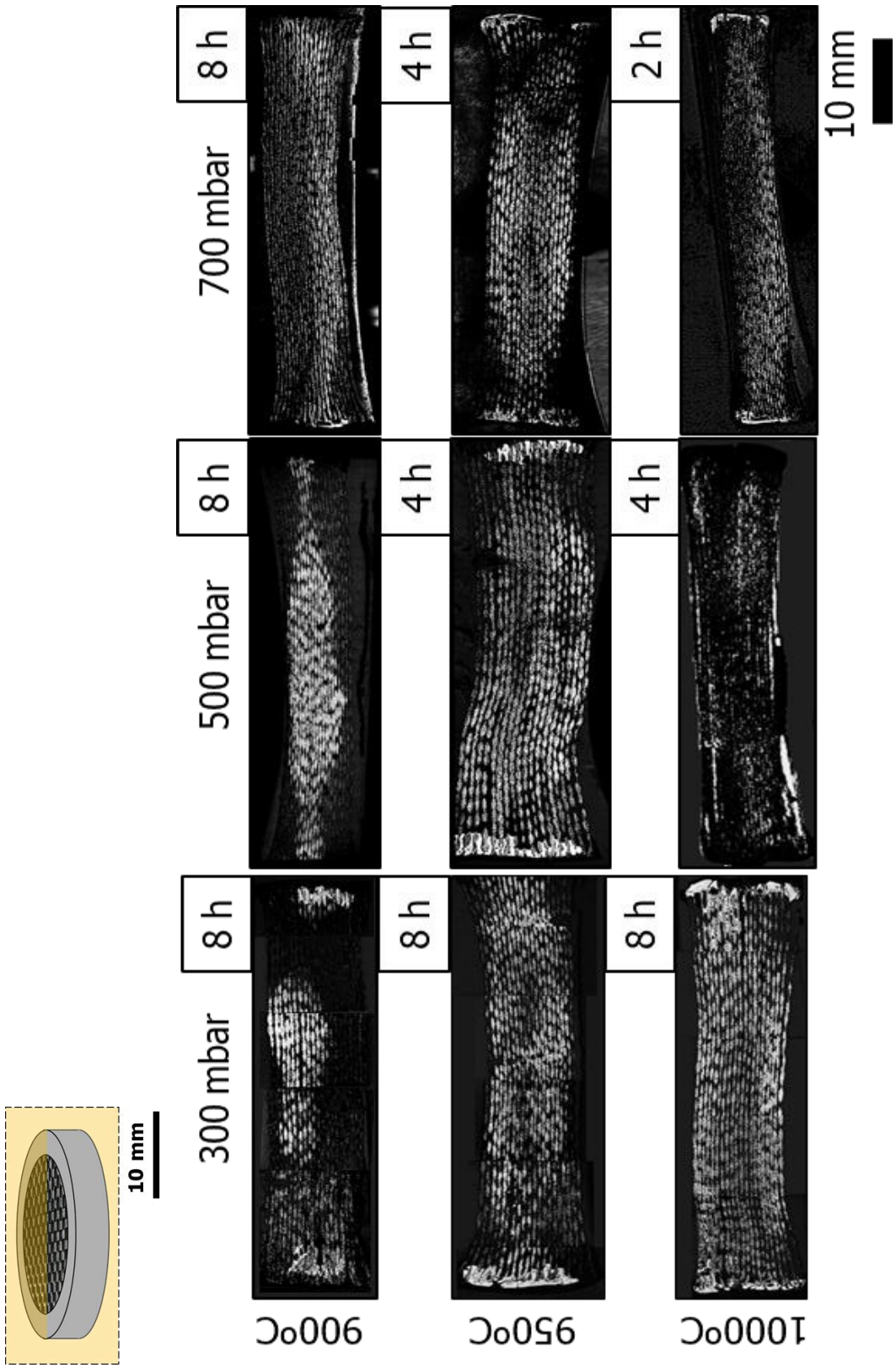


Figure 4.7. Optical micrographs of the samples infiltrated at different temperatures and different pressures showing the densification profiles as seen by the lighter regions indicating SiC deposition.

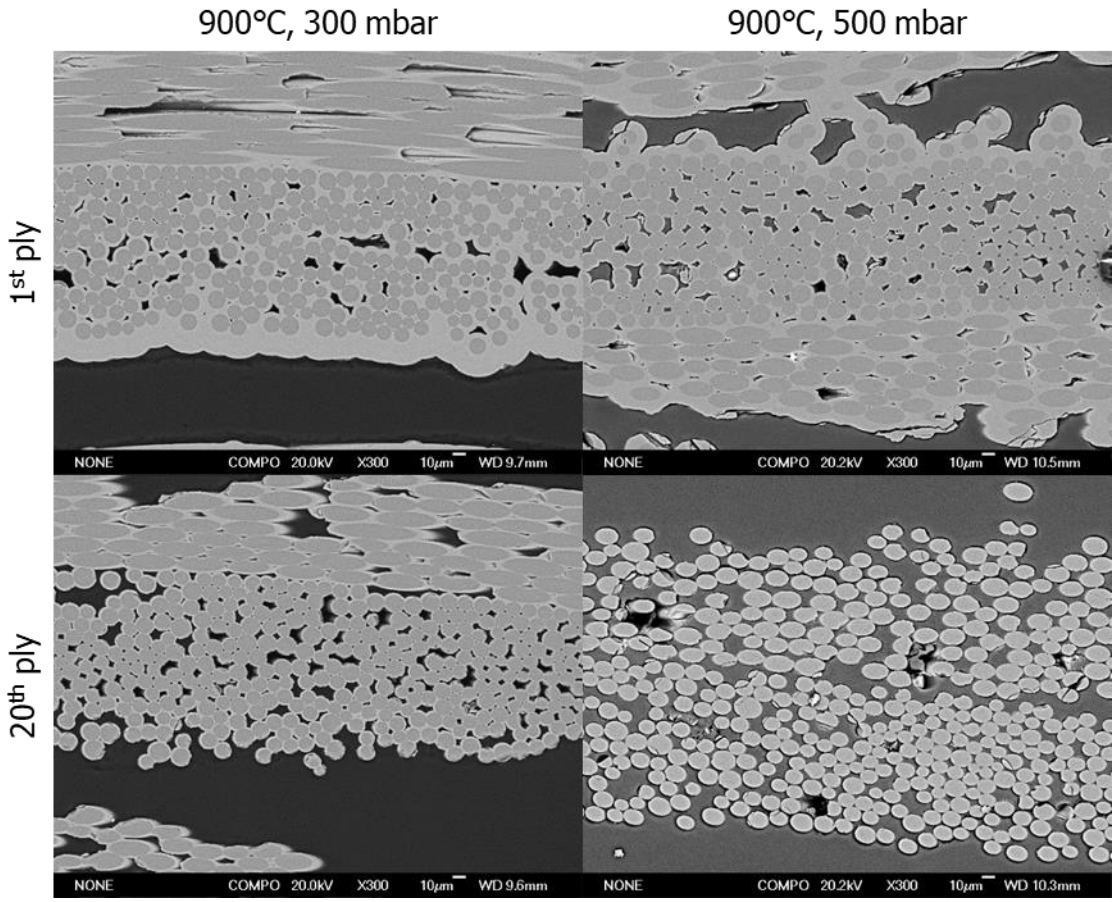


Figure 4.8. The difference in fibre coating thickness between the 1st ply (top row) and the 20th ply (bottom row) in samples infiltrated at 900°C at different pressures.

Referring back to figure 4.7. the samples infiltrated at higher temperatures appear to have a more generalised SiC deposition profile. This is logical as infiltrating the samples when the centre of the bottom surface is at a higher temperature means that the rest of the sample is most likely at a higher temperature too. Therefore, unlike the samples infiltrated at 900°C, the bottom surface and sides of samples are hot enough that the reactants overcome their activation energy barrier and react to deposit SiC. Figure 4.9. demonstrates this trend for the 1000°C 300 mbar sample, with the fibres showing a uniform deposition thickness of 4.8 ± 2.5 µm.

The effect of pressure on the densification profile is difficult to evaluate. This is in part due to the reduced infiltration time of samples infiltrated at higher temperatures

and pressures, which prevents like-for-like comparisons being made. One feature that appears in two of the samples infiltrated with SiC at 700 mbar is the apparent localised deposition of SiC on the lower surface closest to the gas inlet. Whilst this might appear to contradict an earlier statement made with reference to figure 4.9., it is thought that for the samples shown in figure 4.10. the deposition has occurred at the bottom surface of the preform because of the higher pressures caused by the increase in the gases viscosity [366]. As a result, the precursor has not penetrated the preform's porosity network as far and subsequently has deposited at the lower surface once it has reached deposition temperature.

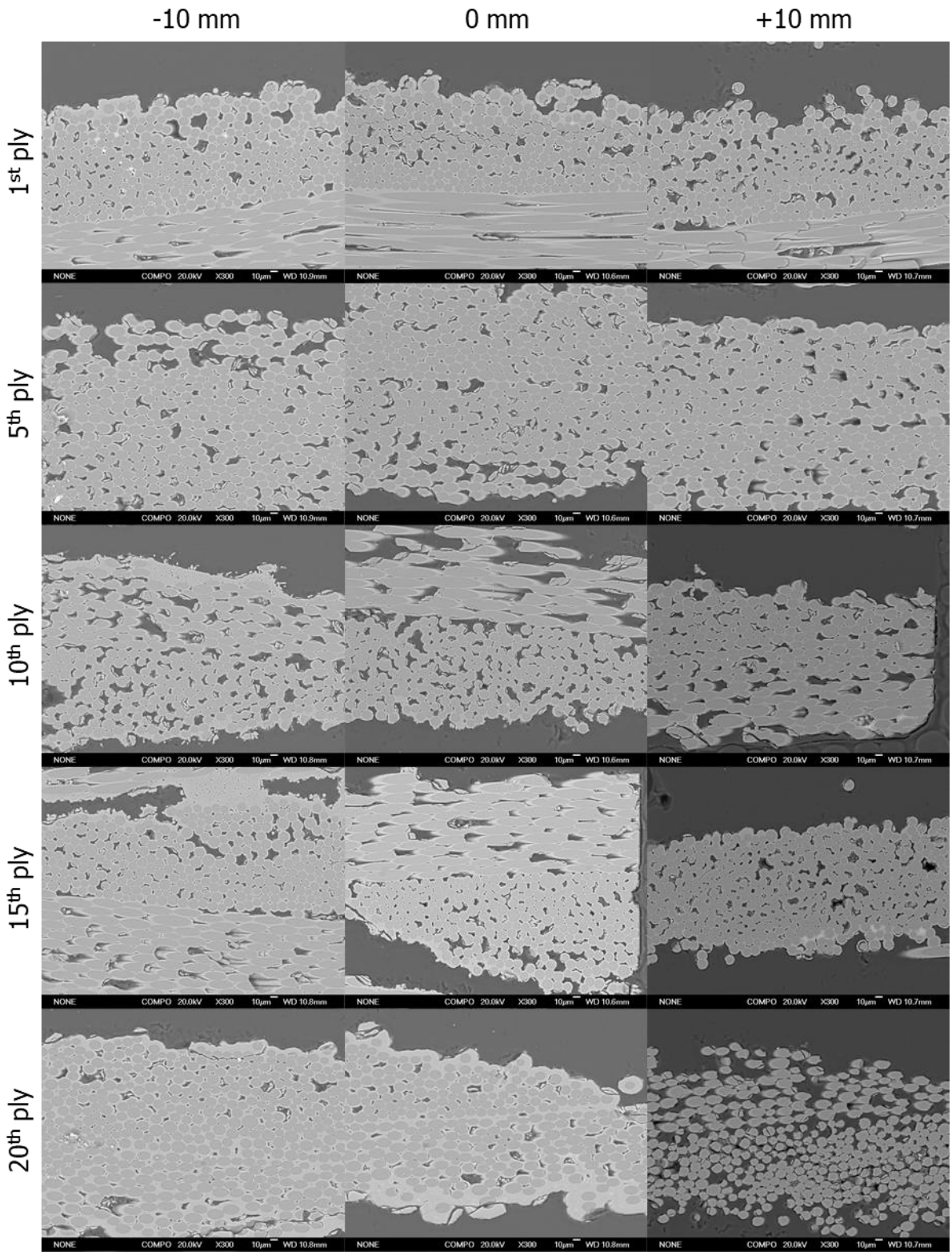


Figure 4.9. Micrographs of the uniform deposition coating seen over the thickness and 20 mm of the sample infiltrated at 1000°C at 300 mbar.

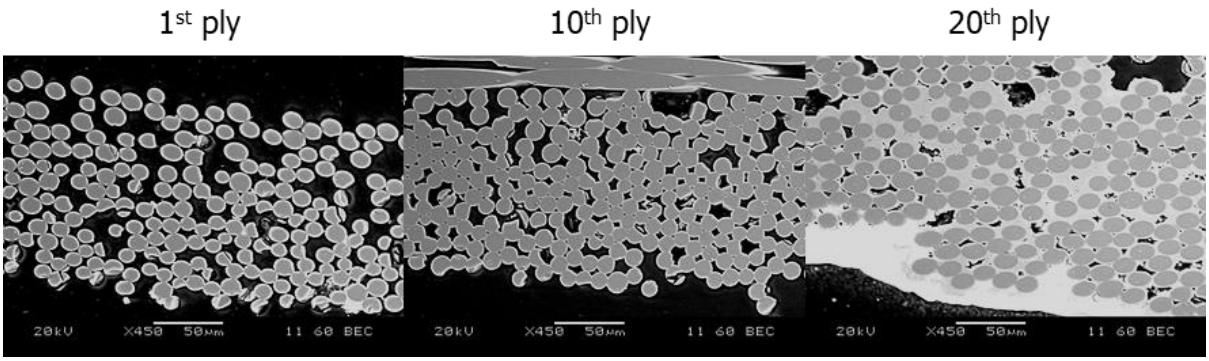


Figure 4.10. Three micrographs showing the localised Si-SiC deposition on the bottom surface of the 1000°C 700 mbar sample compared to the 1st ply.

The bright region on the lower side of the 1000°C 700 mbar sample has been identified as a Si-SiC phase, which is consistent with a number of previous reports [235, 236, 246]. They suggest that this is because of the etching action of Cl_2-containing gas mixtures on the SiC at high pressure, which increases the silicon content [367-369].

Figure 4.11. shows the microstructure of the dense regions from the sides of the images in figure 4.7. This dense region is a result of the SiC coating on the edge of the samples to prevent arc formation in the MW cavity. Figure 4.11. reveals a distinct difference in density between the powder in the near vicinity of the fibre and approximately 1 mm away. This is because the ends of the fibres have a higher charge density creating a significant localised heating effect. Subsequently, this higher temperature means that the gaseous precursors deposit SiC at a higher rate, creating the higher density matrix around the ends. This is an important observation with respect to the powder infiltration aspect of this research. It demonstrates that precursor gases permeate through >1 mm of dense powder coating and deposit within it. This suggests that the powder impregnated into the preforms can be

densified as well. These images also show that it is only the region immediately surrounding the fibre ends that is above the deposition temperature of MTS. The area at the very edge of the composite is not infiltrated at all indicating the temperature is lower than ~850°C.

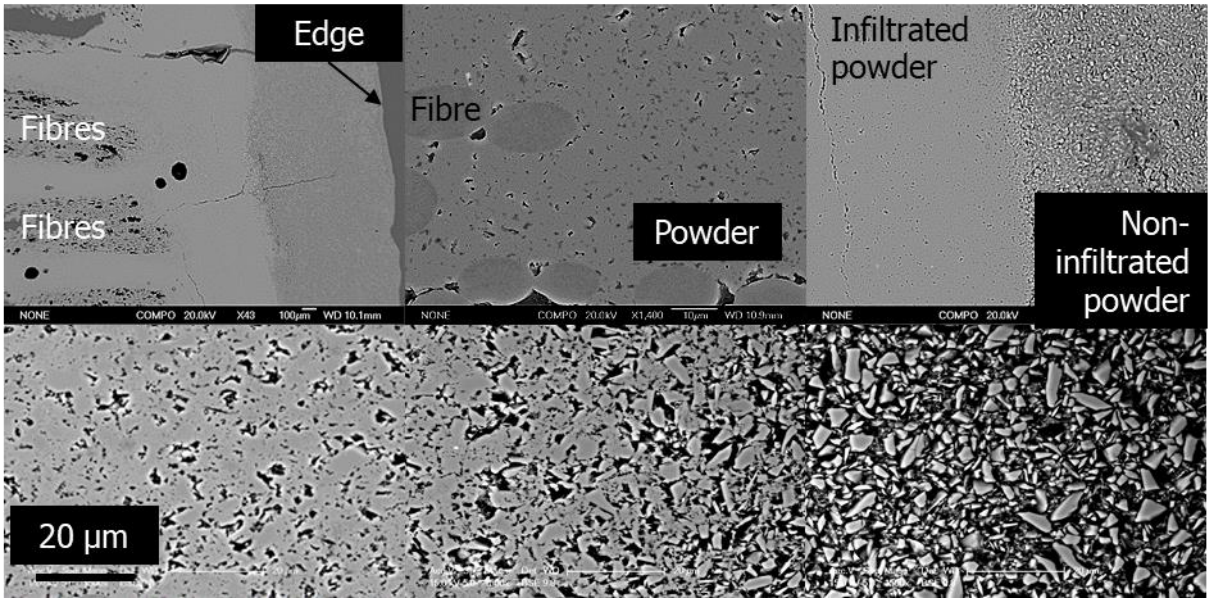


Figure 4.11. The top three images show the densification of the sides of the preform coated in SiC slurry. The bottom three show the transition from infiltrated powder to non-infiltrated powder, from left to right over a 250 µm distance.

A higher magnification view of the dense region of the infiltrated powder, figure 4.12., shows the SiC matrix growing on the SiC powder particles; it appears to be quite porous. This is likely to be because of the angular shape of the powder compared to the fibres, meaning the deposit is often growing in multiple directions. It is expected that the micro-porosity formed between powders with deposit would be filled if the composite had been infiltrated for a longer time.

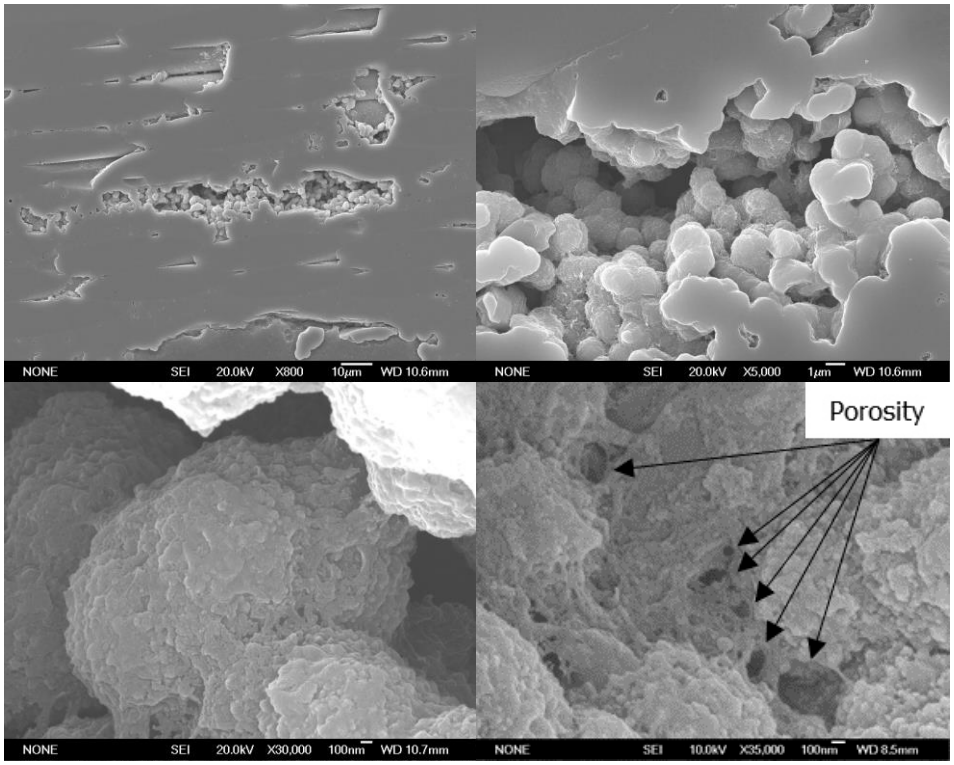


Figure 4.12. High magnification micrographs showing the deposition of SiC onto SiC powder particles and the micro-porosity that appears to have not yet been filled by the deposit.

4.1.2.2. *Effect of alpha ratio*

Figure 4.13. shows the cross-sectional densification profile of four preforms infiltrated at different alpha ratios; the latter is defined as the molar ratio between carrier gas, H_2, and the precursor gas, MTS, at any given time in the system, as shown by equation 2-6. The values on the left-hand axis of the micrographs indicate the alpha ratios that were used during the infiltrations. The values used were based on the thermodynamic calculations from D'Angio (2018) [243] and Naslain et al. (1998) [9]. There were varied primarily to determine the effect of alpha ratio on the Si:C ratio in the deposit, which will be discussed in section 4.1.3.2.2. Preforms were infiltrated for 8 h each at 925°C, a chamber pressure of 400 mbar and a Q_{MTS} = 0.2 g min^{-1}. The Q_{H2} was varied to create the different alpha ratios as shown by table 3.3.

Similarities between alpha 5 and alpha 10 can be seen; most noticeably that there was a uniform densification profile of SiC across the entire cross-section with an average deposit thickness of 2.1 ± 0.4 μm. As mentioned previously, dense regions were found on both sides, as shown in figure 4.14. Alpha 25 and 70 also display a common feature that is that there was a higher density region at the bottom surface; this was most likely because it was closest to the gas stream, figure 4.15. The deposit thickness on the 20^{th} ply was 11.3 ± 3.0 μm thick compared to <1 μm for the rest of the composite. Both of these samples were infiltrated for 16 h to ensure that there was some deposit to observe using SEM as the mass gain was so small. This is an unexpected feature as the higher flow rates suggest a higher permeability as per figure 4.86., which suggests that the deposition should be uniform throughout the preform. One possible explanation is because the gas was much diluted at the ratios used. The reaction proceeds fastest where the MTS concentration was highest, which is consistent with a mass transport limited reaction.

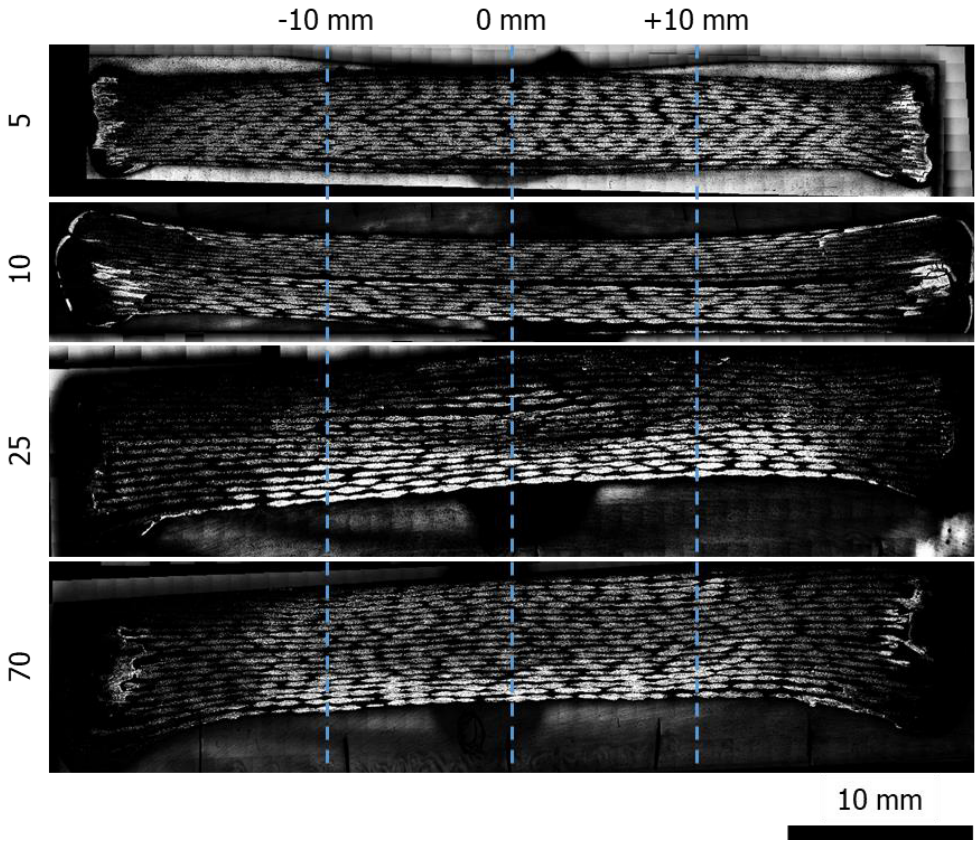


Figure 4.13. Stitched micrographs of the densification profiles of SiC_f preforms infiltrated at alpha ratios 5-70, where T = 925°C, P = 400 mbar, Q_{MTS} = 0.2 g min^{-1} were constant and the Q_{H2} was changed between samples.

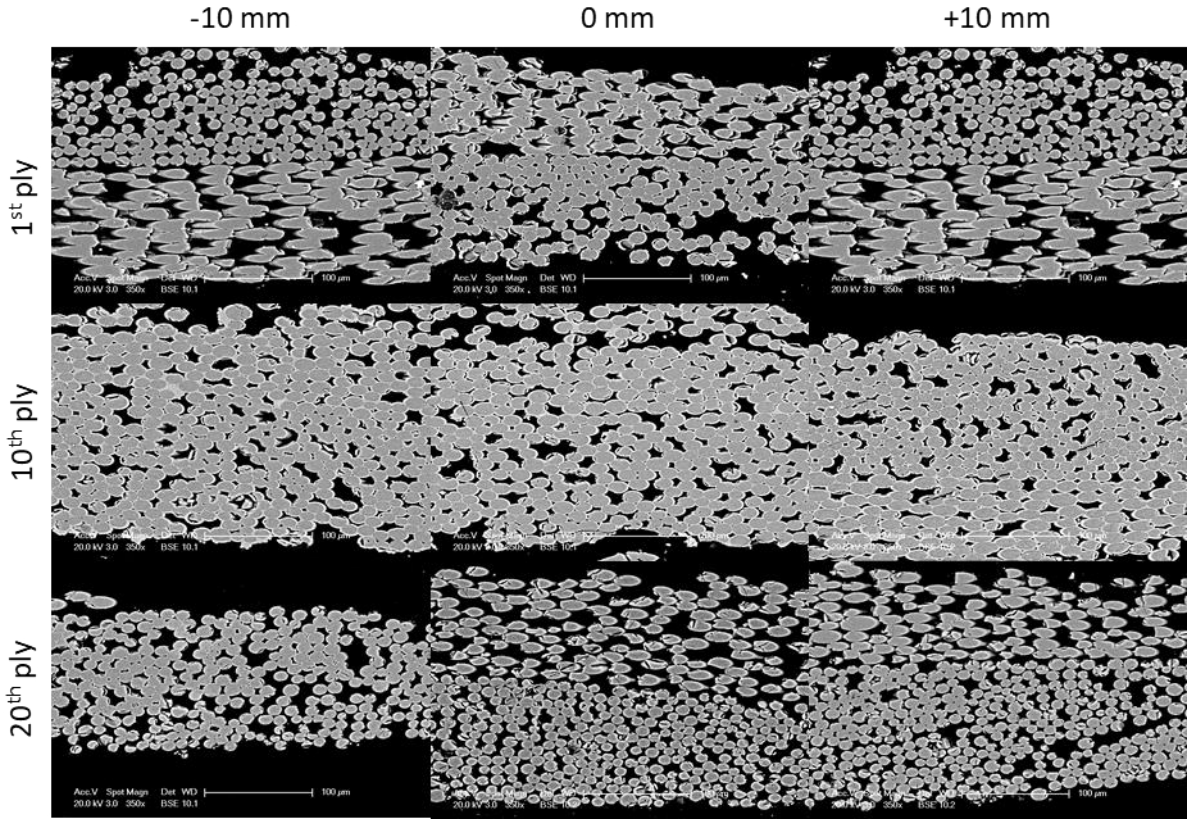


Figure 4.14. Higher magnification micrographs of the alpha 5 sample, showing uniform densification.

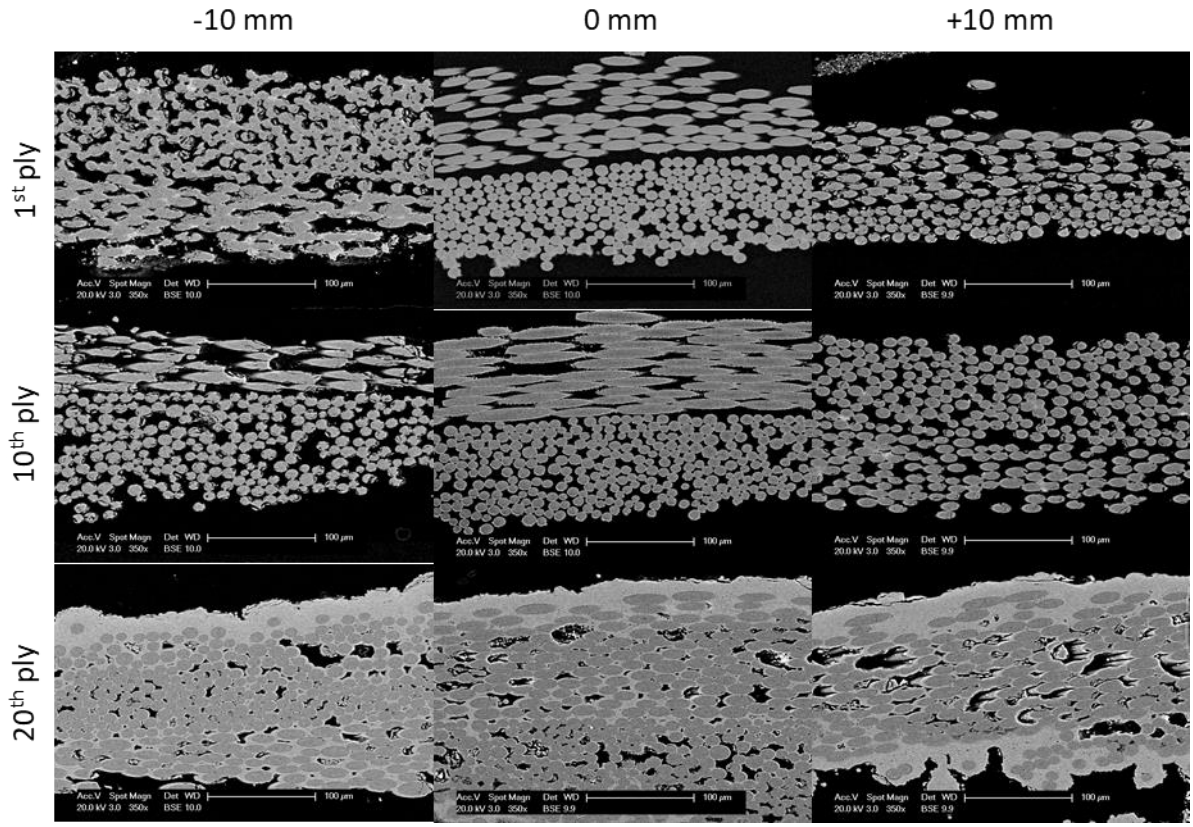


Figure 4.15. Higher magnification micrographs of the alpha 25 sample, showing densification in the 20th ply only.

Figure 4.3. previously showed the kinetics of the deposition process at the different alpha ratios. The orange marker on this graph represents the addition of the quartz bridge that was used to modify the gas flow path inside the bell jar, whilst figure 4.16. is the respective densification profile of this sample. It clearly shows a higher density region located in the centre of the sample with an average deposit thickness across the sample thickness of 4.6 ± 1.9 μm. Conversely, at ± 10 mm from the centre the deposit thickness is 2.0 ± 1.3 μm. This difference is illustrated in figure 4.17.

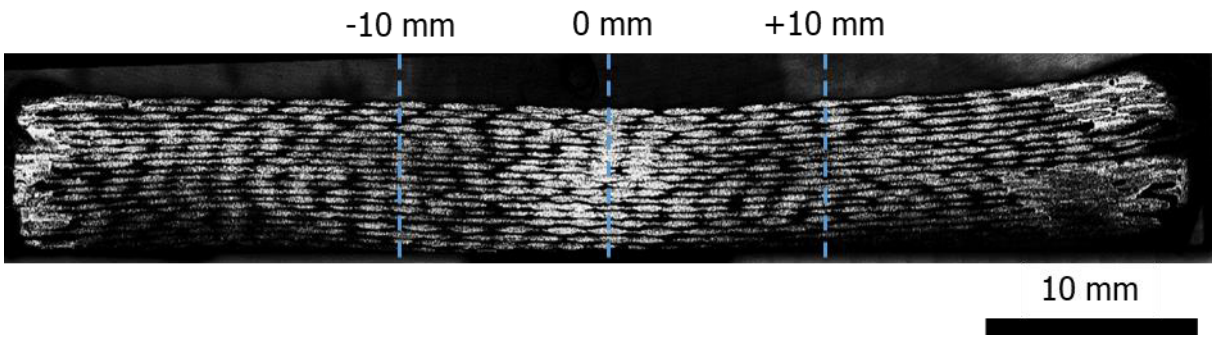


Figure 4.16. A series of stitched micrographs of the densification profile of a SiC_f preform. The conditions by which it was infiltrated are as follows: T = 925°C, P = 400 mbar, alpha = 10 and Q_{MTS} = 0.2 g min^{-1} Q_{H2} = 300 cm^{-3} min^{-1}.

This is critical evidence to show that inverse densification can be achieved, as suggested by the principles of microwave heating. From figure 4.16. and figure 4.17. there is preferential deposition in the middle of the preform and an increased deposition rate seen in figure 4.3. This indicates there was an increased quantity of precursor gas passing through the centre of the composite when compared with tests without the quartz bridge. However, this test cannot conclude that an inverse temperature profile was present as well, rather it shows that the precursor carrier mixture's trajectory through the sample has a very significant impact on how the composites densify and must be carefully controlled in all future work.

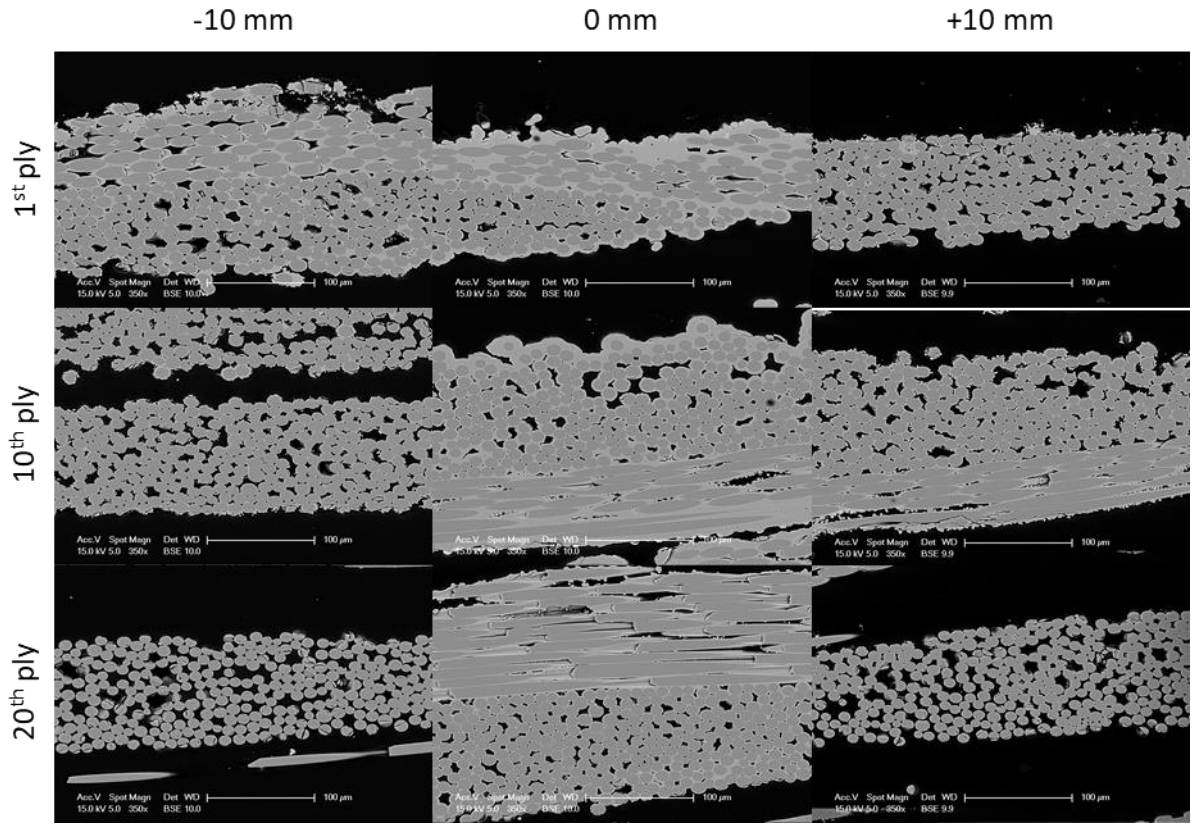


Figure 4.17. Higher magnification micrographs showing the effect of the quartz bridge on another alpha 10 sample, showing densification occurring preferentially in the centre region.

4.1.3. Morphology, composition and crystal structure of SiC deposit

4.1.3.1. *Morphology of SiC*

4.1.3.1.1. Effect of temperature and pressure

Figure 4.18. shows six SEM micrographs of the effect of infiltration temperature on the deposition surface morphology at constant pressure, 300 mbar. All images[x] were collected from within pore channels along the centre line of the composite in order to make direct comparisons between samples. The morphology of the deposit changed more the further from the centre line of the composite because of the temperature associated change. The surface of the sample infiltrated at 900°C shows a globular surface topography with rounded protrusions measuring between 70-200 nm in

[x] Images shown in Figure 4.18-20 were provided by Dr Andrea D'Angio [242]

diameter. This is because the low temperatures favour nucleation of the deposit and, because growth is slower, the nuclei density is higher. As the temperature increased the roughness of the deposit also increased. Samples infiltrated at 950°C and 1000°C clearly show more densely packed and larger protrusions, which at 1000°C range from 150-350 nm in diameter. Literature reports indicate that higher temperatures result in more stable growth of the SiC because of increased surface mobility, which produces the rougher morphology [232, 235]. These observations are similar to a number of other papers on the CVI and CVD of SiC that looked at deposit morphology. However, the temperature used that produced comparable morphologies is typically 200°C higher [241, 244, 254]. This also support the theory of the role of the 'microwave effect' as the same morphology has been seen at a lower deposition temperature, as described in section 4.1.1.3.

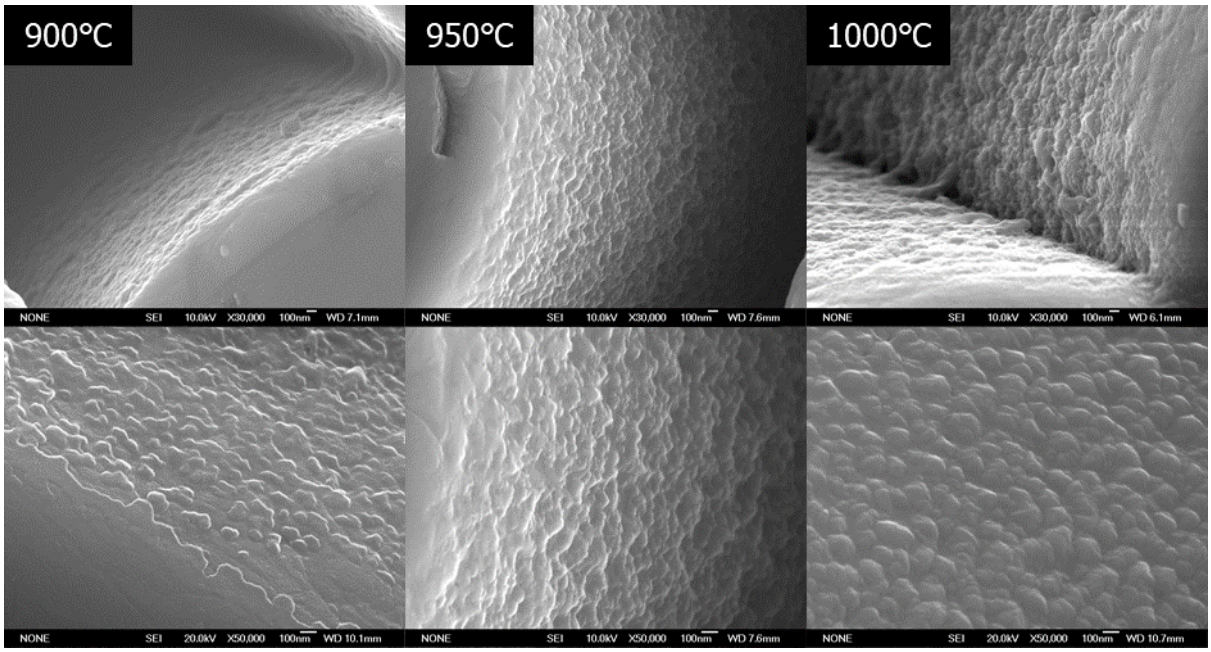


Figure 4.18. Six micrographs showing the effect of different temperatures on the surface morphology of the SiC deposit.

The effect of pressure can be seen in the SEM micrographs in figure 4.19 . These three samples were infiltrated at the same temperature, alpha and gas flow as figure

4.18. and only the pressure of infiltration was changed. The SiC deposit produced at the lowest pressure had a much smoother surface texture comparable to the higher-pressure deposits at 500 and 700 mbar, which were much rougher and more faceted. These results are consistent the CVD literature. Cheng [249] and Jacobson [250] found that at high pressure, the SiC that was deposited had a more angular appearance. Similar results were found by Sibieude [251], who went on to show using XRD, that smaller crystallite SiC was deposited at lower pressures. Chin [252] and Lespiaux [232] explained that the surface topography was related to the supersaturation of gases at the surface of the deposit. As the pressure increased, this supersaturation decreased, resulting in a more angular, larger and featured morphology. The opposite was seen at lower pressure where the surface had a higher degree of supersaturation. This supports the research carried out by Chui [241], who looked at the effect of the molar ratio of reactants on topography and showed that decreasing the alpha ratio increased the surface roughness. This is the same as effectively decreasing the degree of supersaturation, as explained previously by Lespiaux and Chin [40, 41]. Another example of this is represented by the large elongated structures seen in figure 4.20., which show the SiC deposited at 1000°C and 700 mbar. This deposition is much more typical of the morphology seen in the CVD regime.

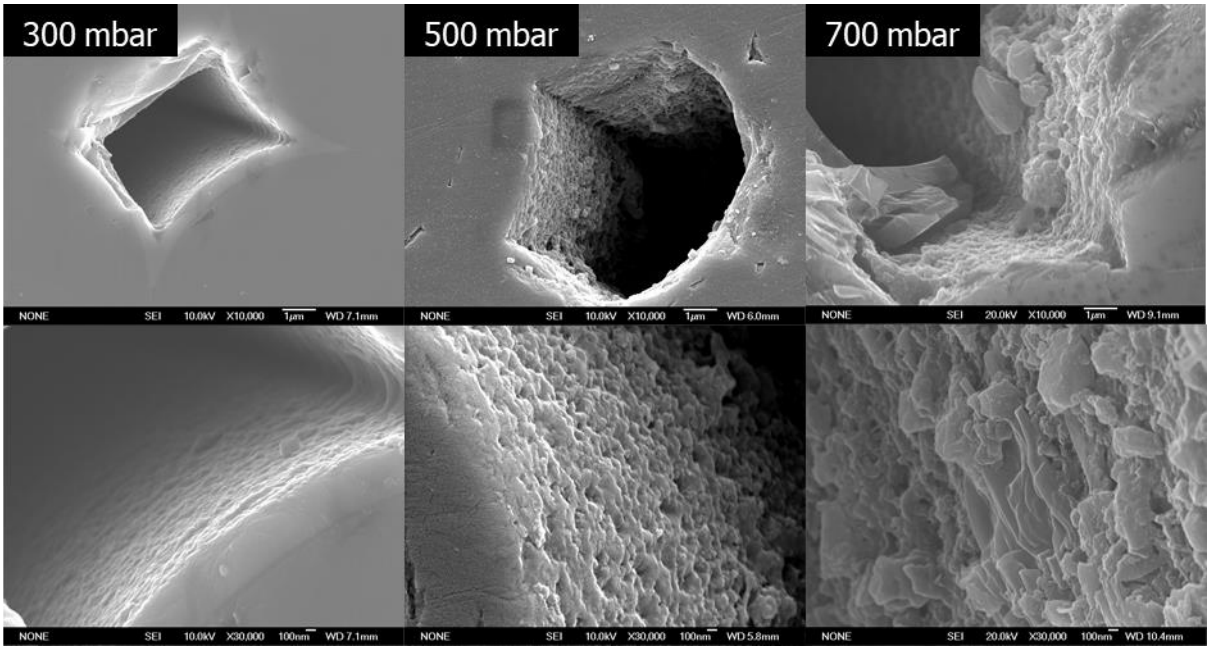


Figure 4.19. Images of the SiC deposit at different pressures but using the same magnification showing a significantly increased surface roughness with increasing pressure.

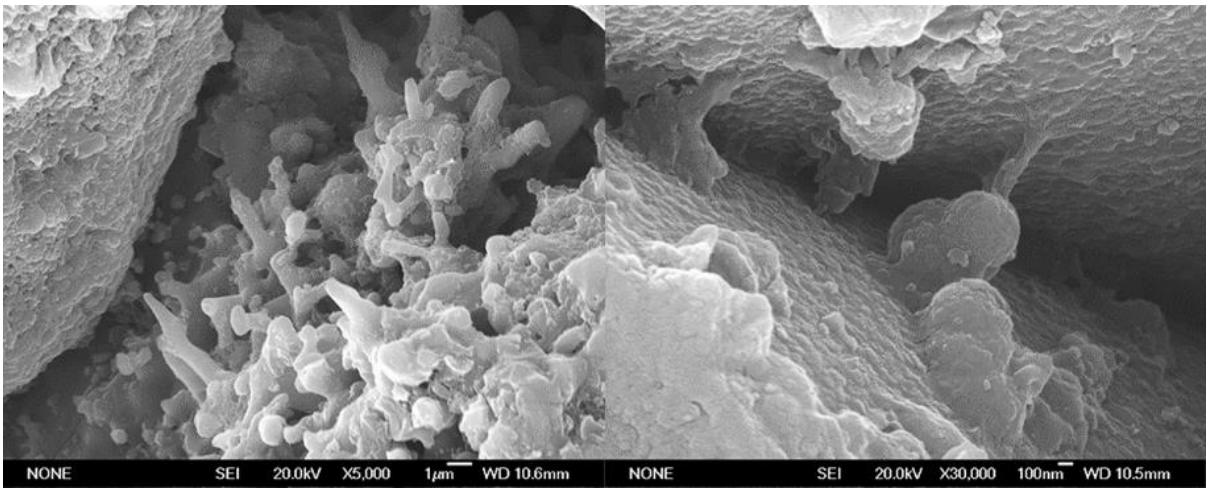


Figure 4.20. SEM micrographs showing the spine-like and large pustule regions of growth seen at 1000°C and 700 mbar.

4.1.3.1.2. Effect of alpha ratio

The effect of alpha ratio was also examined to see the impact of MTS dilution on the deposit structure, see figure 4.21. There is limited literature that describes this effect and none that evaluates the effect over the same range as this work. Papasoulitos and Sotirchos (1999) report the difference between alpha = 10 and 20 [254] and found that the higher dilution of the precursor produced a smaller globular formation.

This is seen in both alpha = 10 and 25 in this work with globular structures measuring approximately 1.0 μm and 0.1 μm respectively. There does not appear to be a significant effect between alpha 5 and 10, but alpha 25 shows a significant decrease in the size of the deposit. This spherical morphology is the result of heterogeneous nucleation [370]. Alpha 70 does not follow this trend, the morphology changes entirely, not forming the globular structure and appearing to show a much smoother texture. This is likely to be an effect of the high flow rate of hydrogen, which meant that there was no etching effect on the deposit because the partial pressure was low [246].

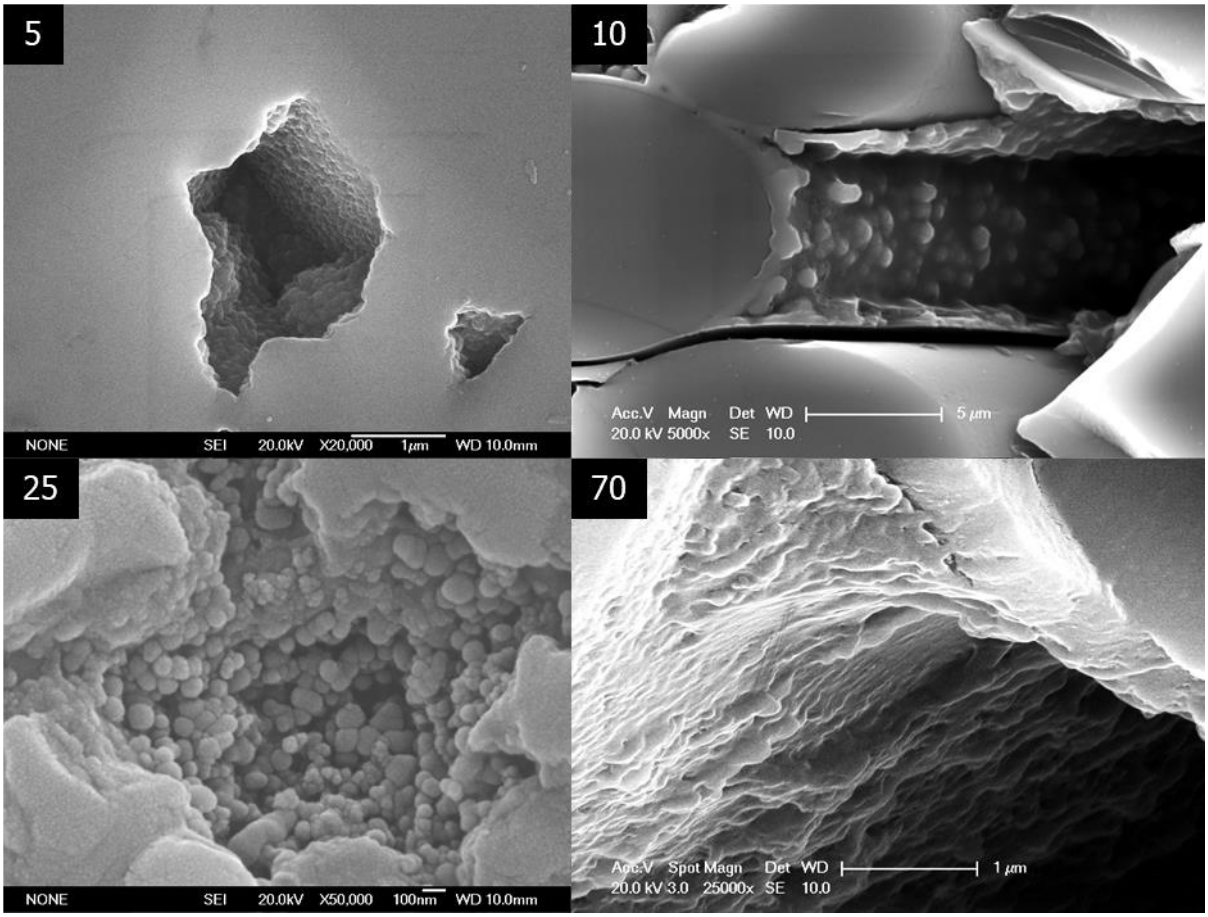


Figure 4.21. SE micrographs showing the variation of the SiC deposit morphology with changing alpha ratios.

4.1.3.2. *Chemical composition of SiC*

4.1.3.2.1. Effect of temperature and pressure

EDS and WDS measurements

The effect of temperature and pressure on the composition of the SiC were evaluated using a range of techniques. Figure 4.22. shows EDS and wavelength WDS. The EDS was fitted with a silicon drift detector that had been optimised for low atomic mass quantification. The wavelength dispersive technique used a translucent semiconductor grade SiC sample as a reference standard. From the bar charts below, the difference in the measured composition is very apparent. The EDS showed the Si:C ratio to be close to 1 with some oxygen detected, whereas the WDS showed the SiC deposit to be carbon-rich with high quantities of oxygen present. Both of these observations, when compared to the literature, are unexpected. Numerous papers state that low temperatures, i.e. T<1050°C, causes the co-deposition of Si (Si-SiC) and carbon co-deposition (C-SiC) at T>1200°C [230-232, 237, 240, 254, 350, 371]. Drieux et al. (2013) stated that the reason for this is the depletion of the reactive silicon species ($SiCl_2$) on the fibre surface in favour of the more stable $SiCl_4$. This increases the HCl concentration and inhibits Si-deposition whilst at higher temperatures forms of more reactive unsaturated hydrocarbons such as C_2H_2 could be responsible for the formation of C-SiC.

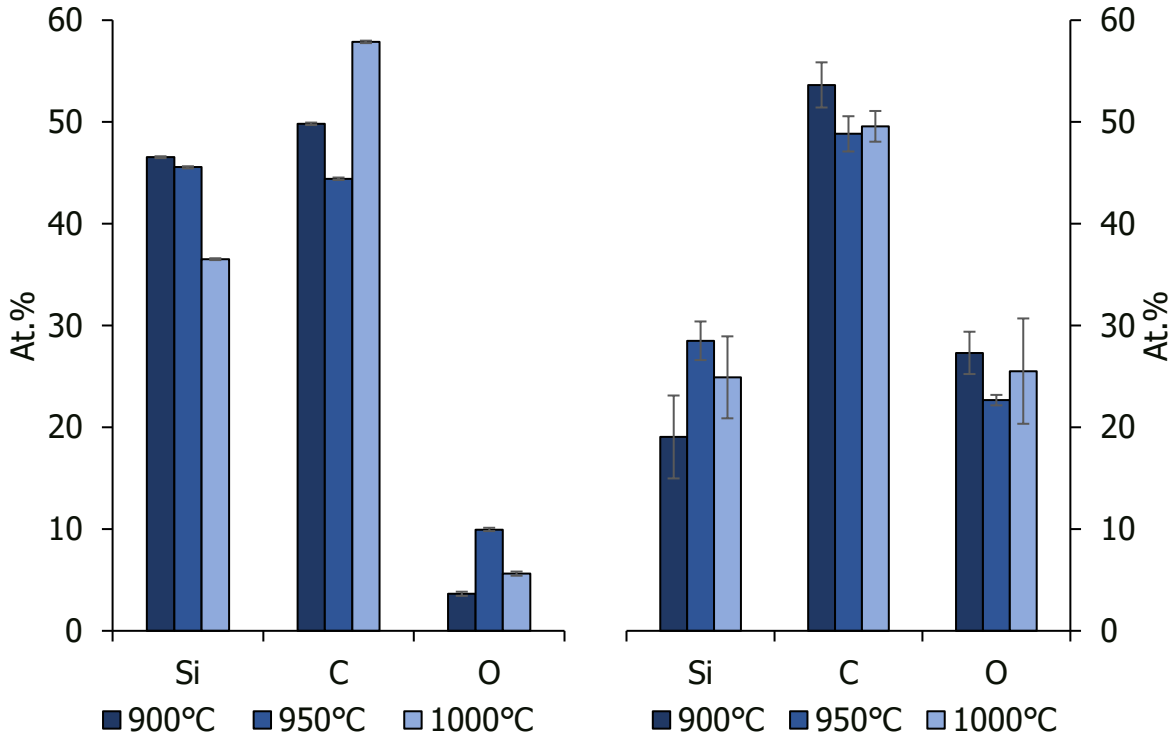


Figure 4.22. Bar graphs showing the composition of the SiC deposit at different temperatures using EDS (left) and WDS (right).

There are a number of arguments for and against both of these measurement techniques. The shorter processing time of the X-rays using EDS facilitates a larger data set to be collected and the whole periodic table can be evaluated at the same time. Whereas WDS requires multiple spectrometers in order to collect this information and it takes much longer. EDS, however, has a much larger energy resolution, meaning overlapping of element is common and accurate detection difficult. WDS is generally considered more sensitive than EDS as it measures only a single wavelength using a much higher count rate and not a spectrum of X-rays. Another benefit of using WDS is that it can be calibrated to a known composition; in this case, a very high purity SiC semiconductor was used, figure 4.23. However, since the semiconductor had no oxygen contamination, the WDS was not calibrated for oxygen prior to the measurement and its intensity was instead calculated by

difference using WDS software, which could have been a source of error. To summarise, both techniques were evaluated a number of times using different samples, on different machines but no consistency between measurements was produced. This prompted further investigation using other techniques in order to verify the composition. The discussion of EDS vs WDS will be returned to after presenting these results.

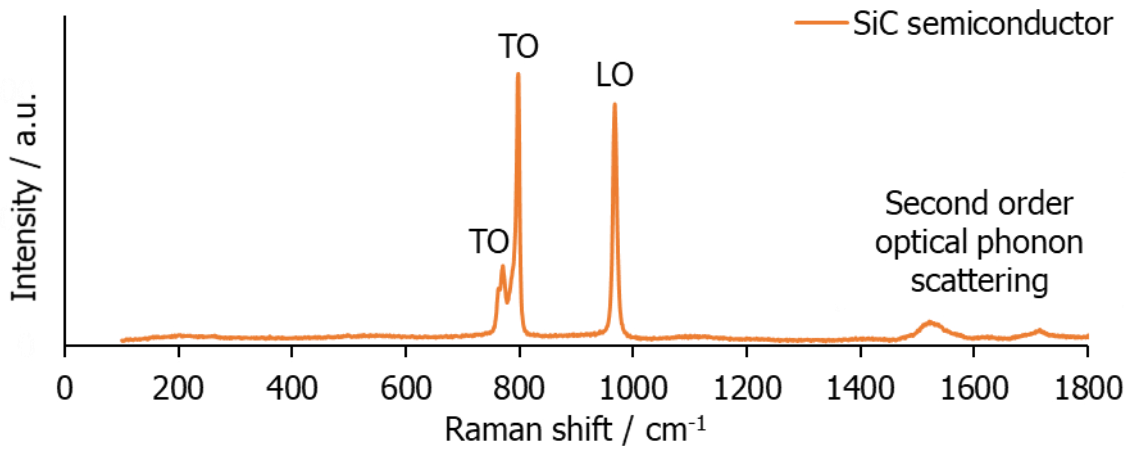


Figure 4.23. Raman spectra for the semiconductor standard showing the presence of both longitudinal and transverse optical phonons.

Raman spectroscopy

Figure 4.24. and figure 4.25. show the Raman spectra of samples infiltrated at different temperatures and pressures, respectively. Both sets of samples produced similar spectra with a number of key identifying features. The region between 100 and 500 cm^{-1} is the result of scattering of acoustic SiC phonons [372]. This occurs for a number of reasons; the translational symmetry of the crystal structure is limited either because of a high stacking fault or crystal boundary density, both of which are associated with small crystallites, <10 nm in size [373].

Table 4.2. Showing the Raman shift for the most common SiC polytypes, adapted from [372, 374]. Raman shifts in bold indicate the overlapping polytypes the commonly occur in SiC making explicit distinction difficult.

Polytype	**Raman shift / cm^{-1}**			
	Transverse acoustic (TA)	Transverse optic (TO)	Longitudinal acoustic (LA)	Longitudinal optic (LO)
3C	250-600	**796**	250-600	972
2H	264	799, 764	-	968
4H	196, 204, **266**	**796**, 776	610	838, 964
6H	145, 150, 236, 241, **266**	**769**, **797**, 789	504, 514	889, **965**
15R	167, 173, 255, 256	**797**, 785, **769**	331, 337, 569, 577	860, 932, 938, **965**

In this case, the occurrence of the two broad components, transverse and longitudinal phonons in the optical region, point to a fine-grained but heavily faulted β-SiC structure [375]. More evidence for this will be provided in section 4.1.3.3. In cubic SiC only two well-defined peaks should be observed, the transverse optical (TO) and longitudinal optical (LO) phonons, at 796 and 972 cm^{-1} according to table 4.2. In a faulted β-SiC structure, only the TO phonon is observed with a broad base indicating a fine grain size. This is consistent with the spectra seen in both figures. The additional broad peak region between 830-1050 cm^{-1} further suggests a loss of translation symmetry in the crystal structure and, more importantly, the lack of a single well-defined polytype [372]. A shoulder at ~765 cm^{-1} can also be indicative of the presence of a folded TO phonon of the 6H structure or the random distribution of stacking faults [372]. This feature does appears to be present in both the samples infiltrated at 1000°C in figure 4.24. and figure 4.25., potentially providing evidence for the production of 6H SiC. It should also be noted that there are no observations of either D-peak (1350 cm^{-1}) or G-peak (1650 cm^{-1}) carbon structures [376] in the spectra, thus providing supporting evidence for the results of the EDS spectra.

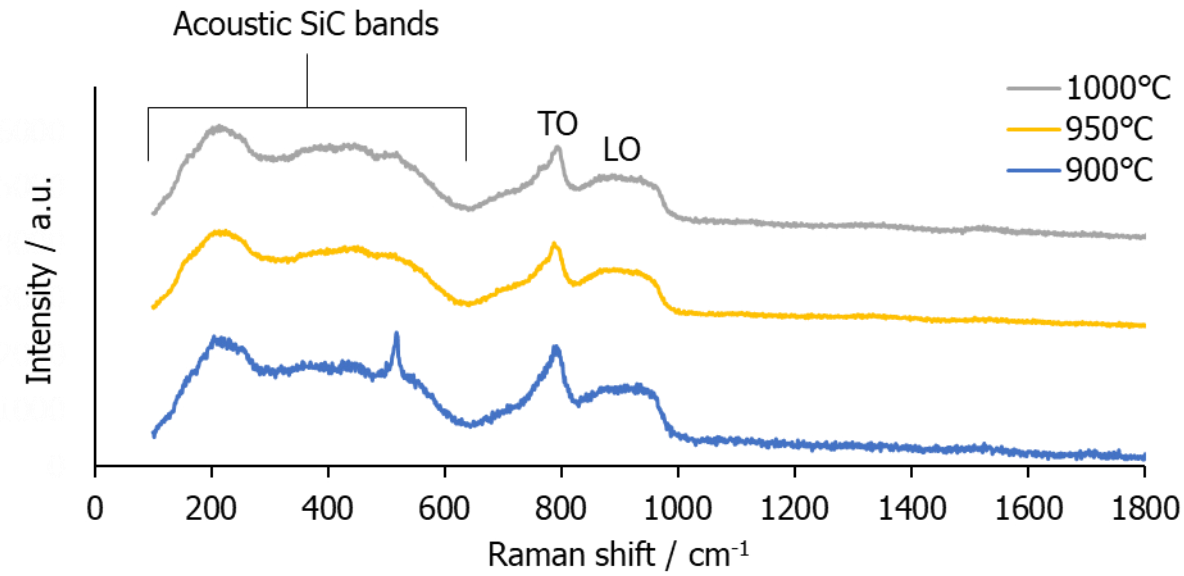


Figure 4.24. Raman spectra of the SiC deposit produced at different infiltration temperatures with a constant pressure of 300 mbar.

The distinct peak seen at 520 cm^{-1} in the 900°C at 300 mbar sample is evidence of free silicon in the crystal structure, which disappears as temperatures increase, see figure 4.24. This is again consistent with the trend observed in the EDS data in figure 4.22. As for the samples infiltrated at different pressures, the features of the spectra are very similar apart from the increasing intensity of the Si peak at 520 cm^{-1} with increasing pressure. This trend is also described in the literature [235, 236, 254] and Loumagne et al. [235] reports that it occurs because higher pressures promote the formation of unreactive methane, which does not consume the Si-containing species resulting in the codeposition of Si in the matrix.

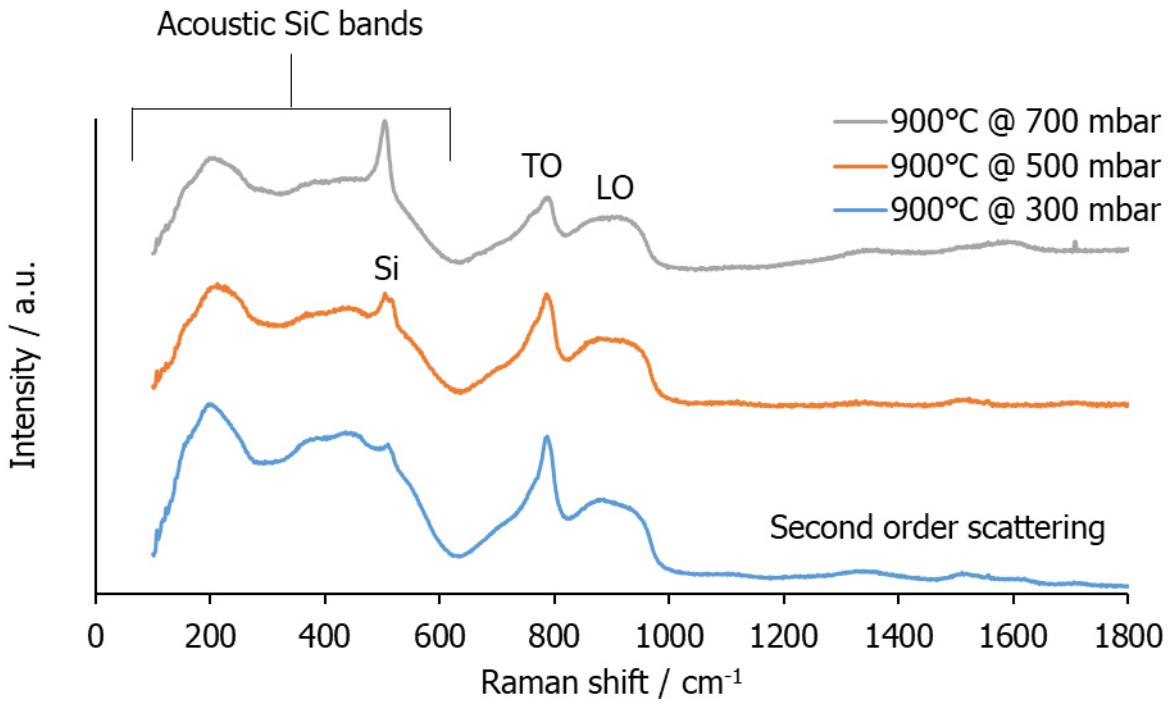


Figure 4.25. Raman spectra of the SiC deposit produced at different infiltration pressures.

This has been observed in the present work; figure 4.26. shows the Raman spectra corresponding to the micrographs shown in figure 4.27. They indicate the presence of free Si in the matrix formed at high pressure, a result also seen by Yang and Zhang (2009) [237].

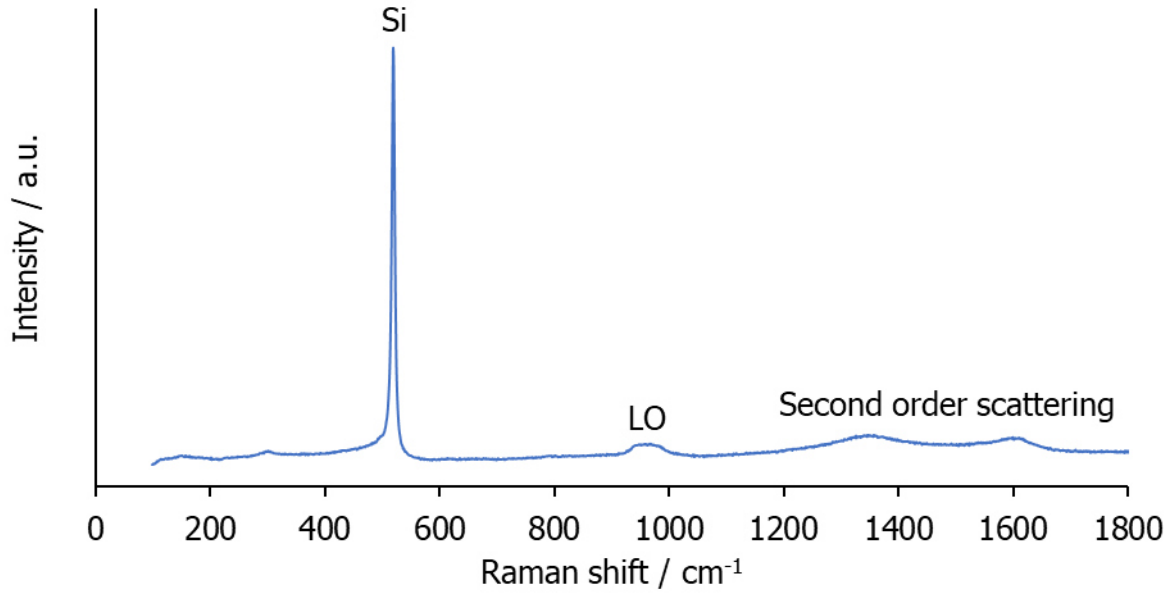


Figure 4.26. Raman spectra of the free silicon in the SiC deposit produced at high infiltration pressures.

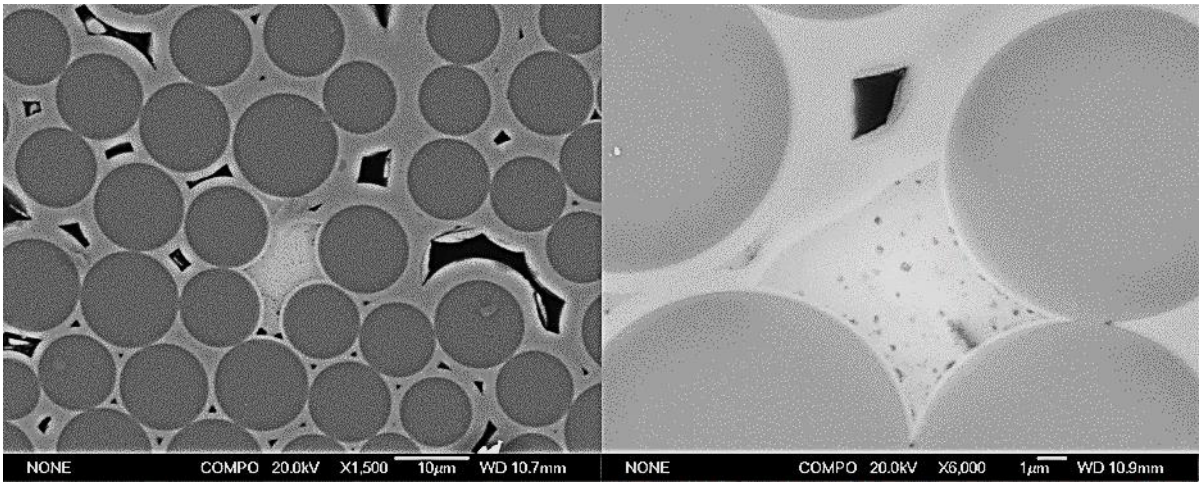


Figure 4.27. Two micrographs showing the free silicon in between the SiC fibres.

From the evidence presented above the EDS data appears to more closely aligned to the data reported using Raman spectroscopy, high-angle aperture dark-field and X-ray diffraction (presented in figure 4.35-37 and reported in the literature). Subsequently, analysis of the composition of the SiC deposit produced using different alpha ratios was evaluated using EDS, a table summarising the evidence for this can be found in Appendix III.

4.1.3.2.2. Effect of alpha ratio

Figure 4.28. shows the composition of the SiC deposit using EDS down the centre line of the composites infiltrated with different alpha ratios. Little variation in the Si:C:O ratio can be seen between samples, which all have an approximate Si:C ratio of 1.45. The alpha = 25 sample showed an increased oxygen content suggesting oxygen contamination had occurred during processing. The consistency of the data is somewhat unexpected. The literature reports that the dilution of the precursor gas with hydrogen, i.e. a higher alpha ratio, inhibits carbon deposition thus favouring the reduction of the cholorsilane species, which results in Si codeposition [231, 235].

Therefore, it was expected that the higher alpha ratio samples would have a higher Si:C ratio but this is not the case. This result strongly indicates that temperature and pressure are the primary factors determining the Si:C ratio of the SiC deposit and therefore the temperature of infiltration should be 950°C≤T≤1000°C and the pressure kept as low as possible.

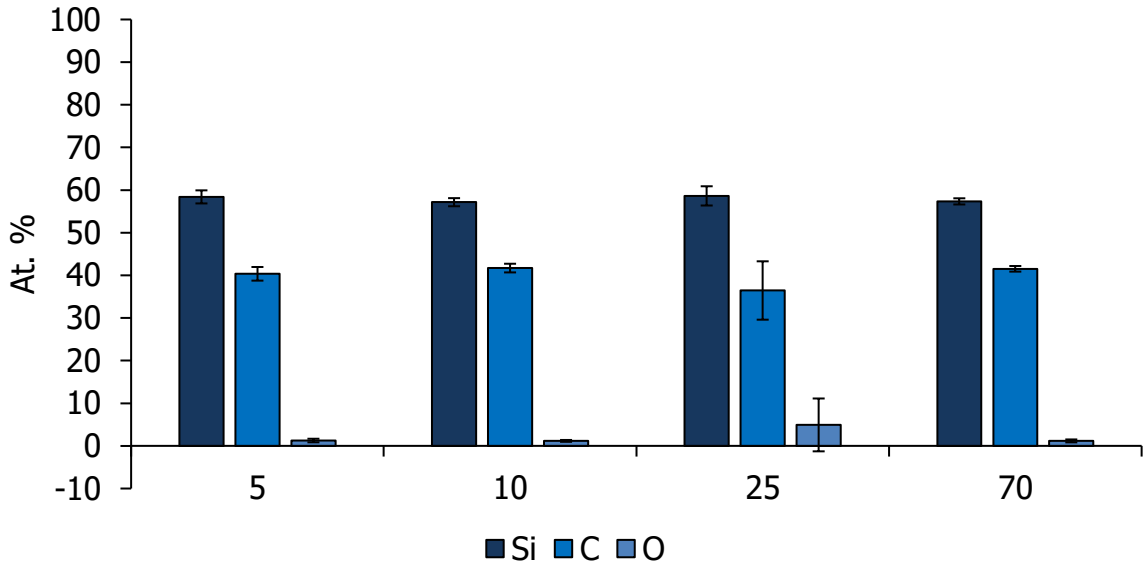


Figure 4.28. The Si:C:O ratio in the SiC_f/SiC samples infiltrated with different alpha ratios with T = 925±15°C and P = 400±8 mbar.

4.1.3.3. *Crystal structure of SiC*

4.1.3.3.1. Effect of temperature and pressure

Figure 4.29. (a) shows a bright-field image of a TEM foil of SiC deposit sandwiched between two amorphous ZMI fibres showing the microstructure and crystal orientation of the matrix grown at 900°C. A SAED pattern was taken of the area as shown in the bottom right-hand corner of (a) showing the position of the aperture. The diffraction pattern (b) showed a ultrafine polycrystalline deposit with a high degree of stacking faults; a featured particularly prevalent in CVD/CVI processes that can affect electron transport and therefore alter EM absorption properties [377]. This

pattern was found to fit a face centre cubic (FCC) structure indicating 3C β-SiC had been formed and then it was indexed using templates built into the TEM software. Dark-field images were taken of the brightest diffraction rings closest to the zone axis, which were 111 and 002 orientations. These dark-field images were then overlaid and assigned a colour to facilitate observation of the grain structures. Figure 4.29 (c) shows some columnar grains, approximately 1 μm in length, growing perpendicular to the fibre surface [378]. These grains appear to form a substrate, from which further nucleation occurs. These grains are less columnar and more equiaxed in shape, potentially because the substrate they grew on was crystalline; the original 111 grains seeded on the amorphous fibres. Figure 4.29 (a) shows a 'flower' like feature in the deposit highlighted in a red circle. Details on this are presented later in this section.

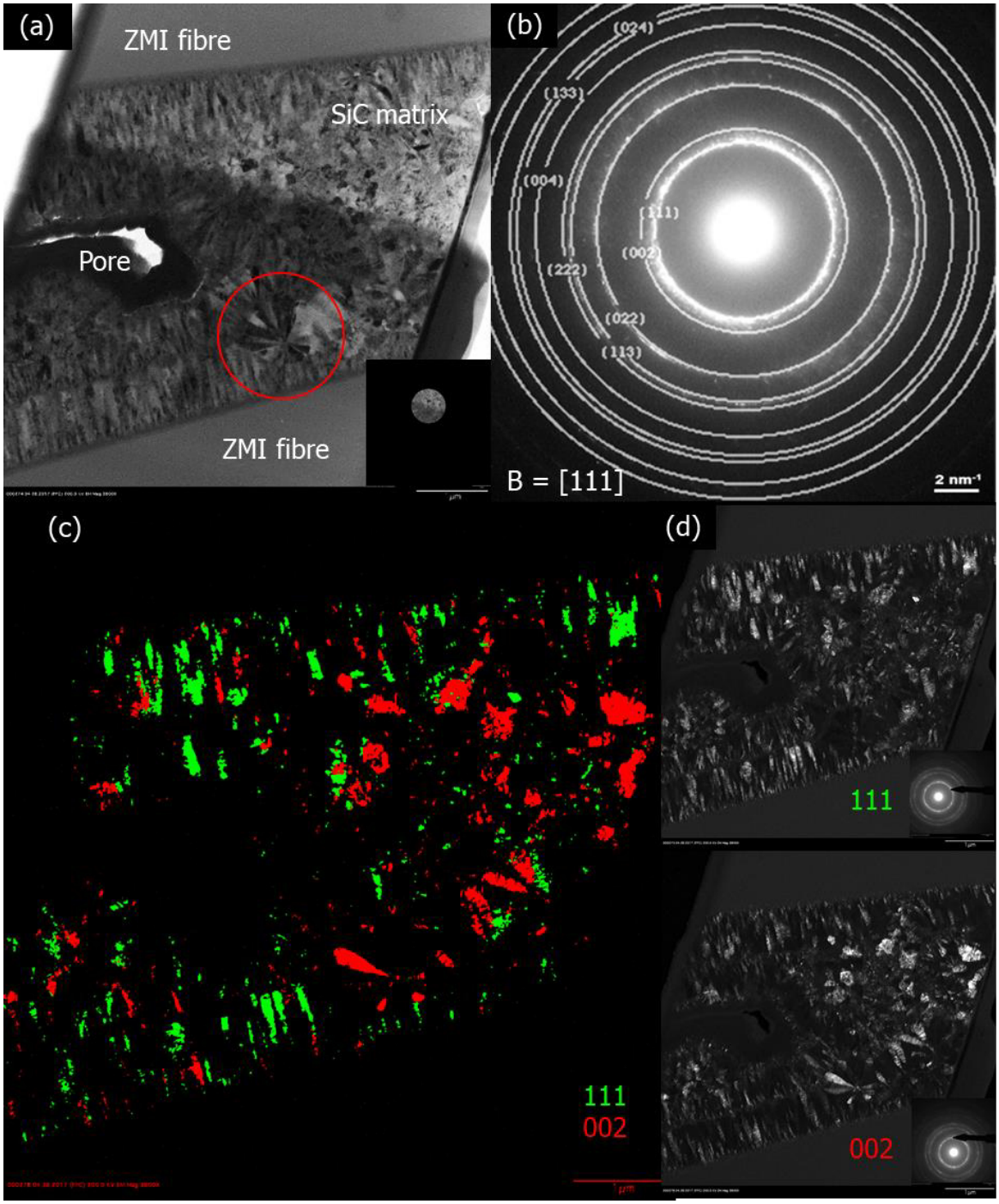


Figure 4.29. (a) A bright-field image of a SiC_f/SiC foil taken at the centre of 900°C 300 mbar sample, (b) selected area electron diffraction pattern of the SiC matrix, (c) two overlaid and coloured dark-field images corresponding to the images in (d).

At 950°C, the degree of texture and length scale of the grains in the SiC deposit increased due to the increased growth rate. Figure 4.30. (b) shows that the crystallinity of the deposit also increased due to the transition from a ring to dot pattern. The grain size increased the further from the fibre they nucleated from the

fibre surfaces, different grain orientations develop, including 220 and 202. This has been reported before in the literature [379, 380] that this is due to different intermediates becoming dominant at higher temperatures. There is also an interface shown in (a) where the matrix has grown together from two adjacent fibres. This explains the broader grains, which have been milled at an angle giving them a larger appearance.

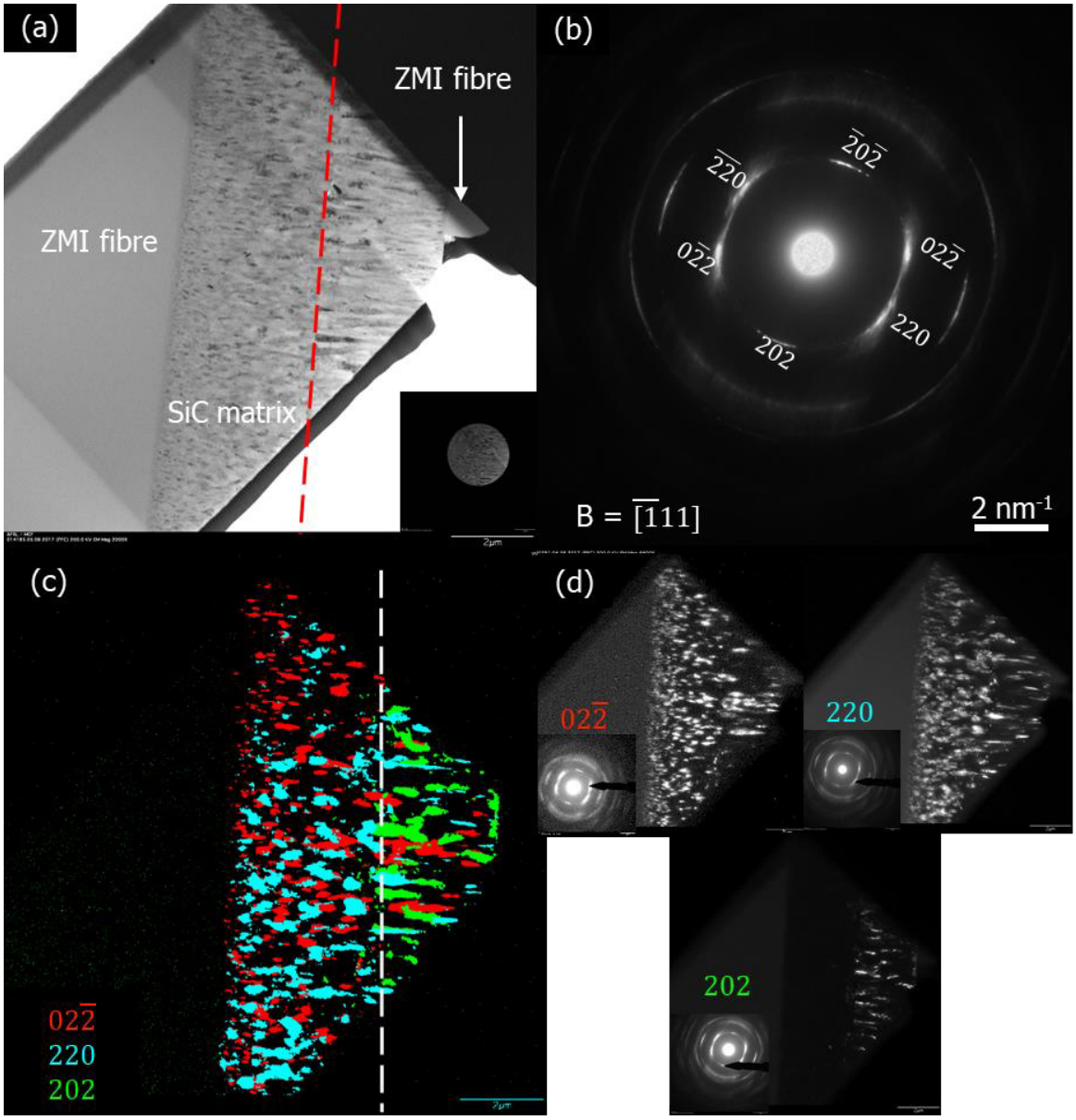


Figure 4.30. (a) A bright-field image of a SiC_f/SiC foil taken at the centre of 950°C 300 mbar sample, the dashed line shows the fibre merging interface, (b) a selected area electron diffraction pattern of the SiC matrix, rotation of the pattern was applied, (c) three overlaid and coloured dark-field images corresponding to the images in (d).

Figure 4.31. shows that a highly anisotropic crystal structure with a large aspect ratio was formed at 1000°C. The initial crystal growth on the fibre surface is seen to be small potentially as the fibre is amorphous. Once the initial SiC has been deposited larger grains nucleate and grow from the textured surface, again were primarily orientated perpendicular to the fibre surface. It is expected that had more dark-field images been taken then different orientations would have been observed similar to the 950°C sample.

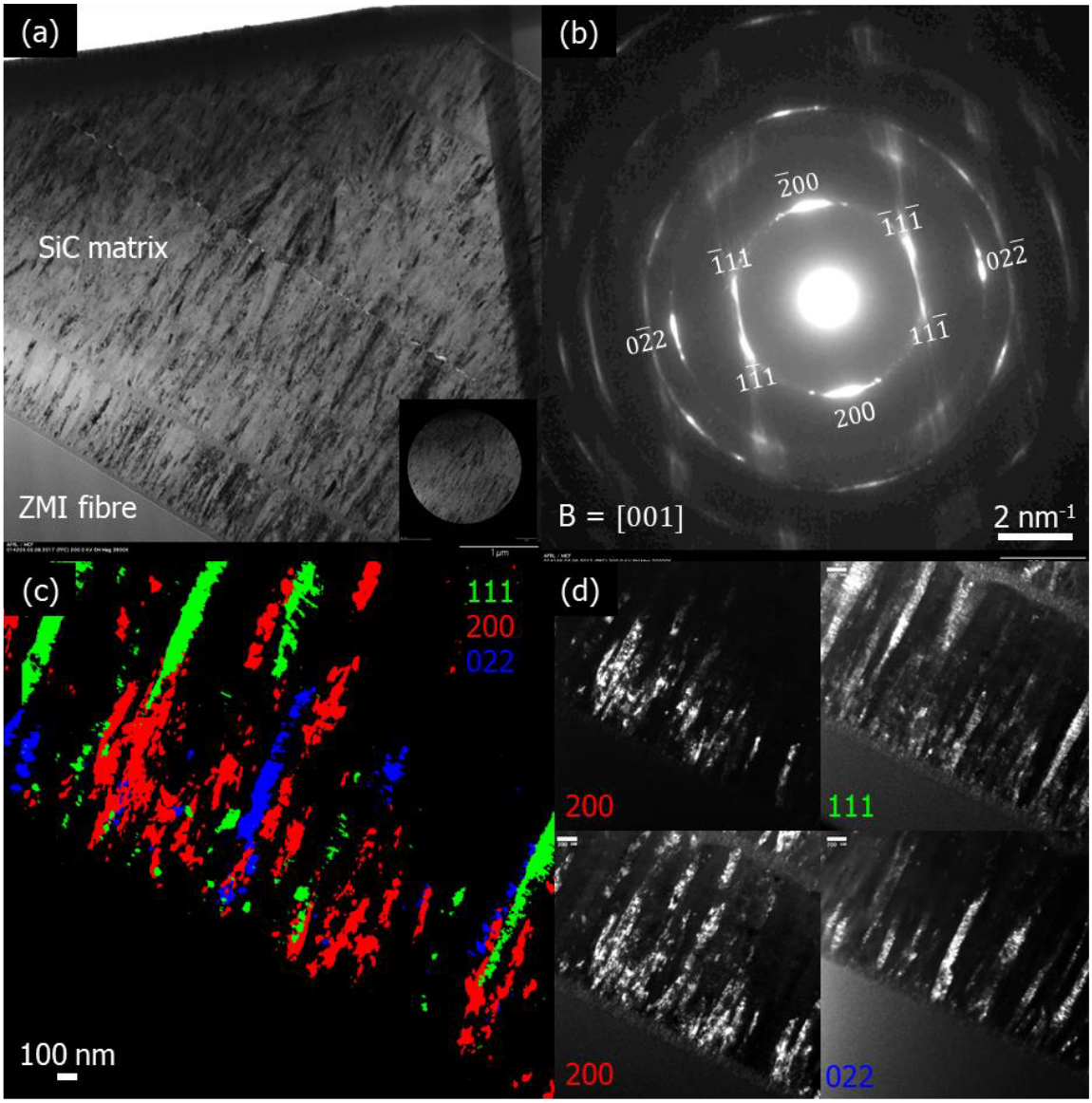


Figure 4.31. (a) A bright-field image of a SiC_f/SiC foil taken at the centre of 1000°C 300 mbar sample, (b) a selected area diffraction pattern of the SiC matrix rotation of the pattern was applied, (c) four overlaid and coloured dark-field images corresponding to the images in (d).

Other matrix features

As mentioned earlier in this section, the 'flower-like' feature in figure 4.29. has also been reported in the literature previously because of similar, low-temperature experiments. Pampuch, Stobierski and Lespiaux [232, 354], Langlais and Naslain [363] both report the formation of these features. Lespiaux goes on to suggest that it is the result of free silicon formation due to stagnation in the boundary layer. This free silicon acts as a secondary substrate for SiC to nucleate on creating radial growth around the central Si grain. This theory was tested using HAADF mode to observe this pure Si grain, however as seen in figure 4.32, no Si concentration was observed and the Si (b) and C (c) appear to be uniform in distribution. Contrast in the 'flower' is seen due to the different orientations. Figure 4.33. shows a series of bright-field images at increasing magnification, and their corresponding diffraction patterns, for the different patterns and striations through the grains. These indicate the presence of stacking faults in the structure, as seen in the Raman spectra and figure 4.29 (b). As there appears to be no concentration of free silicon it is thought that it may simply be a SiC grain forming at one of these stagnation points in the boundary layer which provides a surface for further deposition, nucleation and growth.

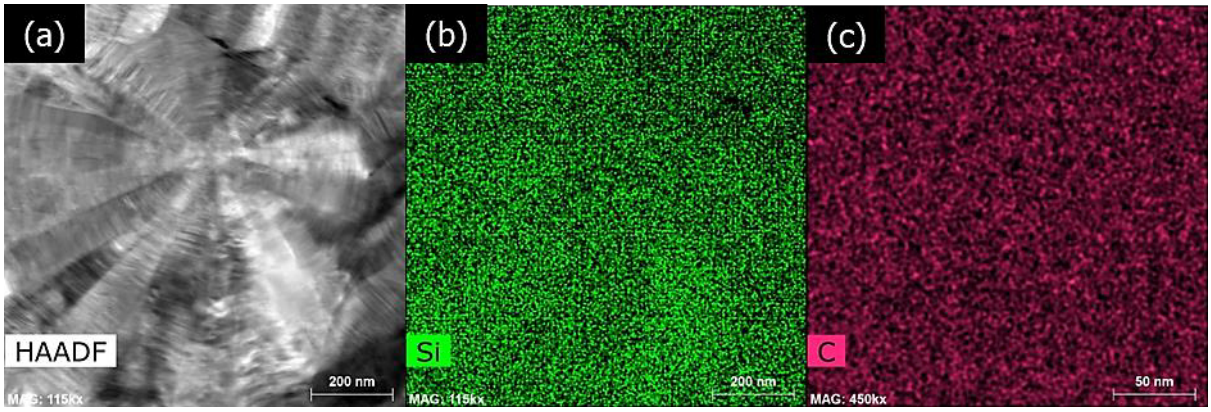


Figure 4.32. (a) High-resolution bright field image of a supposed 'Si' inclusion seen in the 900°C 300 mbar sample, (b) corresponding Si map and (c) C map.

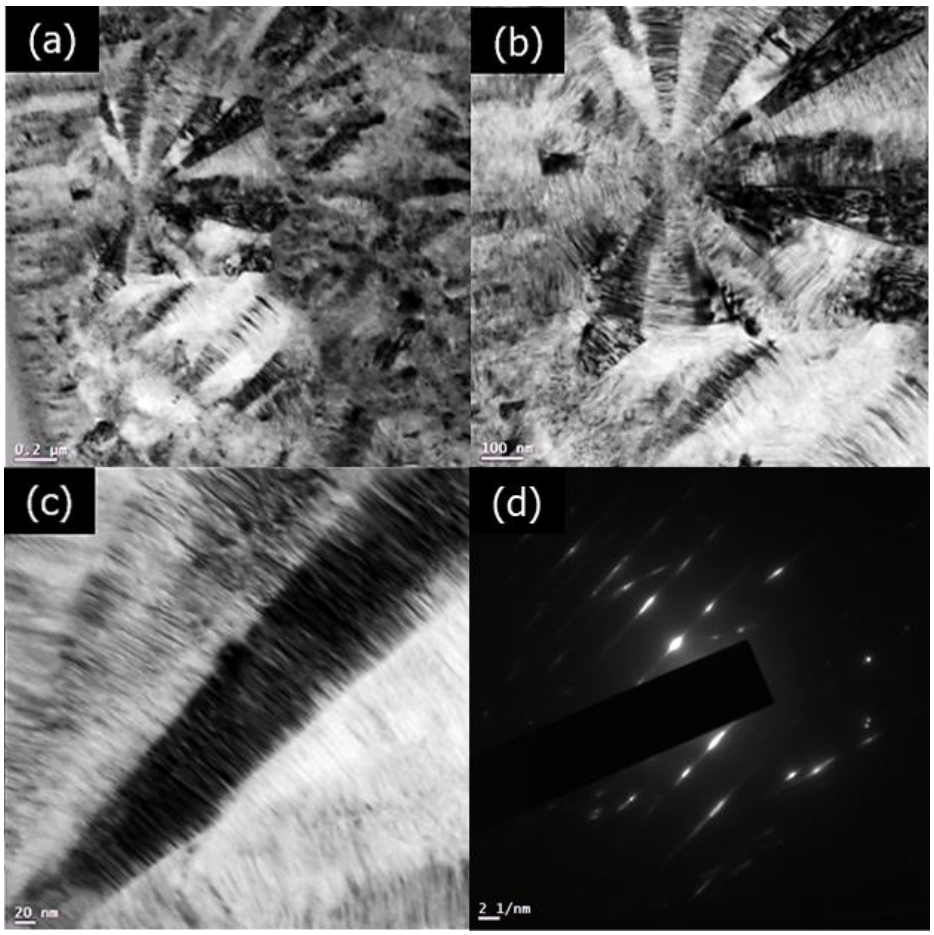


Figure 4.33. (a) A low magnification bright-field image of the 'flower' inclusion near the fibre (bottom left corner), (b) magnified image of the feature, (c) a single grain showing high contrast indicating different orientations and horizontal striations caused by stacking faults in the lattice which were confirmed in the diffraction pattern seen in (d).

Other features observed in the 1000°C sample are shown in figure 4.34. Feature 1 shows amorphous bands in the microstructure and on the fibre surface. These were

analysed using HAADF and found to be oxygen-rich regions indicating SiO_2 formation, see figure 4.35 and figure 4.36. The oxygen-rich region on the fibre surface are likely produced by residual oxygen adhering to the fibre surface prior to heating the fibres up or the residual oxygen in the cavity being absorbed onto the fibre surface. D'Angio [243] suggests the latter is observed experimentally through the temperature drop seen in the initial stages of the MCVI process due to the endothermic formation of SiO_2 from MTS [381]. Best practise for future work would be to store the SiC fibres under vacuum or initially pass a high concentration of H_2 through the system in order to minimise this effect. The second and third amorphous layers of SiO_2 are seen in the matrix; these are produced in the time between infiltrations when the system is shut down to allow the samples to be removed so that their masses can be measured. Once this was discovered, samples were stored under vacuum and not removed from the cavity whilst hot in order to minimise these amorphous layers forming. The wavy shape of the oxidation seen in figure 4.36. is a consequence of the angular termination of growth of the SiC crystals. Feature 2 is the coming together of matrices growing normal to parallel fibres. Due to the angular deposition front where the deposition meets, they do not completely coalesce resulting in the formation of nano-porosity measuring ~50 nm in length. At present, it is not known if this porosity is open or closed. If it is open then simply increased processing time may be sufficient to close these pores. If the latter operating at as lower pressure as possible will be able to reduce or eliminate its formation.

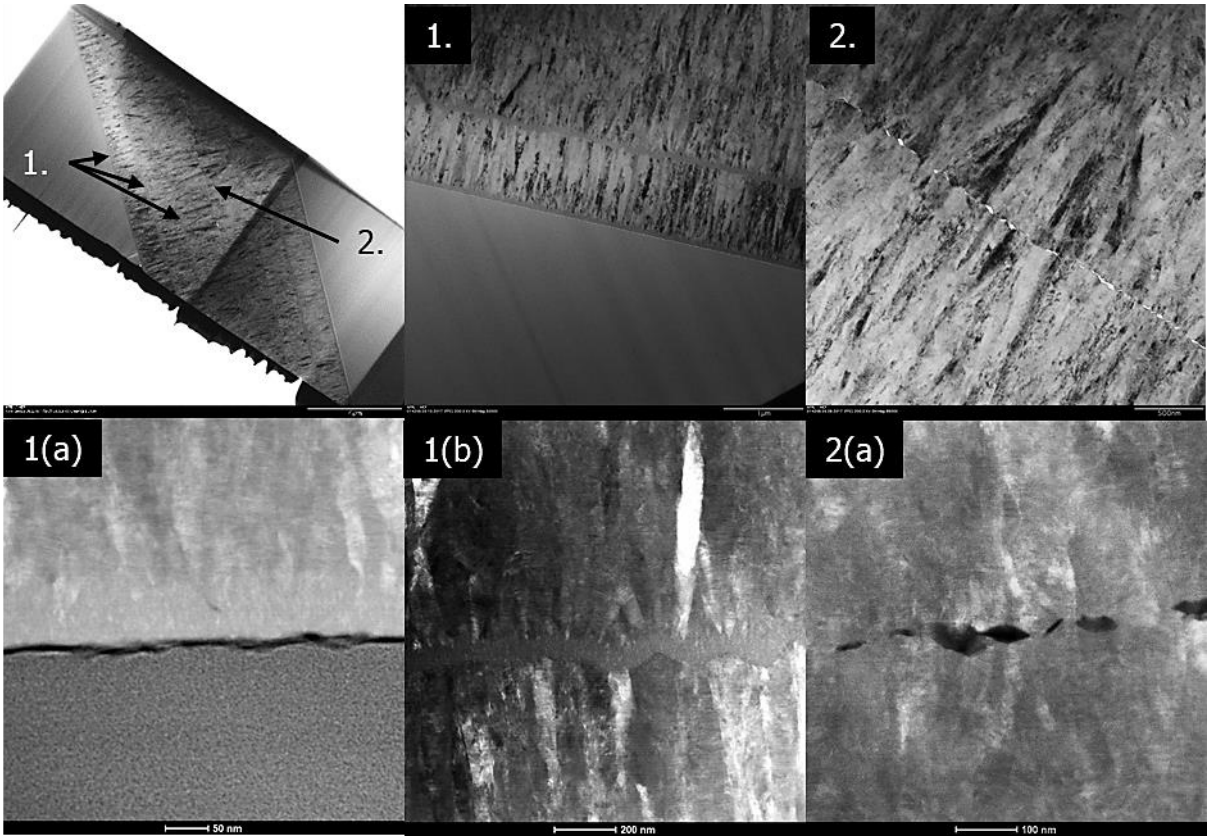


Figure 4.34. High-resolution BF images of the microstructural features seen in 1000°C 300 mbar sample. 1. Amorphous SiO_2 banding at the fibre-matrix interface, and 2. Nano-porosity formed between converging SiC grains from neighbouring fibres.

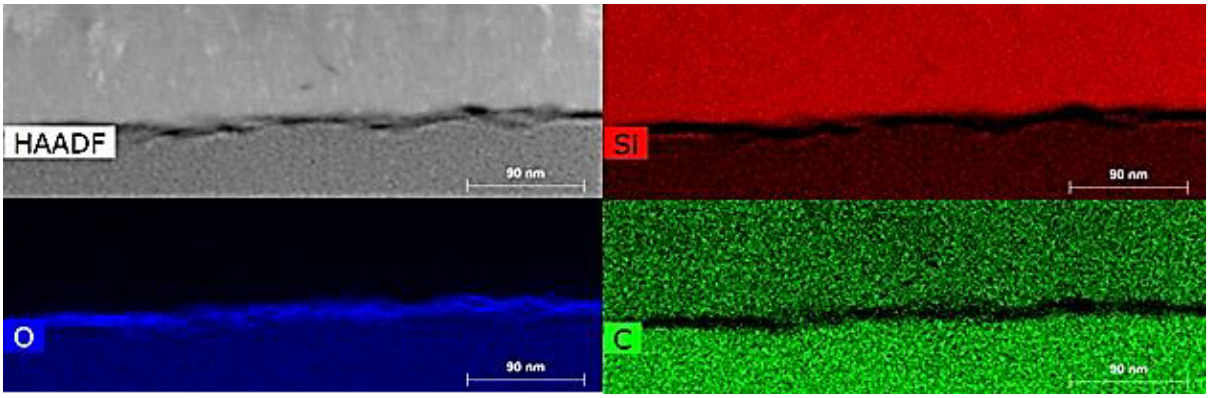


Figure 4.35. Elemental maps of the amorphous oxide band, most likely SiO_2, found at the matrix-fibre interface, corresponding to 1(a) in figure 4.34.

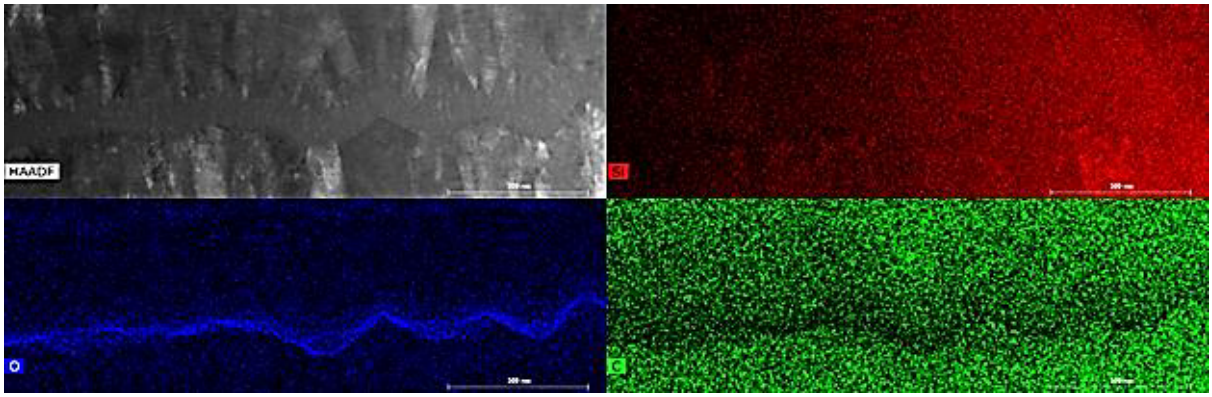


Figure 4.36. Elemental maps of the amorphous oxide band found in the matrix that was produced between infiltrations, corresponding to 1(b) in figure 4.34.

4.1.3.3.1. Effect of alpha ratio

Figure 4.37. shows five XRD diffractograms for the ZMI fibre and the samples infiltrated at different alpha ratios. The traces were produced using the method described in section 3.3.3. Both the alpha = 5 and alpha = 10 samples show narrower peaks than the alpha = 25 and alpha = 70 samples. This is thought to be because of smaller crystallite size rather than an artefact from instrumentation, a statement supported by figure 4.21. This is based on the relationship between peak width and crystallite size in the Scherrer equation [382]. A diffractogram of the ZMI has also been taken showing the 3C β-SiC crystallites in a predominantly amorphous structure. This demonstrates the difference between the fibre and SiC deposit. A number of common phases have been identified as well. All samples tested showed the presence of β-SiC peaks at 2θ = 35.8°, 60.2° and 72.1° corresponding to the crystallographic planes: 111, 220, 311, respectively. Both alpha = 5 and 10 also showed a single α-SiC peak at 2θ = 34.8. Some carbon peaks were also detected in the alpha = 10, which was unexpected based on previous results but does support the WDS analysis mentioned earlier in this chapter, though this could be from the fibre. The occurrence of α-SiC peaks was unexpected as typically α-SiC is formed at

much higher temperatures [77] than were used in the MCVI experiments. This mixed-phase deposition has been reported in the literature, all of which use temperatures >1000°C [244, 255, 378]. A mechanism for its formation has not been proposed due to the time constraints of this project but it could be hypothesised that this again could be a result of the microwave effect detailed earlier.

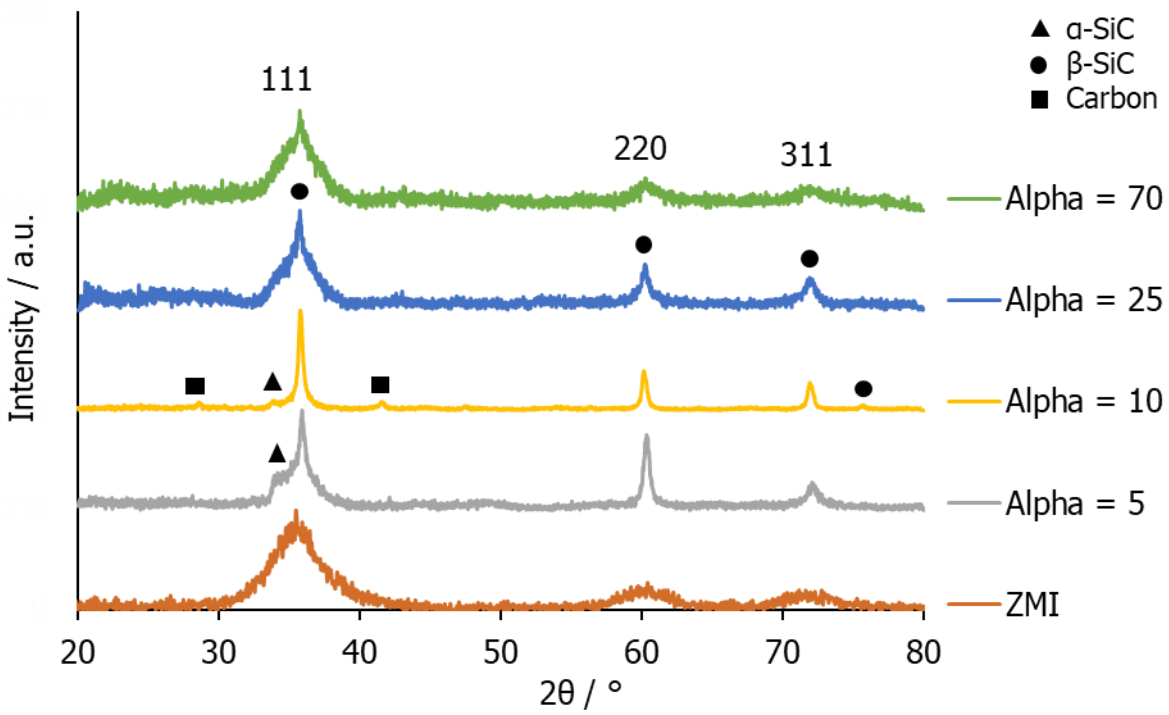


Figure 4.37. XRD diffraction patterns for the samples infiltrated using different alpha ratios.

Further observations were then made on alpha = 5 and 10 using TEM to examine the α and β-SiC phases. Figure 4.38.(a) shows another milled section of the alpha = 5. Similar to previous images, it shows common features of the crystal structure; nano-porosity, grain growth perpendicular to fibre direction and an increased grain size further from the fibre surface. Interestingly there appears to be a degree of debonding between the fibre and matrix that has not been seen previously; Figure 4.38.(b) shows a higher magnification BF image. This delamination is thought to be, either, a product of the FIB process or the result of the directionality of the grain

growth, the latter because of the residual stress normal to the fibre-matrix interface. If true, this indicates, as expected, that an interface will be required to facilitate fibre pull out in the CMC.

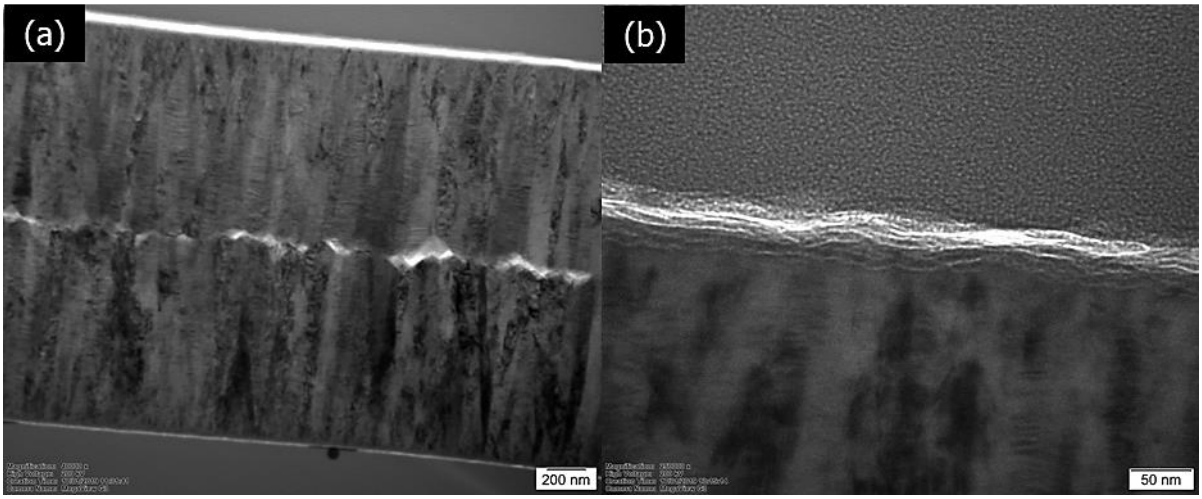


Figure 4.38. BF images showing delamination of the matrix from the fibre from alpha = 5.

Figure 4.39. shows the various textures seen in the alpha = 10 sample. (a) shows a diffraction pattern taken of the dark grain seen in 4.39.(a*) beneath it; it shows an HCP pattern and so corresponds to α-SiC, as seen in the XRD diffractogram. Figure 4.39.(b) shows the presence of a heavily faulted β-SiC structure and in (b*) a significant number of twins can be seen around the dark grain in the centre of the image. Figure 4.39.(c) shows a polycrystalline structure at the interface between the bulk deposit and the fibre. This is because in the initial stages of SiC deposition, the number of nucleation events is high but the growth of grains is small, relative to the later stages of processing.

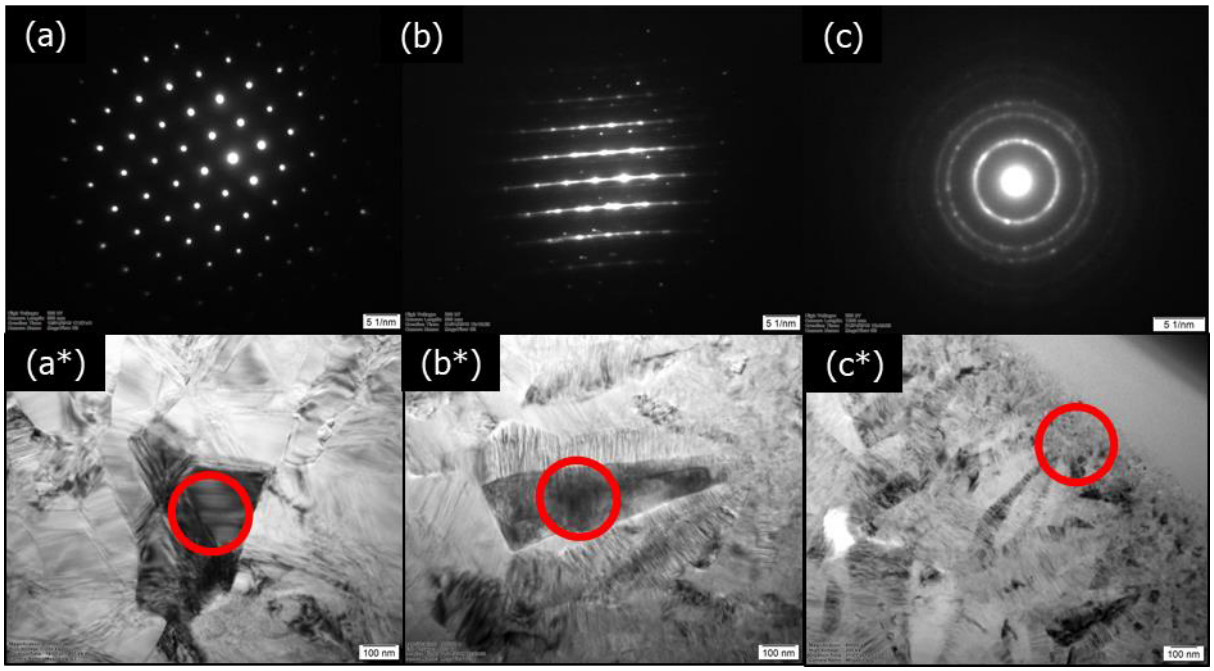


Figure 4.39. (a) SAD pattern showing a grain α-SiC found in the alpha = 10 sample, (b) a crystalline but heavily twinned grain of SiC and (c) the transitional region between the fibre and textured region of the SiC as indicated.

Figure 4.40.(a) shows a BF image illustrating the direction of deposit growth from the fibres showing specifically how the deposit crystal size changes the greater the displacement from the fibre surface. The red circle indicates the step change from a nucleation favoured regime to a growth regime. This transition might be the result of the substrate the deposit grows on changing from amorphous to crystalline as the deposit reaches a critical coverage of the fibres. This nucleation regime may be eliminated if a fully crystalline fibre was used. This would mean that the substrate would be crystalline from the outset of the deposition, thus the growth regime would be favoured earlier in the process, which, in turn, might increase the deposition rate further. Similarly to figure 4.29. and figure 4.33., Figure 4.40.(b) shows the presence of a 'flower-like' growth that is created by the XY cross-section as indicated by (c). The reason for the radial growth from a single point is still unknown.

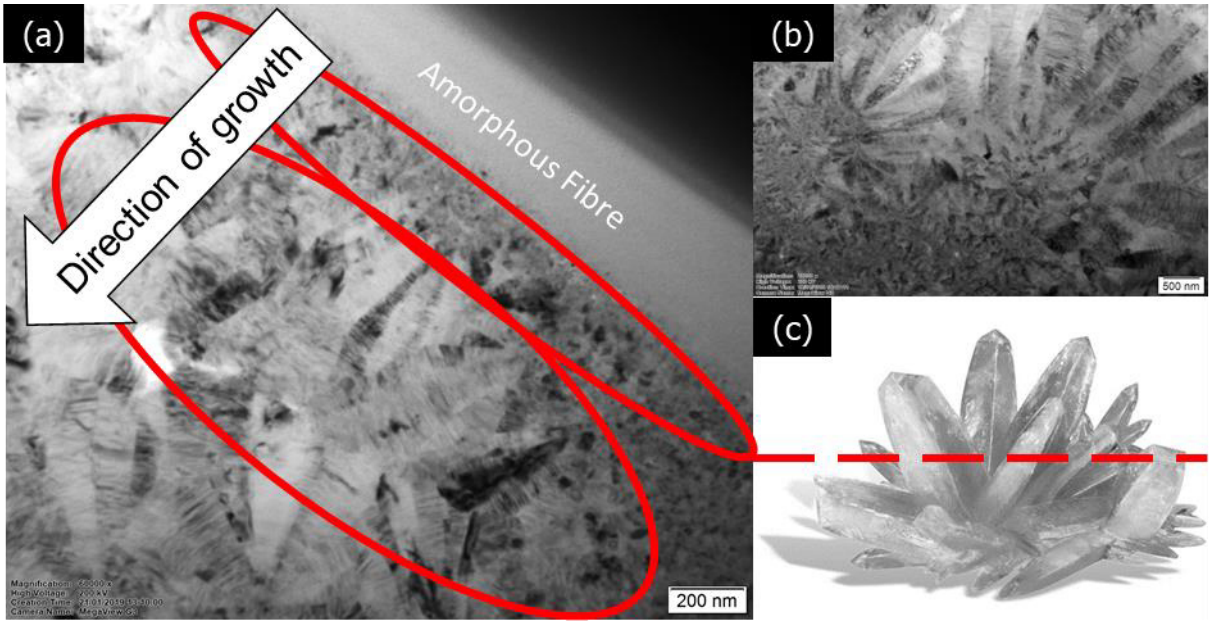


Figure 4.40. (a) Change in the crystal size as the grain growth proceeds from the fibre in alpha = 10, (b) higher mag image of the flow-like structures produced by the sectional of crystals growing radially from a central point, as illustrated in (c).

4.1.4. Summary

A suite of characterisation techniques has been used to evaluate the effects of temperature, pressure and alpha ratio on the deposition pattern, composition, crystal structure and kinetics of the MCVI process. The results of this study have shown MCVI produces an inverse temperature profile that is reflected in the progression of the deposition of the SiC matrix. The deposit is crystalline and close to stoichiometric in regions but processing parameters have a significant impact on both of these properties. Perhaps most significantly, MCVI has shown a significant increase in the kinetics of the deposition even over a short period of time. Further work is needed to establish the extent of this effect by attempting to achieve full densification of these composites.

4.2. Inverse temperature profile development using MCVI

4.2.1. Thermal camera observations

A thermal imaging camera, TIC, (FLIR A656SC, USA), was positioned in an available port above the microwave cavity so that it looked down on the SiC_f preform positioned on top of the quartz tube. The samples were then heated up, with no quartz bell jar over them, using the microwave field and the resulting temperature profile formed was filmed. Video post-processing software was then used to determine if an inverse profile had been created. Various sample geometries were tested, see table 4.3. Due to material availability constraints, only seven samples were trialled at this stage with a maximum diameter of 55 mm and a maximum of 30 ply.

Table 4.3. Sample properties used in the thermal imaging evaluation of ZMI fibres

Sample no.	Diameter/ mm	Number of SiC ply
1	16	10
2	34	10
3	55	10
4	34	20
5	55	20
6	34	30
7	55	30

It was quickly established that the 16 mm diameter was unsuitable for processing in the MCVI cavity. It readily formed an annular heating profile at low temperatures, which did not evolve despite the application of more power and repositioning of the E/H field tuners. The sample was very difficult to heat and the maximum temperature achieved was 686°C after nearly 9 min of processing. Improved heating rates were observed using the 34 mm diameter samples, which heated at ~300°C min^{-1} and reached temperatures as high as 800°C. The heating profiles of two

different samples are shown in figure 4.41. Both are 34 mm in diameter, made of 10 and 20 ply respectively, and their corresponding temperature scales are indicated on the right of the images. The figure shows an annular temperature profile was formed at 700°C. The figure on the right is a 34 mm sample composed of 30 ply showing a side temperature of 700°C due to the localised heating of the fibre ends from the electric field, whereas the top of the sample at the centre of the preform is approximately 500°C. This evolved into a number of different shapes but not an inverse profile as heating continued up to 800°C, at which point arcing was observed and the experiment stopped. No observable difference in the heating rate or the shapes of temperature profiles achieved were seen when the number of ply were varied but the maximum temperature achieved was improved with more ply. This is most likely because the preform was larger in volume and therefore absorbed more incident microwaves.

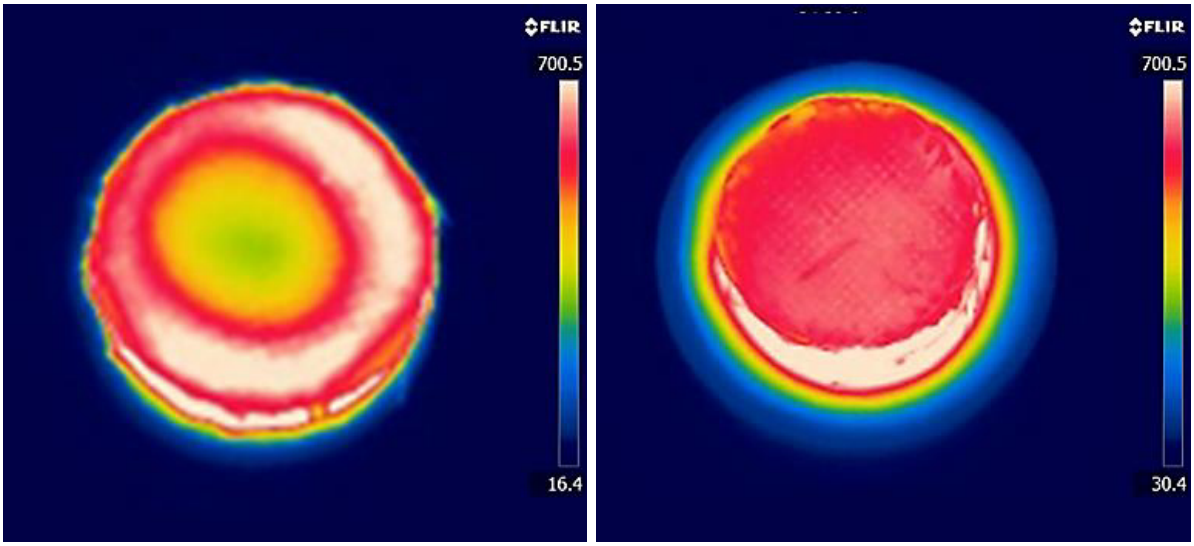


Figure 4.41. Left: An annular temperature profile of 10 ply 34 mm diameter SiC preform heated using microwave energy. Right: Non-uniform heating of 34 mm diameter sample made with 30 ply showing hot edges.

55 mm discs were then tested with a varying number of layers. Results again showed similar observations to the 34 mm samples in that samples during the

heating stage had evolving temperature profiles. Compared to the 34 mm samples, the 55 mm samples could be heated at a faster rate at an average of 450°C min^{-1}. Figure 4.42 again shows an annular and non-uniform temperature profile at 600°C and ~900°C.

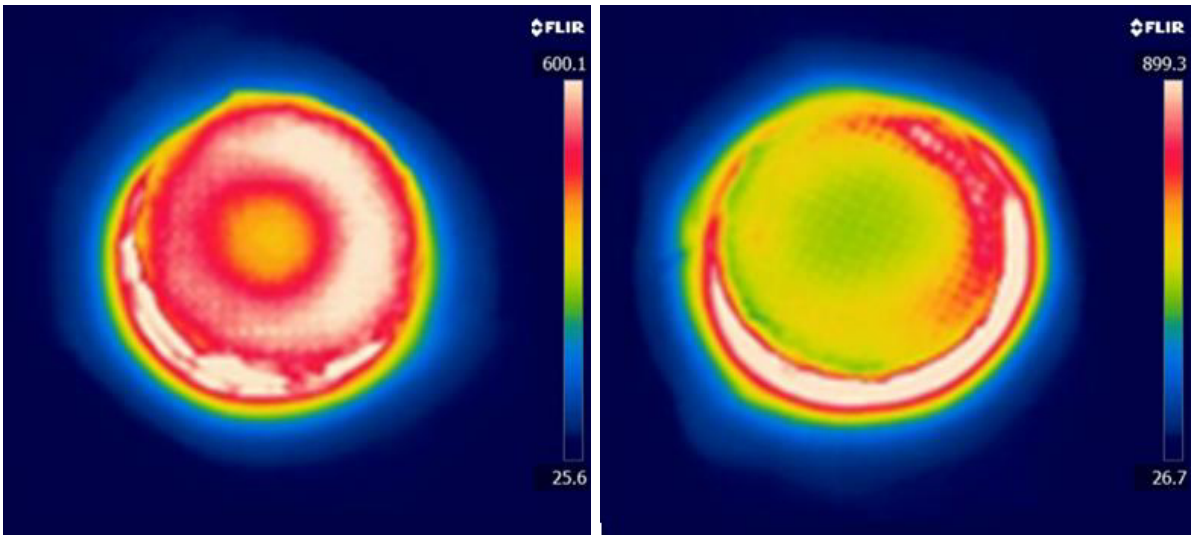


Figure 4.42. Left: An annular temperature profile of 10 ply 55 mm diameter SiC preform heated using microwave energy. Right: Non-uniform heating of 55 mm diameter sample made with 30 ply showing hot edges.

However, sample five did show inverse temperature profiles for extended periods, see figure 4.43 indicated by the red arrow and the graph. The inverse temperature profile fluctuated with time but was achieved on a number of occasions and using the E/H tuning could be brought back to this profile when the frequency drifted. This observation was again independent of the number of plies used. Unfortunately, due to the experimental setup, it was not possible to obtain *in situ* temperature profile, observations using the TIC. This was because the quartz bell jar was not transparent in the infrared wavelength, which meant that only the bell jar's temperature could be observed. This was a major reason for the use of the alumina foams to insulate the preform centre to increase the likelihood of an inverse temperature profile forming in the SiC_f preforms when they could not be directly observed. A secondary observation

was the ability of the 55 mm samples to be heated to higher temperatures when compared to the smaller samples. Figure 4.44 shows sample seven at >1000°C, exhibiting a non-uniform temperature distribution sitting atop an Al_2O_3 foam block.

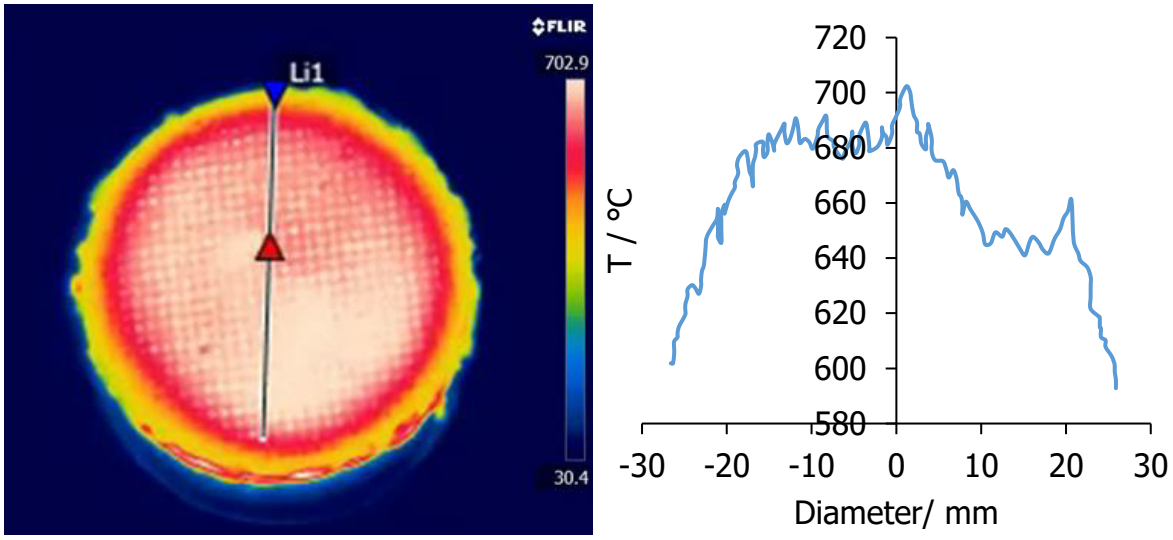


Figure 4.43. The formation of inverse temperature profiles at ~700°C in a 55 mm 20 ply SiC fibre preform using microwave energy and the concordant graph showing temperature profile along the intersecting line.

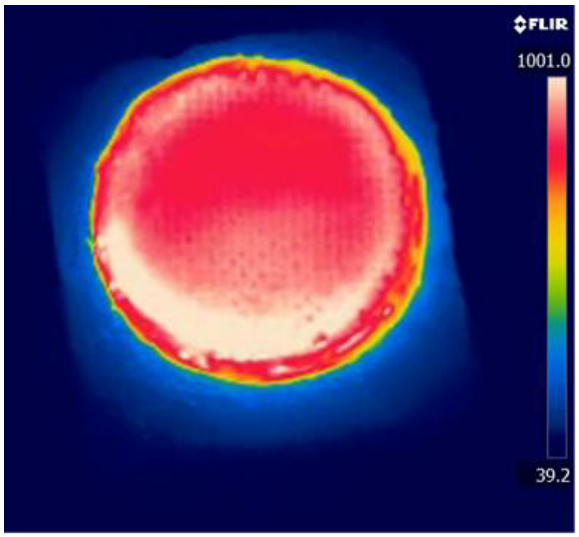


Figure 4.44. TIC image showing the SiC preform at 1001°C after 2 minutes of heating.

4.2.2. Electromagnetic and thermal simulation of MCVI

The MCVI system was reproduced computationally to provide insight into various unexplained phenomena in microwave heating of the SiC_f process and verify the result of the TIC experiments. Its utilisation informed processing condition selection

for further trials by providing information on temperature profiles and coupling information that experimentation could not.

4.2.2.1. *Materials parameters*

Electromagnetic properties

While an exact computational reproduction of the microwave is important, an accurate compilation of materials' parameters as a function of temperature of the constituent materials is essential. Electromagnetic and thermal properties of the SiC fibres, Al_2O_3 foam and quartz glassware were measured or derived from the literature from room temperature (RT) to 1200°C. To enhance the validity of the data, the morphology of the physical testing was matched as closely as possible to the morphology of the materials in the MCVI system. Regression analysis was then carried out to interpolate the data so that the software had a database to access data at any given temperature for all the materials in the model.

Figure 4.45. show the electromagnetic properties of the SiC fibres; the data were gathered using the technique described in section 3.3.7. It can be seen that as the temperature increased, the SA3 and ZMI fibres exhibited unreal values of ε' at high temperatures (square and triangle markers, respectively). This behaviour is very similar to the results seen in section 4.3.4. and there are multiple possible explanations for it. The fibres each have different compositions due to the precursor they were derived from; for the ZMI a poly(carbozirconosilane) was used which produced a SiC fibre with 1 wt.% Zr present. The SA3 fibres were made from poly(carboaluminosilane), where the aluminium acts as a sintering aid to increase the

density. Lastly, the Hi Nicalon S used only polycarbosilane, so didn't have any dopants [100]. This could provide an explanation for the decrease in the dielectric permittivity at high temperature, as the metallic elements carry a current and reduce the SiC fibre's dielectric character. This mechanism could also work in conjunction with the dielectric breakdown of the fibre at high temperature, enhancing this mechanism further. This explains the step-change in behaviour as electrons are liberated across the wide bandgap to the conduction band at high temperature. Another potential factor is that both the other fibre types are known to have higher carbon concentrations than the Hi Nicalon S. The carbon in the ZMI fibre is present in its general microstructure due to the Si_xO_xC glassy-matrix in which the SiC grains are contained, whilst the SA3 has free carbon on the grain boundaries concentrated in its core [379, 383]. The carbon network is highly electrically conductive so at high temperature has a high resistance, which explains the high loss factor compared to the Hi Nicalon fibre and possibly the change in ε' [352]. Ultimately, any combination of the three factors will have affected the ZMI and SA3 fibre's dielectric properties. As with the powders, more work is needed to establish the effects of the dopants and carbon content on conductivity as well as the polytypes present in the fibres to evaluate the breakdown strength. As the Hi Nicalon S fibre was more predictable at higher temperatures, modelling efforts were therefore focused on this fabric which behaved better in a microwave field, consistently showing an increasing ε' and ε'' as temperature increased.

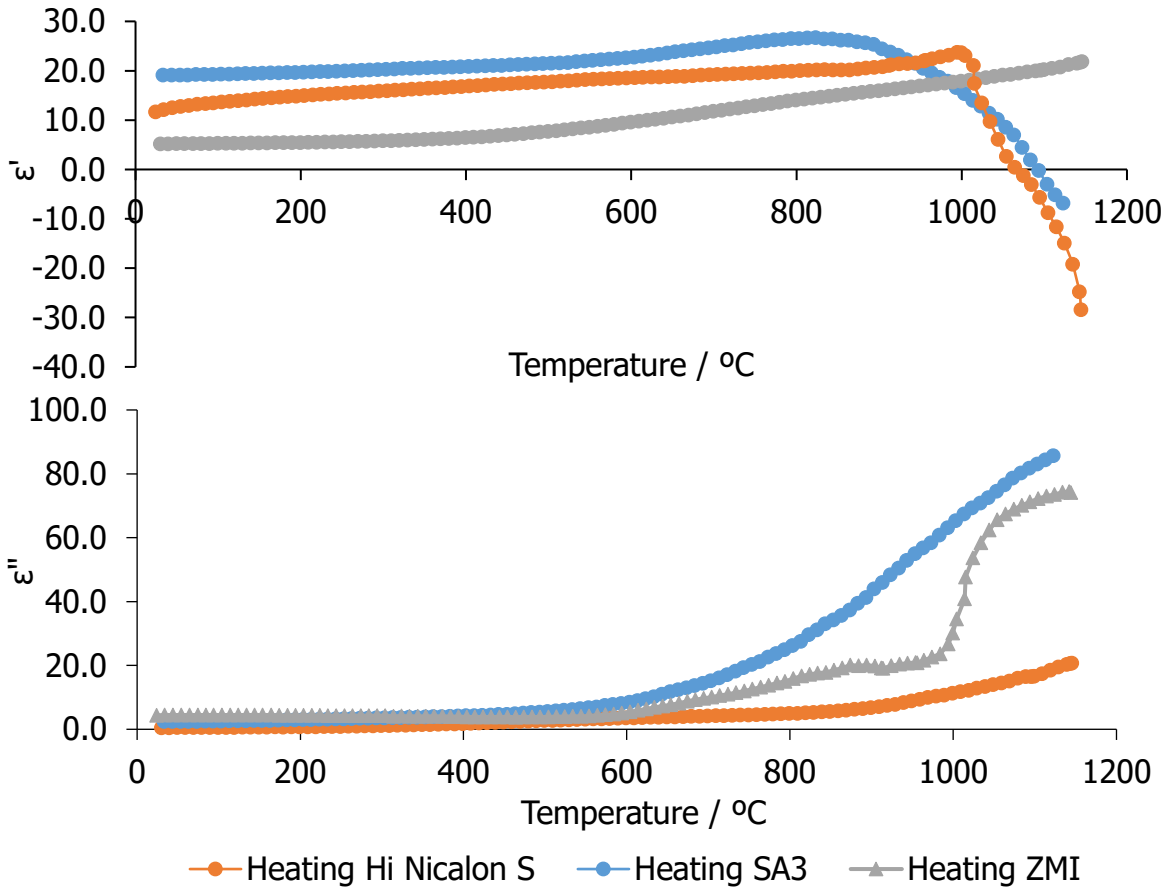


Figure 4.45. Changing dielectric properties of the 3 types of SiC fibres, top: ε', bottom: ε''; note the unusual behaviour of the SA3 and ZMI fibres at temperatures >800°C.

This experimental data collected for the SiC was then fitted to a curve for interpolation purposes, figure 4.46. This was done to align the temperature increments between the material systems to improve simulation efficiency. The increments between data points decreased from 100°C to 25°C above 900°C. This was to decrease simulation resources between room temperature and 900°C, which was not considered a region of interest as not SiC deposition occurs below this temperature. Only the Hi Nicalon S was used for simulation as it was the only fibre that did not show a negative ε'. The Hi Nicalon S data was then interpolated using the Levenburg-Marquardt algorithm and extrapolated to 1200°C using a variety of curve fitting models built into the Origin software [384]. The fitting model used and R^2 value for said fits can be found in the respective figure captions.

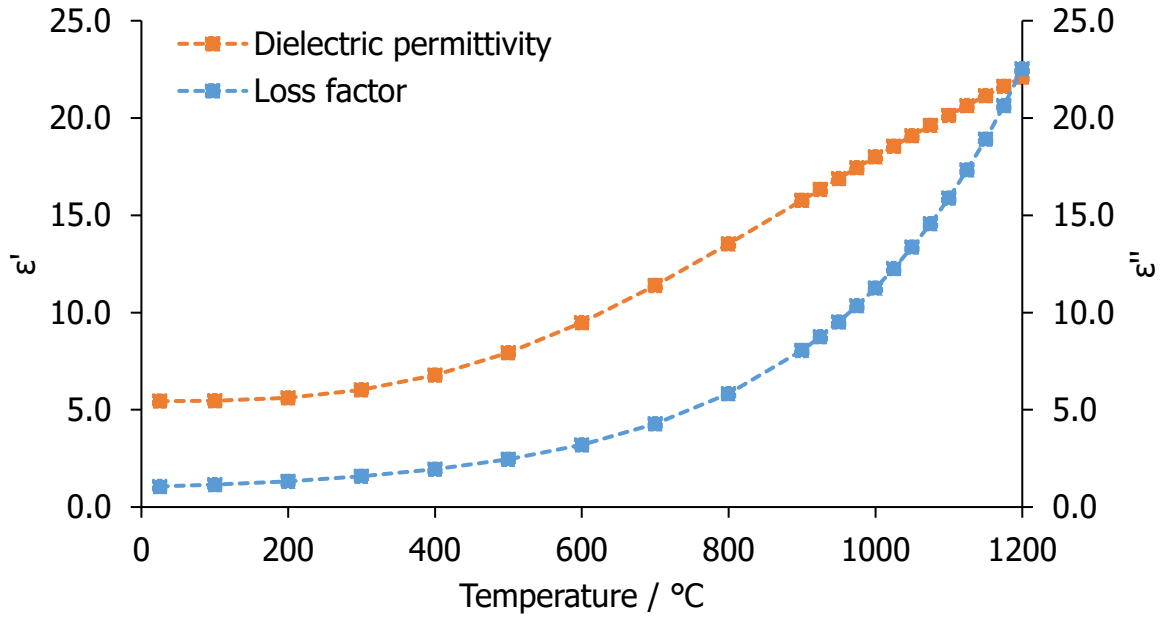


Figure 4.46. The dielectric permittivity (primary axis) and the loss factor (secondary axis) of the Hi Nicalon S fibres after interpolation using Origin. ε' was fitted with a logistic model with R^2 = 0.99, the ε'' was fitted using a Boltzmann model with R^2 = 0.97.

The Al_2O_3 foam's electromagnetic properties were extracted from the literature [263]. However, due to their low density (TD = 18%), the rule of mixtures formula was used to factor in the effect of the gaseous medium inside the porosity on the electromagnetic properties. In reality, the gas for the experiments was hydrogen and MTS, however, neither was used in the calculation due to lack of data in the literature, particularly at elevated temperatures. The maximum reported temperature of ε' and ε'' for hydrogen and MTS was 226°C [385] and 19°C [386], respectively. This was considered insufficient to extrapolate accurately to 1200°C and no data was found for MTS in the literature. Subsequently, dielectric properties for air were used which are ε' = 1.006 and ε'' = 0.000 [387].

The ε' of quartz glass is almost constant with increasing temperature, increasing by 0.01 between room temperature and 1200°C. Quartz also has a negligible ε'', meaning that it can be considered microwave transparent; data was taken from

[388]. Electromagnetic data for these two materials were plotted in post-processing using the Origin software in the same manner as for the SiC fibres. The scales of these figures are identical to figure 4.46 to aid comparison of the magnitudes between figures.

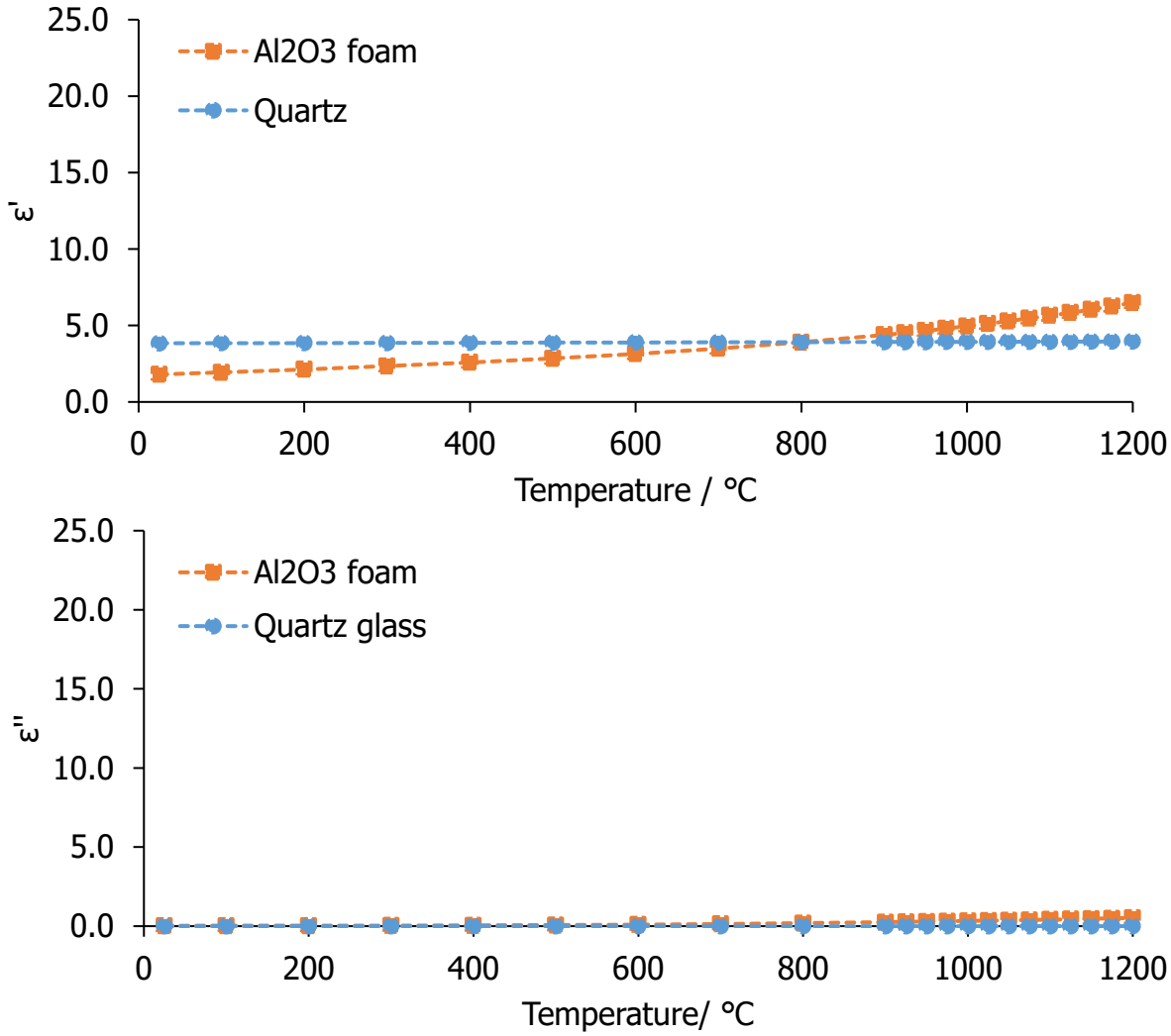


Figure 4.47. Top: The dielectric permittivity for the Al_2O_3 foam and quartz after interpolation using Origin. ε' for the Al_2O_3 foam was fitted with a two-phase exponential decay function with R^2 = 0.96 and ε′ for the quartz was fitted using a Boltzmann model with R^2 = 0.98. Bottom: Dielectric loss factor for the Al_2O_3 foam and quartz after interpolation using Origin. ε'' for the Al_2O_3 foam with a Logistic model with an R^2 = 0.98. ε″ for quartz was fitted using an exponential growth model with an R^2 = 0.93.

Thermal and physical properties

Section 3.3.6. described the methods used to collect the thermal properties of the SiC fibres. The thermal diffusivity measurements were carried out by Dr. Roger

Morell at the National Physical Laboratory, London. The specific heat of the fibres was also measured experimentally and the thermal conductivity calculated from these measurements. Details for the density of the fibres were taken from the supplier's data sheets and then the density of the preform calculated based on the volume fraction of fibres, meaning the SiC preforms were estimated to have a density of ~0.48 g cm^{-3}. Figure 4.48 shows the thermal diffusivity of the three SiC fibre types up to 700°C. The values, as expected, decrease for all three fibres as the temperature increases. The trends seen in the data are consistent with datasheets for the materials, in that the SA3 fibre has the highest thermal diffusivity of the three and the ZMI the lowest. However, the values are consistently lower for all samples compared to the supplier's datasheets. The coefficient of thermal expansion was accounted for in the below graph using equation 3-16.

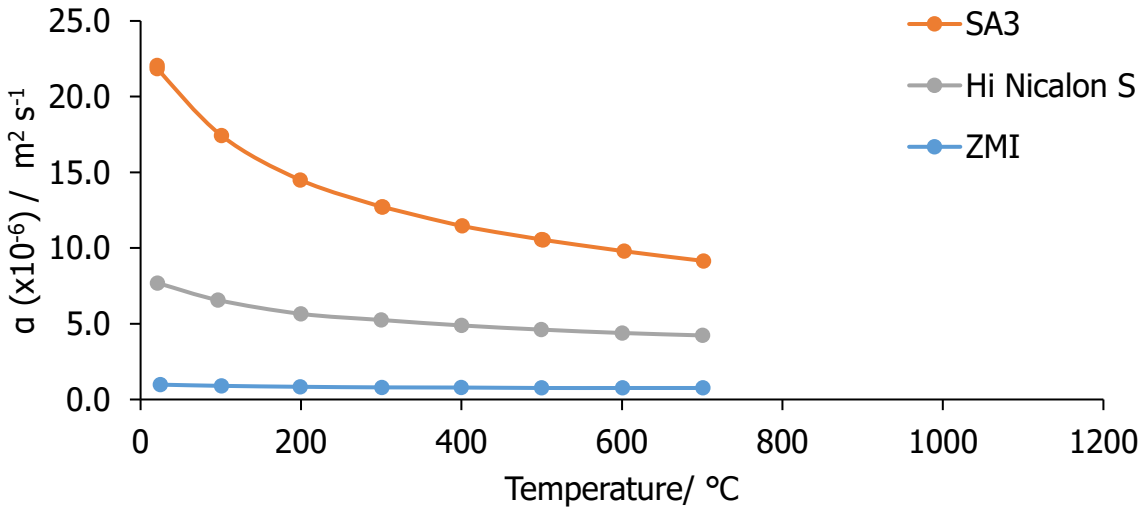


Figure 4.48. Measured thermal diffusivity values for the three SiC fibres. Note that the units used are SI as QWED did not require thermal diffusivity data input for the simulation.

The fibres' specific heat capacity was also measured, as this data was required directly for the software and for the thermal conductivity calculation. Figure 4.49 shows the specific heat capacity of the SiC fibres with increasing temperatures.

Again, as expected, the data plateaus above ~600°C and becomes noisier. The tests were done in flowing argon to prevent oxidation of the fibres and the subsequent formation of SiO_2 that would have affected the measurement. It is not clear what the explanation is for the noise in the data, however, it can be seen to be sufficiently small that the interpolation of the data to 1200°C was unaffected.

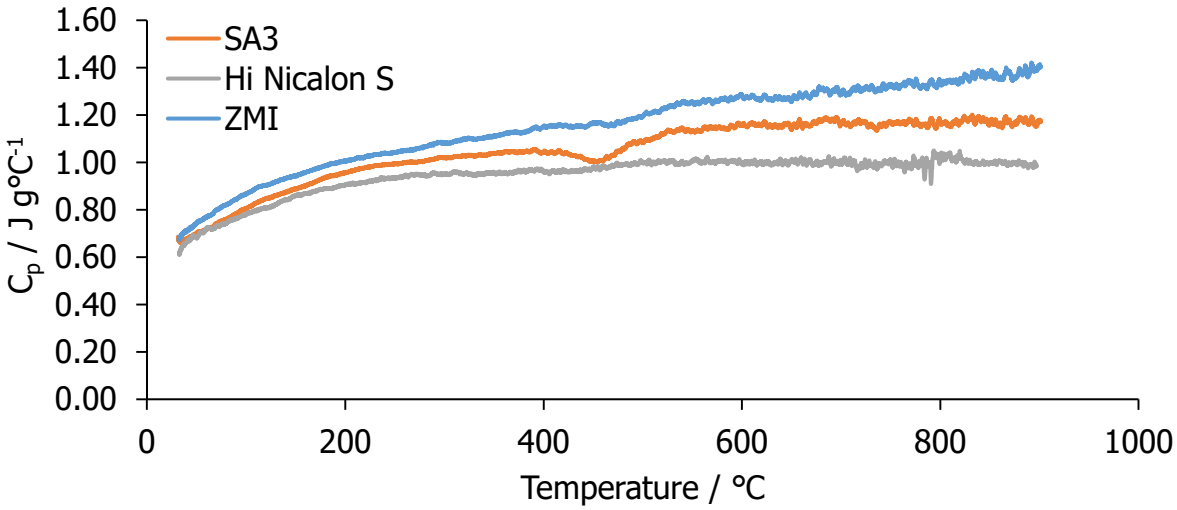


Figure 4.49. Measured specific heat capacity data for the three fibres up to 900°C, in the units required for the QWED 3D simulation.

The data for these two measurements, diffusivity and specific heat capacity, were fitted to curves using the Origin software in order calculate the thermal conductivity by aligning measurement points across the temperature range before it was extrapolated to 1200°C.

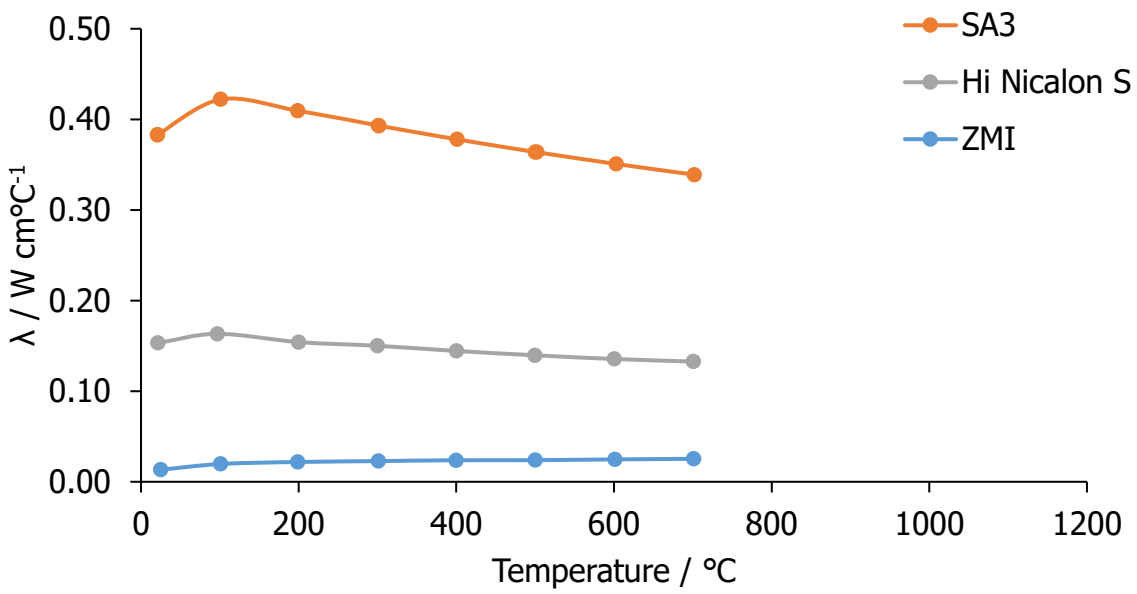


Figure 4.50. Thermal conductivity data for the three fibre types with increasing temperature calculated from measured values and accounting for thermal expansion. Note that the unit on the Y-axis is specific to the QWED 3D requirements and is not an SI notation.

The density of the fibres was 3.1 g cm^{-3} [100] and was used despite the density of the fibre bundle used in the thermal diffusivity measurements being only ~50% of the TD. This is because the time-response from the laser pulse in the thermal diffusivity measurements was not an artefact of the packing density of the fibres, rather the average time response of all the fibres put together was measured. As each fibre transmitted the thermal energy at approximately the same rate, it was the intrinsic property of the individual fibres that was measured rather than the total heat flow. Since only the Hi Nicalon S fibre was used for the simulation, figure 4.51 shows the specific heat capacity and thermal conductivity data that were used post curve fitting. A full table of the properties used in the simulation can be found in appendix II.

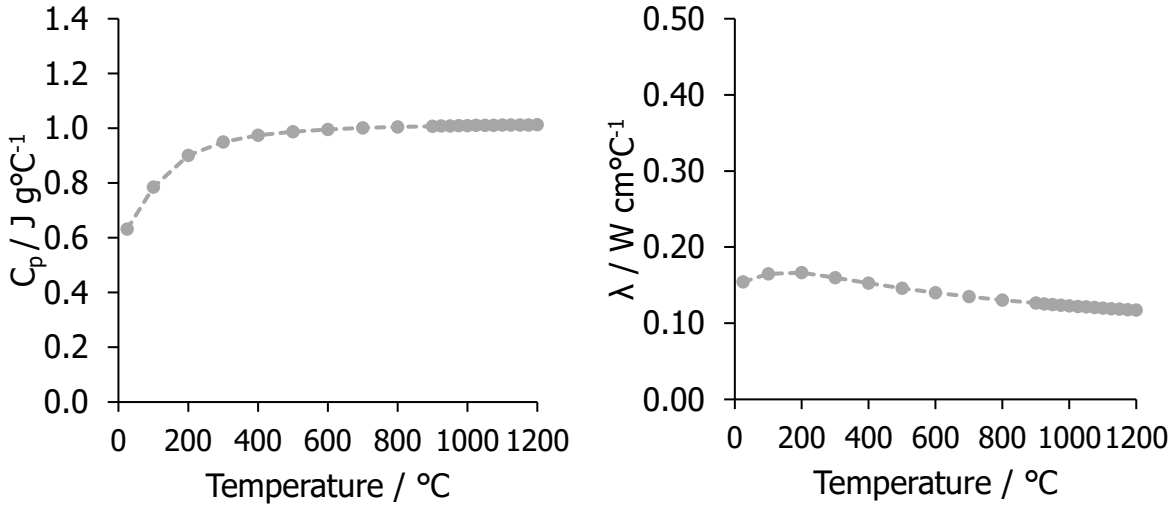


Figure 4.51. Left: Specific heat capacity of the Hi NiC S SiC fibre after post-processing, which was fitted with a logistic model with R^2= 0.98. Right: the thermal conductivity of the SiC fibre after processing fitted to a logistic curve with R^2= 0.99. Note that the units are specific to the QWED 3D software.

The thermal and physical properties for the Al_2O_3 foams and quartz were again extracted from the literature. The density for the foams came from the supplier's datasheet, whilst it was taken from [10] for the quartz; the values were 0.71 g cm^{-3} and 2.2 g cm^{-3} respectively. The thermal property data for the two materials is shown in figure 4.52 after the data had been fitted to a curve for the simulation. The specific heat capacity of the foams and quartz was slightly higher at high temperature when compared to the SiC fibre by ~0.25 J g°C^{-1}.

The thermal conductivity was then calculated for both materials. The foam's thermal conductivity decreased with temperature from 0.39 W cm°C^{-1} to 0.09 W cm°C^{-1} between RT-1200°C, whilst the quartz remained relatively constant at a mean value of 0.02 W cm°C^{-1}. Like the SiC fibres, the thermal conductivity of the foams was calculated using the TD of Al_2O_3, 3.91 g cm^{-3}. This is instead of the foam's relative density, which is 0.71 g cm^{-3} because thermal conductivity is an intrinsic material property that is irrespective of morphology. Subsequently, the Al_2O_3 foam's thermal

conductivity was higher than the SiC fibre up to 500°C. This value for density was used because the model had a separate input for the density that was specific to the morphology of the materials used, as shown in table 3.4.

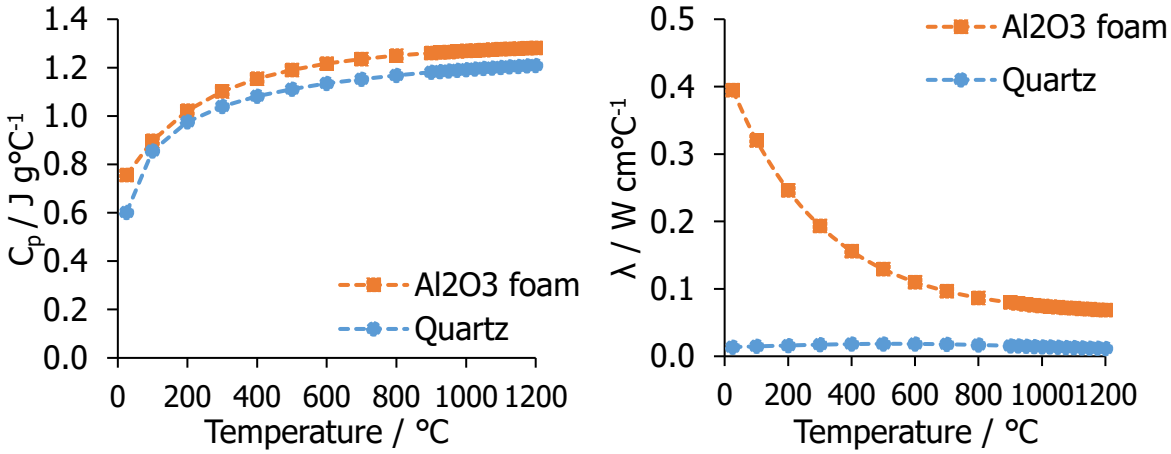


Figure 4.52. Left: Specific heat capacity of the Al_2O_3 foam and quartz after post-processing. These were fitted with a Lorentz fit with R^2 = 0.99 and a logistic model with R^2= 0.99, respectively. Right: the thermal conductivity of the Al_2O_3 foam and quartz after processing, fitted to a first-order exponential decay with R^2= 0.97 and a Lorentz fit with R^2 = 0.99. The graphs are plotted on the same Y-axis scale as figure 4.50 for comparative purposes.

4.2.2.2. *Reflection coefficient*

Simulations of the reflection coefficient (S_{11}) of the SiC fibre preform in the microwave chamber were made using the QWED 3D software. The simulations ran for approximately 30 min until they reached a steady-state for the various geometries tested. This required the microwave cavity, wave-guide position and sample position to be accurately reproduced in 3D in the software. Data for the ε' and ε'' was required to solve the electromagnetic part of the problem and calculate the coefficient of reflection. This calculation was independent of MW power and was initially carried out at room temperature before being simulated at 300, 600, 900 and 1200°C to observe the effect of the changing dielectric properties of the SiC_f at elevated temperatures, as according to figure 4.46.

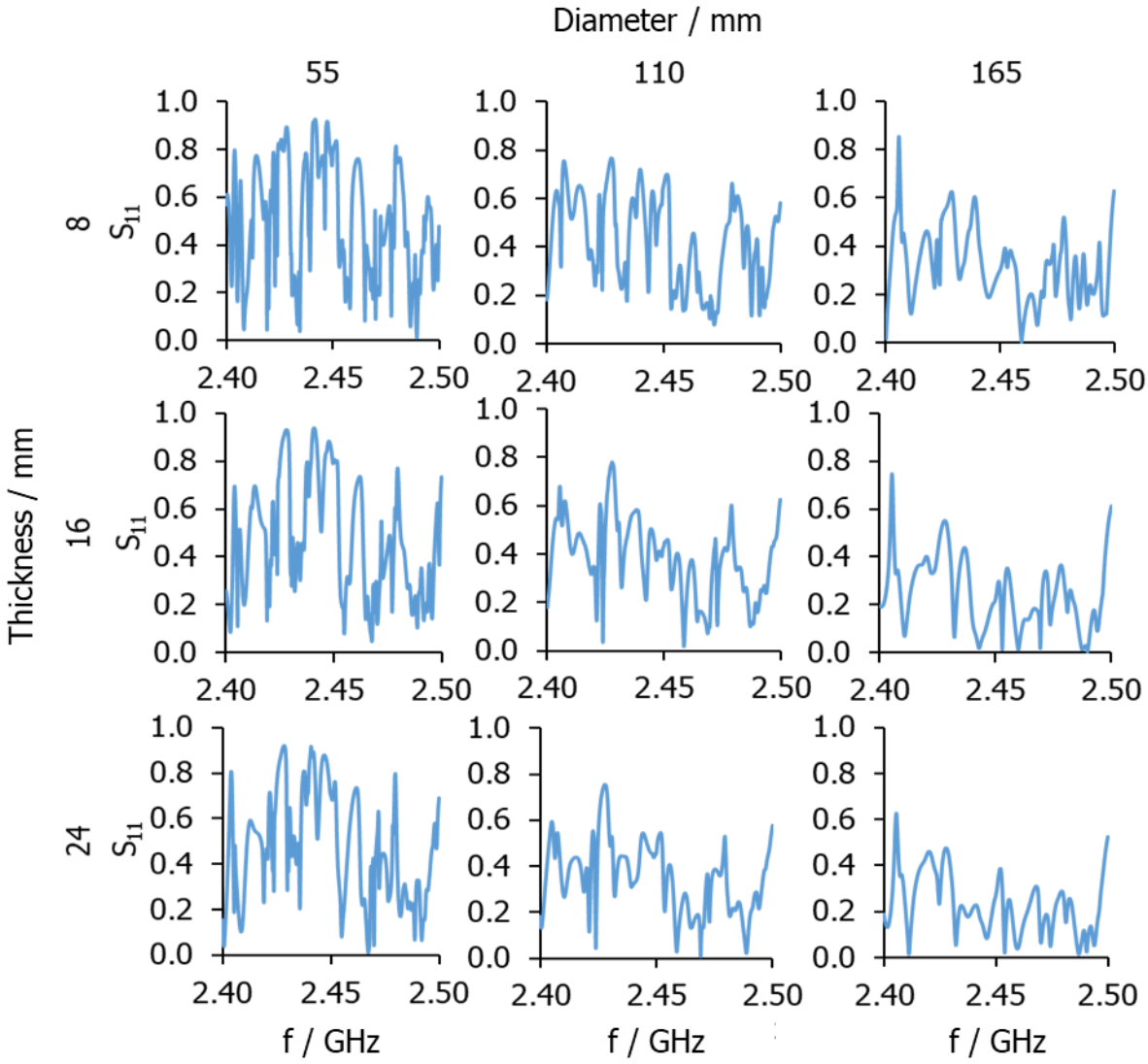


Figure 4.53. Nine graphs showing the effect of SiC fibre preform dimensions on the reflection coefficient inside the cavity and the number of induced resonances at room temperature.

Figure 4.53. shows the effect of altering the diameter and thickness of the SiC fibre preform on the reflection coefficient. The data showed that samples that were 55ϕ x 8 mm thick had the highest reflection coefficient with a mean of 0.51, whilst the largest samples, which measured 165ϕ x 24 mm thick, had the lowest reflection coefficient with a mean value of 0.23; i.e. they had the highest absorption [389]. This behaviour is typical of a non-resonant cavity where the electric field distribution and reflections are governed by the permittivity and geometry of the material.

Unfortunately, the dimensions of the samples used for the MCVI experimental section 4.1 of the project were chosen to be 55ϕ x 8 mm based on the results from section 4.2.1. This was due to the high cost of SiC fibre fabric. A single preform made out of Hi Nicalon S fabric measuring 55ϕ x 8 mm in diameter cost £204, whilst a sample measuring 165ϕ x 24 mm cost £5520. The latter was simply unaffordable given that multiple parameters needed to be investigated. The result of this decision was that samples had a high reflection coefficient and a larger number of resonances. This meant that samples were harder to heat reproducibly in the microwave cavity as the likelihood of the sample reflecting the microwaves rather than absorbing them was greatly increased. Furthermore, the 55ϕ x 8 mm samples were more susceptible to the occurrence of magnetron frequency drift affecting the absorption, a phenomenon described in section 2.6.4.1. As an example calculation, a drift of ~0.0032 GHz will change the S_{11} value from an absorbing condition of 0.04 at 2.4346 GHz to a reflecting condition of 0.73 at 2.4378 GHz. This amount of drift was frequently observed with the MCVI microwave generator and was not helped by the changing dielectric properties of the fibres. It is believed this drift was too severe a change for the auto-tuning feature in the Labotron software to correct automatically which is why manual tuning by the operator was favoured in most cases. It also explains the inconsistency in the ability of the 55ϕ x 8 mm samples to heat to operating temperature, as described in section 4.2.1.

Figure 4.54. shows how the frequency characteristics of the reflection coefficient change with increasing temperature. It clearly shows that the reflections of the system are strongly influenced by the temperature of the preform. The general trend

is that the preform becomes more absorbing at a higher temperature, see figure 4.55; however, the number of deep resonances remains relatively constant. This improvement is non-linear as some frequencies actually make the absorption of microwave worse at higher temperatures. This is consistent with what was observed experimentally and explains why the heating rate was highly variable, ranging from 50 – 700°C min^{-1}. There was no method by which the operator could exercise control directly to combat this effect, at best, the operator could guide the frequency by using the E/H tuning wands to keep the reflected power at a minimum and then adapting to significant changes as they occurred if the auto-tuner was ineffective.

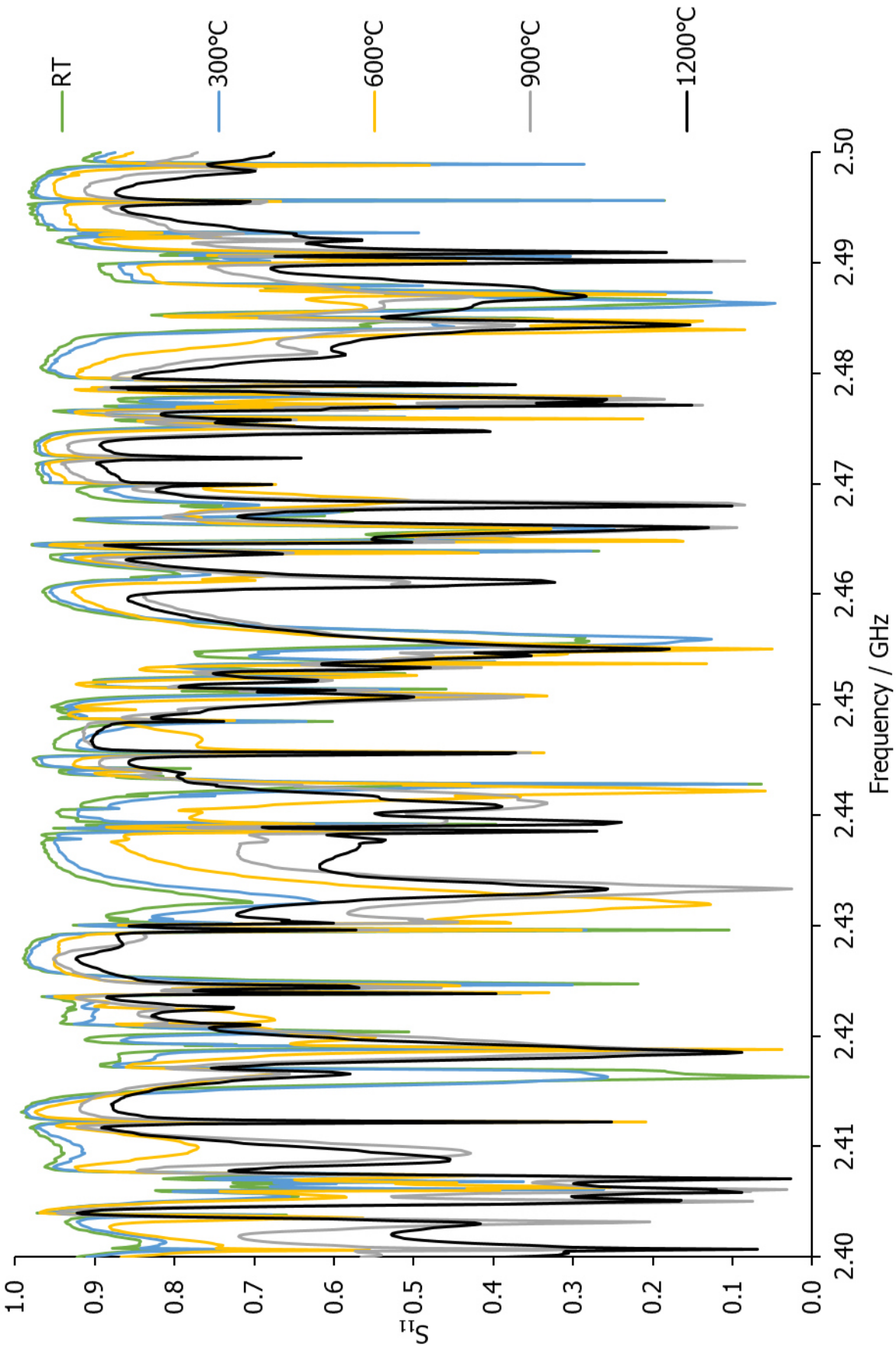


Figure 4.54. Two graphs showing the effect of temperature on the S_{11} parameter for the 55ϕx8 mm samples. Note the extended x-axis.

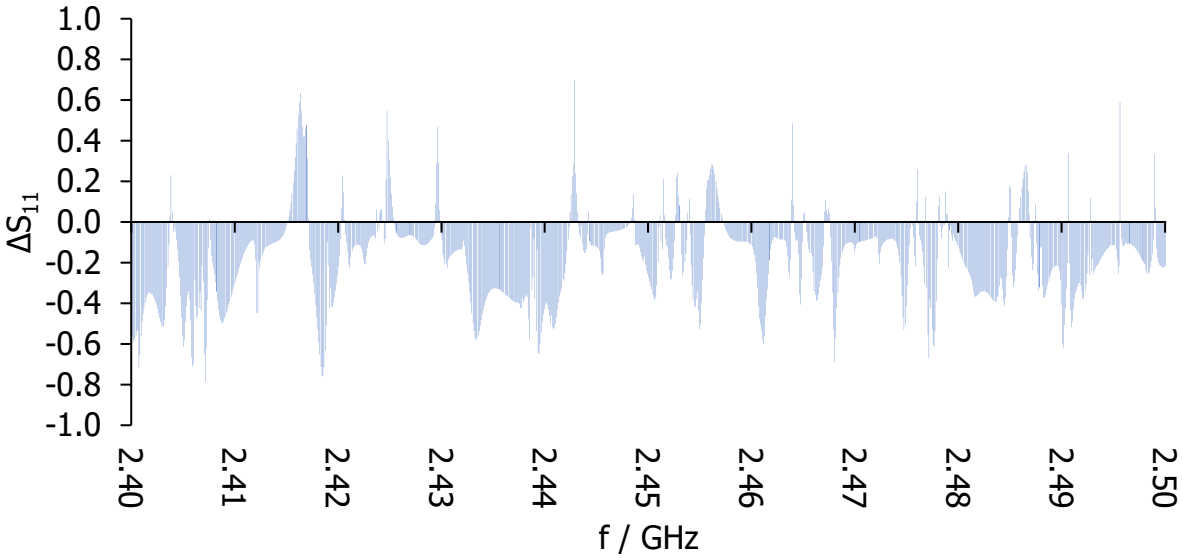


Figure 4.55. Bar graph representing the change in the value of S_{11} parameter between RT and 1200°C, showing across all frequencies a 23% decrease in the mean value of the reflection coefficient.

4.2.2.3. *Thermal simulation of microwave heating*

A number of frequencies, both resonant and non-resonant, were selected to evaluate the differences in heating rates within the 55ϕ x 8 mm Hi Nicalon S samples; the rest of the apparatus in the cavity, the alumina foams and the quartz glassware were also modelled to produce a representative view of the MCVI scenario. The data for the three material properties' can be found in appendix II. All simulations were carried out by Prof. Vadim Yakovlev using the computer cluster detailed in section 3.4.1. Table 4.4. shows which frequencies were later selected for further testing and the justifications behind their selection.

Table 4.4. Showing the ten frequencies selected from figure 4.54. that were used to compare four key scenarios in terms of how the respective heating rates changed with temperature.

Scenario	Frequency / GHz	Heating rate / °C min^{-1}
Increasing S_{11} (Decreasing coupling)	I – 2.4163*	371.1
	II – 2.4428	323.4
	III – 2.4296	291.3
Decreasing S_{11} (Increasing coupling)	IV – 2.4185	229.1
	V – 2.4680	230.3
	VI – 2.4901*	304.0
Near constant low S_{11} (High coupling)	VII – 2.4189*	511.5
	VIII – 2.4238	334.7
Near constant high S_{11} (Low coupling)	IX – 2.4632*	48.9
	X – 2.4480	140.9
* = indicates the frequencies selected for extended testing and temperature profile visualisation.		

Simulations of the heating rate used a time step of 0.5 s to solve the coupled electromagnetic-thermal problem. This time step was found to be sufficient to capture the change in temperature of the system accurately but still be practical in terms of processing time and computational resources of the simulation. Each heating curve took ~16 h to compute the 120 s of heating as the model contained more than 2.2 million cells. Figure 4.56. shows the heating curves of the Hi Nicalon S fabric at ten different frequencies, showing the maximum cell temperature observed in model using an input power of 1.10 kW[xi]. A comparison of the heating rates observed experimentally using the thermal imaging camera and the microwave 2CP data concluded that the model yielded a good representation of the MCVI cavity, see section 4.2.1.

[xi] This input power was typical of the power required to heat samples up to the desired infiltration temperature.

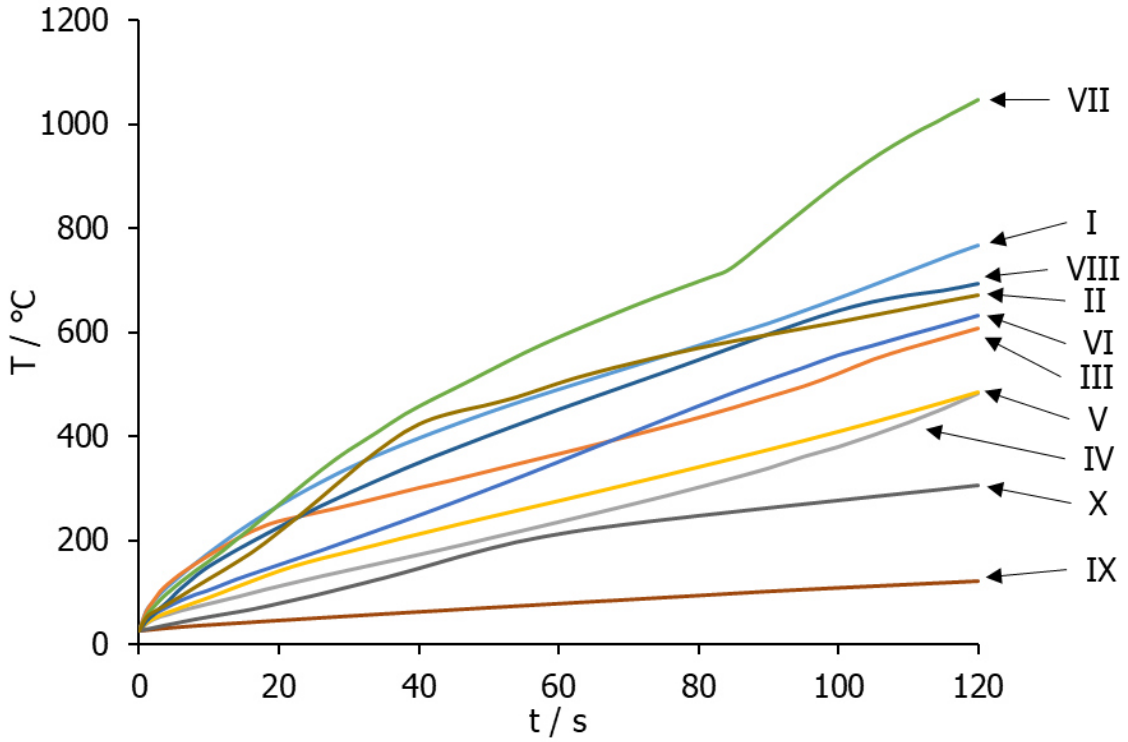


Figure 4.56. Graph showing the ten frequencies selected and how the temperature of the SiC_f preform changed with time.

A frequency with a consistently low S_{11} parameter yielded the fastest heating rate, as demonstrated by curve VII which displayed a heating rate of 511.5°C min^{-1}, reaching >1000°C in less than 120 s. Meanwhile, curves I and VI showed similar heating rates despite them having opposing S_{11} characteristics with temperature. Curve IX showed a very low heating rate as the reflection coefficient was consistently high which meant the sample didn't reach even 200°C after 120 s. The variability in the heating rates at different frequencies is consistent with what was observed during tests. As previously mentioned the E/H impedance tuners on the MCVI could manipulate the reflection coefficient, but with no specific feedback to the operator on the magnetron output frequency the user has to rely on the instantaneous power reflection to lower the S_{11} parameter; this is not the best information with which to do this. Furthermore, given the magnetron output frequency drifts, maintaining good

coupling consistently was very difficult. Nevertheless, heating curves I, VI, VII and IX were selected for further testing. The simulations that were selected based on the gradients of the curves that after two minutes were most likely out of each of the four scenarios in table 4.4 to reach 1200°C when the heating time was increased.

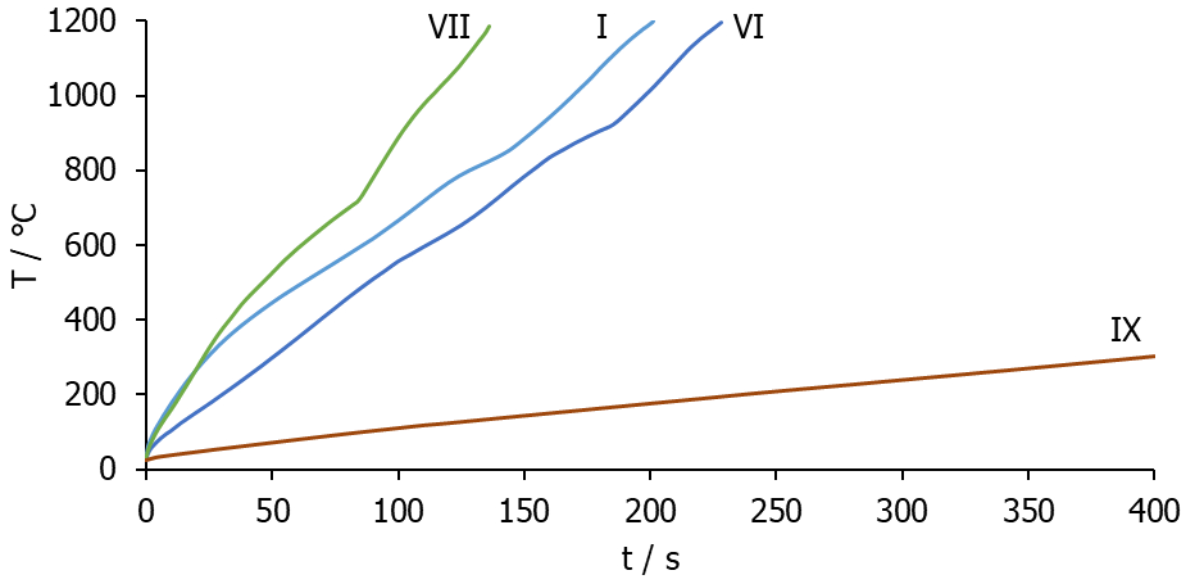


Figure 4.57. A graph showing the four frequencies selected as representative of the four scenarios showing how the temperature of the SiC_f preform changed with time.

Figure 4.57. shows the heating curves I, VI, VII AND X, which were selected for further simulation. Simulations were carried out for a total heating time of 400 s or up to 1200°C before being terminated, whichever came first. Simulation VII reached 1200°C after 136 s confirming a consistently low S_{11} value with increasing temperature provided the fastest heating rate. Curves I and VI had an increasing S_{11} and decreasing S_{11} with temperature also reached 1200°C after 201 s and 228 s, respectively. Curve IX, which had a consistently high S_{11} value as temperature increased reached a maximum temperature of 304 °C after 400 s of heating. These results are again consistent with experimental observations; when reflections are low the heating rate is high and vice versa. This is because the low S_{11} value means the

SiC fibre is absorbing the majority of the incident microwaves and converting the electromagnetic energy to thermal energy.

Visualisations were created of the samples at 925°C to compare temperature profiles of the Al_2O_3 foam-SiC_f-Al_2O_3 foam sandwich in the XY and XZ cross-sections. Figure 4.58. shows the changing relative temperature profiles for I, VI, VII and IX over 180 s.

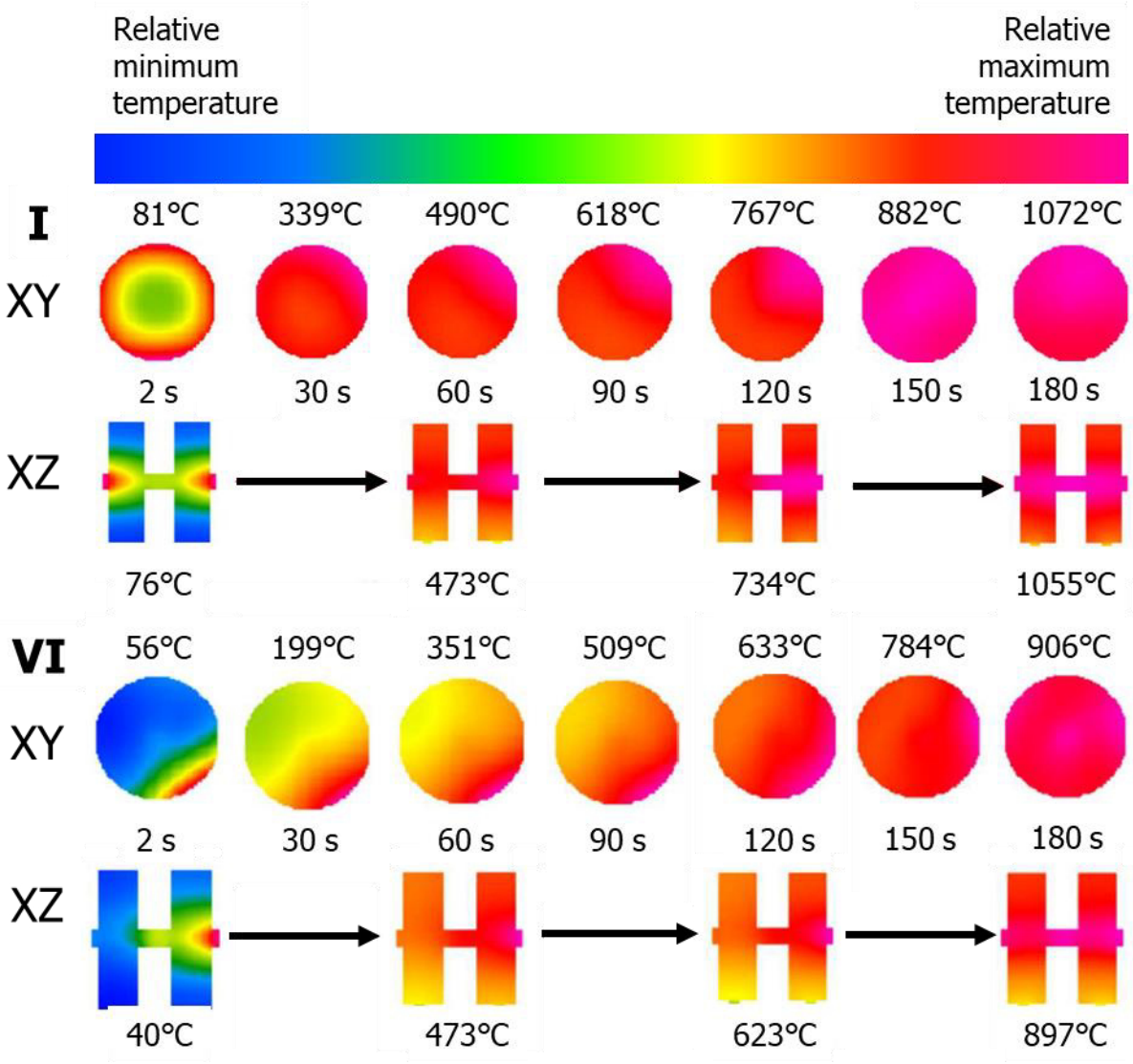


Figure 4.58. Visualisations of the temperature profile during heating at two different frequencies, I = 2.4163 GHz and VI = 2.4901 GHz over 180 s showing how the temperature profile changes with time, temperature and frequency.

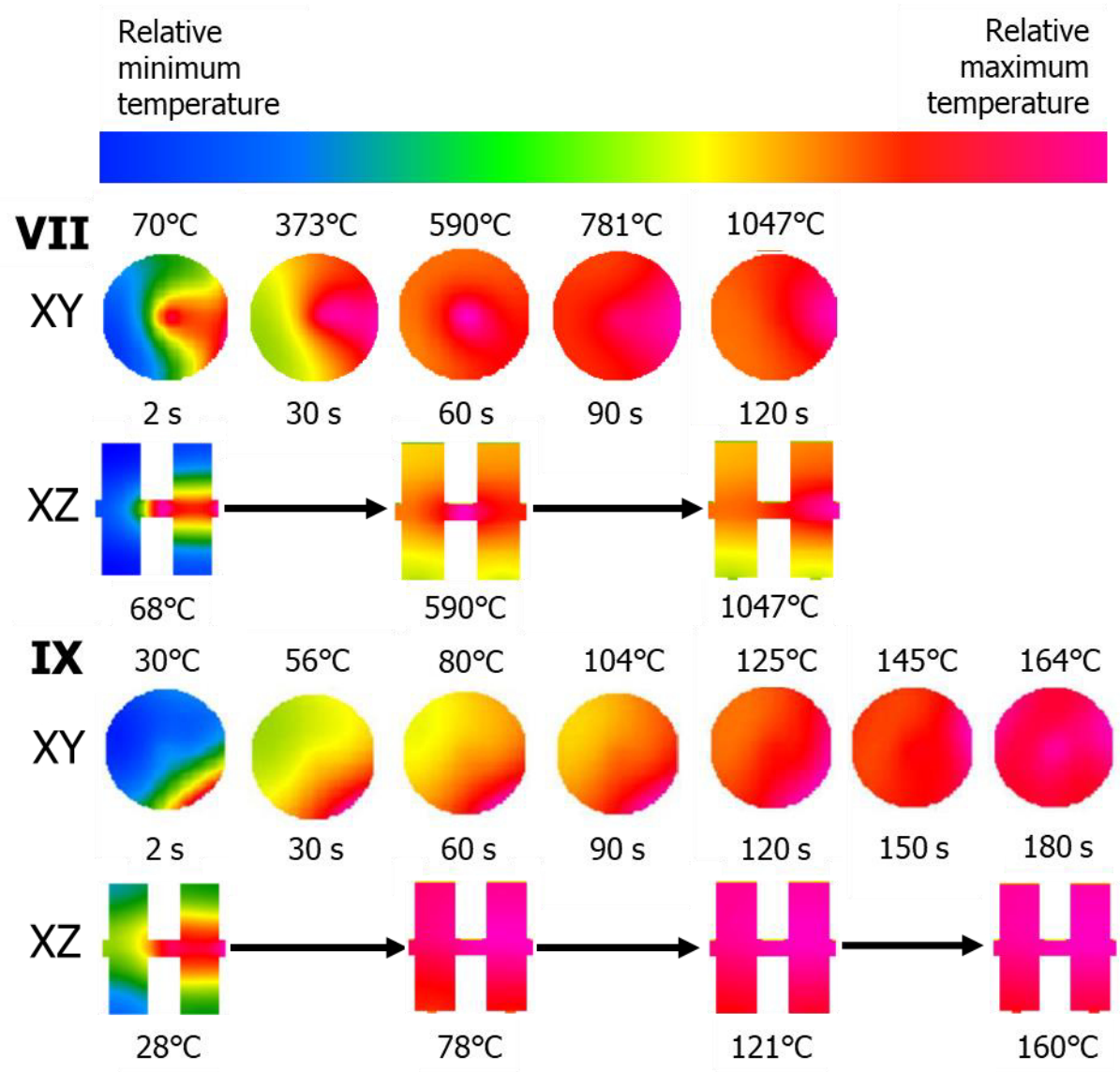


Figure 4.58. (Continued) Visualisation of curves VII and IX, 2.4189 GHz and 2.4632 GHz, respectively.

Figure 4.58. shows visualisations of the temperature distribution of curve I, VI, VII and IX. Curve I shows a relatively uniform temperature profile in both the XY and XZ planes when the coupling with the preform was decreasing with increasing temperature at 2.4162 GHz. This begins from approximately 30 s into the heating of the preform and does not change significantly up to 180 s in either plane. For curve VI at 2.4901 GHz, where increasing coupling is seen with increasing temperature, a lateral gradient forms across XY plane when heated for 180 s. This starts to homogenise after 150 s in both planes with a slight hot spot in the center of the

preform measuring ~900°C. Curve VII, which has a near-constant low S_{11} parameter, also has a uniform temperature profile at high temperature in the XY plane, but due to it having the highest heating rate this forms after 90 s. In the XZ plane, however, there is a distinct hot spot formed on the right hand side of the preform after 120 s of heating. For IX, which has the lowest heating rate the preform and alumina foam show a very uniform temperature profile in the XY and XZ orientations after 180 s, with a maximum temperature of 160°C. This shows slow heating rates produce a more uniform temperature distribution than the faster ones; in the latter (VII), when T_{max} ~1,200°C the T_{min} is only ~900°C.

Analysis of these patterns suggests that the evolution of their temperature profiles may be a combinations of two trends: amplification of the electromagnetic field magnitude in the hot stops and the spreading of the peaks of the temperature distributions due to high thermal conductivity of the SiC_f, relative to the Al_2O_3 foam. This thermal uniformity was commonly observed in the densification profiles and deposit thickness in section 4.1. despite the fibre type being different. This indicates the foam is having a significant impact on the temperature distribution as it is insulating the SiC_f, which was to be expected, and is helping to dissipate any hot spots formed due to its low thermal conductivity. This behavior is favourable as if there are increases in the thermal conductivity of the insulating material this can decrease the penetration of the EM waves and reduce the highly desirable 'microwave effect' [390].

4.2.3. Summary

An inverse temperature profile was observed in the SiC_f preforms measuring 55 mm in diameter using a TIC but it was not consistently formed and varied vastly with temperature. Verification work, in the form of a FTDT model, was therefore carried out to provide insight and explain this observation that experimentation could not and suggest better means of control over the equipment. The model used a mixture of empirical and literature data to construct a simulation that showed how the EM absorption and subsequent temperature profile changed with frequency. This showed good alignment with the TIC observations and will provide valuable insight for future work.

The model developed did not consider any chemical reactions occurring in the preform or changes in density due to the deposition of the SiC matrix that would have certainly affected the thermal and dielectric properties. It also did not consider the flow of gas into the preform, which had a cooling effect on the fibres. Rotation of the preform in the cavity was also not modelled due to the additional computational resources that would have been required, although this was within the capabilities of QWED 3D. These results provide new information to modify the experimental setup and verifies the TIC results that would otherwise not have been possible. These results mean that future work must use larger diameter preforms in the cavity to improve the microwave absorption and use the foam to modify the temperature profile favourably. This will also improve the heating and help understand how the temperature profile changes relative to the magnetron output frequency. This will be discussed in more detail in the future work section.

4.3. Impregnation of SiC fibre with SiC slurry

This chapter reports the work investigating the impregnation of a SiC slurry into the SiC_f prior to infiltration step. From preliminary testing, three powders were selected based primarily on the ability to be applied onto the fabric. For the remainder of this thesis these will be the only powders referred to using this nomenclature:

Table 4.5. Nomenclature of the three powders used and the respective solids content of the slurries they were used to create.

	Manufacturer	20.0 vol.%	22.5 vol.%	25.0 vol.%
StarCeram®UF-25	H.C. Starck	UF-25-20	UF-25-225	UF-25-25
StarCeram®UF-05	H.C. Starck	UF-05-20	UF-05-225	UF-05-25
SuperVac SiC	Testbourne	SV-20	SV-225	SV-25

A slurry made out of powdered fibre was considered to reduce the number of materials used, but due to costs, lead times and the value associated with SiC_f. As such, this was not investigated, though the option of creating a powder with the same composition as the fibres through PIP remains an option.

4.3.1. Particle size distribution analysis

Particle size distribution measurements were carried out on the three powders outlined in table 4.5. Results showed that all three powders were within one deviation of the technical data sheet provided by the manufacture.

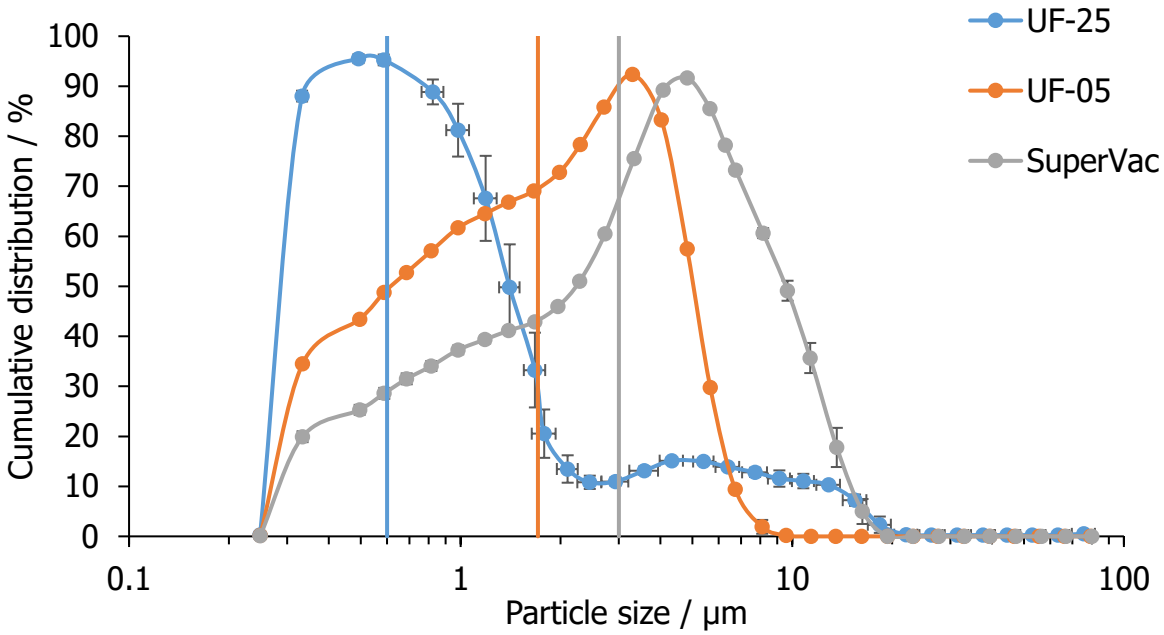


Figure 4.59. The particle size distribution of the three SiC powders and their respective D_{50} values are indicated by the dashed lines.

Table 4.6. Details of the commercially available SiC used in the project from the manufacturer's technical datasheets.

	UF-25	UF-05	SuperVac
Polymorph	Alpha	Alpha	Alpha
Particle size / µm	0.3-0.4	1-2	3-4
Specific surface area / $m^2\ g^{-1}$	23-26	4-6	-
Green density / kg m^{-3}	1.6	1.8	-

The UF-05 and Supervac powders had D_{50} values 1.71 µm and 3.0 µm respectively, with both showing a significant spread of particles smaller than the D_{50}, see figure 4.59. This is likely to be a combination of SiC and Al_2O_3 from the milling media. This is due to the disparity between the hardness of the SiC and Al_2O_3 that will have caused some alumina to be removed from the milling media surface and incorporated into the measurement. A small amount of slurry was analysed using an EDS map which showed no significant aluminium or oxygen content, this, however, could have been avoided had a SiC or an even harder milling media been used. The

UF-25 shows the largest deviation from the stated D_{50}, at 0.6 µm, similarly to the other two powders this could have been an effect of the milling media shifting the curve to the right. There is also the presence of larger particles between the 3-10 µm ranges, which could be an agglomeration of the powder as it is so fine. As a precaution to prevent this, the powder was typically milled with more energy and for a longer time in an attempt to break up the larger agglomerates, which can be seen in figure 4.60. However, this was always a traded-off with the quantity of Al_2O_3 incorporation.

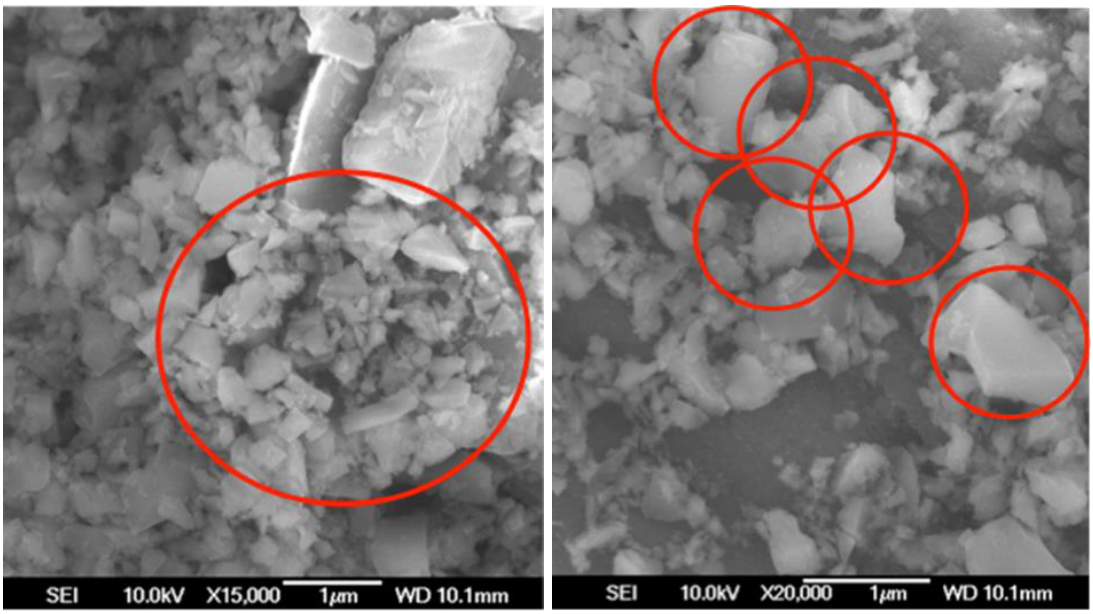


Figure 4.60. SEM images show agglomeration of powders on the right and ~1 µm sized powders on the right.

4.3.2. Room temperature slurry viscosity measurements

A number of trends were observed during rheological testing related to the particle size, the solids content and shear rate. All three powders at all three solids content showed shear thinning behaviour, typically Hershel-Buckley, as the shear rate increased to 500 s^{-1}, which indicates that the concentrations of surfactant in the slurries was correct and there was a low level of agglomeration. The decrease in

viscosity as the shear rate increased was probably due to particle orientation effects. This model of behaviour is desirable for the calendaring and vacuum bagging processes as both apply shearing forces which will decrease the slurry's viscosity. This meant that the penetration of the slurry into the fibre tows was improved and resulted in the slurry flowing readily and predictably when pressure was applied during vacuum bagging causing the SiC particles to distribute evenly. This was an essential quality for the MCVI process to prevent pore closure and hot spot formation. As expected, increases in the solids content resulted in increased viscosity, most noticeably in UF-25-25. This is because of the large specific surface area of the particles meant the powder had higher surface energy, therefore there were are increased particle-particle interactions, which increased the viscosity. The opposite trend is also observed as the particle size increases for the same reason.

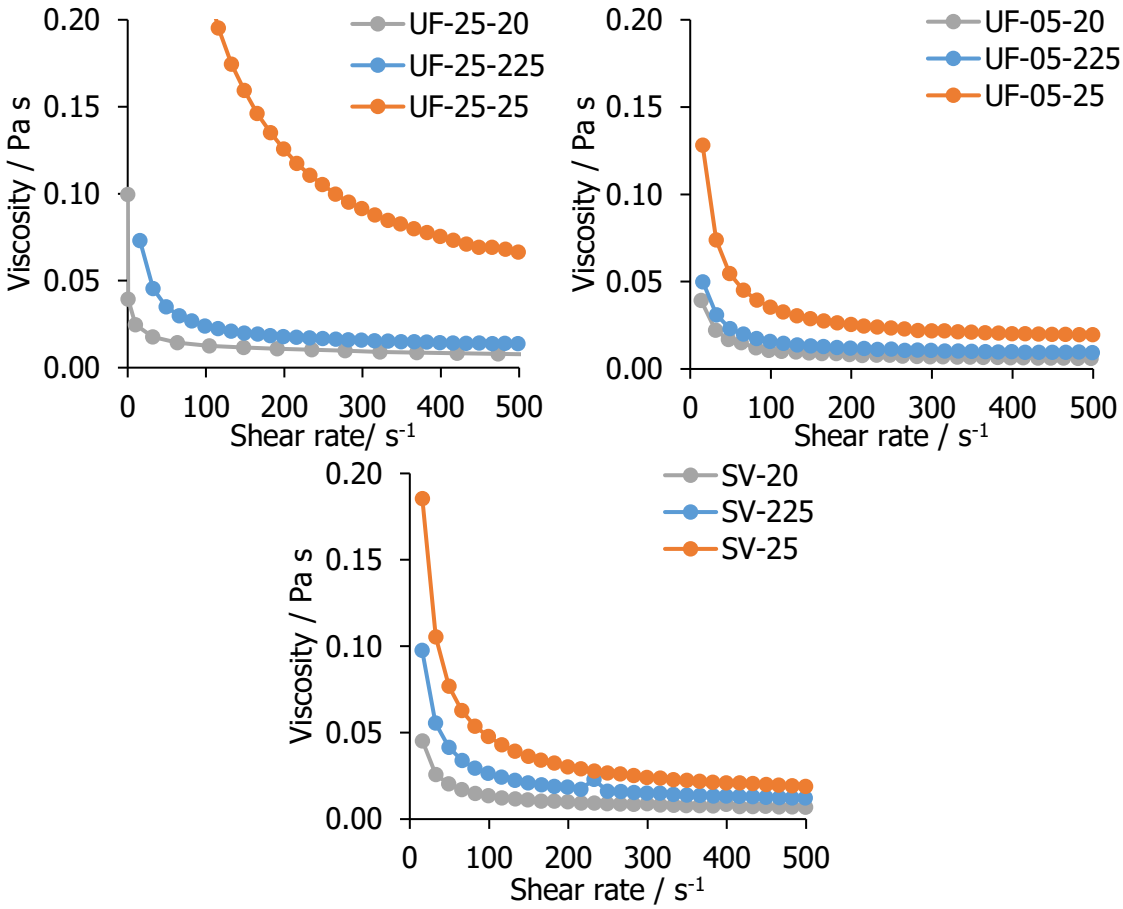


Figure 4.61. Three graphs showing the change in viscosity as a function of shear rate, with changing solids loading of the slurry and increasing particle size, from left to right UF-25, UF-05 and SuperVac.

4.3.3. The relative density of impregnated preforms

The relative density is important as it determines the porosity of the preform, which is directly proportional to the time required to fill the voids with SiC using CVI. From figure 4.62. it can be seen, as expected, that the addition of SiC slurry to a SiC fibre preform increases the relative density. A non-impregnated preform was typically 15% dense. Across the range of solids content and particle, size there was an approximately 20% increase in relative density to 35%. However, there appears to have been no significant effect of particle size and solids content on the impregnated slurry. This is likely due to the low reproducibility of the process at lab scale, as although a number of controls were put in place and standardised methods

employed neither were effective enough to indicate any differences in the relative densities of the resulting preforms.

The preforms all seemed to gain the same relative percentage of slurry as seen by figure 4.63, which shows the volume fraction of powder in the dried SiC_f/SiC_p composite. There appeared to be more discrete trends developing at the higher solids content as the range of the mean values increased. Most noticeably, the UF-25 slurries appeared to follow a decreasing trend, likely caused by the increasing thickness of the samples. This increased mass of the sample was negated by the increased thickness, indicating the sample thickness had a greater effect on the relative density than mass, which is confirmed by figure 4.64.

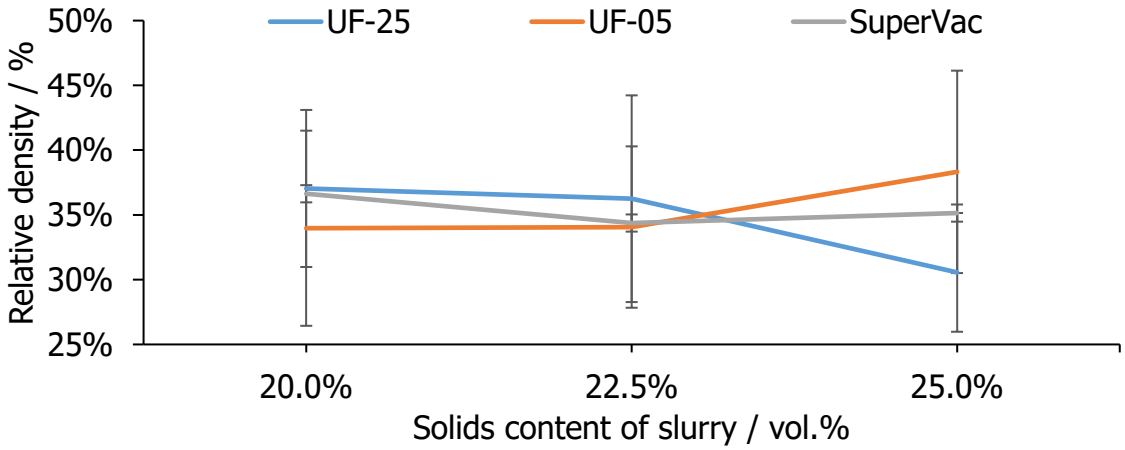


Figure 4.62. The relative density of SiC_f/SiC_p preforms impregnated with different solids content slurries and different particle sizes.

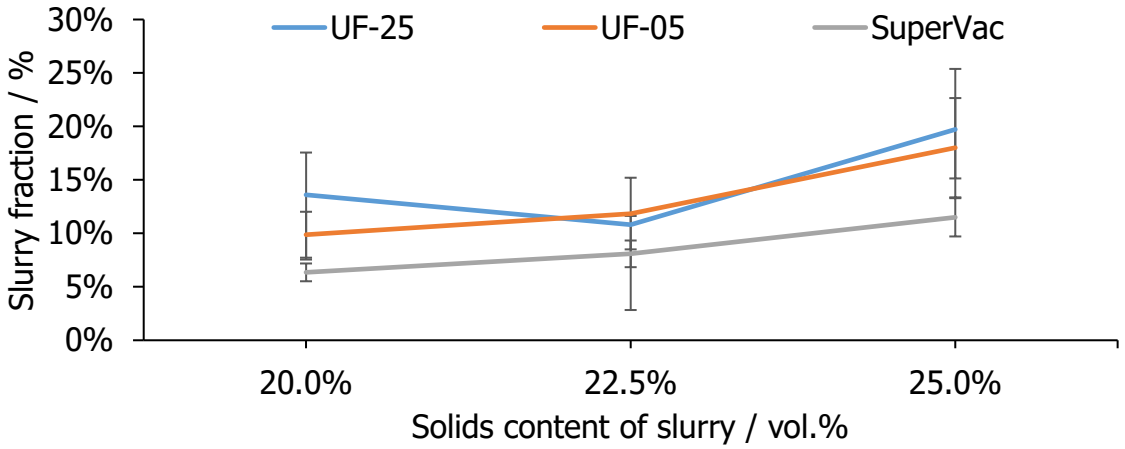


Figure 4.63. The volume fraction as a percentage of slurry added to the SiC_f/SiC_p preforms impregnated with different solids content slurries and different particle sizes.

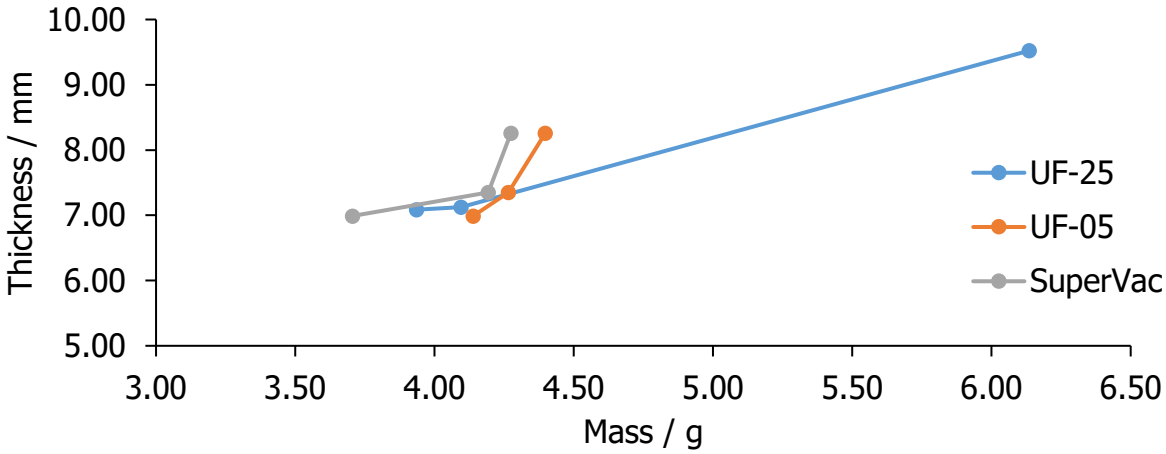


Figure 4.64. The increase in thickness as a function of the mean mass gain of the preforms when impregnated with different powders and solids content. From left to right in terms of data points (20, 22.5, 25 vol.%).

This thickness change has been observed using SEM, which shows the smaller particle size, with high solids content formed a thick ceramic layers in-between the SiC fabric ply. This is due to the high viscosity and fast drying rate of the UF-25-25 slurry, which meant that it did not flow readily through the preform in the vacuum bagging process. This translates to a thicker overall composite with a lower subsequent relative density. The two images below depict a sample impregnated with UF-25-25 and SV-25.

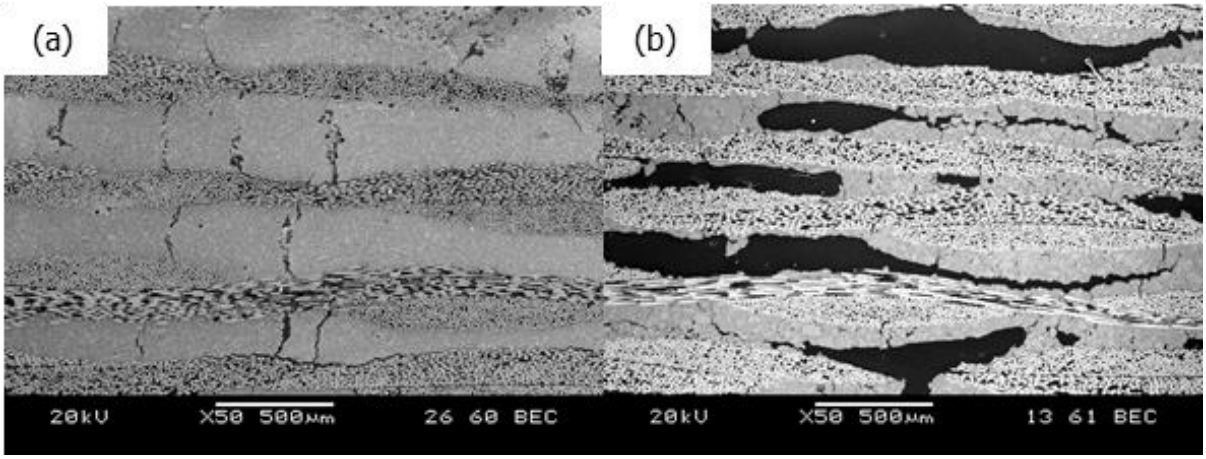


Figure 4.65. (a) An SEM cross-section of UF-25-25 preform, showing the fibres crossing the image horizontally and the large crack SiC powder matrix, (b) the thinner and more porous cross-section of the SV-25 preform.

4.3.4. Dielectric properties of SiC powder

The dielectric data for the three powders are shown in figure 4.66. The UF-25 powder behaved quite differently to the other two; it is not known whether this was due to the smaller particle size or slight differences in impurities. The UF-25 exhibited very promising dielectric properties, the values smoothly increased as a function of the temperature for both ε' and ε''. This is a desirable trait for use in microwave processing, despite the low loss factor, as it means the properties are predictable; a quality that is very valuable when working with a semiconductor material at high temperature in a dynamic system.

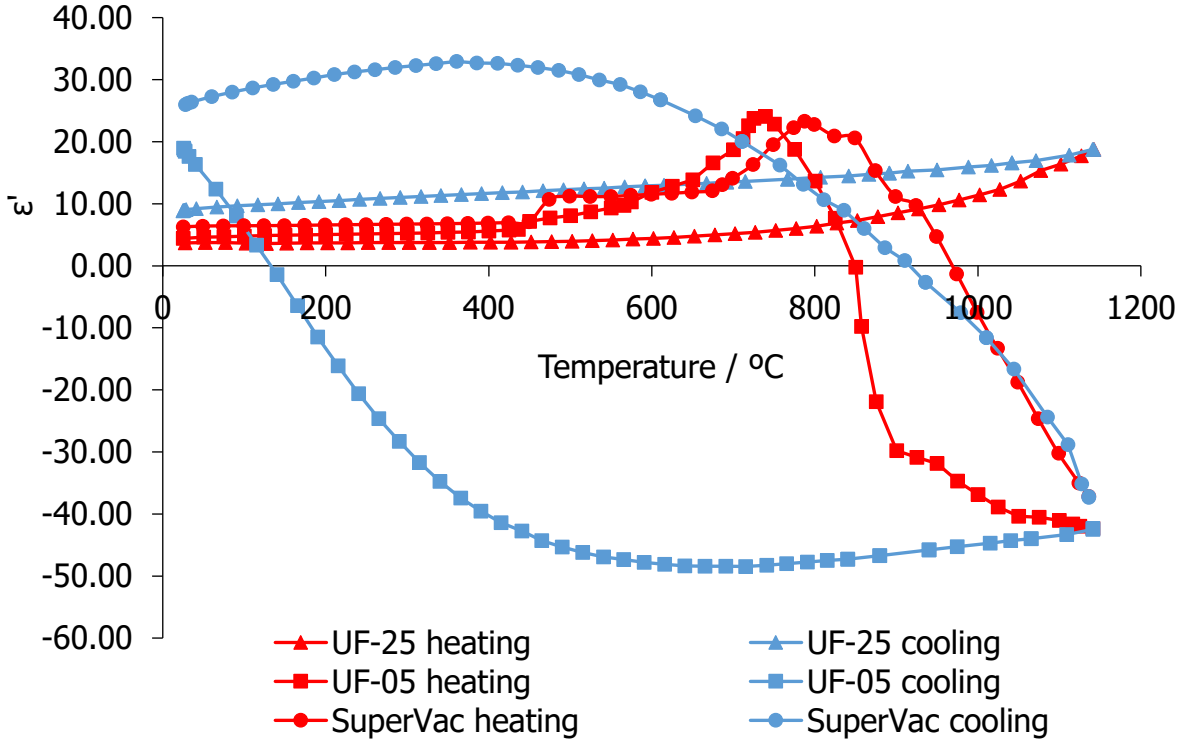


Figure 4.66. The changing dielectric permittivity (real part) of the three powders with increasing temperature upon heating (red) and cooling (blue).

All powders show an increasing ε' and ε'' up to approximately 600°C. In the case of the UF-05 and SuperVac powder from around 740-800°C both these powders' dielectric permittivity start to decrease and by 900°C they exhibit negative values of ε'. This is non-physical measurement as ε' cannot be less than one, which means that the relative dielectric permittivity is now also negative according to equation 2-8. This suggests that the dominant heat mechanism is no longer a dielectric mechanism but was more ohmic-like. This is likely to have occurred due to a change in the electrical conductivity of the powder so that it behaved more like a metallic material, which at high-temperature becoming a resistor [352]. This is supported by the observations in the test as electrical discharge from the material was seen.. This behaviour is thought to have occurred for two reasons. The first is that common impurities in the powder such as carbon, silicon, aluminium, or boron [391], all could

have formed compounds that are very electrically conductive making them resistors at high-temperature [352]. The other explanation is because SiC is a wide-band gap semiconductor, which becomes conductive at high temperature and acts more like conventional conductor where resistance increases with temperature. This happens due to thermal excitation of electrons causing them to move across the large band gap (~3 eV) from the valence into the conduction band permitting electron movement [392, 393]. This breakdown temperature is highly dependent on the SiC polymorph and polytype, but a generic value reported in literature was ~700°C [394]. This would mean the SiC would lose its dielectric character at the temperatures experienced. The SuperVac powder showed this effect to a lesser extent when compared to the UF-05 powder, with ε' becoming a positive value at around 900°C. Conversely, the UF-05 powder does not show this return to dielectric behaviour until 140°C. This result could indicate that the UF-05 has more impurities than the SuperVac and that impurities in the powder have a very strong interaction with the electric component of the microwave field. Interestingly the UF-25 does not demonstrate this behaviour up to 1142°C, instead its ε' increases steadily up to the maximum temperature and shows only a small amount of hysteresis when cooled. This suggests that the UF-25 powder is composed of a different polytype that has higher dielectric breakdown strength. However, more work is needed to determine the polytypes present in the powders to help explain their high-temperature conductive behaviour.

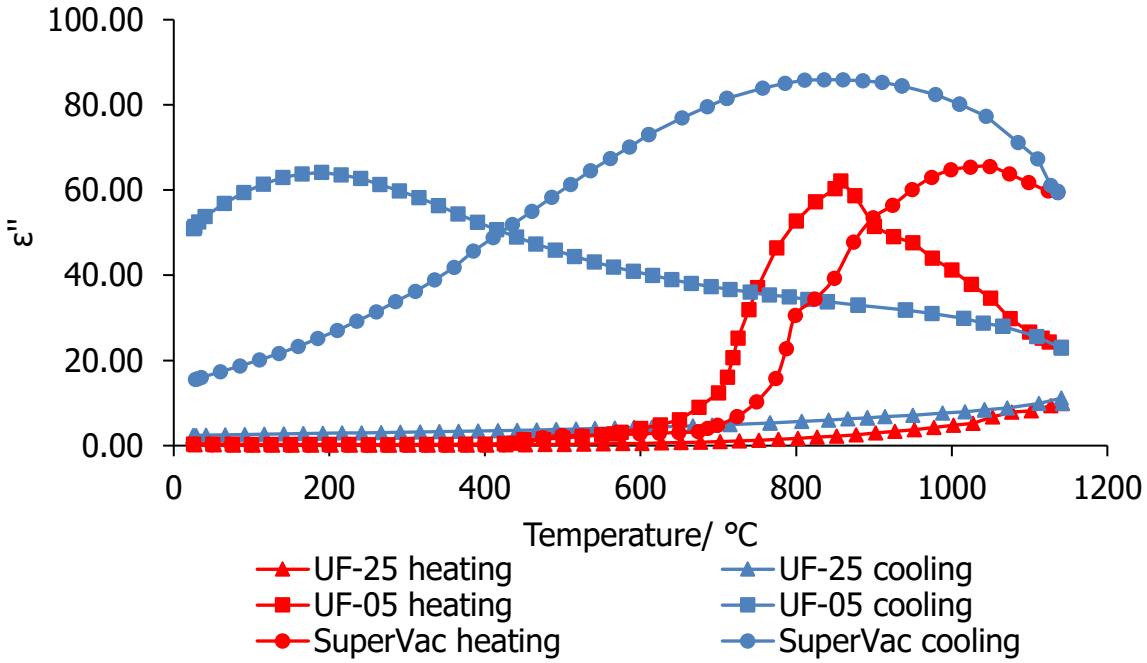


Figure 4.67. The changing loss component of the dielectric permittivity (imaginary part) of the three powders with increasing temperature upon heating (red) and cooling (blue).

From figure 4.67. it can be seen that the loss factor of UF-05 and SuperVac above 750°C become significantly larger. The ε" of the UF-05 powder peaked at a value of 62 at 850°C, before decreasing rapidly to 23 when heated further to 1100°C. Similar The SuperVac powder exhibited similar behaviour its peak was comparable in magnitude it occurred at a higher temperature ~1050°C and displayed a smaller decrease at the maximum temperature. Again, both these powders demonstrated hysteresis with the SuperVac powder measuring at least double the value of ε" during heating at all temperatures and whilst cooling. The UF-05 also displayed unexpected behaviour as its loss factor increased with decreasing temperature; this is most likely due to the semiconductor properties of SiC. This behaviour could be indicative of a thermal runaway process occurring during the test as the input power was being decreased [259]. These results could have a negative impact on the ability to heat impregnated SiC_f preforms to the desired temperature. However, the high

loss factor of the UF-05 and SuperVac will aid the heating of a composite but potentially only whilst they display dielectric behaviour. Conversely, the UF-25 powder displayed a low loss factor at all temperatures but increased slowly to 9.9 at 1142°C. This can be considered as both a positive and negative outcome; the powder doesn't heat very well in a microwave field but it does behave like a predictable dielectric material at all temperatures and did not display semiconductor-like properties at any temperatures.

4.3.5. Contact angle measurements

Contact angle measurements were made to establish how the slurries wetted SiC. Wetting refers to the ability of a liquid to maintain contact with a solid when in contact and held together by intermolecular interactions, the degree of which is characterised by cohesive and adhesive forces [395]. It should be noted at this point that all samples loaded with 20 vol.% slurries and the SuperVac impregnated sample were not taken forward for further testing due to their very low strength, which made them unsuitable.

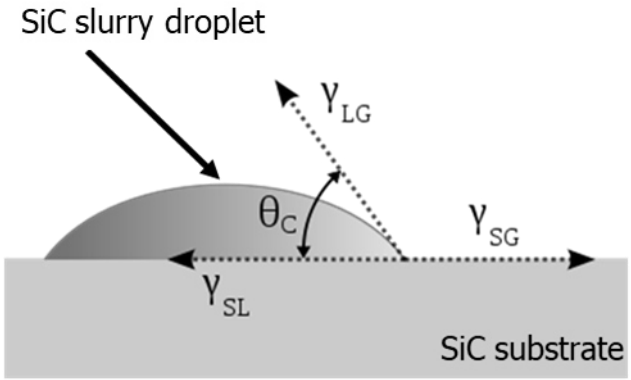


Figure 4.68. A schematic representation of the sessile drop test of the SiC slurry droplet on a SiC substrate where γSL, γLG and γSG are solid-liquid, liquid-gas and solid-gas respectively. Figure adapted from [396].

Collection of the data was very user subjective, which led to the errors seen in figure 4.70. being large making it difficult to draw definitive conclusions. In an attempt to combat this, 60 samples were tested using a macro lens camera to increase the confidence and accuracy of the measurement. Tests were carried out on the same day to reduce the effect of variation in ambient temperature and humidity having an effect. The measurements were then made using ImageJ using the angle-measuring tool, where the substrate basal plane and angle of the drop drawn were done manually, see figure 4.69.

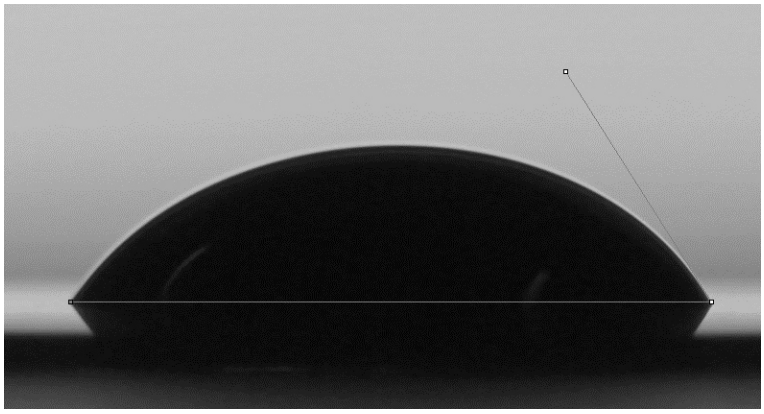


Figure 4.69. A photo showing the ImageJ angle-measuring tool used to measure the wetting of the droplet on the substrate.

From figure 4.70. it can be seen that all slurries wetted the SiC substrate as the contact angle measured was <90º. The slurries UF-25-225 and UF-25-25 had the highest contact angles respectively, with UF-25-25 being statistically different from the UF-25-225, whilst the UF-05 slurries had a noticeably lower contact angle. Similarly, as expected, lower viscosity slurries had a lower contact angle. This is because the surface energy is greater than the surface tension of the liquid, so wetting occurred. The higher viscosity slurries though still wetting had higher contact angles since the liquid was trying to minimise its contact with the surface and form a 'bead', see figure 4.72.

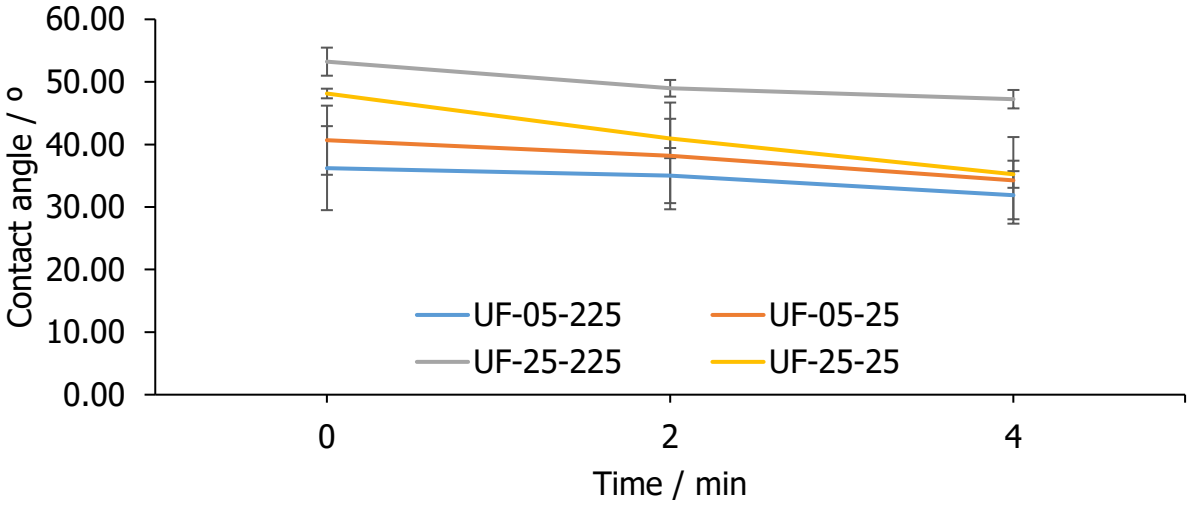


Figure 4.70. Change in contact angle of SiC slurry droplet as a function of time.

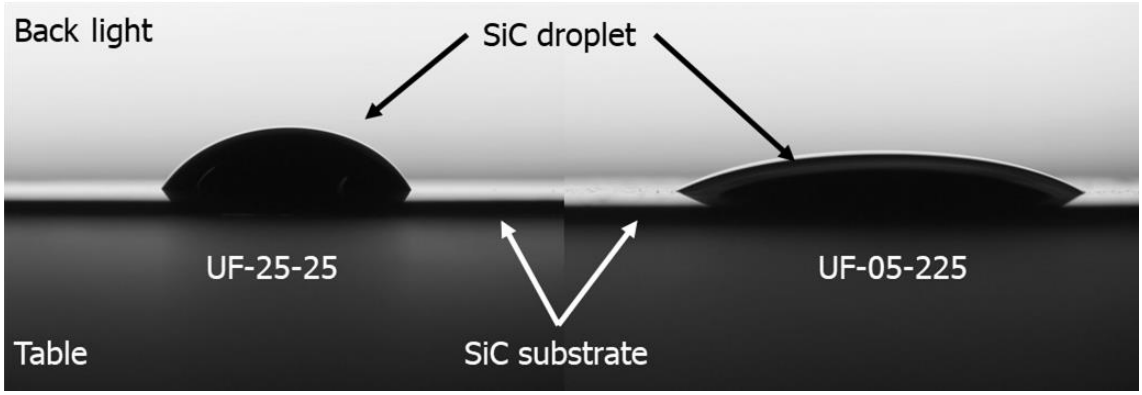


Figure 4.71. Difference between the least wetting and most wetting slurries respectively at T_0.

A time-variant was added to observe if any effect was seen as the slurry dried in ambient conditions on the substrate. A decreasing angle was measured, as seen in Figure 4.72., in addition, the total decrease observed can be seen in

figure 4.73. In terms of the calendaring process to impregnate the SiC fabric with the slurry, wetting must occur for the slurry to distribute the SiC particles uniformly. This significantly affects the resulting green density post-impregnation, and, potentially, the CVI process through the generation of hot spots from uneven distribution. This makes the lower wetting angle slurries more favourable. It can also be seen that the higher solids content slurries dried more quickly due to the lower initial water

content. A four-minute period was used because that was the approximate time to impregnate, cut the fabric, layup and apply the vacuum to the SiC_f/SiC_p green body. This indicates that during the impregnation of the SiC fabric the wetting character of the SiC slurry changed significantly.

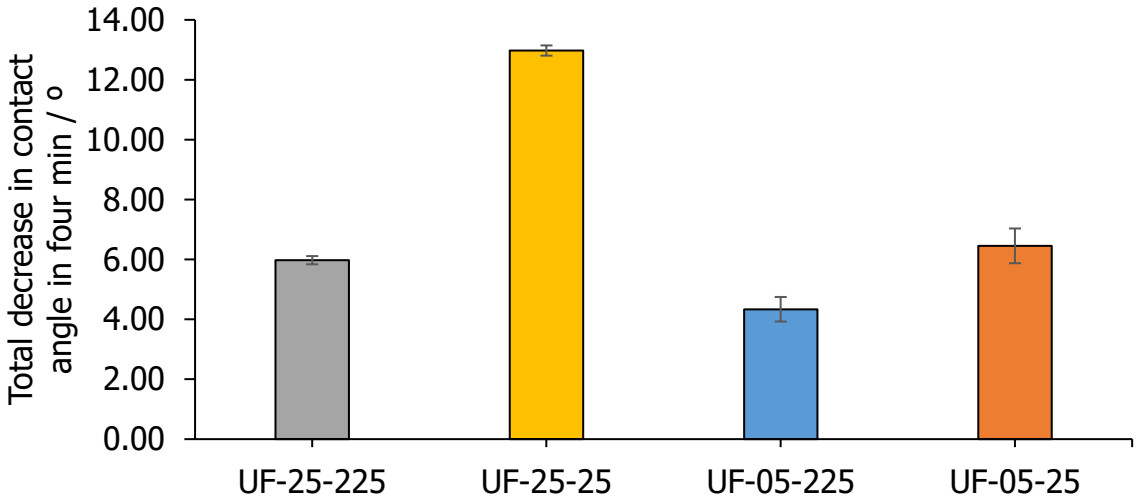


Figure 4.72. The total decrease in contact angle over a four-minute period of the four different slurries.

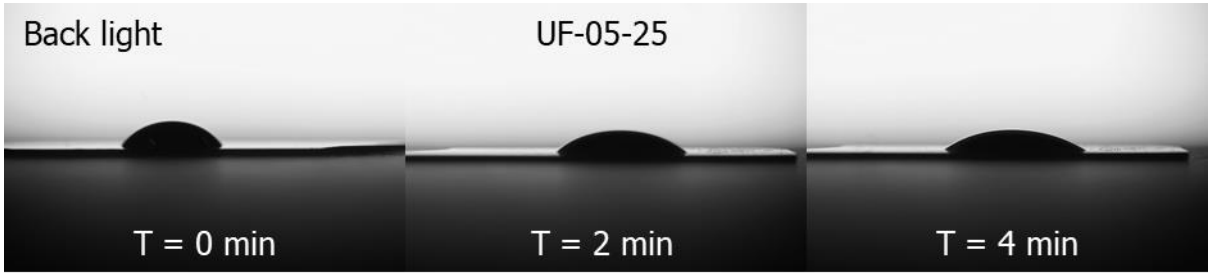


Figure 4.73. Series of photographs showing the change in drop shape as time increased.

4.3.6. Porosity network analysis of impregnated composite

Preliminary analysis was carried out on the CT data using the Avizo software. Results showed that the porosity was interconnected across all three dimensions within the SiC_f/SiC_p composites, which meant the software was unable to quantify the porosity. The software was able to detect a very small volume of closed porosity, see figure 4.74.

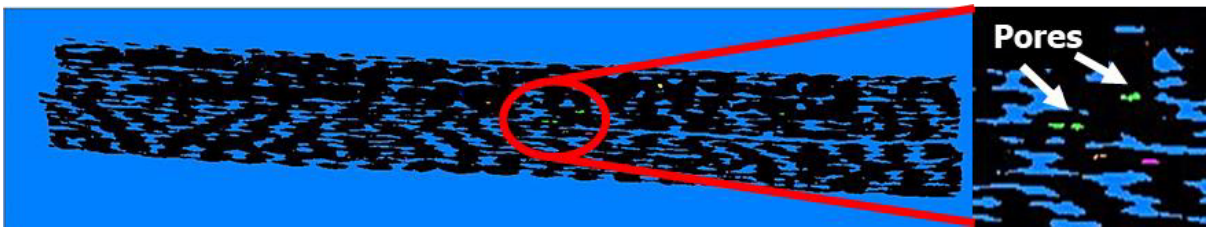


Figure 4.74. Images from Avizo showing the identification of small closed porosity in the green SiC_f/SiC composite.

It was determined that the software was unable to distinguish the edge of the impregnated preform and thus not quantify the internal porosity because it could not define a boundary condition at the edge. This meant that the pore network was connected via pores as small as 0.025 mm^2, the resolution of the micro-CT images, making it very porous even with the addition of the powder. These preliminary results meant a modified approach was required to evaluate the porosity in the green preform. To do this a MATLAB script was developed that was able to quantify pores for entire CT image stacks in 2D, similar to what Avizo was capable of for a single image. Results from the analysis using the script provided information on a slice-by-slice basis so the information produced was an area rather than a volume.

Figure 4.75 shows the effect of impregnating the SiC fibre preform with SiC slurry on the mean pore area. As expected, the addition of the slurry decreased the mean cross-sectional area of porosity by ~50%, which can be seen by the difference in the mean area of the non-impregnated sample (0.156 mm^2), compared to the other four samples, which were all <0.09 mm^2. The magnitude of the error bars of three of the four of the samples was comparable, but the UF-25-25 sample had a significantly larger standard deviation. This was found to be because of internal delamination inside one of the samples, see figure 4.76, which at its largest measured 6.32 mm^2.

No significant trend is seen with changing the particle size or solids content of the slurry.

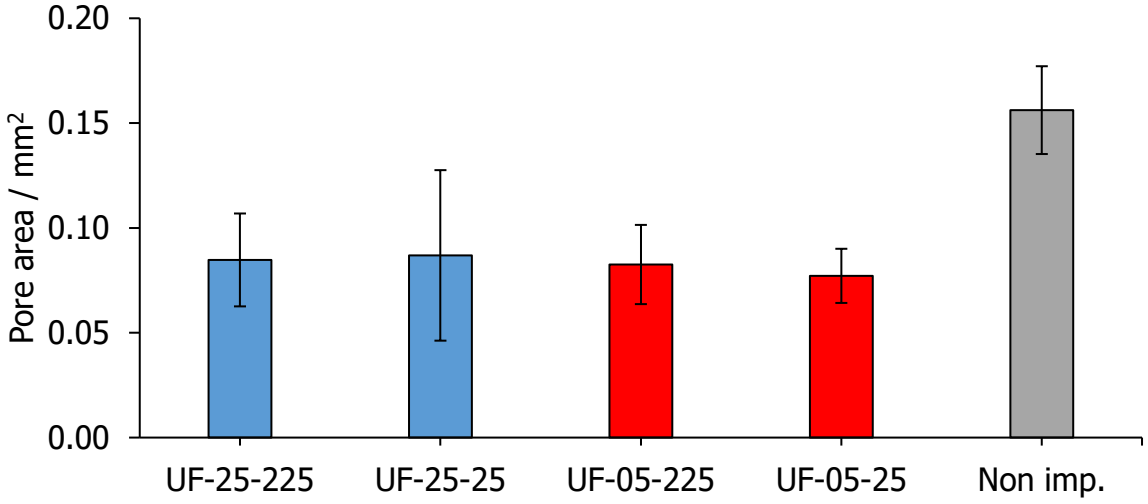


Figure 4.75. A bar graph showing the mean pore area inside the SiC_f/SiC.

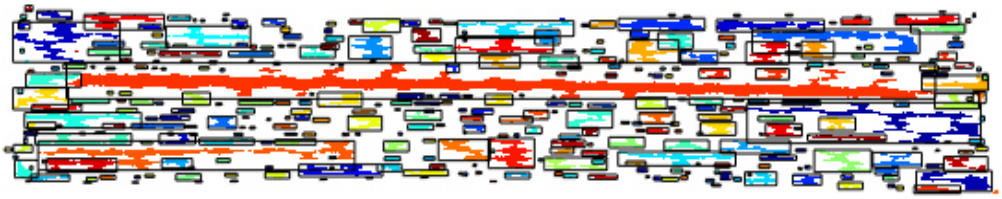


Figure 4.76. Image produced by the MATLAB script highlighting the internal delamination (orange) in UF-25-25 thus skewing the error bar.

The script also measured the maximum pore area, which is a very important parameter as it is the rate-limiting step in terms of the densification of the SiC_f/SiC composites in any form of the CVI process.

Figure 4.77 shows the maximum pore area in mm^2, it should be noted that data from the sample shown in figure 4.76 has not been excluded from this graph hence the large error bar on the UF-25-25 sample. The data shows three distinct results:

(i) The non-impregnated sample had a much larger mean maximum area in terms of porosity when compared to impregnated samples;

(ii) The solids content of 25 vol.% reduced the maximum pore size more than the 22.5 vol.% slurries;

(iii) The UF-05 powder decreases the maximum pore size more when compared to equivalent solids contents of slurries, indicating that a particle a size of D_{50} = 1.71 µm was better than the smaller particle size UF-25 powder.

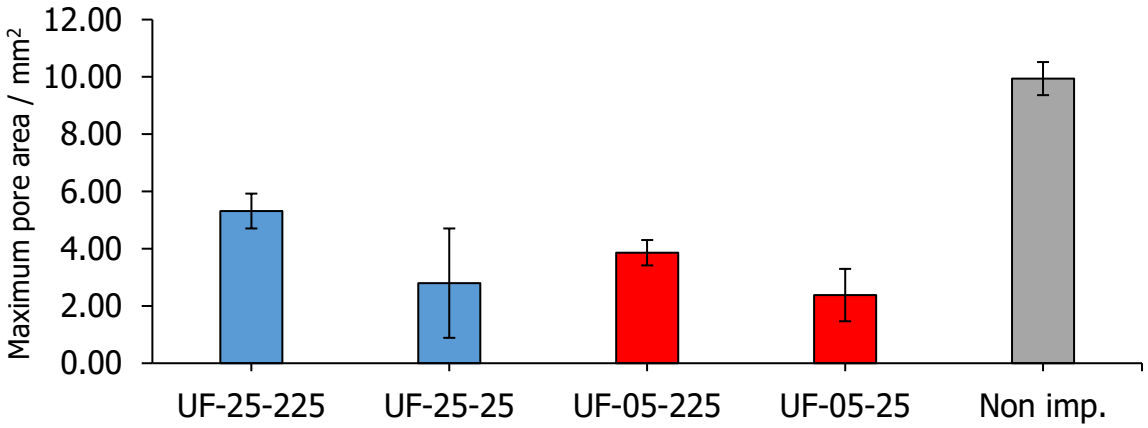


Figure 4.77. The mean maximum pore area measured using the MATLAB script based on micro-CT data.

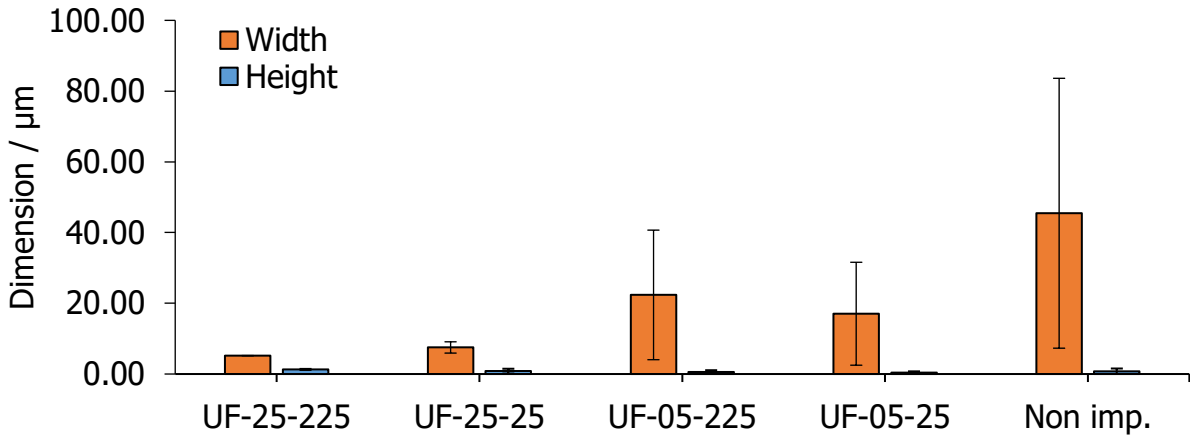
In principle, the largest pores will be the last to be filled by the SiC deposit as all other porosity, if not closed prior to starting the MCVI, will be filled by this point. However, this is dependent on two factors;

(i) The location of the largest pore since the temperature gradients associated with MCVI the deposition rate of SiC varies accordingly. This means that if the large pore is a colder area it will be filled slower and therefore it will have a greater effect on the final density.

(ii) The ability of the pore network to supply the reactant gases into the pore to fill the pore. If the pore has a high volume of gas input, it will be filled readily and close at a similar rate to smaller, less well-supplied pores. An investigation into the behaviour of these factors was not undertaken due to time constraints.

Another parameter that was considered important was the aspect ratio of the porosity, as this would affect the flow of fluid in the pores and subsequent deposition

of the SiC. Figure 4.78 shows the width vs the height of the pores between the various samples measured. There is a clear relationship between solids content and particle size, and therefore viscosity, that the lower the viscosity, the larger the aspect ratio of the pores. This is likely because the slurries with lower viscosities flow and spread over the fabric tows more readily. Whereas the more viscous slurries, with a higher solids content or smaller particle size, were sufficiently viscous and not displaced uniformly over the plies to the same extent during the vacuum bagging process, and form high powder concentration regions that form more equiaxed pores.



Aspect ratio	4.06	38.68	153.03	120.65	200.12

Figure 4.78. A bar graph showing the ratio of width to height in the impregnated samples with a table below corresponding to the aspect ratio.

The standard deviation of the pore size was also calculated by the MATLAB script. In order to produce a metric for the uniformity of the pore size distribution the coefficient of variation was calculated. This allowed direct comparison of the pore distribution between samples as it was a dimensionless parameter irrespective of the number of images in the dataset, which varied by up to 300. The coefficient of variation was calculated according to equation 4-7.

Equation 4-7 $$C_V = \frac{\sigma_D}{\mu_{av.}}$$

C_v = Coefficient of variation

σ_D = Standard deviation / μm^2

$\mu_{av.}$ = Mean / μm^2

Figure 4.79. illustrates this analysis by showing that the higher solids content sample produced a less variable pore size when compared to the lower solids content slurries, and particularly when comparing impregnated samples to the non-impregnated samples. Another trend observed was the larger particle size slurries also showed less variation in the pore size but only when comparing the UF-25-25 samples with the UF-05-25 samples; the UF-25-225 and the UF-05-225 sample were almost identical. This shows that the UF-05-25 slurry was superior to the other slurries, as the resulting porosity network can be considered to have been more consistent in terms of pore sizes. This perhaps indicates that if this sample were to be used during the MCVI process the closure of porosity is more likely to be controlled by the temperature gradients in the sample rather than variation pore sizes. If true, this is particularly relevant to developing a fluid flow model that incorporates pore closure to predict the processing times of the composite to achieve full densification.

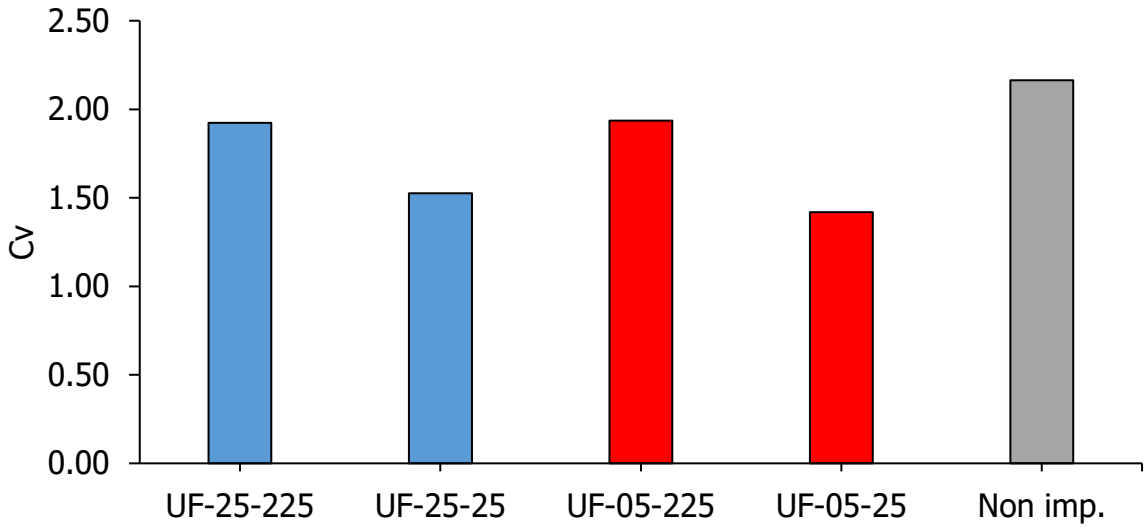


Figure 4.79. A graph showing the coefficient of variation between samples indicating the uniformity of the pore size.

As a secondary output from the MATLAB script a 3D histograms were obtained, that showed the pore count across the YZ plane through the composite. Figure 4.80 shows the corresponding histograms for the five samples. A critical observation from this figure is that the non-impregnated sample shows an uneven pore count distribution in the YZ plane and, as can be seen from the scale bar, a higher pore count as well through the whole sample. The other four samples show visually very similar pore count distributions from the colour scale with no obvious extremes, which indicated homogenously distributed porosity networks were produced. Another observation is that the lower solids content slurry showed better pore filling below the 100-pixel threshold, as seen by the darker blue above 60 pixels. This is likely to be because the lower viscosity meant fewer smaller pores were produced in these composites with the compromise being that these samples had larger maximum pores, as seen previously in figure 4.78.

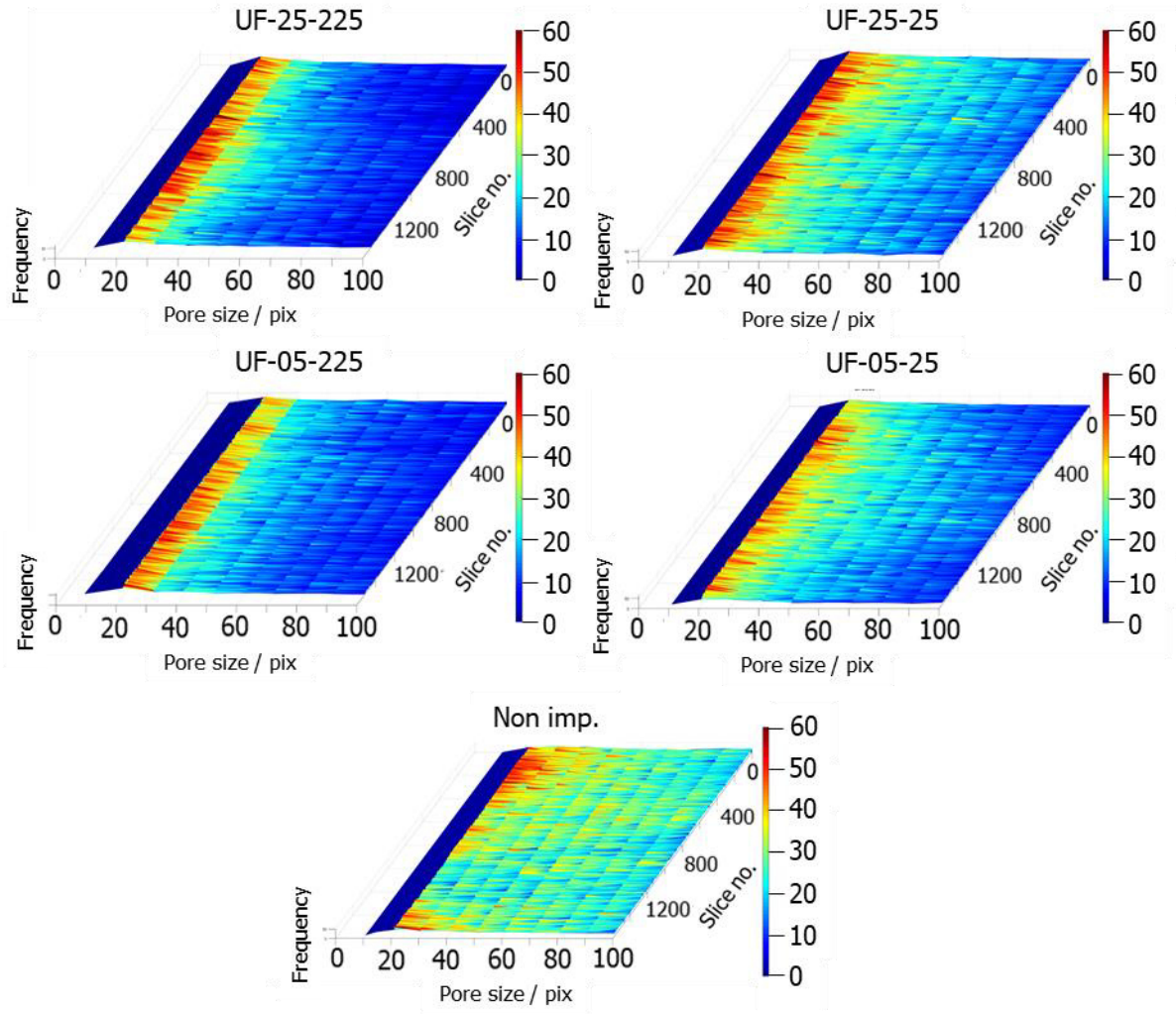


Figure 4.80. Histograms showing the pore count distribution for one composite from each sample set as a function slice number taken from the YZ plane, with a bin size of 10 and a max range of 100 pixels.

It should be noted that pores below 10 pixels were discounted from the MATLAB script based on the validation work carried out in ImageJ and the minimum resolution of the CT scans being 25 μm^2. The output of the script was validated using ImageJ software and its threshold and analyse particles tools. Three raw micro-CT images were randomly selected and loaded into ImageJ from each sample and a threshold value applied manually that was determined to select the porosity correctly. The analyse particle tool was then used to measure the mean pore area and pore number.

The MATLAB script had two parameters that controlled the threshold value of pore selection and the interconnectivity of pixels that were adjacent to one another based on the colour scale. From these two parameters, a matrix was created such that according to the output from ImageJ the result of the MATLAB image for pore area and pore number on the same image could be dialled in to verify the script's value before the entire image stack was evaluated. Figure 4.81 shows the data for a set of samples prior to the validation in process. The average error between the images analysed using ImageJ and the MATLAB script was 19.36%, with the non-impregnated sample showing the largest error.

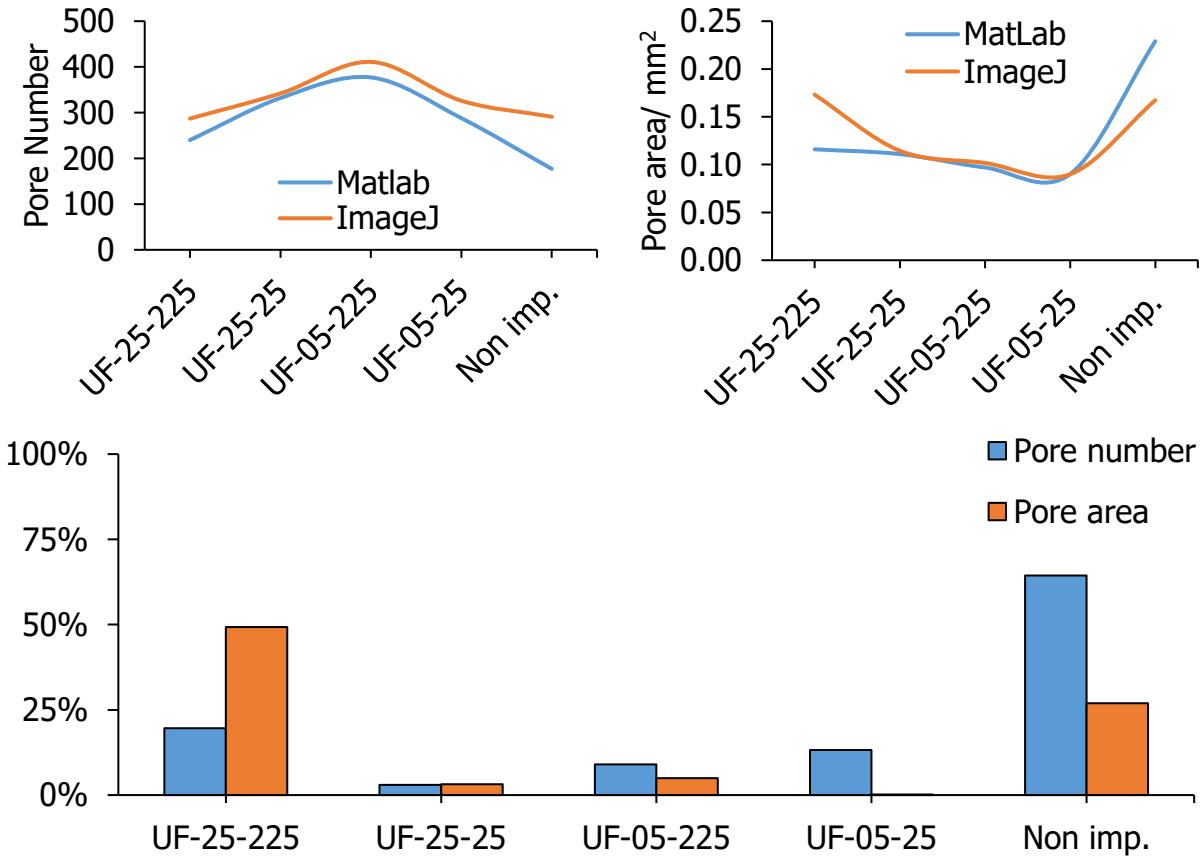


Figure 4.81. Three graphs showing the initial image analysis of the impregnated samples showing the differences in pore number and area and the average error prior to the dialling in process.

Figure 4.82. shows the effect of the dialling in process on these two metrics. This resulted in a reduced average error of 7.91% with the greatest improvements seen in the UF-25-225 and non-impregnated samples, which achieved much closer alignment to the ImageJ tools[xii]. In some cases, the script edge detection in the MATLAB script was shown to supersede the ImageJ tools capabilities, particularly non-imp. samples, which were highly porous, see figure 4.83.

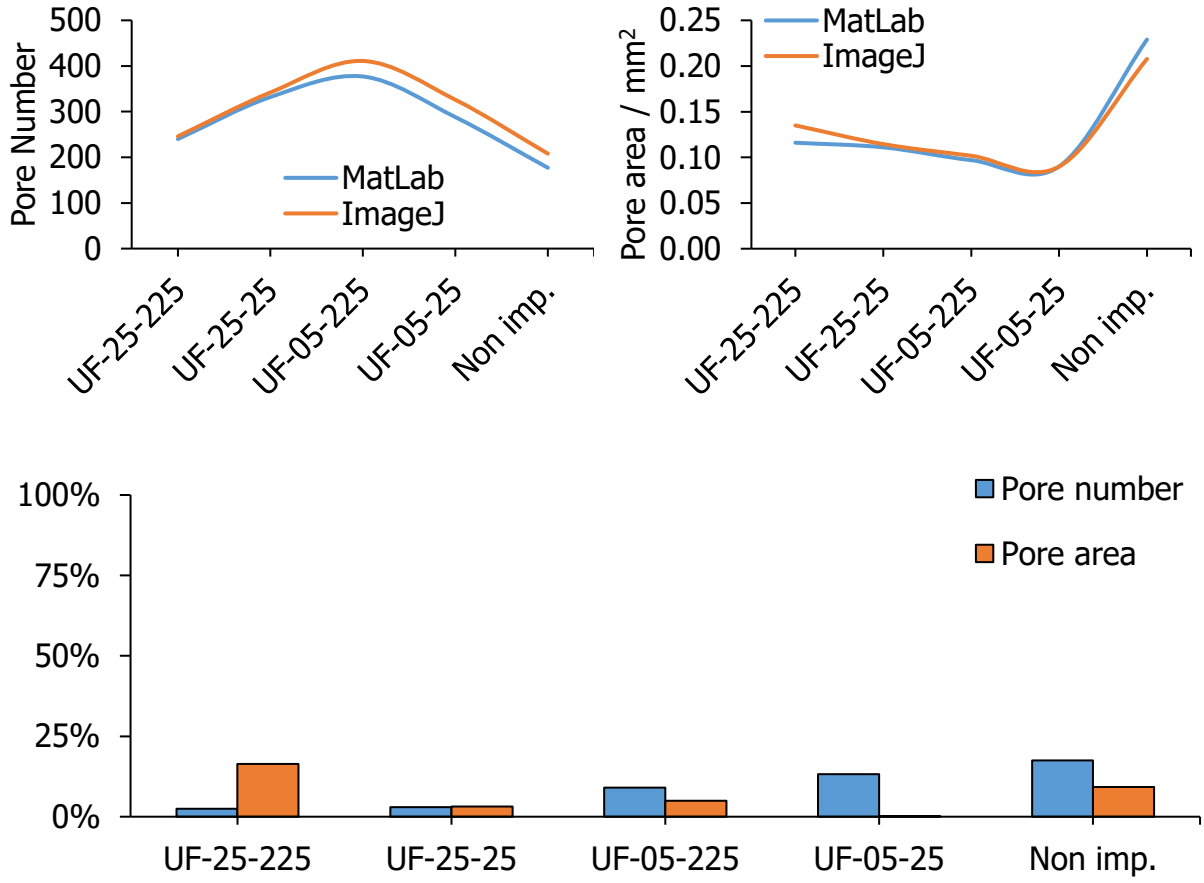


Figure 4.82. Three graphs showing the result of the image analysis with the script variable being tuned in to align the result with that of ImageJ again showing the differences in pore number and area and the reduced average.

[xii] This assumes the ImageJ software is correct.

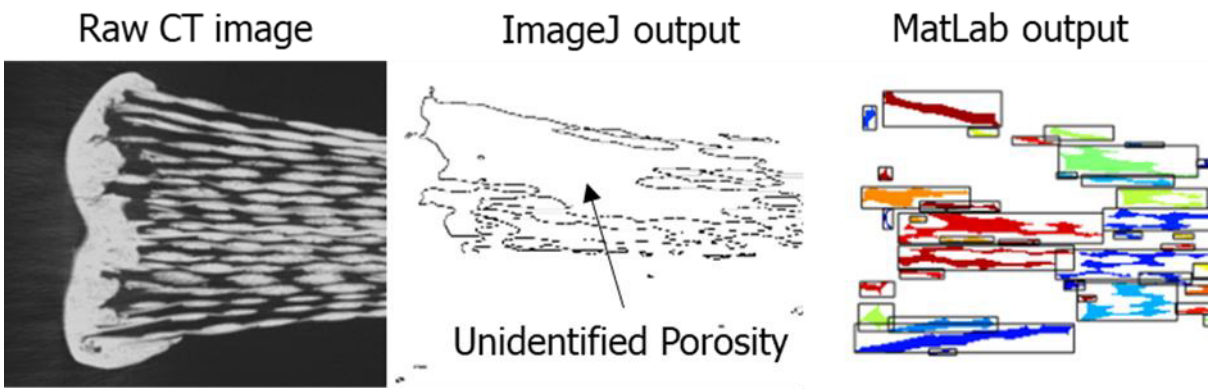


Figure 4.83. Three images detailing the differences pore detection between the ImageJ tools and the MATLAB script.

4.3.7. Gas permeability of impregnated composites

One of the main parameters that needed quantification was the permeability of the impregnated preforms. Preforms needed to be permeable to allow the precursor gases to penetrate the structure to decompose and deposit SiC. Whilst beneficial overall, adding the powder reduced the volume of pathways the reactant gas could traverse. Furthermore, preforms with a low permeability after the powder had been added will potentially have closed porosity, which could not be accessed by the reactant gases, and so densification would be reduced.

The gas permeability of the SiC_f/SiC_p composites was evaluated using a custom-built rig. Direct measurements of the pressure difference across the sample were taken in a flowing air environment using a differential pressure metre. The pressure difference across the sample's thickness at an increasing flow rate of argon is plotted in figure 4.84. It shows that as the flow rate increased so did the pressure difference across the sample, a statement valid for all samples tested. UF-25-25 showed the greatest pressure difference, whereas the UF-05-225 showed the least of the impregnated samples.

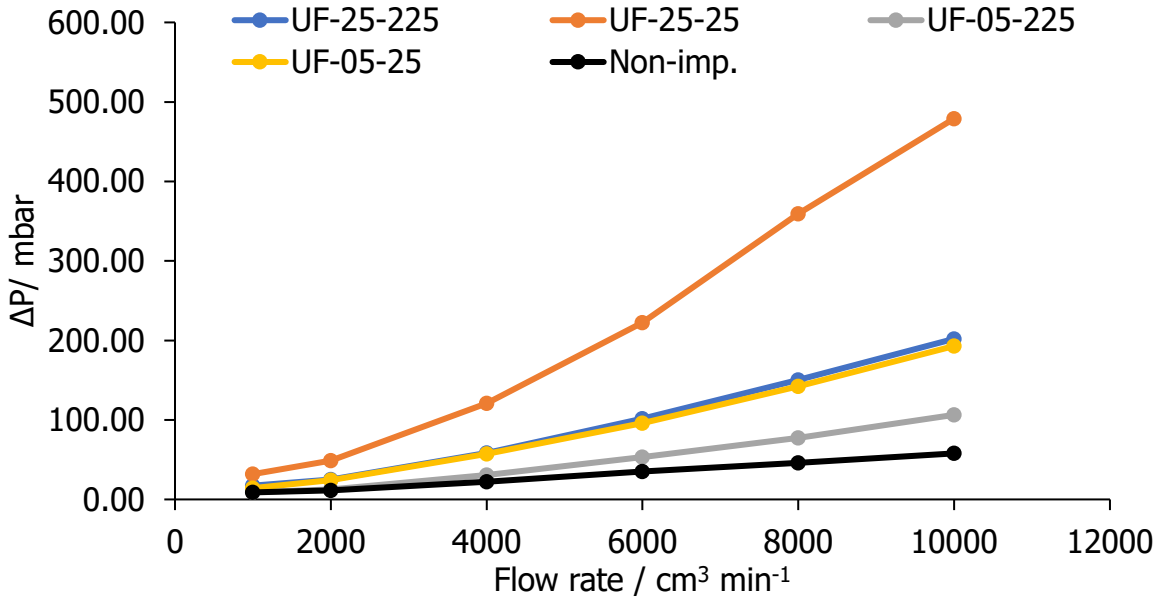


Figure 4.84. The effect of increasing flow rate on the pressure difference across the SiC_f/SiC_p thickness, showing the samples with higher solids content and particle size have a greater difference and vice versa.

The SiC_f/SiC_p sample's permeability were then calculated using equation 3-10, where the viscosity of argon at room temperature was taken to be $2.23x10^{-5}$ Pa S. It would have been preferential to use hydrogen gas as it would have been more representative of the experimental work but it was not used for safety reasons. Darcy's Law was applicable to the test as the Reynold's number (R_e) calculated less than 10 for the flow rates that corresponded to those achieved in the MCVI process; the maximum value that could be used was 2000 cm^3 min^{-1}, which is indicated in figure 4.85.

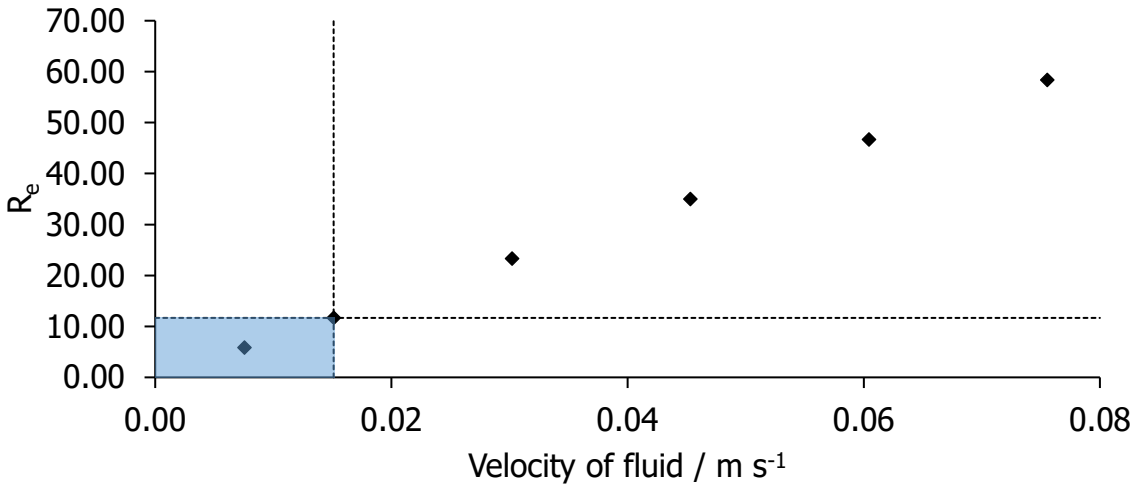


Figure 4.85. Reynold's number as a function of fluid viscosity showing the quadrant the MCVI process operates in highlighted in blue.

The flow was laminar under all conditions as the R_e ≤2300, which is the boundary to the transition regime beyond which flow becomes turbulent. The R_e number was ≥10 at a flow rate of 1716 cm^3 min^{-1}. Darcy's law states that the flow rate of a fluid has a linear relationship with the pressure difference [397], which is obtained by neglecting the inertial terms in the Navier-Stokes equation when the viscous forces of flow are dominant [398]. However, at higher flow rates flow becomes non-Darcian and obeys Forchheimer's law, equation 4-8, for incompressible fluids as the inertial effects of gas flow become significant [399].

Equation 4-8
$$\frac{\Delta P}{\Delta L} = \frac{\mu v}{K_v} + \frac{\rho}{K_i} v^2$$

K_v = Viscous permeability (Darcy) / m^2

K_i = Inertial permeability (Forchheimer) / m

V = Volumetric flux per area / m^3 s^{-1} m^{-2}

This result informed the experimental efforts to limit the flow rate to keep the R_e below 10 to prevent inertial effects of high gas flow affecting the densification of the SiC_f/SiC_p preforms.

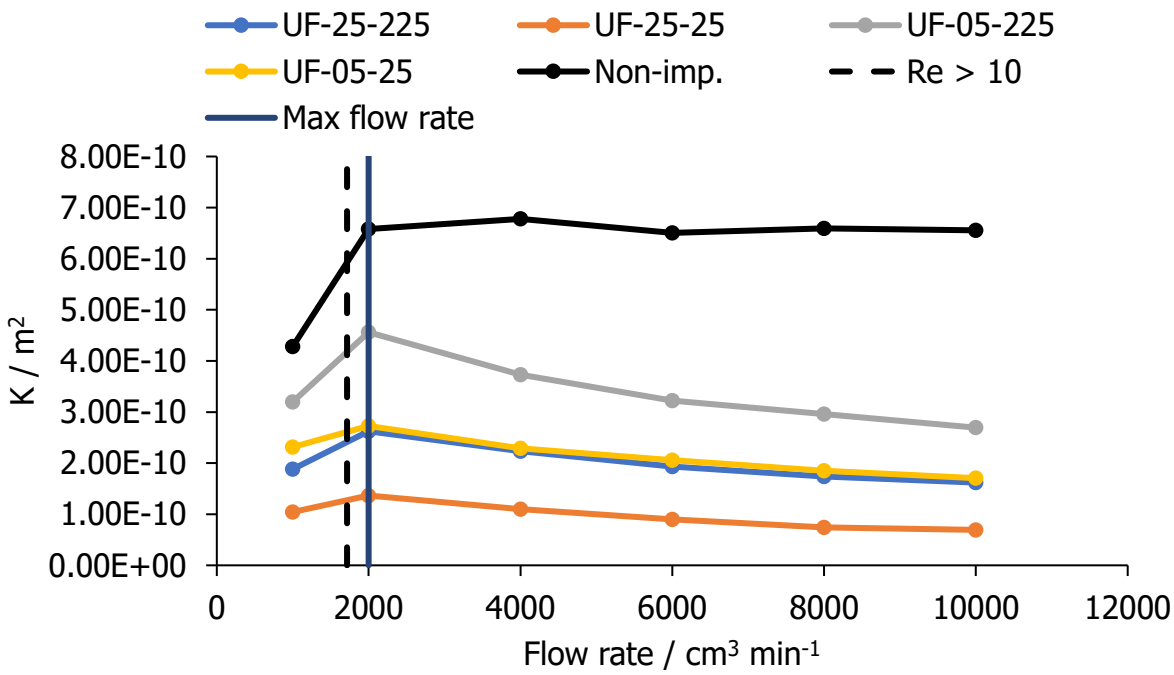


Figure 4.86. The effect of slurry addition to the SiC_f preforms on the permeability, showing the slurry addition decreases the permeability by an order of magnitude for all slurry variations.

Impregnated samples, as anticipated, had a reduced permeability compared to the non-impregnated SiC preforms. The same trend was observed as before, composites impregnated with smaller particle sizes with higher solids content had a lower resulting permeability. This is likely to be because of a greater degree of powder consolidation resulting in less open porosity and leading to a decreased mean free path. The data also shows that increasing the flow rate caused a decrease in the permeability of the bodies. This will have been because of the aforementioned effect of the permeability transition to obey Forchheimer's equation. This created a greater pressure difference at the inlet, which was because the gas flow was sufficiently high that the rate of gas arriving at the composites' surface was greater than that passing through and exiting the composite. This indicates that there was an optimum flow rate for the gas to arrive at the underside of the sample surface that was equal to the flow through the sample; which the data indicates this was approximately 1716

cm^3 min^{-1}. This flow rate is an order of magnitude greater than flow rates used in the literature, which are typically in the range of 3000-7000 cm^3 min^{-1} [313, 318]. This experiment would have been improved by the use of a smaller scale flow metre ranging from 0-2000 cm^3 min^{-1} (equivalent to the MCVI conditions) but the smallest available was 1000-5000 cm^3 min^{-1}.

4.3.8. Summary

The radar diagrams below illustrate how the four impregnated preforms performed against seven different metrics derived from the tests. The samples were ranked one to four on their comparative performance, one being the worst and four the best, therefore, the radar diagram with the largest area was considered the best compromise in terms of properties. Relative density was discounted from this summary due to no significant differences being identified between samples. Figure 4.87. shows that the UF-05-225 and the UF-25-225 slurries have the same score but can be differentiated between; UF-05-225 had the best rheological properties, smallest wetting angle and highest permeability whilst UF-25-225 had the lowest pore number, highest aspect ratio and best dielectric properties. Both slurries using involving 25 vol.% solids content performed poorly in a number of tests, primarily because the viscosity was too high which in turn impacted the pore number, aspect ratio, wetting angle and permeability.

The factor that was considered the determining point was the dielectric properties, as fundamentally a powder with potentially detrimental dielectric properties should not be intentionally used in a microwave-centric processing method. With this considered, it was concluded that the UF-25-225 slurry was most suitable to meet

the specifications of the slurry impregnation objectives, as set out at the start of section 3.3.1.

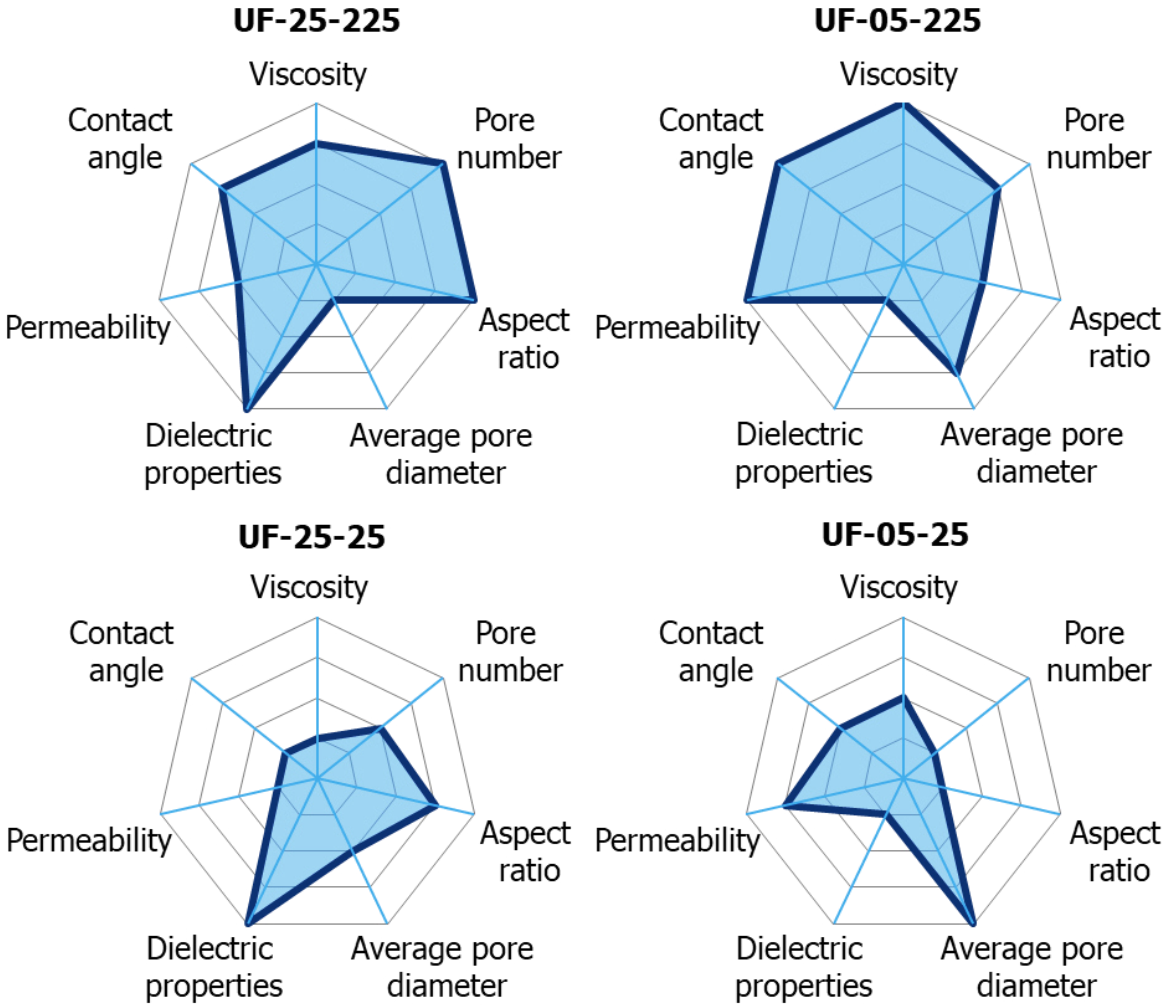


Figure 4.87. Radar diagrams illustrating the best performing slurry across the variety of tests was found to be UF-05-225. Note that no prioritisation was applied to the seven variables evaluated.

5. Conclusions and Future work

5.1. Conclusions

5.1.1. Microwave energy enhanced chemical vapour infiltration study

Studies of the kinetics, densification profile, morphology, chemical composition and crystal structure of the SiC deposited via MCVI were performed to observe and quantify the effects of temperature, pressure and alpha ratio.

- SiC deposition kinetics
    - The study found the deposition of SiC showed an Arrhenius relationship between 900-1000°C, as temperature and pressure increased the rate of deposition increased.
    - An alpha ratio = 10 showed the highest rate of deposition, which was further enhanced by the modification of the gas trajectory in the MCVI cavity. Indicating that this is a suitable precursor ratio to use and the gas flow through the sample is particularly important in increasing the rate of deposition.
    - High gas flow rates showed a cooling effect on the SiC preform, which could have contributed to a decreased deposition amount. Attempts were made to heat the precursor gas in the immediate pipeline before it entered the chamber, which decreased this effect.
    - Extrapolations using a natural logarithmic decay function using the highest deposition rate measured were carried out, which showed densification could be possible in 126 h and, combined with a SiC slurry impregnation route, as little as 98 h. This compares very favourably to the ~1000 h required by the conventional CVI process to densify a sample of an equal size.

- The activation energy of the deposition was calculated to be 125 ± 4 kJ mol^{-1}. This value is on the lower bounds of activation energy reported in the literature. The exact reason for this has not been investigated in this work, but may be an indication of the 'microwave effect' enhancing the deposition process.
- Estimations of the Thiele modulus showed that the deposition process was surface reaction-limited. This is favourable in CVI processes as it encourages pore diffusion at the lower temperatures and pressures used, but a transition to surface reaction regime was seen at the higher pressures and temperatures. This indicates to favour pore channel diffusion temperature and pressure should be minimised.

- Composite densification profile
  - Lower temperatures and lower pressures produced a more desirable (inverse) densification profile. Cross-sectional deposit thickness was 12 μm in the middle of the preform, whereas it was <2 μm at the extremities. Higher temperatures and pressures, in contrast, showed a more uniform deposition profile with a mean thickness of 4.8 ± 2.5 μm, as more of the preform was above the deposition temperature of MTS. The highest temperatures and pressures, however, showed a premature bottom surface sealing effect, which is consistent with a surface reaction being favoured. This again shows selecting processing parameters that favour mass transport is criticial.
  - Densification of the SiC powder coating the edges was seen due to the sharp points created in the electric field by the fibre edges. Since this is unlikely to have involved sintering of the SiC at the temperatures reached, this suggests

the powder could still be penetrated by gas as SiC deposition was observed there. Alpha ratios equal to 5 and 10 showed a uniform deposition of SiC with an average thickness of 2.1 ± 0.4 μm across the cross-section, whilst alpha = 25 and 70, similarly to the 1000°C 700 mbar sample, showed premature bottom surface sealing.

- The addition of the quartz bridge showed the best densification profile observed, showing a clearly defined more dense centre when compared to the outer edges. The deposit was 4.6 μm thick and <2 μm on the edge, indicating there is a significant effect of the gas flow path on the resulting densification profile.

- SiC morphology
  - Higher temperatures and pressures produced a more textured topography; the inverse was seen with lower temperatures and pressures. This effect was due to the difference in the competition between nucleation and growth. At higher temperatures the growth regime was dominant, hence the highly textured surface; whereas at the lower temperatures nucleation was dominant and growth was slow yielding a smooth deposit.
  - Higher pressures exaggerated the effect of higher or lower temperatures due to the lower or higher supersaturation of precursor gases, respectively.
  - The morphology of the deposit varied with displacement from the centre line due to the inverse temperature gradient.
  - The alpha = 5, 10 and 25 samples produced similar morphologies with a decreasing cauliflower topography. Alpha = 70 had a SiC deposit that was

much smoother and it is thought this was because the high dilution meant there was no etching action of the precursors or by-products on the deposit.

- SiC composition
  - A variety of techniques, microscopes and detectors were used to quantify the Si:C ratio of the SiC deposited using MCVI.
  - These produced conflicting results, however, EDS was observed to yield the most believable results.
  - Using an infiltration temperature of 950°C, at 300 mbar with an alpha ratio = 10, SiC was produced with a Si:C ratio of 1.03.
  - The alpha ratio had little effect on the composition of the SiC, but provided further evidence that temperature and pressure are the key determinants of the Si:C ratio. It is expected a temperature between 950≤T≤1000°C will produce stoichiometric SiC.
  - Silicon peaks were detected using Raman spectroscopy at 520 cm^{-1} with the peaks' intensity decreasing with increasing temperature but increasing with increasing reaction pressure. No free carbon peaks were identified in any of the measurements. This indicated that temperature was not sufficiently high enough to energetically favour carbon deposition.
  - Based on the smaller interaction volume, the number of data points collected and the similarity with literature EDS was the most appropriate technique available to this project.
  - A number of features were observed using Raman spectroscopy including acoustic SiC, which was most likely formed due to a combination of the heavily

faulted crystal structure and small crystallite size, both of which can affect current transport and subsequently the EM properties.

- Translational and longitudinal optical phonons were identified at 796 cm^{-1} and 972 cm^{-1} respectively, but due to the close proximity and overlapping of these features, it was difficult to conclude there was a single well-defined polytype with a high level of confidence but this was to be expected due SiC's large number of polytypes.
- HAADF mapping also showed no significant difference in the Si:C ratio indicating stoichiometric SiC was formed in some cases but free silicon was observed in the microstructure in other regions.

- Crystal structure
  - FCC β-SiC was the major polymorph observed in all samples analysed using TEM. The SiC grew perpendicularly from the surface of the fibres along of lowest energy crystallographic plane [111], which is in agreement with the literature.
  - Increasing the temperature increased the grain size and texture with other orientations forming in the [110] and [001], which was again consistent with the literature.
  - Using HAADF, other observations were made including the formation of SiO_2 in-between infiltrations due to residual oxygen, and the formation of nano-porosity as SiC matrices from parallel fibres grew together and coalesced. This indicated that the methods used should be improved to irradiate these defects.

- sc analysis also revealed the presence of α-SiC in samples infiltrated using alpha = 5 and 10, which was later confirmed using TEM as a minor phase. This was surprising due to the low temperatures used in these studies, perhaps indicating the 'microwave effect' had occurred.
- Debonding seen at the fibre-matrix interface suggests the need for an interfacial system in order to prevent this and to facilitate fibre pull out to increase the CMCs toughness.

5.1.2. Inverse temperature profile

A number of different SiC_f preform sizes were tested to establish the geometry that could consistently produce an inverse temperature profile experimentally. This was done using a thermal imaging camera to observe the top surface of the preform. Results found that the largest sample test measuring 55 mm in diameter was the most consistent in producing a higher temperature in the middle of the sample at the deposition temperature. The number of SiC ply was also varied but no significant trend was seen. Experimental trials concluded that for trials 55x 8 mm samples were suitable as they produced an inverse temperature profile consistently enough for testing in both sections 4.1 and 4.3. It should be noted the MCVI equipment was not limited to these size samples, these dimensions were chosen to reduce the cost per sample.

Attempts were then made to verify the temperature profile that was being seen experimentally. Using the QWED 3D software to reconstruct the MCVI apparatus accurately, FDTD modelling was carried out to produce concordant electromagnetic

and thermal models. A heating model was produced using empirical dielectric and thermal properties data for the Hi-Nicalon type S SiC fibres and data from the literature for the Al_2O_3 foams and quartz. It revealed a highly reflective system with low microwave absorption (S_{11}) for the 55 mm samples, with a large number of resonances in the MW cavity. Simulations were then carried out on larger preforms, which showed a 50% increase in diameter that corresponded to a 16% increase in the coupling efficiency; a 37% increase for the latter was observed with a doubling of the sample diameter. A much smaller improvement was seen when doubling the number of SiC ply.

Due to the changing dielectric properties of the fibres, the S_{11} was modelled at RT, 300°C, 600°C, 900°C and 1200°C. This was very revealing of how the reflection coefficient of the fibres changed with temperature, both randomly increasing and decreasing at different frequencies. This resulted in an accurate representation of the experimental observations. Ten frequencies were then selected for simulations at different frequencies where the S_{11} either increased or decreased with increasing temperature, or stayed consistently low or consistently high as the temperature increased. Results showed frequencies with a consistently low S_{11} heated the SiC_f preforms the fastest up to 1200°C in 137 s, whereas frequencies where the S_{11} was consistently high never even reached 400°C after 400 s. The visualisation was then made of four of the ten heating curves to see the effect on the cross-sectional temperature profile in both the XY and XZ planes. Results showed that the temperature across the samples was relatively uniform. This was because the Al_2O_3 foams insulated the higher thermal conductivity SiC_f meaning any hot spots that

developed were dissipated to create a uniform temperature profile at high temperatures.

5.1.3. Fabric impregnation with SiC slurry

A parametric study was carried out to evaluate the effectiveness of various slurry compositions used to impregnate SiC_f preforms with SiC powder. This was carried out to offset the volume of porosity required to be filled using the CVI process, which in all forms is inherently slow compared to other advanced techniques. The effect of changing the solids content and particle size on the viscosity, green density, permeability and porosity structure were all investigated.

- As expected, the viscosity of all the slurries reduced when either the particle size increased or solids content decreased. The SV-225 slurry showed the lowest viscosity of the nine slurries that were selected from the preliminary trial for the extensive suite of testing.
- No significant correlation was found in terms of which slurry increased the green density of the composite. The addition of slurry increased the relative density by ~20%, which was later on extrapolated to correspond to a 28 h decrease in processing time using the MCVI with the techniques combined. Multiple methods of slurry application were trialled and calendaring was determined to be most effective for uniform slurry distribution and minimal closed porosity formation.
- The dielectric properties were measured as a function of temperature for the powder selected after preliminary trials. The SV and UF-05 powders showed highly variable ε′ and ε″ at temperatures greater than 600°C, which was deemed very unfavourable for process control. A number of hypotheses for this behaviour

were presented in the text, but none were confirmed due to the time constraints of the project. The UF-25 powder has a small but steadily increasing ε' and ε'' that was determined to be preferable behaviour.

- Both higher solids content and larger particle size increased the contact angle between the SiC slurry and SiC substrate. The contact angle of all slurries decreased with time, but the previous trend remained. Larger particle size slurries (UF-05) saw better wetting when compared to smaller particle size (UF-25) which is preferable in creating a uniformly distributed powder layer between ply.
- A validated MATLAB script was produced capable of quantifying the porosity network of the impregnated preforms where commercial software had failed. The script evaluated a number of spatial parameters with respect to the porosity. Results showed that the UF-05-25 slurry produced pores with the smallest mean and smallest maximum pore area. The smaller particle sizes with high solids content produced samples that are more equiaxed in shape. It is assumed that this would mean the pores would decrease in size uniformly as deposit grows on the channel walls.
- A custom permeability rig was developed to measure the pressure difference across the thickness of the sample. All samples were found to have a high degree of permeability due to the interconnected porosity network that was revealed in the MATLAB results. The UF-05-225 sample had the highest permeability across the range of flow rates of interest because of its extensive porosity network essential for ensuring precursor gas flow to enable densification.

- Radar diagrams were produced to compare the rankings of the various properties detailed above to determine the optimum slurry for creating green preform suitable for MCVI according to the conditions set out in section 3.3.1. The UF-05-225 and the UF-05-225 slurries were equally ranked, but it was determined that the superior dielectric properties of the UF-05 powder meant the samples prepared with the UF-05-225 slurries were selected in terms of processing potential.

In conclusion, this doctoral thesis has provided an update to the literature on MCVI and has reinforced the potential of the technique to improve SiC_f/SiC manufacturing as technology advances. A better understanding is still needed of the interplay between the chemistry of the deposition process and the interaction of the composite with the EM field, temperature and density to exploit its full potential. To achieve this it is likely a two-year post-doctoral project.

5.2. Future work

Future work on MCVI must focus on the full densification of SiC_f/SiC composites to evaluate the technique's capability. Based on the present work, it is thought that MCVI can produce stoichiometric SiC at a lower temperature, 950-1000°C, than reported in the conventional CVI literature using an alpha ratio of 10 and an infiltration pressure of 400 mbar. Work should involve evaluating the effect of higher flow rates and explore the optimisation of the gas flow path through the preform in more depth. Combining this with the slurry impregnation work, should yield dense

composites in <100 h; i.e. only about 10% of the time required using conventional CVI.

It should be noted at this point that there will be a 'sweet spot' in terms of gas flow where there is a transition to the less favourable mass transfer regime. With this in mind, the pressures used in this work are not best suited for full densification. Work needs to explore the possibility of a staged pressure increase starting from 100 mbar to avoid arcing, up to a maximum of 400 mbar as densification proceeds. This will ensure infiltration of precursor and deposition of SiC into the smallest pores during the early stages of MCVI. It should be noted that parallel work in the carbon fibre / ultra-high temperature ceramic powder system, using RF-enhanced CVI, is able to produce samples up to approximately 90% of theoretical density in no more than about 24 hours; i.e. about 4 times faster than that predicted for the SiC_f-SiC composites using microwave heating [400]. One difference between the two systems is that the RF-CVI work does start at a low pressure than increase it over the course of the process as densification proceeds.

An alternative approach, which could be combined with that outlined above, is to use a multi-stage hybrid system. This would use a very low-pressure conventional CVI route initially to produce an interface [401] and then the first few microns of SiC material to fill ~10% of the porosity. Then MCVI would then be used to fill the bulk of the porosity up to ~80-90% of TD before switching back to the conventional low-pressure route to close up the remaining 10% of surface porosity.

In terms of the characterisation of the SiC_f/SiC composites, the relationship between porosity and permeability needs to be better established. This will enhance the

understanding of how the densification occurs. Based on the results of this work there are two hypothesise as to how this occurs; the first is the closure of central porosity by MCVI diverts precursor gases to the extremities of the sample where, due to the higher concentration, there is an increased deposition rate that continues propagation outward from the centre. The second is the dielectric properties of the SiC being deposited in the centre increase the microwave coupling occurring, therefore exacerbating the heating of the sample centre that causes the proliferation of the densification front outwards. Further to this point, the deposit's dielectric properties need to be measured as there is currently no understanding as to whether the densification improves or inhibits microwave absorption; this is particularly important to the direction of the progression of MCVI research in terms of the deposit composition. The use of a lower frequency microwave source may also need to be investigated, particularly if larger preforms are being used to ensure the penetration of the microwaves into the material as according to equation 2-10 to ensure the process in not limited to smaller components.

All further work must proceed using the Hi Nicalon Type S fibre because of its superior dielectric properties, though there is clearly still further opportunity for developing an even better SiC fibre with a highly crystalline, stoichiometric microstructure with low amorphous content [110, 402]. Experiments must also utilise the conclusions made regarding the inverse temperature profile in terms of optimising the sample size. A major learning point from this work is the size of the sample is defined by the size of the cavity. This was determined using FDTD modelling, but the size selected will need to be traded off with the cost of fibres until they become cheaper. Another goal should be to investigate improving the

microwave absorption of the preform. This has been demonstrated in a number of publications through the addition of SiC nano-wires [403], reducing carbon impurities [404], using a BN or Si_xO_xC interface and annealing of the fibres [401, 405]. This would be very beneficial; as it would make the process more energy-efficient as lower powers would be required to achieve operating temperatures, reducing the likelihood of arcing incidents and improving the reproducibility of the samples.

The influence of shape on the processability of the MCVI is not well understood; in this research, only different sizes of cylinders were tested. The FDTD modelling carried out in this work will be particularly useful in the understanding of microwave field and subsequent temperature distribution in the materials. Shapes of particular interest are long thin tubes for nuclear fuel rod cladding applications [406], complex 3D shapes, such as the blades and shrouds in the compressor of turbofan engines used by GE [407], and various unconventional form factors as seen in figure 5.1. for combustor liners used by NASA [408].



Figure 5.1. (a) Nuclear fuel cladding rods, (b) GE CMC blade from LEAP engine and (c) various components of combustor liner for simulated gas turbine engine cycle.

The potential key to unlocking technology for MCVI's utilisation is the use of solid-state microwave generators. The use of a solid-state generator would allow the operator to select specific high-coupling frequencies with low reflection coefficients to enable heating that is more effective. This ability, combined with measurements of dielectric properties of the constituents of the composite and the appropriate S_{11} curves at different temperatures and dielectric properties, will enable ultimate process control and insight into the interaction of the microwaves with the system as densification proceeds. This, in theory, will be a very informative process that the user can modify accordingly based on intuitive feedback from the system, thus removing almost all the unknowns currently associated with the process.

6. Appendices

6.1. Appendix I

The findings of this research work have been disseminated in international scientific conferences:

- 3rd Global congress on microwave energy applications, Cartagena, Spain (poster)
- Material Science and Technology 2016 Salt Lake City, USA (poster)
- ECerS 2017 Conference, Budapest, Hungary (talk)
- Engineering conference international – High-temperature ceramic matrix composites – Santa Fe, USA (poster)
- 42nd and 43rd International conference and exposition on advanced ceramics and composites, Daytona Beach, USA (talk and poster)
- A review paper was also published in relation to this project [150]

During the Ph.D, a three-month research exchange program has been carried out at Worcester Polytechnic Institute, MA under the supervision of Prof. Burt Tilley and Prof. Vadim Yakolev. This work was supported by Aerospace Materials for Extreme Environments program of the Air Force Office of Scientific Research (Grant number FA9550-15-1-04655) and the JECS Trust Foundation (Contract No. 2016124-3). The research activity was focused on the thermo-electromagnetic simulation of the MCVI process, the associated fluid dynamic problem related to porosity filling and closure in the SiC_f/SiC composite two papers are currently being prepared.

6.2. Appendix II

Table 6.1. All the input parameters for Hi Nicalon Type S, illustrating the effect of temperature

T/°C	Ɛ'	Ɛ''	S / m^{-1}	ΔH / J cm^{-3}	C_p / J g^{-1} C^{-1}	ρ / g cm^{-3}	λ / W cm^{-1} C^{-1}
25.00	5.44	1.06	0.14	0.00	0.63	0.48	0.15
100.00	5.47	1.15	0.16	0.63	0.79	0.48	0.16
200.00	5.62	1.33	0.18	0.80	0.90	0.48	0.17
300.00	6.02	1.58	0.21	0.93	0.95	0.48	0.16
400.00	6.78	1.94	0.26	1.01	0.97	0.48	0.15
500.00	7.93	2.46	0.33	1.06	0.99	0.48	0.15
600.00	9.49	3.20	0.44	1.09	1.00	0.48	0.14
700.00	11.39	4.28	0.58	1.12	1.00	0.48	0.13
800.00	13.52	5.83	0.79	1.14	1.00	0.48	0.13
900.00	15.77	8.06	1.10	1.14	1.01	0.48	0.13
925.00	16.33	8.75	1.19	1.04	1.01	0.48	0.13
950.00	16.89	9.51	1.29	1.04	1.01	0.48	0.12
975.00	17.45	10.35	1.41	1.04	1.01	0.48	0.12
1000.00	18.00	11.26	1.53	1.04	1.01	0.48	0.12
1025.00	18.55	12.27	1.67	1.04	1.01	0.48	0.12
1050.00	19.09	13.36	1.82	1.04	1.01	0.48	0.12
1075.00	19.62	14.57	1.98	1.04	1.01	0.48	0.12
1100.00	20.14	15.88	2.16	1.04	1.01	0.48	0.12
1125.00	20.64	17.32	2.36	1.04	1.01	0.48	0.12
1150.00	21.14	18.90	2.57	1.04	1.01	0.48	0.12
1175.00	21.63	20.63	2.81	1.04	1.01	0.48	0.12
1200.00	22.10	22.53	3.07	1.0	1.01	0.48	0.12

Table 6.2. All the input parameters for Al_2O_3 foam, illustrating the effect of temperature

T/°C	Ɛ'	Ɛ''	S / m^{-1}	ΔH / J cm^{-3}	C_p / J g^{-1} C^{-1}	ρ / g cm^{-3}	λ / W cm^{-1} C^{-1}
25.00	1.80	0.02	0.00	0.00	0.76	0.49	0.40
100.00	1.93	0.03	0.00	0.78	0.90	0.49	0.32
200.00	2.13	0.03	0.00	0.92	1.02	0.49	0.25
300.00	2.34	0.04	0.00	1.05	1.10	0.48	0.19
400.00	2.58	0.05	0.01	1.12	1.15	0.48	0.16
500.00	2.84	0.07	0.01	1.17	1.19	0.48	0.13
600.00	3.15	0.10	0.01	1.21	1.22	0.48	0.11
700.00	3.50	0.14	0.02	1.23	1.24	0.48	0.10
800.00	3.90	0.19	0.03	1.25	1.25	0.48	0.09

900.00	4.38	0.25	0.03	1.27	1.26	0.48	0.08
925.00	4.52	0.27	0.04	1.27	1.26	0.48	0.08
950.00	4.66	0.29	0.04	1.27	1.27	0.48	0.08
975.00	4.80	0.31	0.04	1.27	1.27	0.48	0.08
1000.00	4.96	0.33	0.04	1.27	1.27	0.48	0.07
1025.00	5.12	0.35	0.05	1.27	1.27	0.48	0.07
1050.00	5.29	0.37	0.05	1.28	1.27	0.48	0.07
1075.00	5.46	0.39	0.05	1.28	1.27	0.48	0.07
1100.00	5.65	0.41	0.06	1.28	1.28	0.48	0.07
1125.00	5.84	0.44	0.06	1.28	1.28	0.48	0.07
1150.00	6.05	0.46	0.06	1.28	1.28	0.48	0.07
1175.00	6.26	0.49	0.07	1.29	1.28	0.48	0.07
1200.00	6.49	0.52	0.07	1.29	1.28	0.48	0.07

Table 6.3. All the input parameters for quartz, illustrating the effect of temperature

T/°C	Ɛ'	Ɛ''	S / m^{-1}	ΔH / J cm^{-3}	C_p / J g^{-1} C^{-1}	ρ / g cm^{-3}	λ / W cm^{-1} C^{-1}
25.00	3.84	0.00	0.00	0.00	0.60	2.20	0.01
100.00	3.84	0.00	0.00	0.60	0.86	2.20	0.01
200.00	3.85	0.00	0.00	0.86	0.98	2.20	0.02
300.00	3.86	0.00	0.00	0.98	1.04	2.20	0.02
400.00	3.87	0.00	0.00	1.04	1.08	2.20	0.02
500.00	3.88	0.00	0.00	1.08	1.11	2.20	0.02
600.00	3.89	0.00	0.00	1.11	1.13	2.20	0.02
700.00	3.90	0.00	0.00	1.13	1.15	2.20	0.02
800.00	3.91	0.00	0.00	1.15	1.17	2.20	0.02
900.00	3.92	0.00	0.00	1.17	1.18	2.20	0.02
925.00	3.92	0.00	0.00	1.18	1.18	2.20	0.02
950.00	3.93	0.00	0.00	1.18	1.19	2.20	0.01
975.00	3.93	0.00	0.00	1.19	1.19	2.20	0.01
1000.00	3.93	0.00	0.00	1.19	1.19	2.20	0.01
1025.00	3.93	0.00	0.00	1.19	1.19	2.20	0.01
1050.00	3.94	0.00	0.00	1.19	1.20	2.20	0.01
1075.00	3.94	0.00	0.00	1.20	1.20	2.20	0.01
1100.00	3.94	0.00	0.00	1.20	1.20	2.20	0.01
1125.00	3.94	0.00	0.00	1.20	1.20	2.20	0.01
1150.00	3.95	0.00	0.00	1.20	1.21	2.20	0.01
1175.00	3.95	0.00	0.00	1.21	1.21	2.20	0.01
1200.00	3.95	0.00	0.00	1.21	1.21	2.20	0.01

6.3. Appendix III

Table 6.4. EDS VS WDS comparison table

EDS		**WDS**	
Measurements found the codeposition of Si		**Measurements found the codeposition of C**	
For	**Against**	**For**	**Against**
Free Si was detected by Raman	Standard less	Standards used calibration for better quantification of Si:C ratio	Carbon concentration measured was high. This is unlikely due to associated processing temperatures.
Homogenous deposit seen used HAADF	Doesn't separate out X-ray peaks so peak intensity overlapping is common	Method of collecting and sorting X-rays is better	Carbon formation does not correlate with thermodynamic calcs.
Free Si seen in MS		Carbon traces found in XRD	No free carbon was seen in the Raman spectroscopy
Faster sampling time so a larger data set can be collected			

7. References

1. Okada, A., Ceramic-Matrix Composites in *Handbook of Advanced Ceramics*, F. Aldinger, et al., Editors. 2003, Academic Press: Oxford. p. 417-443.
2. Yang, J.M., Lin, W., Shih, C.J., Kai, W., Jeng, S.M., and Burkland, C.V., Mechanical behaviour of chemical vapour infiltration processed 2 dimensional and 3 dimensional nicalon SiC composites. *Journal of Materials Science*. **26** [11]1991: p. 2954-2960.
3. Shimoda, K., Hinoki, T., Katoh, Y., and Kohyama, A., Development of the tailored SiC/SiC composites by the combined fabrication process of ICVI and NITE methods. *Journal of Nuclear Materials*. **384** [2]2009: p. 103-108.
4. Yin, X.W., Cheng, L.F., Zhang, L.T., Travitzky, N., and Greil, P., Fibre-reinforced multifunctional SiC matrix composite materials. *International Materials Reviews*. **62** [3]2017: p. 117-172.
5. Timms, L.A., Westby, W., Prentice, C., Jaglin, D., Shatwell, R.A., and Binner, J.G.P., Reducing chemical vapour infiltration time for ceramic matrix composites. *Journal of Microscopy-Oxford*. **201** 2001: p. 316-323.
6. PLC, R.-R. Future Products. 2019; Available from: https://www.rolls-royce.com/products-and-services/civil-aerospace/future-products.aspx#/.
7. Davidson, D.L., Ceramic-matrix composites fatigue and fracture. *JOM*. **47** [10]1995: p. 46-50.
8. Miller, J.H. and Liaw, P.K., Fracture Toughness of Ceramics and Ceramic Matrix Composites, in *Mechanical Testing and Evaluation*, H. Kuhn and D. Medlin, Editors. 2000, ASM International. p. 0.
9. Naslain, R., F. Langlais, and R. Fedou., The Cvi-Processing of Ceramic Matrix Composites. *Journal De Physique*. **50(C-5)** 1989: p. 191-207.
10. Granta, CES EduPack. 2016, Granta: Cambridge.
11. PLC, R.-R. Trent 700. 2019; Available from: https://www.rolls-royce.com/products-and-services/civil-aerospace/airlines/trent-700.aspx#/.
12. Campbell, F.C., Chapter 10 - Ceramic Matrix Composites, in *Manufacturing Technology for Aerospace Structural Materials*. 2006, Elsevier Science: Oxford. p. 459-493.
13. Jaglin, D., Binner, J., Vaidhyanathan, B., Prentice, C., Shatwell, B., and Grant, D., Microwave heated chemical vapor infiltration: Densification mechanism of SiCf/SiC composites. *Journal of the American Ceramic Society*. **89** [9]2006: p. 2710-2717.
14. Lazzeri, A., *CVI Processing of Ceramic Matrix Composites*. 2012.
15. Lazzeri, A., Cioni, B., Origgi, E., Cercignani, G., and Nardini, G. Production of ceramic matrix composites by means of an innovative pilot-plant for microwave assisted chemical vapour infiltration (MWCVI). 2005.
16. Binner, J., Vaidhyanathan, B., Jaglin, D., and Needham, S., Use of Electrophoretic Impregnation and Vacuum Bagging to Impregnate SiC Powder into SiC Fiber Preforms. *International Journal of Applied Ceramic Technology*. **12** [1]2015: p. 212-222.
17. Askeland, D.R., *The science and engineering of materials*. 3 ed. 1999, Cheltenham: Stanley Thornes.

18. Roylance, D., Introduction to Fracture Mechanics. 2001, Massachusetts Institute of Technology.
19. Chawla, K.K., *Ceramic Matrix Composites*. 1993, London: Chapman & Hall.
20. Faber, K.T., Ceramic Composite Interfaces: Properties and Design. *Annual Review of Materials Science*. **27** [1]1997: p. 499-524.
21. Kerans, R.J., Hay, R.S., Parthasarathy, T.A., and Cinibulk, M.K., Interface Design for Oxidation-Resistant Ceramic Composites. *Journal of the American Ceramic Society*. **85** [11]2002: p. 2599-2632.
22. Economy, J. and Anderson, R. Boron nitride fibers. in *Journal of Polymer Science Part C: Polymer Symposia*. 1967. Wiley Online Library.
23. Shi, C., Zhu, Y., Qian, H., and Lu, L., Fabrication of silicon nitride fiber–PMMA composite through free radical polymerization in batch. *Materials Research Bulletin*. **51** 2014: p. 161-166.
24. Rubin, L., Chapter 9 - Applications of Carbon-Carbon, in *An overview Carbon-Carbon*, J.D. Buckley, Editor. 1993, Noyes: New jersey. p. 364-368.
25. Concorde Brakes by Dunlop are Carbon/Carbon Composite *Aircraft Engineering and Aerospace Technology*. **48** 1976: p. 22 - 26.
26. Han, K., Ono, H., goto, K. and St. Pierre, G., Rate of Oxidation of Carbon Fiber/Carbon Matrix Composites with Antioxidation Treatment at High Temperature. *Journal of the electrochemical society* **134** [4]1987: p. 1003-1009.
27. Hatta, H., Goto, K., Sato, T., and Tanatsugu, N., Applications of carbon-carbon composites to an engine for a future space vehicle. *Advanced Composite Materials*. **12** [2/3]2003: p. 237-259.
28. Lu, Z.L., Lu, F., Cao, J.W., and Li, D.C., Manufacturing Properties of Turbine Blades of Carbon Fiber-Reinforced SiC Composite Based on Stereolithography. *Materials and Manufacturing Processes*. **29** [2]2014: p. 201-209.
29. Ozaki, T. and Kume, M., Pitch-based carbon fiber reinforced SiC composites for space optics. *Advanced Composite Materials*. **12** [2-3]2003: p. 185-203.
30. Fan, S., Sun, H., Ma, X., Deng, J., Yang, C., Cheng, L., and Zhang, L., Microstructure and properties of a new structure-function integrated C/C-SiC brake material. *Journal of Alloys and Compounds*. **769** 2018: p. 239-249.
31. Krnel, K., Stadler, Z., and Kosmač, T., Carbon/Carbon-Silicon-Carbide Dual-Matrix Composites for Brake Discs. *Materials & Manufacturing Processes*. **23** [6]2008: p. 587-590.
32. Krenkel, W. and Berndt, F., C/C–SiC composites for space applications and advanced friction systems. *Materials Science and Engineering: A*. **412** [1–2]2005: p. 177-181.
33. Zhang, W., Li, A., Reznik, B., and Deutschmann, O., Thermal expansion of pyrolytic carbon with various textures. *ZAMM - Journal of Applied Mathematics and Mechanics / Zeitschrift für Angewandte Mathematik und Mechanik*. **93** [5]2013: p. 338-345.
34. Kobayashi, S., Wakayama, S., Aoki, T., and Hatta, H., Oxidation behavior and strength degradation of CVD-SiC coated C/C composites at high temperature in air. *Advanced Composite Materials*. **12** [2-3]2003: p. 171-183.
35. Naslain, R., Design, preparation and properties of non-oxide CMCs for application in engines and nuclear reactors: an overview. *Composites Science and Technology*. **64** 2003: p. 16.

36. Ogasawara, T., Aoki, T., Hassan, M.S.A., Mizokami, Y., and Watanabe, N., Ablation behavior of SiC fiber/carbon matrix composites under simulated atmospheric reentry conditions. *Composites Part A: Applied Science and Manufacturing*. **42** [3]2011: p. 221-228.
37. Orbiter Thermal Protection System, in *Engineering innovations*. NASA: Jonson Space centre.
38. Wilson, D.M., New High Temperature Oxide Fibers, in *High Temperature Ceramic Matrix Composites*. 2006, Wiley-VCH Verlag GmbH & Co. KGaA. p. 1-12.
39. Wilson, D.M. and Visser, L.R., High performance oxide fibers for metal and ceramic composites. *Composites Part A: Applied Science and Manufacturing*. **32** [8]2001: p. 1143-1153.
40. Krenkel, W., *Ceramic Matrix Composites: Fiber Reinforced Ceramics and their Applications*. 2008: Wiley.
41. Di Salvo, D.T., Sackett, E.E., Johnston, R.E., Thompson, D., Andrews, P., and Bache, M.R., Mechanical characterisation of a fibre reinforced oxide/oxide ceramic matrix composite. *Journal of the European Ceramic Society*. **35** [16]2015: p. 4513-4520.
42. Blanchard, C.R., Chan, K. S., Evidence of Grain-Boundary-Sliding-Induced Cavitation in Ceramics under Compression. *Journal of the American Ceramic Society*. **76** [7]1993: p. 1651-1660.
43. Awaji, H., Ebisudani, M., Choi, S., and Ohashi, T., , Crack Deflection Toughening Mechanism in Brittle Materials. *ASTM International*, 2002: p. 137-151.
44. Lee, C., Lui, B., Lu, H., Huang, J., Indentation Deformation and Microcracking in β-Si3N4-Based Nanoceramic. *American Ceramic Society*. **95** [4]2012: p. 1421-1428.
45. Faber, K.T., Evans, A. G., Crack deflection processes—I. Theory. *Acta Metallurgica*. **31** [4]1983: p. 565-576.
46. Green, D.J., Fracture Toughness Predictions for Crack Bowing in Brittle Particulate Composites. *Journal of the American Ceramic Society*. **66** [1]1983: p. C-4-C-5.
47. Cook, R.F., Fairbanks, C. J., Lawn, B. R., Mai, Y., Crack resistance by interfacial bridging: Its role in determining strength characteristics. *Journal of Materials Research*. **2** [3]1987: p. 345-356.
48. Nemat-Nasser, S. and Hori, M., Toughening by partial or full bridging of cracks in ceramics and fiber reinforced composites. *Mechanics of Materials*. **6** [3]1987: p. 245-269.
49. Xiu, C., Composite materials science and engineering - CMCs. Henan University of science and technology.
50. Vicbase, Summary of epoxy toughening mechanism. 2011.
51. Tyrrell, T., CNTs reinforce alumina composites, in *Nanotechweb.org*. 2008, Nanotechweb.org.
52. Huan, Z., Yang, J., Liu, Y., Shuba, R., Novel Sialon-Based Ceramics Toughened by Ferro-Molybdenum Alloy. *Journal of the American Ceramic Society* **95** [3]2012: p.

53. Chaudhary, S., Parasarathy, S., Kumar, D., Rajagopal, C., Roy, P., Simple toughening of epoxy thermosets by preformed thermoplastics. *Society of plastics engineers*, 20114: p.
54. Goto, K., Kagawa, Y., Nojima, K., Iba, H., Effects of crack—fiber interactions on crack growth rate in fiber-reinforced brittle matrix composite under cyclic loading: model experiment. *Materials Science and Engineering: A*. **212** [1]1996: p. 69-74.
55. Green, D.J., Hannik, R.H.J and Swain, M.V., *Transformation toughening of ceramics*. 1989, Boca ranton, Florida: CRC Press.
56. Fox, K. Transformation toughened ceramics. 1999.
57. He, M.-Y. and Hutchinson, J.W., Kinking of a crack out of an interface: tabulated solution coefficients. *Cambridge, MA: Harvard University Report MECH-113A*, 1989: p.
58. Ming-Yuan, H. and Hutchinson, J.W., Crack deflection at an interface between dissimilar elastic materials. *International Journal of Solids and Structures*. **25** [9]1989: p. 1053-1067.
59. Dundurs, J., Mathematical theory of dislocations. *American Society of Mechanical Engineers, New York*, 1969: p. 70-115.
60. Shimoda, K., Park, J.-S., Hinoki, T., and Kohyama, A., Influence of pyrolytic carbon interface thickness on microstructure and mechanical properties of SiC/SiC composites by NITE process. *Composites Science and Technology*. **68** [1]2008: p. 98-105.
61. Rebillat, F., Lamon, J., Naslain, R., Lara-Curzio, E., Ferber, M.K., and Besmann, T.M., Properties of multilayered interphases in SiC/SiC chemical-vapor-infiltrated composites with "weak" and "strong" interfaces. *Journal of the American Ceramic Society*. **81** [9]1998: p. 2315-2326.
62. Leuch, S., CVI pullout. MT Aerospace AG: Augsburg.
63. *Composite Materials Handbook Volume 5 - Ceramic Matrix Composites*. Composite materials handbook. **Vol. 1**. 2017: SAE international.
64. DiCarlo, J.A., Yun, H., Handbook of Ceramic Composites, in *Non-oxide (Silicon Carbide) Fibers*, N.P. Basnal, Editor. 2005.
65. Lino Alves, F.J., Baptista, A.M., and Marques, A.T., 3 - Metal and ceramic matrix composites in aerospace engineering, in *Advanced Composite Materials for Aerospace Engineering*, S. Rana and R. Fangueiro, Editors. 2016, Woodhead Publishing. p. 59-99.
66. Chawla, K.K., Xu, Z.R., and Ha, J.S., Processing, Structure, and Properties of Mullite Fiber/Mullite Matrix Composites. *Journal of the European Ceramic Society*. **16** [2 SPEC. ISS.]1996: p. 293-299.
67. Cinibulk, M.K., Keller, K.A., and Mah, T.I., Effect of yttrium aluminum garnet additions on alumina-fiber-reinforced porous-alumina-matrix composites. *Journal of the American Ceramic Society*. **87** [5]2004: p. 881-887.
68. Zhang, J., Fan, J., Zhang, J., Zhou, J., Liu, X., Qie, D., and Zhang, D., Developing and preparing interfacial coatings for high tensile strength silicon nitride fiber reinforced silica matrix composites. *Ceramics International*. **44** [5]2018: p. 5297-5303.
69. bulletin, A.c.s., Ceramics in the skies, in *American ceramic society bulletin*. 2019.
70. Zok, F.W., Ceramic-matrix composites enable revolutionary gains in turbine engine efficiency. *American Ceramic Society Bulletin*. **95** [5]2016: p. 7.

71. Meyer, P. and Waas, A.M., Experimental results on the elevated temperature tensile response of SiC/SiC ceramic matrix notched composites. *Composites Part B: Engineering*. **143** 2018: p. 269-281.
72. Ryan, C.E., Marshall, R.C., Hawley, J.J., Berman, I., and Considine, D.P., The Conversion of Cubic and Hexagonal Silicon Carbide as a Function of Temperature and Pressure, in *Anisotropy in Single-Crystal Refractory Compounds: Proceedings of an International Symposium on Anisotropy in Single-Crystal Refractory Compounds, held on June 13–15, 1967, in Dayton Ohio. Sponsored by the Ceramics and Branch of the air Force Materials Laboratory, United States Air Force.*, F.W. Vahldiek and S.A. Mersol, Editors. 1968, Springer US: Boston, MA. p. 177-197.
73. Hong, J.D., Hon, M. H., Davis, R. F., Self-diffusion in alpha and beta silicon carbide. *Ceramurgia International*. **5** [4]1979: p. 155-160.
74. Azom, Silicon Carbide (SiC) Properties and Applications. 2001: p.
75. Goldberger, W.M., Booth, P., Using silicon carbide in advanced ceramics. *Ceramic Industry*. **148** [6]1998: p. 64.
76. Materials, M.A. Silicon Carbide (SiC). 2016; Available from: http://www.morgantechnicalceramics.com/en-gb/materials/silicon-carbide-sic/.
77. Poco Graphite, I., Properties and Characteristics of Silicon Carbide, A.H. Rashed, Editor. 2002: Decatur, TX.
78. Haase, V., Kirschstein, G., List, H., Ruprecht, S., Sangster, R., Schröder, F., Töpper, W., Vanecek, H., Heit, W., Schlichting, J., and Katscher, H., The Si-C Phase Diagram, in *Si Silicon: System Si-C. SiC: Natural Occurrence. Preparation and Manufacturing Chemistry. Special Forms. Manufacture. Electrochemical Properties. Chemical Reactions. Applications. Ternary and Higher Systems with Si and C*, H. Katscher, R. Sangster, and F. Schröder, Editors. 1985, Springer Berlin Heidelberg: Berlin, Heidelberg. p. 1-5.
79. Elliot, R.P., *Constiutions of Binary Alloys*. 1965, New York: McGraw-Hill.
80. Accuratus. Silicon Carbide, SiC Ceramic Properties. 2013; Available from: http://accuratus.com/silicar.html.
81. Elements, A. Silicon Carbide SDS. [cited 2019; Available from: https://www.americanelements.com/silicon-carbide-409-21-2.
82. Izhevskyi, V.A., Genova, L.A., Bressiani, J.C., and Bressiani, A.H.A., Review article: silicon carbide. Structure, properties and processing. *Cerâmica*. **46** 2000: p. 4-13.
83. Pensl, G. and Choyke, W.J., Electrical and optical characterization of SiC. *Physica B: Condensed Matter*. **185** [1]1993: p. 264-283.
84. Fisher, G.R., Barnes, P., Towards a unified view of polytypism in silicon carbide. *Philosophical Magazine Part B*. **61** [2]1990: p. 217-236.
85. Bechstedt, F., Käckell, P., Zywietz, A., Karch, K., Adolph, B., Tenelsen, K. and Furthmüller, J., Polytypism and Properties of Silicon Carbide. *physica status solidi (b)*. **202** 1997: p. 35-62.
86. Verma, A.R. and Krishna, P., Polymorphism and polytypism in crystals. *1966, 341 P. JOHN WILEY AND SONS, INC., 605 THIRD AVENUE, NEW YORK, N. Y. 10016*, 1965: p.
87. Jepps, N.W. and Page, T.F., Polytypic transformations in silicon carbide. *Progress in Crystal Growth and Characterization*. **7** [1–4]1983: p. 259-307.

88. Kingery, W.D., Bowen, H.K., and Uhlmann, D.R., *Introduction to ceramics*. Wiley series on the science and technology of materials. **Vol. 2**. 1976, New York: Wiley.
89. Flores, O., Bordia, R. K., Nestler, D., Krenkel, W., Motz, G., Ceramic Fibers Based on SiC and SiCN Systems: Current Research, Development, and Commercial Status. *Advanced Engineering Materials*. **16** [6]2014: p. 621-636.
90. Leucht, R. and Dudek, H.J., Properties of SiC-fibre reinforced titanium alloys processed by fibre coating and hot isostatic pressing. *Materials Science and Engineering: A*. **188** [1]1994: p. 201-210.
91. Idesaki, A., Narisawa, M., Okamura, K., Sugimoto, M., Tanaka, S., Morita, Y., Seguchi, T., and Itoh, M., Fine SiC fiber synthesized from organosilicon polymers: relationship between spinning temperature and melt viscosity of precursor polymers. *Journal of Materials Science*. **36** [23]2001: p. 5565-5569.
92. Narisawa, M., Shimoda, K.,Niskioka, M., Iseki, T.,Mabuchi, H., Okamurai, K., Oka, K., Domhmaru, T., Silicon Carbide Base Ceramic Fiber Synthesis from Polycarbosilane-Polymethylsilane Blend Polymers by Melt Spinning. *Journal of the Ceramic Society of Japan*. **114** 2006: p. 511-516.
93. Idesaki, A., Narisawa, M., Okamura, K., Sugimoto, M., Morita, Y., Seguchi, T., and Itoh, M., Application of electron beam curing for silicon carbide fiber synthesis from blend polymer of polycarbosilane and polyvinylsilane. *Radiation Physics and Chemistry*. **60** [4]2001: p. 483-487.
94. Zheng, C.-m., Li, X.-d., Wang, H., and Zhu, B., Thermal stability and curing kinetics of polycarbosilane fibers. *Transactions of Nonferrous Metals Society of China*. **16** [1]2006: p. 44-48.
95. Hong, J., Cho, K.-Y., Shin, D.-G., Kim, J.-I., Oh, S.-T., and Riu, D.-H., Low-temperature chemical vapour curing using iodine for fabrication of continuous silicon carbide fibres from low-molecular-weight polycarbosilane. *Journal of Materials Chemistry A*. **2** [8]2014: p. 2781-2793.
96. Su, Z., Tang, M., Wang, Z., Zhang, L., and Chen, L., Processing of Silicon Carbide Fibers from Polycarbosilane with Polypropylene as the Additive. *Journal of the American Ceramic Society*. **93** [3]2010: p. 679-685.
97. Fibres, F.F. Our Patent Pending Process. 2019; Available from: https://fffibers.com/process/.
98. Yajima, S., Hayashi, J., Omori, M., and Okamura, K., Development of a silicon carbide fibre with high tensile strength. *Nature*. **261** [5562]1976: p. 683-685.
99. Kohyama, A., Park, J.-S., and Jung, H.-C., Advanced SiC fibers and SiC/SiC composites toward industrialization. *Journal of Nuclear Materials*. **417** [1]2011: p. 340-343.
100. Ichikawa, H., Polymer-Derived Ceramic Fibers. *Annual Review of Materials Research*. **46** [1]2016: p. 335-356.
101. Yamamura, T., Ishikawa, T., Shibuya, M., Hisayuki, T., and Okamura, K., Development of a new continuous Si-Ti-C-O fibre using an organometallic polymer precursor. *Journal of Materials Science*. **23** [7]1988: p. 2589-2594.
102. Vahlas, C., Rocabois, P., and Bernard, C., Thermal degradation mechanisms of Nicalon fibre:a thermodynamic simulation. *Journal of Materials Science*. **29** [22]1994: p. 5839-5846.

103. Mah, T., Hecht, N.L., McCullum, D.E., Hoenigman, J.R., Kim, H.M., Katz, A.P., and Lipsitt, H.A., Thermal stability of SiC fibres (Nicalon®). *Journal of Materials Science*. **19** [4]1984: p. 1191-1201.
104. Schawaller, D., Clauß, B., and Buchmeiser, M.R., Ceramic Filament Fibers – A Review. *Macromolecular Materials and Engineering*. **297** [6]2012: p. 502-522.
105. DiCarlo, J.A., Creep limitations of current polycrystalline ceramic fibers. *Composites Science and Technology*. **51** [2]1994: p. 213-222.
106. Cinibulk, M. Constituent development for high-temperature capable ceramic matrix composites. in *Materials Science and Technology*. 2016. Salt Lake City.
107. IEST. Cef-NITE Business. 2008; Available from: http://www.iest.jp/english/business2.html.
108. N. Nakazato, J.S.P., S. Makimura, S. Matoba, N. Kawamura, T. Ishida and H. Kishimoto, Present Status of NITE-SiC/SiC Composites R&D as proton accelerator target material, in *5th RaDIATE Collaboration Meeting*. 2018: Switzerland.
109. Kohyama, A., Advances in Ceramic Materials SiC/SiC Composite, in *Fission Energy Workshop: Opportunities for Fundamental Research and Breakthrough in Fission, Global Climate & Energy Project*. 2007: Massachusetts Institute of Technology, Cambridge, MA.
110. Wolford, I.M., Quantifying the amorphus content of commercially available silicon carbide fibres. 2015, Wright State University.
111. Harrison, S. Technical Data Sheet - Silicon Carbide Fiber LP-30SC. 2019; Available from: https://fffibers.com/wp-content/uploads/2018/04/SiCDataSheet2.pdf.
112. Harrison, S. Summary of Free Form Fibers LCVD-Produced Fiber Manufacturing Capabilities and Material Properties Available from: https://fffibers.com/wp-content/uploads/2018/03/DetailedSiCFiberTechnicalPropertiesSummary.pdf.
113. Zhu, B., Wang, R., Harrison, S., Williams, K., Goduguchinta, R., Schneiter, J., Pegna, J., Vaaler, E., and Wang, X., Thermal conductivity of SiC microwires: Effect of temperature and structural domain size uncovered by 0 K limit phonon scattering. *Ceramics International*. **44** [10]2018: p. 11218-11224.
114. ToolBox, T.E. Smaller Circles within a Larger Circle. 2013 20/01/2019]; Available from: https://www.engineeringtoolbox.com/smaller-circles-in-larger-circle-d_1849.html.
115. Ko, F.K., Preform Fiber Architecture for Ceramic-Matrix Composites. *American Ceramic Society Bulletin*. **68** [2]1989: p.
116. inc., K.c. Laminated panels. Available from: http://www.kcinc.com/solidpanels.htm.
117. NetComposites. Woven frabric. Reinforcements; Available from: https://netcomposites.com/guide-tools/guide/reinforcements/woven-fabrics/.
118. Fitzer, E. and Manocha, L.M., Carbon Fiber Architecture, in *Carbon Reinforcements and Carbon/Carbon Composites*. 1998, Springer Berlin Heidelberg: Berlin, Heidelberg. p. 82-96.
119. Weaver, W., Sett or how to work out which yarn to use in your rigid heddle loom.

120. Lee, K.S., Jang, K.S., Park, J.H., Kim, T.W., Han, I.S., and Woo, S.K., Designing the fiber volume ratio in SiC fiber-reinforced SiC ceramic composites under Hertzian stress. *Materials & Design*. **32** [8]2011: p. 4394-4401.
121. Wasik, T., Effect of fiber volume fraction on fracture mechanics in continuously reinforced fiber composite materials. 2005, University of South Florida.
122. Xu, H.H.K., Ostertag, C.P., Braun, L.M., and Lloyd, I.K., Effects of Fiber Volume Fraction on Mechanical Properties of SiC-Fiber/Si3N4-Matrix Composites. *Journal of the American Ceramic Society*. **77** [7]1994: p. 1897-1900.
123. Wang, P., Liu, F., Wang, H., Li, H., and Gou, Y., A review of third generation SiC fibers and SiCf/SiC composites. *Journal of Materials Science & Technology*. **35** [12]2019: p. 2743-2750.
124. aviation, G. GE9X Commerical Aircraft Engine. 2019; Available from: https://www.geaviation.com/commercial/engines/ge9x-commercial-aircraft-engine.
125. Rodeghiero, E.D., Moore, B.C., Wolkenberg, B.S., Wuthenow, M., Tse, O.K., and Giannelis, E.P., Sol–gel synthesis of ceramic matrix composites. *Materials Science and Engineering: A*. **244** [1]1998: p. 11-21.
126. Rosso, M., Ceramic and metal matrix composites: Routes and properties. *Journal of Materials Processing Technology*. **175** [1]2006: p. 364-375.
127. J. Kolczyk, Ł.J., N. Kaźnica, Rheological Properties of Typical Ceramic Slurries Used in the Lost Wax Technology. *Foundary Engineering*. **17** [1]2017: p. 5.
128. Dong, S., Katoh, Y., and Kohyama, A., Preparation of SiC/SiC Composites by Hot Pressing, Using Tyranno-SA Fiber as Reinforcement. *Journal of the American Ceramic Society*. **86** [1]2003: p. 26-32.
129. Ceramic Matrix Composites. 2012, General Electric.
130. GE Aviation fired up on CMCs. 2015, General Electric: Delaware, US.
131. Alhart, T. GE Recognized by the American Ceramics Society for World First Commercializing Ceramic Matrix Composites (CMCs) in Aircraft Engines. GE Reports 2019; Available from: https://www.genewsroom.com/press-releases/ge-recognized-american-ceramics-society-world-first-commercializing-ceramic-matrix?fbclid=IwAR0GkXLjRfQ7iuPZan7qUm-hV8w51Fci85EE6FStXIt94-1MsgoIRLB7Jz0.
132. Ceramic Matrix Composites Improve Engine Efficiency. 2016, General Electric.
133. Duan, L., Zhao, X., and Wang, Y., Comparative ablation behaviors of C/SiC-HfC composites prepared by reactive melt infiltration and precursor infiltration and pyrolysis routes. *Ceramics International*. **43** [18]2017: p. 16114-16120.
134. Stewart, T., Williams, B., and Brockmeyer, J., Melt-Infiltrated Refractory Ceramic Matrix Composites. *Ceramic Industry*. **164** [8]2014: p. 22-25.
135. Einset, E.O., Analysis of reactive melt infiltration in the processing of ceramics and ceramic composites. *Chemical Engineering Science*. **53** [5]1998: p. 1027-1039.
136. Zhang, L., Dong, S., Zhou, H., Kan, Y., Zhou, F., and Wang, Z., 3D Cf/ZrC–SiC composites fabricated with ZrC nanoparticles and ZrSi2 alloy. *Ceramics International*. **40** [8, Part A]2014: p. 11795-11801.
137. Chen, X., Feng, Q., Gao, L., Zhang, X., Dong, S., Wang, J., Zhong, Q., Kan, Y., and Ni, D., Interphase degradation of three-dimensional Cf/SiC–ZrC–ZrB2

composites fabricated via reactive melt infiltration. *Journal of the American Ceramic Society*. **100** [10]2017: p. 4816-4826.
138. Kütemeyer, M., Schomer, L., Helmreich, T., Rosiwal, S., and Koch, D., Fabrication of ultra high temperature ceramic matrix composites using a reactive melt infiltration process. *Journal of the European Ceramic Society*. **36** [15]2016: p. 3647-3655.
139. Zhang, M.-y., Li, K.-z., Shi, X.-h., and Tan, W.-l., Effects of SiC interphase on the mechanical and ablation properties of C/C-ZrC-ZrB2-SiC composites prepared by precursor infiltration and pyrolysis. *Materials & Design*. **122** 2017: p. 322-329.
140. Sangsuwan, P., Tewari, S.N., Gatica, J.E., Singh, M., and Dickerson, R., Reactive infiltration of silicon melt through microporous amorphous carbon preforms. *Metallurgical and Materials Transactions B*. **30** [5]1999: p. 933-944.
141. Singh, M., Studies on the reactive melt infiltration of silicon and silicon-molybdenum alloys in porous carbon, in *Annual Meeting of the American Ceramic Society*. 1992, NASA: Minneapolis, MN; United States.
142. GE Aviation and the Ceramic Matrix Composite Revolution. 2015, General Electric.
143. Liu, Y., Fu, Q., Zhang, J., Li, L., and Zhuang, L., Erosion resistance of C/C-SiC-ZrB2 composites exposed to oxyacetylene torch. *Journal of the European Ceramic Society*. **36** [15]2016: p. 3815-3821.
144. Tang, S. and Hu, C., Design, Preparation and Properties of Carbon Fiber Reinforced Ultra-High Temperature Ceramic Composites for Aerospace Applications: A Review. *Journal of Materials Science & Technology*. **33** [2]2017: p. 117-130.
145. Kollins, K., Przybyla, C., and Amer, M.S., Residual stress measurements in melt infiltrated SiC/SiC ceramic matrix composites using Raman spectroscopy. *Journal of the European Ceramic Society*. **38** [7]2018: p. 2784-2791.
146. Hillig, W.B., Melt Infiltration Approach to Ceramic Matrix Composites. *Journal of the American Ceramic Society*. **71** [2]1988: p. C-96-C-99.
147. Muolo, M.L., Ferrera, E., Novakovic, R., and Passerone, A., Wettability of zirconium diboride ceramics by Ag, Cu and their alloys with Zr. *Scripta Materialia*. **48** [2]2003: p. 191-196.
148. An, Q., Cong, X.-s., Shen, P., and Jiang, Q.-c., Roles of alloying elements in wetting of SiC by Al. *Journal of Alloys and Compounds*. **784** 2019: p. 1212-1220.
149. Xu, Y., Cheng, L., and Zhang, L., Carbon/silicon carbide composites prepared by chemical vapor infiltration combined with silicon melt infiltration. *Carbon*. **37** [8]1999: p. 1179-1187.
150. Binner, J., Porter, M., Baker, B., Zou, J., Venkatachalam, V., Diaz, V.R., D'Angio, A., Ramanujam, P., Zhang, T., and Murthy, T.S.R.C., Selection, processing, properties and applications of ultra-high temperature ceramic matrix composites, UHTCMCs – a review. *International Materials Reviews*, 2019: p. 1-56.
151. Compton, J. Multiphysics Analysis of Advanced Materials: Ceramic Matrix Composites. 2014.

152. Cinibulk, M.K., Apostolov, Z.D., Boakye, E.E., Key, T.S., and King, D.S., Constituent Development for Higher-Temperature Capable Ceramic Matrix Composites. [51128]2018: p. V006T02A010.
153. Interrante, L. and Shen, Q., Hyperbranched Polycarbosilanes via Nucleophilic Substitution Reactions, in *Silicon-Containing Dendritic Polymers*, P.R. Dvornic and M.J. Owen, Editors. 2009, Springer Netherlands: Dordrecht. p. 315-343.
154. Lodhe, M., Babu, N., Selvam, A., and Balasubramanian, M., Synthesis and characterization of high ceramic yield polycarbosilane precursor for SiC. *Journal of Advanced Ceramics*. **4** [4]2015: p. 307-311.
155. Wang, L.-Y., Luo, R.-Y., and Cui, G.-Y., Effect of pyrolysis temperature on the mechanical evolution of SiCf/SiC composites fabricated by PIP. *Ceramics International*. **46** [2]2020: p. 1297-1306.
156. Lu, C., Fabrication of a silicon carbide fiber-reinforced ceramic composite by the polymer pyrolysis method 1994, University of Delaware: Delaware.
157. Okamura, K., Ceramic fibres from polymer precursors. *Composites*. **18** [2]1987: p. 107-120.
158. Ziegler, G., Richter, I., and Suttor, D., Fiber-reinforced composites with polymer-derived matrix: processing, matrix formation and properties. *Composites Part A: Applied Science and Manufacturing*. **30** [4]1999: p. 411-417.
159. Xiang, Y., Li, W., Wang, S., Zhang, B., and Chen, Z., Microstructures and mechanical properties of CVD-SiC coated PIP-C/SiC composites under high temperature. *Surface and Coatings Technology*. **209** 2012: p. 197-202.
160. Huang, D., Zhang, M., Huang, Q., Wang, L., and Tong, K., Mechanical Property, Oxidation and Ablation Resistance of C/C–ZrB2–ZrC–SiC Composite Fabricated by Polymer Infiltration and Pyrolysis with Preform of Cf/ZrB2. *Journal of Materials Science & Technology*. **33** [5]2017: p. 481-486.
161. Xie, J., Li, K., Li, H., Fu, Q., and Guo, L., Ablation behavior and mechanism of C/C–ZrC–SiC composites under an oxyacetylene torch at 3000°C. *Ceramics International*. **39** [4]2013: p. 4171-4178.
162. Li, M., Yang, D., Wang, H., and Zhou, X., Property evolvements in SiCf/SiC composites fabricated by combination of PIP and electrophoretic deposition at different pyrolysis temperatures. *Ceramics International*. **45** [12]2019: p. 15689-15695.
163. Parthasarathy, T.A., Przybyla, C.P., Hay, R.S., and Cinibulk, M.K., Modeling Environmental Degradation of SiC-Based Fibers. *Journal of the American Ceramic Society*. **99** [5]2016: p. 1725-1734.
164. Rak, Z.S., A Process for Cf/SiC Composites Using Liquid Polymer Infiltration. *Journal of the American Ceramic Society*. **84** [10]2001: p. 2235-2239.
165. Takeda, M., Kagawa, Y., Mitsuno, S., Imai, Y., and Ichikawa, H., Strength of a Hi-Nicalon™/Silicon-Carbide-Matrix Composite Fabricated by the Multiple Polymer Infiltration-Pyrolysis Process. *Journal of the American Ceramic Society*. **82** [6]1999: p. 1579-1581.
166. Xu, Y. and Zhang, L., Three-Dimensional Carbon/Silicon Carbide Composites Prepared by Chemical Vapor Infiltration. *Journal of the American Ceramic Society*. **80** [7]1997: p. 1897-1900.
167. Xu, Y., Cheng, L., Zhang, L., Yin, H., and Yin, X., Microstructure and Mechanical Properties of Three-Dimensional Textile Hi-Nicalon SiC/SiC

Composites by Chemical Vapor Infiltration. *Journal of the American Ceramic Society*. **85** [5]2002: p. 1217-1221.
168. Kopeliovich, D., Fabrication of Ceramic Matrix Composites by Chemical vapour infiltration 2012.
169. Pierson, H.O., *Handbook of refractory carbides and nitrides: Properties, characteristics, processing and applications*. 1997: Noyes Publication, New York, NY (United States). Medium: X; Size: 340 p.
170. Pierson, H., *Handbook of Chemical Vapour Deposition: Principles, Technology and Applications*. 1999, New York: William Andrew Publishing.
171. Arnold, J., et al., Nanostructured Thermal Protection Systems for Space Exploration Missions. 2005: p.
172. Allemand, A., et al., Protection against Oxydation by CVD or SPS Coatings of Hafnium Carbide and Silicon Carbide on Carbon/Carbon Composites. *Advanced Ceramic Coatings and Materials for Extreme Environments II*, 2013: p. p. 161-169.
173. Wunder, V., et al.,, Multilayer coatings on CFC composites for high-temperature applications. *Surface and Coatings Technology*. **100** 1998: p. p. 329-332.
174. Subramanian, C. and Strafford, K.N., Review of multicomponent and multilayer coatings for tribological applications. *Wear*. **165** [1]1993: p. 85-95.
175. Smeacetto, F., Ferraris, M., Salvo, M., Ellacott, S.D., and Ahmed, A.e.a., Protective coatings for carbon bonded carbon fibre composites. *Ceramics International*. **34** 2008: p. pp. 1297-1301.
176. Naslain, R., Hannache, H., Heraud, L., Christin, F., Rossignol, J.Y., and Colmet, R. , Advanced Ceramic-Ceramic Composite-Materials from the CVI Process. *American Ceramic Society Bulletin*. **62** [11]1983: p.
177. Yee, K., Protective coatings for metals by chemical vapour deposition. *International Metals Reviews*. **23** [1]1978: p. p. 19-42.
178. Golecki, I., Rapid vapor-phase densification of refractory composites. *Materials Science & Engineering R-Reports*. **20** [2]1997: p. p. 37-124.
179. Leuchs, M., Chemical Vapour Infiltration Processes for Ceramic Matrix Composites: Manufacturing, Properties, Applications, in *Ceramic Matrix Composites*. 2008, Wiley-VCH Verlag GmbH & Co. KGaA. p. 141-164.
180. Singh, I., Mod-06 Lec-04 Chemical Vapour Infiltration. 2014, National Programme on Technology Enhanced Learning.
181. Xu, Y., Yan, X., Chemical Vapour Infiltration, in *Chemical Vapour Deposition: An Integrated Engineering Design for Advanced Materials*. 2010, Springer London: London. p. 165-213.
182. Pierson, H., Handbook of chemical vapor deposition (CVD) : principles, technology and applications. 1999, Noyes Publications: Norwich, NY.
183. Besmann, T.M., Stinton, D.P., Lowden, R.A., and Lee, W.Y., Chemical Vapor Deposition (CVD) and Infiltration (CVI), in *Carbide, Nitride and Boride Materials Synthesis and Processing*, A.W. Weimer, Editor. 1997, Springer Netherlands: Dordrecht. p. 547-577.
184. Vignoles, G.L., 8 - Chemical vapor deposition/infiltration processes for ceramic composites, in *Advances in Composites Manufacturing and Process Design*, P. Boisse, Editor. 2015, Woodhead Publishing. p. 147-176.

185. Ofori, J.Y.a.S.V.S., Optimal pressures and temperatures for isobaric, isothermal chemical vapor infiltration. *Aiche Journal*. **42** [10]1996: p. p. 2828-2840.
186. Ma, X., Yin, X., Cao, X., Chen, L., Cheng, L., and Zhang, L., Effect of heat treatment on the mechanical properties of SiCf/BN/SiC fabricated by CVI. *Ceramics International*. **42** [2]2016: p. p. 3652-3658.
187. Li, H.-J., et al.,, A MoSi 2–SiC–Si oxidation protective coating for carbon/carbon composites. . *Surface and Coatings Technology*. **201** [24]2007: p. p. 9444-9447.
188. Kotlensky, W.a.P., J., Properties of CVD Infiltrated Composites. *Carbon*. **7** [6]1969: p. 729-730.
189. Roman, Y.G., Stinton, D.P., and Besmann, T.M., Development of High-Density Fiber Reinforced Silicon-Carbide Fcvi Composites. . *Journal De Physique Ii*. **1** [689-695]1991: p.
190. Roman, Y.G., Decroon, M.H.J.M. and Metselaar, R., Analysis of the Isothermal Forced Flow Chemical-Vapor Infiltration Process - Experimental-Study. *Journal of the European Ceramic Society*. **15** [9]1995: p.
191. Rasi, M., Permeability properties of paper materials. *Research report/Department of Physics, University of Jyväskylä*, [13/2013]2013: p.
192. Matlin, W.M., Stinton, D., and Besmann, T. M., Development of a two-step, forced chemical vapor infiltration process. *Ceramic Transactions*. **58** 1995: p. 119-123.
193. Probst, K.J., Besmann, T. M., Stinton, D. P., Lowden, R. A., Anderson, T. J., Starr, T. L., Recent advances in forced-flow, thermal-gradient CVI for refractory composites, in *International conference; 26th, Metallurgical coatings and thin films*. 1999, Surface and coating technology: San Diego, CA.
194. Caputo, A.J.a.L., W.J. , Continued Development of the Fabrication of Ceramic Fiber-Reinforced Ceramic Composites. . *American Ceramic Society Bulletin*. **63** [12]1984: p. p. 1477-1477.
195. Stinton, D.P., Caputo, A.J., and Lowden, R.A. , Synthesis of Fiber-Reinforced SiC Composites by Chemical Vapor Infiltration. *American Ceramic Society Bulletin*. **65** [2]1986: p. p. 347-350.
196. Bertrand, S., Lavaud, J.F., Hadi, R. El., Vignoles, G., and Pailler, R. , The thermal gradient—pulse flow CVI process: A new chemical vapor infiltration technique for the densification of fibre preforms. . *Journal of the European Ceramic Society*. **18(7)** 1998: p. p. 857-870.
197. Roman, Y.G., Forced flow chemical vapour infiltration., in *Department of Chemical Engineering and Chemistry*. 1994, Technische Universiteit Eindhoven.: Eindhoven.
198. Besmann, T.M., McLaughlin, J., and Lin, H.-T. , Fabrication of ceramic composites: forced CVI. *Journal of Nuclear Materials*. **219** 1995: p. p. 31-35. .
199. Gupte, S.a.T., J., Forced-Flow Chemical Vapor Infiltration of Porous Ceramic Materials. , . *Journal of the Electrochemical Society*. **137** [11]1990: p. p. 3675-3682.
200. Lackey, W.J., Starr, T.L. , *Fabrication of fiber-reinforced ceramic composites by chemical vapour infiltration: Processing, structure and properties.* . Fiber Reinforced Ceramic Composites. **Vol. 49**. 1990, Park Ridge, New Jersey: Noyes Publications.

201. Naslain, R., Lamon, J. and Doumeingts, D.,, *High temperature ceramic matrix composites.* . 1993: Woodhead Publishing.
202. Dupel, P., Bourrat, X, and Pailler, R., Structure of pyrocarbon infiltrated by pulse-CVI. . *Carbon*. **33** [9]1995: p. p. 1193-1204.
203. Naslain, R. Ceramic Matrix Composites in *5th Conference of the European Ceramic Society*. 1998. Versailles, France: Journal of the European Ceramic Society.
204. Allen, S.D., Laser Chemical Vapor Deposition (LCVD), in *Emergent Process Methods for High-Technology Ceramics*, R.F. Davis, H. Palmour, and R.L. Porter, Editors. 1984, Springer US: Boston, MA. p. 397-413.
205. Tuersley, I.P., Hoult, T.P., and Pashby, I.R., The processing of SiC/SiC ceramic matrix composites using a pulsed Nd–YAG laser: Part I: Optimisation of pulse parameters. *Journal of Materials Science*. **33** [4]1998: p. 955-961.
206. Roy, S.K., Laser chemical vapour deposition. *Bulletin of Materials Science*. **11** [2]1988: p. 129.
207. Yan, L.S., Li, H.J., Cui, H., and Wang, T., Low-cost C/SiC composites prepared by CVI+pressure-PIP hybrid process. *Wuji Cailiao Xuebao/Journal of Inorganic Materials*. **21** [3]2006: p. 664-670.
208. Kim, W.-J., Kim, D., and Park, J.Y., Fabrication and material issues for the application of SiC compoites to LWR fuel cladding. *Nuclear Engineering and Technology*. **45** [4]2013: p. 565-572.
209. Zok, F.W., Ceramic-matrix composites enable revolutionary gains in turbine engine efficiency.
210. Ortona, A., Donato, A., Filacchioni, G., De Angelis, U., La Barbera, A., Nannetti, C.A., Riccardi, B., and Yeatman, J., SiC–SiCf CMC manufacturing by hybrid CVI–PIP techniques: process optimisation. *Fusion Engineering and Design*. **51-52** 2000: p. 159-163.
211. Nannetti, C.A., Riccardi, B., Ortona, A., La Barbera, A., Scafè, E., and Vekinis, G., Development of 2D and 3D Hi-Nicalon fibres/SiC matrix composites manufactured by a combined CVI–PIP route. *Journal of Nuclear Materials*. **307-311** 2002: p. 1196-1199.
212. Park, J.Y., Han, J., Kim, D., Kim, W.-J., and Lee, S.H., Fracture Behaviors of SiCf/SiC Composites Prepared by Hybrid Processes of CVI and PIP. *J. Korean Ceram. Soc*. **51** [5]2014: p. 430-0.
213. Xiao, P., Xie, J.W., Xiong, X., and Yan, Z.Q., Microstructure and flexural properties of C/SiC composites by CVI-RMI method. *Zhongnan Daxue Xuebao (Ziran Kexue Ban)/Journal of Central South University (Science and Technology)*. **38** [3]2007: p. 381-385.
214. Srinivasan, G.V., Venkateswaran, V., and Lau, S.K., Engineering analysis for CMC material design considerations using carborundum's sintered SiC fiber and slurry cast/melt infiltration process. *Ceramic Engineering and Science Proceedings*. **16** [4]1995: p. 63-72.
215. Li, J., Liu, Y., Nan, B., Zhao, Z., Feng, W., Zhang, Q., and Cheng, L., Microstructure and Properties of C/SiC-Diamond Composites Prepared by the Combination of CVI and RMI. *Advanced Engineering Materials*. **0** [0]2018: p. 1800765.

216. Iveković, A., Dražić, G., and Novak, S., Densification of a SiC-matrix by electrophoretic deposition and polymer infiltration and pyrolysis process. *Journal of the European Ceramic Society*. **31** [5]2011: p. 833-840.
217. Zhu, Y., Huang, Z., Dong, S., Yuan, M., and Jiang, D., Manufacturing 2D carbon-fiber-reinforced SiC matrix composites by slurry infiltration and PIP process. *Ceramics International*. **34** [5]2008: p. 1201-1205.
218. Fitzer, E. and Hegen, D., Chemical Vapor Deposition of Silicon Carbide and Silicon Nitride—Chemistry's Contribution to Modern Silicon Ceramics. *Angewandte Chemie International Edition in English*. **18** [4]1979: p. 295-304.
219. Avigal, Y., Schieber, M., and Levin, R., The growth of hetero-epitaxial SiC films by pyrolysis of various alkyl-silicon compounds. *Journal of Crystal Growth*. **24-25** 1974: p. 188-192.
220. Ge, Y., Gordon, M.S., Battaglia, F., and Fox, R.O., Theoretical study of the pyrolysis of methyltrichlorosilane in the gas phase. 1. Thermodynamics. *The Journal of Physical Chemistry A*. **111** [8]2007: p. 1462-1474.
221. Ge, Y., Gordon, M.S., Battaglia, F., and Fox, R.O., Theoretical study of the pyrolysis of methyltrichlorosilane in the gas phase. 2. Reaction paths and transition states. *The Journal of Physical Chemistry A*. **111** [8]2007: p. 1475-1486.
222. Loumagne, F., Langlais, F., and Naslain, R., *Reactional Mechanisms of the Chemical Vapor Deposition of SiC-Based Ceramics from CH3SiCl3/H2 Gas Precursor*. **Vol. 155**. 1995. 205-213.
223. Roman, Y.G., Forced flow chemical vapour infiltration. 1994, Technische Universiteit Eindhoven: Eindhoven.
224. Schnack, E., Li, A., Rahman, A., and Zhu, Y., *A coupled numerical modelling and experimental approach in chemical vapour infiltration (CVI) process of SiC/SiC composites*. **Vol. 3**. 2015. 230-249.
225. E. Schnack, A.L., A.M. Rahman & Y. Zhu, A coupled numerical modelling and experimental approach in chemical vapour infiltration (CVI) process of SiC/SiC composites. *International Journal of Computational Methods and Experimental Measurements*. **3** [3]2015: p. 19.
226. M. D. Allendorf, T.H.O.a.C.F.M., The decomposition of methyltrichlorosilane: Studies in a high-temerpature flow reactor, C.R. Facility, Editor. 1994, Advanced Industrial Materials Program of the U.S. Dept. of Energy Office of Industrial Technologies.: Sandia National Laboratories, Livermore, CA.
227. D'Angio, A., Microwave enhanced chemical vapour infiltration of silicon carbide fibre preforms. 2018, University of Birmingham.
228. Rossignol. J.Y., L., F., and Naslain, R. Proc. 9th Int. Conf. CVD. 1984. The Electrochemical Society.
229. Fedou, R., Langlais, F. and Naslain, R., Model for the Isothermal Isobaric Chemical Vapor Infiltration(CVI) in a Straight Cylindrical Pore. Application to the CVI of SiC. *Journal of Materials Synthesis and Processing*, 1993: p. 61-74.
230. Cagliostro, D.E., Riccitiello, S.R., Ren, J., and Zaghi, F., Comparison of the Pyrolysis Products of Dichlorodimethylsilane in the Chemical Vapor Deposition of Silicon Carbide on Silica in Hydrogen or Argon. *Journal of the American Ceramic Society*. **77** [10]1994: p. 2721-2726.
231. Drieux, P., Chollon, G., Jacques, S., Allemand, A., Cavagnat, D., and Buffeteau, T., Experimental study of the chemical vapor deposition from

CH3SiHCl2/H2: Application to the synthesis of monolithic SiC tubes. *Surface and Coatings Technology*. **230** 2013: p. 137-144.
232. Lespiaux, D., Langlais, F., Naslain, R., Schamm, S., and Sevely, J., Correlations between gas phase supersaturation, nucleation process and physico-chemical characteristics of silicon carbide deposited from Si-C-H-Cl system on silica substrates. *Journal of Materials Science*. **30** [6]1995: p. 1500-1510.
233. Loumagne, F., Langlais, F., and Naslain, R., Kinetic laws of the chemical process in the CVD of SiC ceramics from CH3SiCl3-H2 precursor. *Le Journal de Physique IV*. **3** [C3]1993: p. C3-527-C3-533.
234. Loumagne, F., Langlais, F., and Naslain, R., Experimental kinetic study of the chemical vapour deposition of SiC-based ceramics from CH3SiCl3H2 gas precursor. *Journal of Crystal Growth*. **155** [3-4]1995: p. 198-204.
235. Loumagne, F., Langlais, F., Naslain, R., Schamm, S., Dorignac, D., and Sévely, J., Physicochemical properties of SiC-based ceramics deposited by low pressure chemical vapor deposition from CH3SiCl3H2. *Thin Solid Films*. **254** [1-2]1995: p. 75-82.
236. Langlais, F., Prebende, C., Tarride, B., and Naslain, R., *On the Kinetics of the CVD of Si from SiH2Cl2/H2 and SiC from CH3SiCl3/H2 in a Vertical Tubular Hot-Wall Reactor*. **Vol. 50**. 1989.
237. Yang, Y. and Zhang, W.-g., Chemical vapor deposition of SiC at different molar ratios of hydrogen to methyltrichlorosilane. *Journal of Central South University of Technology*. **16** [5]2009: p. 730.
238. Zhang, W.G. and Hüttinger, K.J., CVD of SiC from Methyltrichlorosilane. Part II: Composition of the Gas Phase and the Deposit. *Chemical Vapor Deposition*. **7** [4]2001: p. 173-181.
239. Féron, O., Chollon, G., Dartigues, F., Langlais, F., and Naslain, R., In situ kinetic analysis of SiC filaments CVD. *Diamond and Related Materials*. **11** [3]2002: p. 1234-1238.
240. Zhang, W.G. and Hüttinger, K.J., CVD of SiC from Methyltrichlorosilane. Part I: Deposition Rates. *Chemical Vapor Deposition*. **7** [4]2001: p. 167-172.
241. Chiu, C.C., Desu, S.B., and Tsai, C.Y., Low pressure chemical vapor deposition (LPCVD) of β–SiC on Si(100) using MTS in a hot wall reactor. *Journal of Materials Research*. **8** [10]1993: p. 2617-2626.
242. Papasouliotis, G.D. and Sotirchos, S.V., Hetergenous kinetic of the chemical vapour deposition of silicon carbide from methyltrichlorosilane in *Gas-Phase and Surface Chemistry in Electronic Materials Processing*, T.J. Mountziaris, et al., Editors. 1994. p. 111-116.
243. D'Angio, A., Microwave enhanced chemical vapour infiltration of silicon carbide fibre preforms, in *School of Metallurgy and Materials*. 2018, University of Birmingham.
244. Kim, H.-S. and Choi, D.-J., Effect of Diluent Gases on Growth Behavior and Characteristics of Chemically Vapor Deposited Silicon Carbide Films. *Journal of the American Ceramic Society*. **82** [2]1999: p. 331-337.
245. Langlais, F., *On the chemical steps involved in the chemical vapour infiltration processing of ceramic matrix composites*. **Vol. 30**. 2005. 579-592.

246. Papasouliotis, G.D. and Sotirchos, S.V., Hydrogen Chloride Effects on the CVD of Silicon Carbide from Methyltrichlorosilane. *Chemical Vapor Deposition*. **4** [6]1998: p. 235-246.
247. Chang, H.-C., Morse, T.F., and Sheldon, B.W., Minimizing Infiltration Times during Isothermal Chemical Vapor Infiltration with Methyltrichlorosilane. *Journal of the American Ceramic Society*. **80** [7]1997: p. 1805-1811.
248. Langlais, F., Prebende, C., and Couderc, J.P., Physical and chemical kinetic processes in the CVD of silicon from SiH2Cl2/H2 gaseous mixtures in a vertical cylindrical hot-wall reactor. *Journal of Crystal Growth*. **113** [3]1991: p. 606-632.
249. Cheng, D.J., Shyy, W. J., Kuo, D. H. and Hon, M. H. , Growth Characteristics of CVD Beta-Silicon Carbide *Journal of the Electrochemical Society*. **134** 1987: p. 3145-3149.
250. Jacobson, K.A., Growth, Texture, and Surface Morphology of SiC Layers. *Journal of the Electrochemical Society*. **118** 1971: p. 1001-1006.
251. Sibieude, F. and Benezech, G., Chemical vapour deposition of silicon carbide: An X-ray diffraction study. *Journal of Materials Science*. **23** [5]1988: p. 1632-1636.
252. Chin, J., Gantzel, P.K., and Hudson, R.G., The structure of chemical vapor deposited silicon carbide. *Thin Solid Films*. **40** [Supplement C]1977: p. 57-72.
253. van der Putte, P., Giling, L.J., and Bloem, J., Surface morphology of HCl etched silicon wafers: I. Gas phase composition in the silicon HCl system and surface reactions during etching. *Journal of Crystal Growth*. **41** [1]1977: p. 133-145.
254. Papasouliotis, G.D. and Sotirchos, S.V., Experimental study of atmospheric pressure chemical vapor deposition of silicon carbide from methyltrichlorosilane. *Journal of Materials Research*. **14** [8]1999: p. 3397-3409.
255. Yu, X.-M., Zhou, W.-C., Luo, F., Zheng, W.-J., and Zhu, D.-M., Effect of fabrication atmosphere on dielectric properties of SiC/SiC composites. *Journal of Alloys and Compounds*. **479** [1]2009: p. L1-L3.
256. Sun, J., Wang, W., and Yue, Q., Review on Microwave-Matter Interaction Fundamentals and Efficient Microwave-Associated Heating Strategies. *Materials (Basel, Switzerland)*. **9** [4]2016: p. 231.
257. Satnam Singh, D.G., Vivek Jain, An Energy Efficient Processing Route for Advance Ceramic Composites Using Microwaves, in *Advanced Ceramic Materials*. 2016. p. 97-143.
258. Sutton, W.H., Microwave Processing of Ceramic Materials. *American Ceramic Society Bulletin*. **68** [2]1989: p. 173.
259. Council, N.R., *Microwave Processing of Materials*. 1994, Washington, DC: The National Academies Press. 164.
260. Thostenson, E.T. and Chou, T.W., Microwave processing: fundamentals and applications. *Composites Part A: Applied Science and Manufacturing*. **30** [9]1999: p. 1055-1071.
261. Tan, E., Kagawa, Y., and Dericioglu, A.F., Electromagnetic wave absorption potential of SiC-based ceramic woven fabrics in the GHz range. *Journal of Materials Science*. **44** [5]2009: p. 1172-1179.

262. Mishra, R.R. and Sharma, A.K., Microwave–material interaction phenomena: Heating mechanisms, challenges and opportunities in material processing. *Composites Part A: Applied Science and Manufacturing*. **81** 2016: p. 78-97.
263. Greenacre, N.R., Measurement of the high-temperature dielectric properties of ceramics at microwave frequencies. 1996, University of Nottingham: Nottingham.
264. Gaone, J.M., Tilley, B.S., and Yakovlev, V.V. Permittivity-based control of thermal runaway in a triple-layer laminate. in *2017 IEEE MTT-S International Microwave Symposium (IMS)*. 2017. IEEE.
265. Kriegsmann, G.A., Thermal runaway in microwave heated ceramics: A one-dimensional model. *Journal of Applied Physics*. **71** [4]1992: p. 1960-1966.
266. Barmatz, M.a.H.W.J. Steady State Temperature Profile in a Sphere Heated by Microwaves. in *Microwave Processing of Materials III*. 1992. Pittsburgh, USA: Materials Research Society Symposium Proceedings.
267. Arai, M., Open-Ended Coaxial Probes for High Temperature Dielectric Measurements. 1995, University of Nottingham.
268. Resonant cavities and waveguides. Massachusetts Institute of Technology. p. 356-407.
269. Microwaves101.com. Quality factor. [cited 2019 23/04]; Available from: https://www.microwaves101.com/encyclopedias/quality-factor.
270. Venkatesh, M.S. and Raghavan, V., An Overview of Dielectric Properties Measuring Techniques. *Canadian Biosystems Engineering / Le Genie des biosystems au Canada*. **47** 2005: p. 15-30.
271. Kumar, A., Sharma, S., and Singh, G., Measurement of dielectric constant and loss factor of the dielectric material at microwave frequencies. *Progress In Electromagnetics Research*. **69** 2007: p. 47-54.
272. Arai, M., Binner, J.G.P., Carr, G.E., and Cross, T.E. High temperature dielectric measurements on ceramics. in *1992., Sixth International Conference on Dielectric Materials, Measurements and Applications*. 1992.
273. Park, M.K., Kim, H.N., Baek, S.S., Kang, E.S., Baek, Y.K., and Kim, D.K. Dielectric properties of alumina ceramics in the microwave frequency at high temperature. in *Solid State Phenomena*. 2007. Trans Tech Publ.
274. Ghodgaonkar, D.K., Varadan, V.V., and Varadan, V.K., A free-space method for measurement of dielectric constants and loss tangents at microwave frequencies. *IEEE Transactions on Instrumentation and Measurement*. **38** [3]1989: p. 789-793.
275. Ho, W.W., High-Temperature Dielectric Properties of Polycrystalline Ceramics. *MRS Proceedings*. **124** 2011: p. 137.
276. Retrowow, 70s high tech household.
277. Nave, R. The Magnetron. Available from: http://hyperphysics.phy-astr.gsu.edu/hbase/Waves/magnetron.html.
278. Aardema, D., What is a MAGNETRON - How Does it Work, Blueprint, Editor. 2018.
279. Difference between solid state radar and magnetron, in *LIDAR and RADAR Information*. 2017.
280. Wesson, R., RF Solid State Cooking White Paper. *Ampleon RF power innovation*, 2016: p.

281. Sairem. Microwave and radio-frequency generators. Available from: https://www.sairem.com/microwave-radio-frequency-rf-products/microwave-generators-components/microwave-generators/.
282. Thostenson, E. and Chou, T.W., *Microwave processing: fundamentals and applications*. **Vol. 30**. 1999. 1055-1071.
283. Connor, F.R., *Wave transmission*. 1972: E.Arnold.
284. Sun, J., Wang, W., and Yue, Q., Review on Microwave-Matter Interaction Fundamentals and Efficient Microwave-Associated Heating Strategies. *Materials*. **9** [4]2016: p. 231.
285. Lindroth, D.P., Berglund, W.R., Morrell, R.J., and Blair, J.R., *Microwave assisted drilling in hard rock*. **Vol. 25**. 1993. 24-27.
286. Shukla, M. and Ghosh, S., Microwave Joining of Ceramics: An Overview. 2016: p.
287. Aravindan, S. and Krishnamurthy, R., Joining of ceramic composites by microwave heating. *Materials Letters*. **38** [4]1999: p. 245-249.
288. Yussuf, A.A., Sbarski, I., Hayes, J.P., Tran, N., and Solomon, M., *Single-mode microwave sealing of polymer-based microfluidic devices using conductive polymer*. Photonics Europe. **Vol. 5455**. 2004: SPIE.
289. GmbH, A.P. Which microwave synthesis reactor is the best one for your research? ; Available from: https://wiki.anton-paar.com/en/which-microwave-synthesis-reactor-is-the-best-one-for-your-research/.
290. Celuch-Marcysiak, M. and Gwarek, W. Advanced features of FDTD modeling for microwave power applications. in *35th Microwave Power Symposium, July 2000, Montreal, Canada*. 2000.
291. Yakovlev, V.V. Commercial EM Codes Suitable for Modeling of Microwave Heating — a Comparative Review. 2001. Berlin, Heidelberg: Springer Berlin Heidelberg.
292. Hill, J.M. and Marchant, T.R., Modelling microwave heating. *Applied Mathematical Modelling*. **20** [1]1996: p. 3-15.
293. Yakovlev, V.V. Examination of Contemporary Electromagnetic Software Capable of Modeling Problems of Microwave Heating. 2006. Berlin, Heidelberg: Springer Berlin Heidelberg.
294. Pitchai, K., Electromagnetic and heat transfer modeling of microwave heating in domestic ovens. 2011: p.
295. Mechenova, V.A.a.V.V.Y., Efficiency optimization for systems and components in microwave power engineering. *Journal of Microwave Power and Electromagnetic Energy*. **39(1)** 2004: p. 15-30.
296. Yakovlev, V.V. Multiphysics Modeling Goals, Options, and State of the Art. in *17th International conference on microwave and high frequency heating*. 2019. Valencia, Spain: AMPERE.
297. Celuch, M., W. K. Gwarek and M. Sypniewski, A novel FDTD system for microwave heating and thawing analysis with automatic time-variation of enthalpy dependent media parameters. *Advances in Microwave and Radio Frequency Processing*, 2006: p. 199-209.
298. Mohekar, A.A., Tilley, B.S., and Yakovlev, V.V., A 2D Model of a Triple Layer Electromagnetic Heat Exchanger with Porous Media Flow.

299. Kiley, E.M. and Yakovlev, V.V. Two-dimensional multiphysics model of microwave sintering. in *2017 IEEE MTT-S International Microwave Symposium (IMS)*. 2017.
300. Ayappa, K., Modelling transport processes during microwave heating: A review. *Reviews in chemical engineering*. **13** [2]1997: p. 1-69.
301. Mo, R., Yin, X., Ye, F., Liu, X., Cheng, L., and Zhang, L., Mechanical and microwave absorbing properties of Tyranno® ZMI fiber annealed at elevated temperatures. *Ceramics International*. **43** [12]2017: p. 8922-8931.
302. Sutton, W.H., Microwave Processing of Ceramic Materials. *American Ceramic Society Bulletin*. **68** [2]1989: p. 376-386.
303. Ye, F., Zhang, L., Yin, X., Liu, Y., and Cheng, L., Dielectric and Electromagnetic Wave Absorbing Properties of Two Types of SiC Fibres with Different Compositions. *Journal of Materials Science & Technology*. **29** [1]2013: p. 55-58.
304. Chollon, G., Pailler, R., Canet, R., and Delhaes, P., Correlation between microstructure and electrical properties of SiC-based fibres derived from organosilicon precursors. *Journal of the European Ceramic Society*. **18** [6]1998: p. 725-733.
305. Ding, D., Zhou, W., Zhang, B., Luo, F., and Zhu, D., Complex permittivity and microwave absorbing properties of SiC fiber woven fabrics. *Journal of Materials Science*. **46** [8]2011: p. 2709-2714.
306. Liu, C., Yu, D., Kirk, Donald W., and Xu, Y., Electromagnetic wave absorption of silicon carbide based materials. *RSC Advances*. **7** [2]2017: p. 595-605.
307. Giancoli, D.C., *Physics : principles with applications*. 1995, Englewood Cliffs: Prentice-Hall.
308. cafe, R. Conductor Bulk Resistivity & Skin Depths. Available from: http://www.rfcafe.com/references/electrical/cond-high-freq.htm.
309. Qingsong, M. and Zhaohui, C., *Electrical resistivity of silicon oxycarbide ceramics fabricated via polysiloxane pyrolysis*. **Vol. 36**. 2007. 619-621.
310. Lu, K., Erb, D., and Liu, M., Thermal stability and electrical conductivity of carbon-enriched silicon oxycarbide. *Journal of Materials Chemistry C*. **4** [9]2016: p. 1829-1837.
311. Morell, J.I., Economou, D.J., and Amundson, N.R., Chemical vapor infiltration of SiC with microwave heating. *Journal of Materials Research*. **8** [5]1993: p. 1057-1067.
312. Sorrell, C., Innovative composite materials research at the U.S department of energy, office of energy efficiency and renewable energy. *Composites engineering*. **4** [8]1994: p. 857-882.
313. Devlin, D.J., Currier, R.P., Barbeo, R.S.,Espinoza, B.F., and Elliot, N. , Microwave assisted chemical vapour infiltration L.A.N.L. Materials Science and Technology Division, Editor. 1994: Los Alamos
314. Scholz, R., dos Santos Marques, F., and Riccardi, B., Electrical conductivity of silicon carbide composites and fibers. *Journal of Nuclear Materials*. **307–311, Part 2** 2002: p. 1098-1101.
315. Devlin, D.J., Currier, R.P., Laia Jr, J.R., and Barbero, R.S., Chemical vapor infiltration using microwave energy. 1993, Google Patents.
316. Day, P.S., Skamser, D.J., Jennings, H.M., Johnson, D.L., and Spotz, M.S., Fabrication of SiC matrix surface composites by chemical vapor infiltration with

microwave heating: Temperature effects. *Ceramic Engineering and Science Proceedings*. **15** [5]1994: p. 908-915.
317. Cioni Beatrice, O.E., Lazzeri Andrea Microwave Assisted Chemical Vapour Infiltration for the Production of Ceramic Matrix Composites. *Récents Progrès en Génie des Procédés*. **94** 2007: p.
318. Binner, J., Vaidhyanathan, B., and Jaglin, D., Microwave heated chemical vapour infiltration of SiC powder impregnated SiC fibre preforms. *Advances in Applied Ceramics*. **112** [4]2013: p. 235-241.
319. Day, P.S., Spotz, M.S., Skamser, D.J., Jennings, H.M., and Johnson, D., Microwave-assisted chemical vapour infiltration. *Ceram. Trans.* **42** 1993: p. 95-102.
320. Yin, Y., Binner, J., and Cross, T., Microwave assisted chemical vapor infiltration for ceramic matrix composites. *Microwaves: Theory and Application in Materials Processing IV*, 1997: p. 349-356.
321. Toolbox, T.E. Emissivity Coefficients Materials. 2003; Available from: https://www.engineeringtoolbox.com/emissivity-coefficients-d_447.html.
322. Jenkins, A.C. and Chambers, G.F., Vapor Pressures of Silicon Compounds. *Industrial & Engineering Chemistry*. **46** [11]1954: p. 2367-2369.
323. Brizhinev, M.P., Golubev, S.V., Dorozhkina, D.S., Eremin, B.G., Zorin, V.G., Litvak, A.G., Plotnikov, I.V., Razin, S.V., Semenov, V.E., Strikovskii, A.V., and Tolkacheva, O.N., Microwave discharge on a dielectric surface in vacuum. *Journal of Experimental and Theoretical Physics*. **92** [6]2001: p. 986-990.
324. COI Ceramics, I., Polymer Infiltration and Pyrolysis (PIP) Process, A.s. system, Editor.
325. industries, U. Tyranno Fiber®. Available from: https://www.ube.com/contents/en/chemical/continuous_inorganic_fiber/tyranno_fiber.html.
326. Chattopadhyay, R., 1 - Introduction: types of technical textile yarn, in *Technical Textile Yarns*, R. Alagirusamy and A. Das, Editors. 2010, Woodhead Publishing. p. 3-55.
327. Project, H. Advanced processing technologies based on high frequency electromagnetic waves (RF and MW) for the thermal treatment / treament of CMC and EG. 2016; Available from: http://www.helm-project.eu/.
328. Ullal, S.J., Singh, H., Vahedi, V., and Aydil, E.S., Deposition of silicon oxychloride films on chamber walls during Cl2/O2 plasma etching of Si. *Journal of Vacuum Science & Technology A*. **20** [2]2002: p. 499-506.
329. Marra, J.E., Kreidler, E.R., Jacobson, N.S., and Fox, D.S., Direct mass spectrometric identification of silicon oxychloride compounds. *Journal of The Electrochemical Society*. **135** [6]1988: p. 1571-1574.
330. Rashband, W.S., ImageJ, U.S.N.i.o. Health, Editor. 1997-2019: Bethesda, Maryland.
331. inc., T.M., MATLAB and statisitics toolbox release 2018b. 2018: Natick, Massachusetts.
332. ASTM, Standard Test Method for Measurement of the Permeability of Unsaturated Porous
Materials by Flowing Air, in *ASTM D6539-13*. 2013, ASTM: West Conshohocken, PA.
333. Steven W., H., *The use of gel-cast ceramic foams as diesel particulate filters*. 2018.

334. Tsai, P.-T., AN EVALUATION OF GAS PERMEABILITY OF SiCf/SiCm CERAMIC MATRIX COMPOSITES, in *School of Metallurgy and Materials*. 2017, University of Birmingham.
335. Bieringer, R.J., Study of Electron Penetration in Solids Using Cathodoluminescent Thin Films. *Physical Review*. **142** [2]1966: p. 550-554.
336. Putz, K.B.a.H., MATCH! , C. Impact, Editor., Crystal Impact.
337. Reinshaw, Windows-based Raman Environment (WIRE ™). 2019, Reinshaw: Gloucester, UK.
338. Choy, K.L., Chemical vapour deposition of coatings. *Progress in Materials Science*. **48** [2]2003: p. 57-170.
339. Berthon, S. and Malé, G., Infiltration of zirconium diboride by ICVI in porous materials. *Composites Science and Technology*. **57** [2]1997: p. 217-227.
340. International, A., Standard Test Method for Determining Specific Heat Capacity by Differential Scanning Calorimetry, in *ASTM E1269-11(2018)*. 2018, ASTM International: West Conshohocken, PA.
341. International, A., Standard Test Method for Thermal Diffusivity by the Flash Method, in *ASTM E1461-13*. 2013, ASTM International: West Conshohocken, PA.
342. Netzsch, LFA 427/ Fiber Sample Holder - 6.256.1-93.3/4, Netzsch, Editor. 2018.
343. Catalá-Civera, J.M., Canós, A.J., Plaza-González, P., Gutiérrez, J.D., García-Baños, B., and Peñaranda-Foix, F.L., Dynamic Measurement of Dielectric Properties of Materials at High Temperature During Microwave Heating in a Dual Mode Cylindrical Cavity. *IEEE Transactions on Microwave Theory and Techniques*. **63** [9]2015: p. 2905-2914.
344. Garcia-Baños, B., Catalá-Civera, J., Peñaranda-Foix, F., Plaza-González, P., and Llorens-Vallés, G., In Situ Monitoring of Microwave Processing of Materials at High Temperatures through Dielectric Properties Measurement. *Materials*. **9** [5]2016: p. 349.
345. Gutiérrez, J.D., Catalá-Civera, J.M., Bows, J., and Peñaranda-Foix, F.L., Dynamic measurement of dielectric properties of food snack pellets during microwave expansion. *Journal of Food Engineering*. **202** 2017: p. 1-8.
346. Celuch, M. and Kopyt, P., Modeling microwave heating in foods, in *Development of packaging and products for use in microwave ovens*. 2009, Elsevier. p. 305-348.
347. Kopyt, P. and Celuch, M., Coupled electromagnetic-thermodynamic simulations of microwave heating problems using the FDTD algorithm. *Journal of Microwave Power and Electromagnetic Energy*. **41** [4]2007: p. 18-29.
348. Cheng, A.H.D. and Cheng, D.T., Heritage and early history of the boundary element method. *Engineering Analysis with Boundary Elements*. **29** [3]2005: p. 268-302.
349. Akin, J.E., Chapter 11 - Scalar fields, in *Finite Element Analysis with Error Estimators*, J.E. Akin, Editor. 2005, Butterworth-Heinemann: Oxford. p. 281-383.
350. Josiek, A., Nonstoichiometry and nanocrystallization of silicon-rich silicon carbide deposited by chemical vapor deposition. *Journal of Crystal Growth*. **160** [3]1996: p. 261-267.

351. Josiek, A., Langlais, F., and Bourrat, X., A study of the transition between growth of stoichiometric and silicon-excess silicon carbide by CVD in the system MTS/H2. *Chemical Vapor Deposition*. **2** [1]1996: p. 17-21.
352. Song, H., Zhou, W., Luo, F., Huang, Z., Qing, Y., Chen, M., and Mu, Y., Temperature dependence of dielectric properties of SiCf/PyC/SiC composites. *Materials Science and Engineering: B*. **195** 2015: p. 12-19.
353. Prentice, C., MCVI installation at the University of Birmingham by Archer Technicoat Ltd., A. D'Angio, Editor. 2013.
354. Pampuch, R. and Stobierski, L., Morphology of silicon carbide formed by chemical vapour deposition. *Ceramurgia International*. **3** [2]1977: p. 43-52.
355. Horikoshi, S., Watanabe, T., Narita, A., Suzuki, Y., and Serpone, N., The electromagnetic wave energy effect(s) in microwave–assisted organic syntheses (MAOS). *Scientific Reports*. **8** [1]2018: p. 5151.
356. Díaz-Ortiz, Á., Prieto, P., and de la Hoz, A., A Critical Overview on the Effect of Microwave Irradiation in Organic Synthesis. *The Chemical Record*. **19** [1]2019: p. 85-97.
357. Booske, J.H., Cooper, R.F., and Dobson, I., Mechanisms for nonthermal effects on ionic mobility during microwave processing of crystalline solids. *Journal of Materials Research*. **7** [2]1992: p. 495-501.
358. Booske, J.H., Cooper, R.F., Freeman, S.A., Rybakov, K.I., and Semenov, V.E., Microwave ponderomotive forces in solid-state ionic plasmas. *Physics of Plasmas*. **5** [5]1998: p. 1664-1670.
359. Freeman, S.A., Booske, J., and Cooper, R., Microwave Field Enhancement of Charge Transport in Sodium Chloride. *Physical review letters*. **74** 1995: p. 2042-2045.
360. Wang, J., Binner, J., Vaidhyanathan, B., Joomun, N., Kilner, J., Dimitrakis, G., and Cross, T.E., Evidence for the Microwave Effect During Hybrid Sintering. *Journal of the American Ceramic Society*. **89** [6]2006: p. 1977-1984.
361. Berlan, J., Giboreau, P., Lefeuvre, S., and Marchand, C., Synthese organique sous champ microondes: premier exemple d'activation specifique en phase homogene. *Tetrahedron Letters*. **32** [21]1991: p. 2363-2366.
362. Haque, E., Khan, N.A., Park, J.H., and Jhung, S.H., Synthesis of a metal–organic framework material, iron terephthalate, by ultrasound, microwave, and conventional electric heating: a kinetic study. *Chemistry–A European Journal*. **16** [3]2010: p. 1046-1052.
363. Steinreiber, A., Stadler, A., Mayer, S.F., Faber, K., and Kappe, C.O., High-speed microwave-promoted Mitsunobu inversions. Application toward the deracemization of sulcatol. *Tetrahedron Letters*. **42** [36]2001: p. 6283-6286.
364. Rodríguez, A.M., Prieto, P., de la Hoz, A., Díaz-Ortiz, Á., Martín, D.R., and García, J.I., Influence of Polarity and Activation Energy in Microwave–Assisted Organic Synthesis (MAOS). *ChemistryOpen*. **4** [3]2015: p. 308-317.
365. Sheldon, B.W. and Besmann, T.M., Reaction and diffusion kinetics during the initial stages of isothermal chemical vapor infiltration. *Journal of the American Ceramic Society*. **74** [12]1991: p. 3046-3053.
366. 2 - PVT Tests and Correlations, in *Developments in Petroleum Science*, A. Danesh, Editor. 1998, Elsevier. p. 33-104.
367. Balooch, M. and Olander, D., Etching of silicon carbide by chlorine. *Surface science*. **261** [1-3]1992: p. 321-334.

368. Marra, J.E., Kreidler, E.R., Jacobson, N.S., and Fox, D.S., Reactions of Silicon-Based Ceramics in Mixed Oxidation Chlorination Environments. *Journal of the American Ceramic Society*. **71** [12]1988: p. 1067-1073.
369. Park, D.S., McNallan, M.J., Park, C., and Liang, W.W., Active Corrosion of Sintered α-Silicon Carbide in Oxygen–Chlorine Gases at Elevated Temperatures. *Journal of the American Ceramic Society*. **73** [5]1990: p. 1323-1329.
370. Deng, Y., Zhang, Y., Zhang, N., Zhi, Q., Wang, B., and Yang, J., Preparation and characterization of pure SiC ceramics by high temperature physical vapor transport induced by seeding with nano SiC particles. *Journal of Materials Science & Technology*. **35** [12]2019: p. 2756-2760.
371. Kmetz, M., Suib, S., and Galasso, F., Silicon Carbide/Silicon and Silicon Carbide/Silicon Carbide Composites Produced by Chemical Vapor Infiltration. *Journal of the American Ceramic Society*. **73** [10]1990: p. 3091-3093.
372. López-Honorato, E., Brigden, C., Shatwell, R.A., Zhang, H., Farnan, I., Xiao, P., Guillermier, P., and Somers, J., Silicon carbide polytype characterisation in coated fuel particles by Raman spectroscopy and 29Si magic angle spinning NMR. *Journal of Nuclear Materials*. **433** [1]2013: p. 199-205.
373. Chollon, G., Naslain, R., Prentice, C., Shatwell, R., and May, P., High temperature properties of SiC and diamond CVD-monofilaments. *Journal of the European Ceramic Society*. **25** [11]2005: p. 1929-1942.
374. Nakashima, S. and Harima, H., Raman Investigation of SiC Polytypes. *physica status solidi (a)*. **162** [1]1997: p. 39-64.
375. Ward, Y., Young, R.J., and Shatwell, R.A., A microstructural study of silicon carbide fibres through the use of Raman microscopy. *Journal of Materials Science*. **36** [1]2001: p. 55-66.
376. Tuinstra, F. and Koenig, J.L., Raman Spectrum of Graphite. *The Journal of Chemical Physics*. **53** [3]1970: p. 1126-1130.
377. Lähnemann, J., Jahn, U., Brandt, O., Flissikowski, T., Dogan, P., and Grahn, H.T., Luminescence associated with stacking faults in GaN. *Journal of Physics D: Applied Physics*. **47** [42]2014: p. 423001.
378. Tank Karan, C., Bhoraskar, S.V., and Mathe, V.L., Growth of faceted SiC nanostructures using vapor phase condensation: Microstructural analysis. *Materials Characterization*. **136** 2018: p. 240-246.
379. Zayachuk, Y., Karamched, P., Deck, C., Hosemann, P., and Armstrong, D.E.J., Linking microstructure and local mechanical properties in SiC-SiC fiber composite using micromechanical testing. *Acta Materialia*. **168** 2019: p. 178-189.
380. Stinton, D.P., Hembree, D.M., More, K.L., Sheldon, B.W., Besmann, T.M., Headinger, M.H., and Davis, R.F., Matrix characterization of fibre-reinforced SiC matrix composites fabricated by chemical vapour infiltration. *Journal of Materials Science*. **30** [17]1995: p. 4279-4285.
381. Lide, D.R. and Kehiaian, H.V., *CRC Handbook of Thermophysical and Thermochemical Data*. 1994: Taylor & Francis.
382. Patterson, A.L., The Scherrer Formula for X-Ray Particle Size Determination. *Physical Review*. **56** [10]1939: p. 978-982.
383. Dong, S.M., Chollon, G., Labrugère, C., Lahaye, M., Guette, A., Bruneel, J.L., Couzi, M., Naslain, R., and Jiang, D.L., Characterization of nearly

stoichiometric SiC ceramic fibres. *Journal of Materials Science*. **36** [10]2001: p. 2371-2381.
384. Corporation, O., Origin(Pro). 2019b: Northampton, MA, USA.
385. Kabusa, Dielectric Constants of Common Materials.
386. May, E.F., Moldover, M.R., and Schmidt, J.W., Reference measurements of hydrogen's dielectric permittivity. *Molecular Physics*. **107** [15]2009: p. 1577-1585.
387. Hector, L.G. and Schultz, H.L., The Dielectric Constant of Air at Radiofrequencies. *Physics*. **7** 1936: p. 133-136.
388. E. Li, Z.N., G. Guo, and Q. Zhang, Broadband measurements of dielectric properties of low-loss materials at high temperatures using circular cavity method. *Progress In Electromagnetics Research*. **92** 2009: p.
389. Tamang, S., Aravindan, S., 3D numerical modelling of microwave heating of SiC susceptor. *Applied Thermal Engineering*. **162** 2019: p. 114250.
390. Smith, R.L., Iskander, M.F., Andrade, O., and Kimrey, H., Finite-Difference Time-Domain (FDTD) Simulation of Microwave Sintering in Multimode Cavities. *MRS Proceedings*. **269** 2011: p. 47.
391. Docekal, B., Broekaert, J.A.C., Graule, T., Tschöpel, P., and Tölg, G., Determination of impurities in silicon carbide powders. *Fresenius' Journal of Analytical Chemistry*. **342** [1]1992: p. 113-117.
392. Casady, J.B. and Johnson, R.W., Status of silicon carbide (SiC) as a wide-bandgap semiconductor for high-temperature applications: A review. *Solid-State Electronics*. **39** [10]1996: p. 1409-1422.
393. Chalker, P.R., Wide bandgap semiconductor materials for high temperature electronics. *Thin Solid Films*. **343-344** 1999: p. 616-622.
394. Diaham, S., Locatelli, M.-L., and Valdez-Nava, Z., Dielectrics for High Temperature SiC Device Insulation: Review of New Polymeric and Ceramic Materials. 2011.
395. Yuan, Y. and Lee, T.R., Contact angle and wetting properties, in *Surface science techniques*. 2013, Springer. p. 3-34.
396. Gillis, J., Contact angle. 2006.
397. Bejan, A., *Convection heat transfer*. 2013: John wiley & sons.
398. Zhou, J.-Q., Chen, Y.-F., Wang, L., and Cardenas, M.B., Universal Relationship Between Viscous and Inertial Permeability of Geologic Porous Media. *Geophysical Research Letters*. **46** [3]2019: p. 1441-1448.
399. Zhong, W., Ji, X., Li, C., Fang, J., and Liu, F., Determination of Permeability and Inertial Coefficients of Sintered Metal Porous Media Using an Isothermal Chamber. *Applied Sciences*. **8** [9]2018: p. 1670.
400. Sciti, D., Silvestroni, L., Monteverde, F., Vinci, A., and Zoli, L., Introduction to H2020 project C3HARME – next generation ceramic composites for combustion harsh environment and space. *Advances in Applied Ceramics*. **117** [sup1]2018: p. s70-s75.
401. Zhou, W., Long, L., Xiao, P., Jia, C.-k., and Li, Y., Comparison in dielectric and microwave absorption properties of SiC coated carbon fibers with PyC and BN interphases. *Surface and Coatings Technology*. **359** 2019: p. 272-277.
402. Key, T.S., Ross, A., Wolford, I.M., Mogeleveski, P., Compostional analysis of Commerical SiC Fibres, M.a.M. Directorate, Editor. 2017.

403. Han, T., Luo, R., Cui, G., and Wang, L., Effect of SiC nanowires on the high-temperature microwave absorption properties of SiCf/SiC composites. *Journal of the European Ceramic Society*. **39** [5]2019: p. 1743-1756.
404. Liu, H., Cheng, H., Wang, J., and Tang, G., Dielectric properties of the SiC fiber-reinforced SiC matrix composites with the CVD SiC interphases. *Journal of Alloys and Compounds*. **491** [1]2010: p. 248-251.
405. Duan, S., Zhu, D., Jia, H., Zhou, W., and Luo, F., Enhanced mechanical and dielectric properties of SiCf/SiC composites with silicon oxycarbide interphase. *Ceramics International*. **44** [1]2018: p. 631-637.
406. D., L. Ceramic matrix composites take flight in LEAP jet engine. 2017; Available from: https://phys.org/news/2017-01-ceramic-matrix-composites-flight-jet.html.
407. Kellner, T., Space Age Ceramics Are Aviation's New Cup Of Tea, G. Reports, Editor. 2016.
408. Verrilli, M.J., Martin, L.C., and Brewer, D.N., RQL sector rig testing of SiC/SiC combustor liners. 2002: p.